Development of a Non-Crimp Fabric Carbon Fiber/Epoxy Composite Technology Demonstrator

by

Pravin Gopal Samy Dharmaraj

A thesis
presented to the University of Waterloo
in fulfillment of the
thesis requirement for the degree of
Master of Applied Science
in
Mechanical and Mechatronics Engineering

Waterloo, Ontario, Canada, 2020

AUTHORS DECLARATION

I hereby declare that I am the sole author of this thesis. This is a true copy of the thesis, including any required final revisions, as accepted by my examiners.

I understand that my thesis may be made electronically available to the public.

Abstract

To achieve the emission and fuel efficiency targets proposed by various regulatory bodies around the world, automotive manufacturers have shifted towards utilization of advanced lightweight materials for automotive structural applications. Owing to high specific mechanical properties and energy absorption characteristics, fiber-reinforced plastic (FRP) composites possess a high potential to replace current steel and aluminum structures in automobiles. Recent developments in cost effective unidirectional (UD) non-crimp fabrics (NCFs), rapid curing resins and automated fabrication processes such as high-pressure resin transfer molding (HP-RTM) or liquid compression molding (LCM) may accelerate the integration of FRP composites into the structures of high volume production vehicles. This thesis investigates the application of carbon fiber reinforced plastic (CFRP) composites in automotive primary frontal crash structures for energy management and light weighting applications. A robust computational modelling strategy was developed for predicting the crash performance of UD-NCF composite components and validated by utilizing available experimental data. The suitability of using NCF CFRP composite materials for a developed front-end energy absorbing technology demonstrator was numerically evaluated based on the New Car Assessment Program (NCAP) test configurations.

To numerically evaluate the performance of an NCF composite material, two macroscale constitutive models were chosen from the composite material library available in the commercial finite element software LS-DYNA (Livermore Software Technology Corporation, Stuttgart). In addition to calibrating ply-level material properties, the existing material models rely on non-physical parameters that must be calibrated using component-level test data. In this study, an NCF composite hat channel component fabricated using HP-RTM was used for this purpose. A stacking sequence of $[0/\pm45/90]_s$ was used for the hat channel component, which was subjected to an axial crush force under dynamic loading rate. The numerically predicted force-displacement profile was evaluated until a good correlation was obtained with the experimental test data. To validate the calibrated material models, a similar hat channel component with a $[\pm45/0_2]_s$ stacking sequence subjected to an axial crush force under dynamic loading rate was simulated and compared against corresponding experimental test data. Two additional simulations were conducted for the same hat channel components with the same stacking sequences under quasi-static condition to further validate the impact simulation model. A good correlation was obtained between the predicted and experimental crush response, crush force and energy absorption.

The next step in the study utilized the validated impact simulation model to design a vehicle frontal crash structure technology demonstrator comprised of the HP-RTM NCF composite material. Using a full-frontal steel structure from a production vehicle as a baseline, a simplified laboratory scale technology demonstrator of 525 mm length was developed, which comprised of redesigned frontal sub-assembly components to accommodate the design of the composite crush rails. Four different technology demonstrator concepts were designed based on the manufacturing feasibility, and the impact performance of each design concept was numerically simulated. Evaluating the performance of the designed composite technology demonstrator against the baseline hot stamped steel by considering overall deformation mode, crush force, energy absorption and deceleration profiles demonstrated that NCF composites provided increased energy absorption capabilities. Furthermore, the effect of stacking sequence and total laminate thickness for the chassis frame were shown to have a notable influence on the predicted crash performance and energy absorption, with similar crush response. Finally, the laminate of the chassis frame was tailored by considering a variation in the numbers of plies across the part by invoking a ply drop off scheme, resulting in a thinner crushable region for energy absorption and a thicker region with high rigidity for intrusion resistance.

The crash performance evaluated, and results supported the suitability of composites in energy absorbing and intrusion management of composites in automotive frontal crash applications. These numerical models predicted that NCF composite structure was 29% (1.6 kg) lighter than the hot-stamped steel structure and 48% (3.7 kg) lighter than a conventional baseline steel structure. In addition to weight savings, the proposed composite primary chassis frame reduced the number of components from three to two. In future work, different loading conditions and experimental tests will be conducted to support the numerical simulations of this thesis.

Acknowledgements

Dedication

To my parents, Dharmaraj and Sasirekha

Table of Contents

List of Figures

List of Tables

List of Abbreviations

BIW	Body in White
CAFE	Corporate Average Fuel Economy
CFRP	Carbon Fiber Reinforced Plastic
CLPT	Classical Laminate Plate Theory
CZM	Cohesive Zone Model
DCB	Double Cantilever Beam
ENCAP	European New Car Assessment Program
ENF	End Notched Flexure
FF	Puck's Fiber Fracture Criterion
FMVSS	Federal Motor Vehicle Safety Standard
FRP	Fiber Reinforced Plastic
GFRP	Glass Fiber Reinforced Plastic
HP-RTM	High Pressure Resin Transfer Molding
IFF	Puck's Inter-Fiber Fracture Criterion
IIHS	Insurance Institute of Highway Safety
LCM	Liquid Compression Molding
LDV	Light Duty Vehicle
NCAP	New Car Assessment Program
NCF	Non-Crimp Fabric
NHTSA	National Highway Traffic Safety Administration
RTM	Resin Transfer Molding
UD	Unidirectional
VCCT	Virtual Crack Closure Technique

Chapter 1
Introduction

1.1 Research Motivation

In recent years, Corporate Average Fuel Economy (CAFE) regulations in the United States and other regulations legislated in Canada, Asia and Europe aim to reduce CO_2 emissions and improve the fuel economy of passenger vehicles [1]-[4]. These strict regulations impose a significant pressure among the automotive manufactures to continuously meet the fuel standards to avoid monetary penalties. The National Highway Traffic Safety Administration (NHTSA) has reported the average fuel economy of light duty vehicles (LDVs) will increase by 28% from 2017 to 2025 (39.6-40.1 mpg to 55.3-56.2 mpg). Correspondingly, during the same time frame the fuel economy of light trucks (including sport utility vehicles) will increase by 26% (29.1-29.4 mpg to 39.3-40.3 mpg) [5].
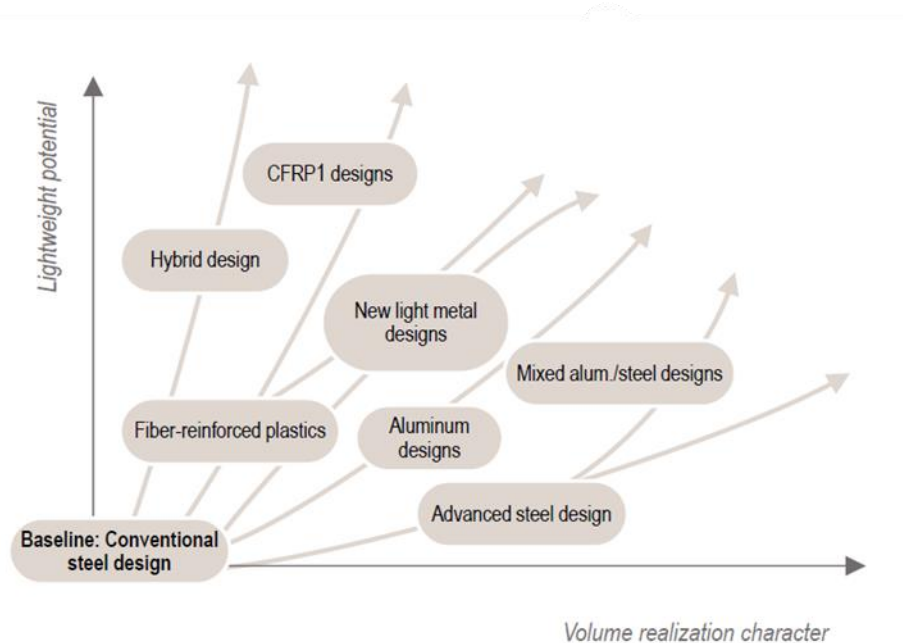
Figure 1. The potential of using carbon fiber reinforced plastics and other conventional materials for lightweight applications [6].

Automakers are developing new techniques to increase the fuel efficiency of vehicles, including improving the aerodynamic efficiency by reducing drag, optimizing the designs of power trains and reducing the body-in-white (BIW) mass of the vehicle [7]. The reduction of the overall vehicle mass by 10% can reduce the fuel consumption by 6-8% [8]. This potential impact of light weighting has led to

substantial research and development in the field of advanced materials for vehicles, with the challenges of maintaining vehicle performance and safety standards at the forefront. Alternative materials such as advanced steel, aluminium, magnesium and fiber reinforced composites have been considered light weighting [9]. Carbon fiber reinforced plastic (CFRP) composite materials (Figure 1) are regarded as a key material to significantly reduce the weight of vehicles, owing to their high specific strength and stiffness. CFRP composites possess additional advantages compared to conventional metallic materials, including high fatigue performance, superior corrosion resistance and excellent energy absorption capabilities [10], [11].
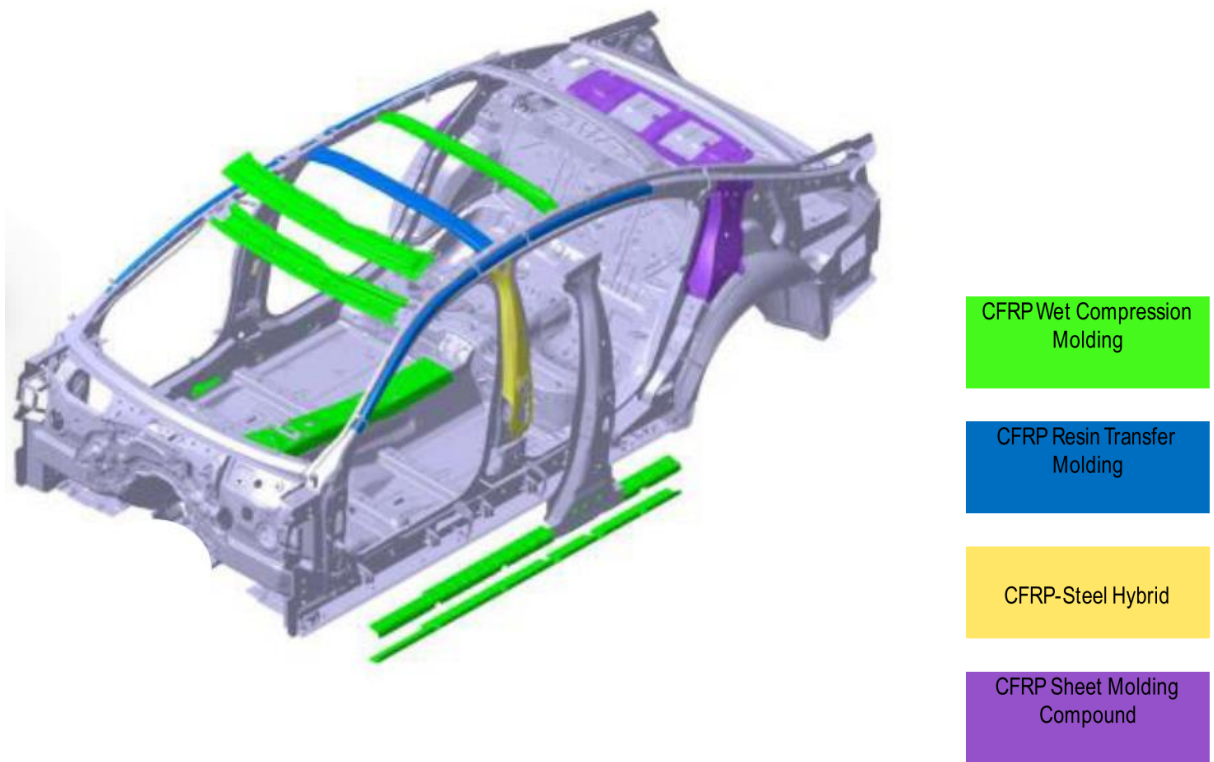
Figure 2. CFRP components integrated in the body-in-white structure of a BMW 7 Series vehicle [12].

CFRPs materials have already been incorporated in vehicle BIW structures as reinforcement panels and non-structural panels, including luxury vehicles such as the BMW 7 series (Figure 2), BMW i3 [12] and Audi A8 [13]. However, usage of CFRPs in vehicle BIW structures is currently limited to luxury and super car models [14] where the manufacturing cost and longer production cycles are acceptable. Conventionally, the CFRP composite parts has been manufactured by various process including compression molding, autoclave curing and resin transfer molding (RTM). These processing methods require several hours for a

processing cycle, which is not suitable for high volume production parts. Although the excellent energy absorption capabilities of CFRP material was established by many researchers [8][10][14] , these advanced materials have not been used for crash energy absorption application in high volume production vehicles. The development of new rapid curing resins, low cost heavy-tow unidirectional (UD) non-crimp fabrics (NCFs) and advanced manufacturing processes such as high pressure resin transfer molding (HP-RTM) [15] and liquid compression molding (LCM) provide a promising opportunity to enable the integration of CFRP composite materials into load-bearing structural components within high volume production vehicles. By implementing an automated HP-RTM process with rapid curing resins, the cycle time of a production CFRP part can be reduced to minutes.
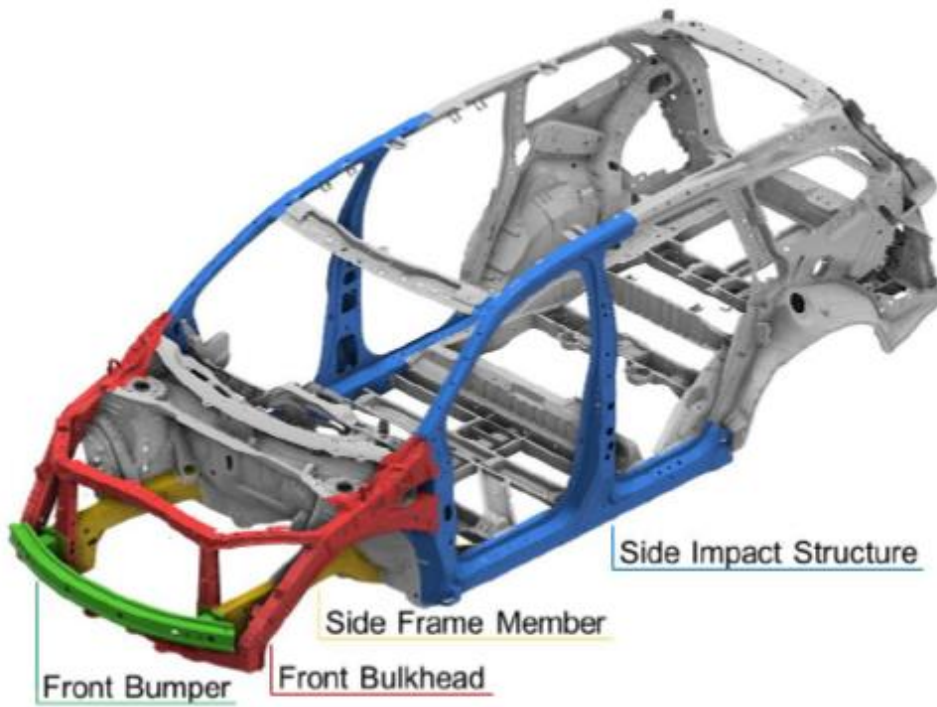
Figure 3. BIW structure of an LDV showing different components in the frontal region[16].

One promising application for CFRPs in high volume production vehicles is for energy absorbing structures, such as the front crush rails (yellow part in Figure 3). The main mechanism of energy absorption in CFRP frontal structures under axial crushing is through formation of multiple cracks. The anisotropic behavior and heterogeneity of CFRP composites result in complex failure processes such as fragmentation and splaying, which stem from local matrix cracking, fiber breakage and delamination [17]-[20]. Thus, predicting the failure behavior of CFRP structures is difficult but necessary to improve the fidelity computer

aided engineering (CAE) crash simulation models. It is especially important to accurately predict the performance of CFRP structures during earlier stages of vehicle development to optimize designs for improving passenger safety and reducing production cost/time prior to full vehicle crash testing. In recent years, suitable material models for composite materials have been integrated into commercial finite element (FE) codes [21], which has improved the prediction capabilities of the impact performance of composite structures. However, most of these models are limited to predicting the linear behavior of composite materials and are not directly suitable for crash applications [22] without extensive calibration.

1.2 Research objectives

There is considerable interest among automakers to incorporate CFRP composite components into LDVs. Development of advanced manufacturing techniques (e.g., HP-RTM) have accelerated the cycles times of CFRP components to the level that may be acceptable in a high-volume production automotive vehicle. The overarching goal of this research is to integrate CFRP materials into the front energy absorbing structure of high-volume production vehicles. The main objectives of this research thesis are summarized below.

- ❖ Develop a numerical modelling strategy to assess the crash performance of HP-RTM fabricated CFRP composite components comprised of a carbon fiber NCF and snap curing epoxy resin to aid in the development of corresponding composite structures.

- ❖ Validate the developed numerical model using available experimental data for NCF carbon fiber/epoxy components under impact loading conditions.

- ❖ Use the validated numerical model to design a CFRP vehicle frontal crush structure technology demonstrator to determine the suitability of using CFRPs for a primary energy absorbing structure compared to a baseline steel structure.

1.3 Outline of thesis

This thesis has been organized into nine chapters to document the design and development of the CFRP composite technology demonstrator. In Chapter 2, background, and literature review relevant to modelling continuous fiber-reinforced plastic (FRP) composites are presented, where the research limitations and gaps are identified. In Chapter 3, the existing material models available in the commercial explicit finite element code LS-DYNA (Livermore Software Technology Corporation, Stuttgart) are described, and selected

material models (constitutive equations) and material parameters are discussed. LS-DYNA is widely used in the automotive sector to perform full-scale vehicle crash simulation and as a result was the focus of this thesis. In Chapter 4, the development of the numerical modelling strategy for composites and boundary conditions used to model axial crush of a hat channel component is presented. In Chapter 5, the chosen material model calibration details, and the results of numerical and experimental axial crush simulations for hat channel components are compared and presented. In Chapter 6, the development and design stages of a CFRP frontal crush structure demonstrator is presented. In Chapter 7, the numerical results for each stage of the developed CFRP technology demonstrator are presented and compared to a conventional steel structures. In Chapter 8, the key research findings and results are discussed. Finally, conclusions and recommendations are provided in Chapter 9.

Chapter 2
Background and Literature Review

This chapter details the background and relevant studies to evaluate the performance of fiber-reinforced plastic (FRP) composite structures. First, a general overview of FRPs is provided, followed by details of damage mechanics, failure criteria and the parameters affecting the failure of FRP composites. In Section 2.2, the outcome of a conducted literature review focused on various modelling strategies for assessing the performance of composite materials and components is presented. Finally, a literature survey focused on predicting the impact performance of FRP automotive components is presented in Section 2.3.

2.1 Overview of Continuous Fiber Reinforced Composites

FRPs are heterogeneous materials composed of a high strength fiber phase and a binding matrix phase. The fibers are main load carrying phase of the FRP material that provide a high stiffness along the fiber direction, while the matrix phase holds the fibers in place and transfers load to the fibers through the phase interfaces [23]-[25]. However, the strength and stiffness of laminated FRP composites are largely dependent on fiber orientation and the laminate stacking. By altering the fiber orientation and stacking sequence, the anisotropic mechanical properties of laminated composite materials can be tailored. There are many types of reinforcement fibers available, such as 2D and 3D woven fabrics, braided fabrics and UD-NCFs. Woven fabrics are the most common and are formed by interlacing the fiber yarns along two orthogonal directions, denoted as wrap and weft, leading to a 2D fabric with crimped yarns. 2D woven fabrics are broadly classified based on the different patterns of warp and weft weavings [26]. The most common types of 2D woven fabrics are plain, twill and satin weaving fabrics (Figure 4).
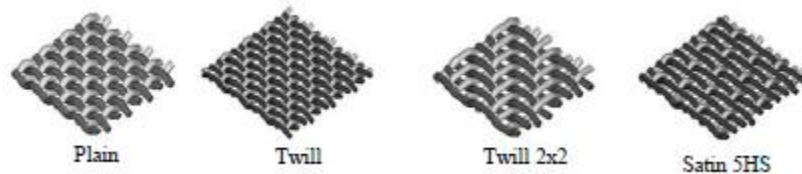
Figure 4. Types of 2D woven fabrics [26].

UD-NCFs possess several advantages when compared to woven fabrics, including superior in-plane properties due to the ideally non-crimped fiber tows and good drapability [27]. The fiber tows are evenly spaced and oriented along the single direction and held together with stitching yarn (Figure 5).

Several multi-directional layers can be combined to tailor the mechanical properties of the laminate. Another important characteristic of UD-NCFs is the potential for an increased number of filaments per tow, which allows for a reduced fabric cost. So-called heavy-tow UD-NCFs may contain up to 50,000 filaments per tow, which have been used for automotive applications [28],[29]where cost is critical.
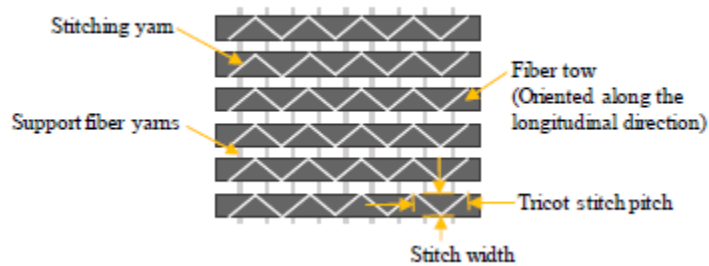
Figure 5. Schematic of a unidirectional non-crimp fabric [29].

For a typical HP-RTM process (Figure 6), the preformed dry fabric layers are placed in a closed mold cavity where the highly reactive premixed resin and hardener is injected under a high flow rate and pressure and allowed to rapidly cure [28]. Thus, HP-RTM has attracted much interest in the automotive industry due to short cycles times [30].
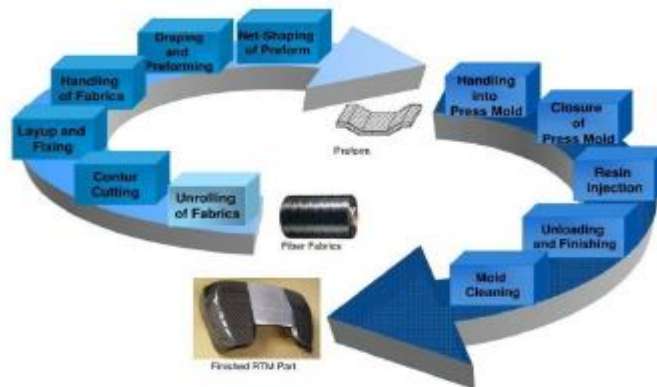
Figure 6. HP-RTM manufacturing process – from fiber fabric to finished HP-RTM part [31].

2.1.1 Mechanics of Fiber Reinforced Plastic Composites

Continuous FRP laminated composite materials are comprised of many layers and are generally regarded as anisotropic. A lamina (also denoted as a ply or layer) may exhibit either a linear elastic response until failure or an elastic-inelastic response prior to failure, which may vary along different material directions. In this study, the so-called 'pre-peak' response of a lamina may undergo two stages of deformation: (i)

7

linear elastic and (ii) inelastic (i.e., pre-peak softening). This section will focus on linear elasticity of an effectively homogeneous lamina and the associated response of laminates. For the purposes of numerical simulations, the 'post-peak' response is often considered; however, this will be discussed in Chapter 3.

The linear elastic anisotropic response of FRPs are governed by three-dimensional generalized Hooke's law, as per the following set of equations represented using index notation:

$$\sigma_{ij} = C_{ijkl}\varepsilon_{kl} \tag{2.1}$$

Here, σ_{ij} represents the components of the second order Cauchy stress tensor, C_{ijkl} represents the fourth order homogenized elastic tensor components and ε_{kl} represents components of the second order infinitesimal strain tensor, where indices $i, j, k, l = 1, 2, 3$. There are 81 components for the elastic tensor for a fully anisotropic material. On applying the principle of equilibrium, symmetry of the stress tensor can be deduced. If symmetry of the strain tensor is also assumed, then the elastic tensor must be symmetric and the number of independent constants are reduced to 21. For unidirectional composites, such as UD-NCF lamina, the existence of three mutually orthogonal planes of material symmetry leads to an orthotropic material response, which further reduces the independent components of the elastic tensor to 9. For a UD lamina the local material coordinate system can be defined based on the 1, 2, 3 indices, with 1 representing the fiber direction, 2 the in-plane transverse fiber direction and 3 the out-of-plane direction (Figure 7a). Stress and strain tensors can be representing in vector form allowing for reduced (Voigt) notation by assuming the following definitions for the indices of the stress, strain and elastic tensors: $11 = 1$, $22 = 2$, $33 = 3$, $23 = 4$, $13 = 5$ and $12 = 6$. The stress-strain relations for a three-dimensional orthotropic lamina in reduced notation is defined as [30]:

$$\begin{bmatrix} \sigma_1 \\ \sigma_2 \\ \sigma_3 \\ \sigma_4 \\ \sigma_5 \\ \sigma_6 \end{bmatrix} = \begin{bmatrix} C_{11} & C_{12} & C_{13} & 0 & 0 & 0 \\ C_{12} & C_{22} & C_{23} & 0 & 0 & 0 \\ C_{13} & C_{23} & C_{33} & 0 & 0 & 0 \\ 0 & 0 & 0 & C_{44} & 0 & 0 \\ 0 & 0 & 0 & 0 & C_{55} & 0 \\ 0 & 0 & 0 & 0 & 0 & C_{66} \end{bmatrix} \begin{bmatrix} \varepsilon_1 \\ \varepsilon_2 \\ \varepsilon_3 \\ \epsilon_4 \\ \varepsilon_5 \\ \varepsilon_6 \end{bmatrix} \tag{2.2}$$

$$C_{ij} = S_{ij}^{-1} \tag{2.3}$$

8

where C_{ij}, represents the components of the elastic tensor and S_{ij}, are the compliance tensor components. The compliance matrix components, S_{ij}, can be written in terms of the orthotropic elastic constants as follows [25]:

$$S_{11} = \frac{1}{E_{11}}, S_{22} = \frac{1}{E_{22}}, S_{33} = \frac{1}{E_{33}}$$ (2.4)

$$G_{23} = \frac{1}{S_{44}}, G_{13} = \frac{1}{S_{55}}, G_{12} = \frac{1}{S_{66}}$$ (2.5)

$$v_{23} = -\frac{S_{23}}{S_{22}}, v_{13} = -\frac{S_{13}}{S_{11}}, v_{12} = -\frac{S_{12}}{S_{11}}$$ (2.6)

Here, E_i, G_{ij} and v_{ij} respectively represent the Young's moduli, shear moduli and Poisson's ratios of the effectively homogeneous lamina with respect to the local material coordinate system.

(a) (b)
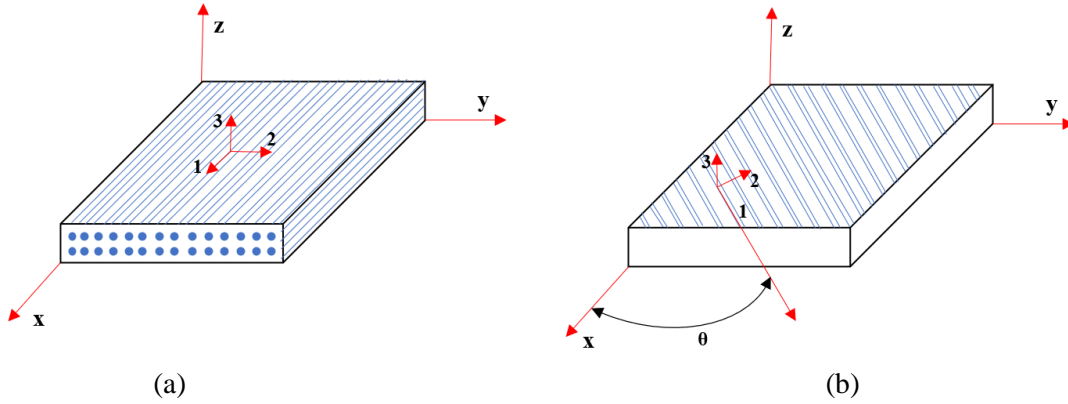
Figure 7. (a) Local material coordinate system for a UD composite (lamina), and (b) orientation of UD lamina with respect to laminate coordinate system.

If the orthotropic lamina is thin, one can assume plane stress conditions for the lamina. Therefore, by setting the out-of-plane stresses to zero, Equation 2.2 is reduced from three dimensions to two dimensions:

$$\begin{bmatrix} \sigma_1 \\ \sigma_2 \\ \sigma_{12} \end{bmatrix} = \begin{bmatrix} Q_{11} & Q_{12} & 0 \\ Q_{12} & Q_{22} & 0 \\ 0 & 0 & Q_{66} \end{bmatrix} \begin{bmatrix} \varepsilon_1 \\ \varepsilon_2 \\ \gamma_{12} \end{bmatrix}$$ (2.7)

9

The reduced stiffness matrix [Q] and components are written in terms of the in-plane lamina elastic constants [24]:

$$Q_{ij} = \begin{bmatrix} \frac{E_1}{1-v_{12}v_{21}} & \frac{v_{12}E_2}{1-v_{12}v_{21}} & 0 \\ \frac{v_{12}E_2}{1-v_{12}v_{21}} & \frac{E_2}{1-v_{12}v_{21}} & 0 \\ 0 & 0 & G_{12} \end{bmatrix} \tag{2.8}$$

For a laminate comprised of many lamina oriented along different directions, it becomes necessary to describe the orientation of each lamina with respect to the laminate coordinate system (see *x*, *y*, *z* in Figure 7b). The orientation of a lamina can be represented as a rotation about the *z*-axis by angle *θ* (see Figure 7.b). The transformation with respect to the laminate coordinate system leads to the following stress-strain relations [23]:

$$\begin{Bmatrix} \sigma_x \\ \sigma_y \\ \sigma_{xy} \end{Bmatrix} = [T_1]^{-1} [Q][T_2] \begin{Bmatrix} \varepsilon_x \\ \varepsilon_y \\ \gamma_{xy} \end{Bmatrix} = [\bar{Q}] \begin{Bmatrix} \varepsilon_x \\ \varepsilon_y \\ \gamma_{xy} \end{Bmatrix} \tag{2.9}$$

Here, $[T_1]$ is the stress transformation matrix and $[T_2]$ is the strain transformation matrix (Equations 2.10 and 2.11), $[\bar{Q}]$ represents the lamina transformed reduced stiffness matrix, $\sigma_x , \sigma_y , \sigma_{xy}$ denote the stresses in the laminate coordinate system and $\varepsilon_x, \varepsilon_y, \gamma_{xy}$ denote the strains in the laminate coordinate system.

$$[T_1] = \begin{bmatrix} m^2 & n^2 & 2mn \\ n^2 & m^2 & -2mn \\ -mn & mn & m^2 - n^2 \end{bmatrix} \tag{2.10}$$

$$[T_2] = \begin{bmatrix} m^2 & n^2 & mn \\ n^2 & m^2 & -mn \\ -2mn & 2mn & m^2 - n^2 \end{bmatrix} \tag{2.11}$$

In Equation 2.10 and 2.11, *m* and *n* denote the transformation coefficients where *m* = cos θ and *n* = sin θ.

In general, laminates are comprised of multiple stacked lamina oriented along different directions to tailor the material properties for a specific application. The elastic response of multi-directional laminates can be defined through Classical Laminate Plate Theory (CLPT) [32], where bending and stretching deformations of assumed thin plates are defined based on Kirchhoff's plate theory. CLPT assumes that the plies are perfectly bonded and under plane stress states, plies undergo linear elastic deformation with small strains and rotations, and that there are no out-of-plane strains [25] (Figure 8). Therefore, the deformation of the laminate can be reduced to a two-dimensional problem by considering the bending and stretching deformation of the laminate geometric mid-plane (Figure 8).

10

(a)

(b)

(c)
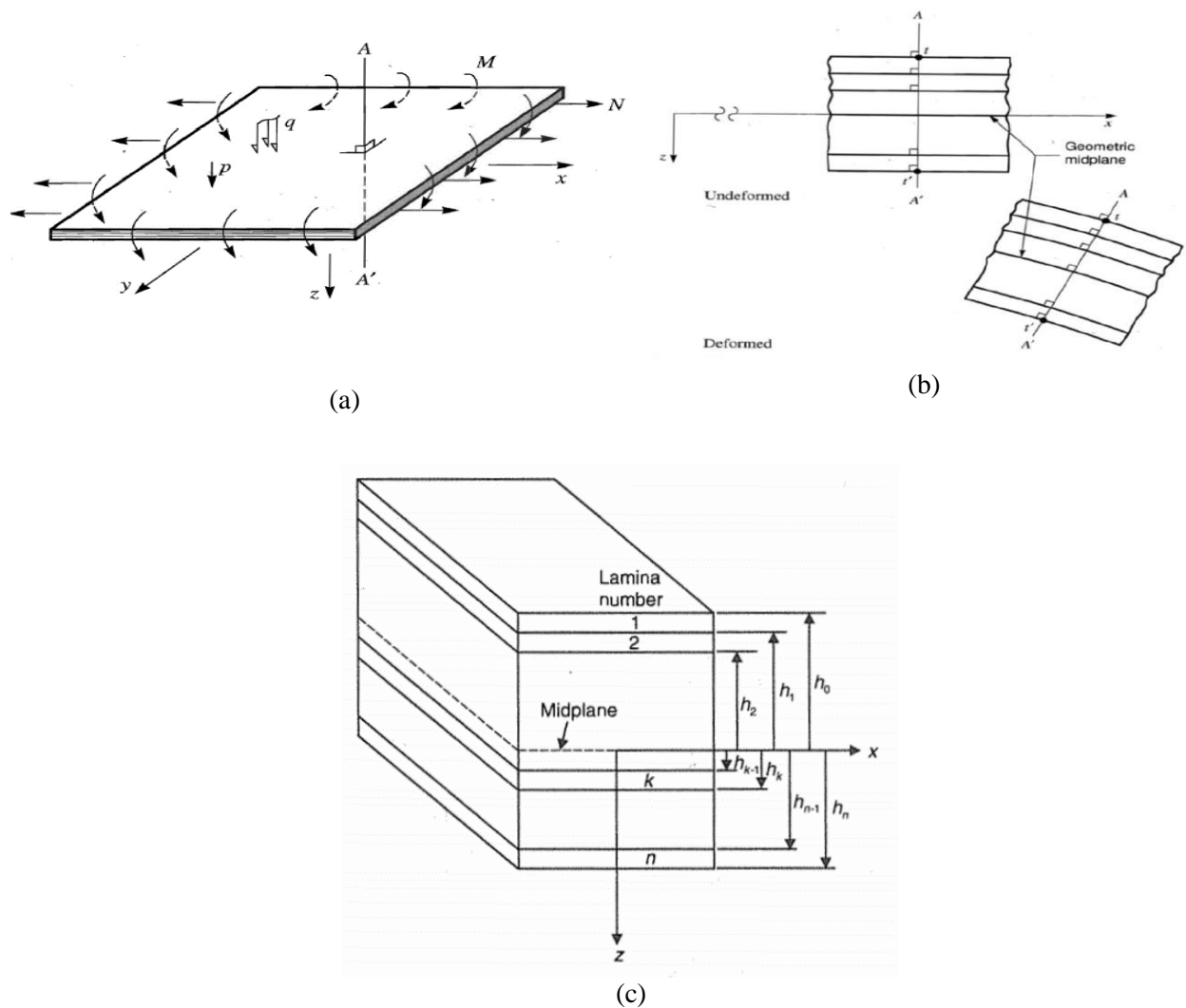
Figure 8. Schematic representation of a thin laminate plate: (a) external loading and resultant forces and moments, and (b) deformed and undeformed state (c) multilayered laminate geometry [25].

The strain distribution through the thickness of the laminate can be obtained from the laminate geometric mid-plane strains $\{\varepsilon^0\}$ and curvatures $\{\kappa^0\}$ and is dependent on the position z with respect to the mid-plane (Figure 8c). The strain distribution in terms of the laminate coordinate system is defined per the following:

$$\begin{Bmatrix} \varepsilon_x \\ \varepsilon_y \\ \gamma_{xy} \end{Bmatrix} = \begin{Bmatrix} \varepsilon_x^0 \\ \varepsilon_y^0 \\ \gamma_{xy}^0 \end{Bmatrix} + z \begin{Bmatrix} \kappa_x^0 \\ \kappa_y^0 \\ \kappa_{xy}^0 \end{Bmatrix} \tag{2.12}$$

The stress distribution for ply k with respect to the laminate coordinate system are calculated based in the strain distribution as follows:

$$\begin{Bmatrix} \sigma_x \\ \sigma_y \\ \sigma_{xy} \end{Bmatrix}_k = \begin{bmatrix} \overline{Q_{11}} & \overline{Q_{12}} & \overline{Q_{16}} \\ \overline{Q_{12}} & \overline{Q_{22}} & \overline{Q_{26}} \\ \overline{Q_{16}} & \overline{Q_{26}} & \overline{Q_{66}} \end{bmatrix}_k \begin{Bmatrix} \varepsilon_x^0 + z\kappa_x^0 \\ \varepsilon_y^0 + z\kappa_y^0 \\ \gamma_{xy}^0 + z\kappa_{xy}^0 \end{Bmatrix} \tag{2.13}$$

where $[\bar{Q}]_k$ is the transformed reduced stiffness matrix for ply k.

The mid-plane strains and curvatures can be evaluated by considering the resultant forces $\{N\}$ and moments $\{M\}$ acting on the laminate (Figure 8a). The laminate governing equations are defined as [24] :

$$\begin{Bmatrix} N \\ \cdots \\ M \end{Bmatrix} = \begin{bmatrix} A & B \\ \cdots & \cdots \\ B & D \end{bmatrix} \begin{Bmatrix} \varepsilon^0 \\ \cdots \\ \kappa^0 \end{Bmatrix} \tag{2.14}$$

The expanded form is shown in Equation 2.15.

$$\begin{Bmatrix} N_x \\ N_y \\ N_{xy} \\ M_x \\ M_y \\ M_{xy} \end{Bmatrix} = \begin{bmatrix} A_{11} & A_{12} & A_{16} & B_{11} & B_{12} & B_{16} \\ A_{12} & A_{22} & A_{26} & B_{12} & B_{22} & B_{26} \\ A_{16} & A_{26} & A_{66} & B_{16} & B_{26} & B_{66} \\ B_{11} & B_{12} & B_{16} & D_{11} & D_{12} & D_{16} \\ B_{12} & B_{22} & B_{26} & D_{12} & D_{22} & D_{26} \\ B_{16} & B_{26} & B_{66} & D_{16} & D_{26} & D_{66} \end{bmatrix} \begin{Bmatrix} \varepsilon_x^0 \\ \varepsilon_y^0 \\ \gamma_{xy}^0 \\ \kappa_x^0 \\ \kappa_y^0 \\ \kappa_{xy}^0 \end{Bmatrix} \tag{2.15}$$

$[A]$, $[B]$ and $[D]$ are the extensional stiffness, coupling stiffness and bending stiffness matrices of the laminate, respectively. The components of the $[A]$, $[B]$ and $[D]$ matrices are given by following expression [24]:

$$A_{ij} = \sum_{k=1}^{n} \left(\overline{Q_{ij}} \right)_k (z_k - z_{k-1}) \tag{2.16}$$

$$B_{ij} = \frac{1}{2} \sum_{k=1}^{n} \left(\overline{Q_{ij}} \right)_k (z_k^2 - z_{k-1}^2) \tag{2.17}$$

$$D_{ij} = \frac{1}{3} \sum_{k=1}^{n} \left(\overline{Q_{ij}} \right)_k (z_k^3 - z_{k-1}^3) \tag{2.18}$$

where Z_k denotes the distance from the laminate mid-plane to the bottom of ply k (Figure 8c).

The ply level stress and strain distributions can be computed along the local material directions by transforming the stresses and strains in the laminate coordinate system:

$$\begin{Bmatrix} \varepsilon_1 \\ \varepsilon_2 \\ \gamma_{12} \end{Bmatrix}_k = [T_2]_k \begin{Bmatrix} \varepsilon_x \\ \varepsilon_y \\ \gamma_{xy} \end{Bmatrix} \qquad (2.19)$$

$$\begin{Bmatrix} \sigma_1 \\ \sigma_2 \\ \sigma_{12} \end{Bmatrix}_k = [T_1]_k \begin{Bmatrix} \sigma_x \\ \sigma_y \\ \sigma_{xy} \end{Bmatrix} \qquad (2.20)$$

2.1.2 Intralaminar and Interlaminar Damage Mechanisms in Laminated FRP Composites

Laminated FRP composite materials with UD plies subjected to mechanical or thermal loading [33] may exhibit irreversible damage at different length scales, the form of which is dependent on the direction of loading (e.g., along or transverse to the fibers) and the type of loading (e.g., tension, compression and shear). Local damage may manifest as local matrix cracks, fiber breakage and fiber-matrix interface cracks, whereas failure of the laminate involves large scale damage at the macroscale. For analysis of laminated components using CLPT, it is convenient to represent damage within the lamina at the meso-scale, i.e., so-called intralaminar damage. In this context, damage that may occur between the plies of the laminate such as delamination can be regarded as interlaminar damage. The following sections describe intralaminar damage modes for UD lamina, as well as interlaminar delamination in laminated FRP composites.

2.1.2.1 Matrix Failure Mode

When a UD lamina undergoes a transverse compressive stress, the resulting damage is a ply crack that has an angle biased to the transverse direction (Figure 9a), and is referred to as compressive matrix failure mode. This failure mode is primarily driven by shearing along the fracture plane. However, when the UD lamina exhibits a transverse tensile stress, the resulting ply crack forms perpendicular to the transverse direction (Figure 9b) [34]. When a UD lamina is subjected to combined in-plane shear and transverse stresses, the corresponding fracture plane orientation angle may vary.

(a)   (b)

Figure 9. Matrix failure mode for a UD lamina: (a) transverse compression, and (b) transverse tension.

13

2.1.2.2 Fiber Failure Mode

If a UD lamina is subjected to a compressive stress along the fiber direction, failure typically occurs as a result of in-phase fiber micro-buckling caused by local matrix degradation, where a kink-band forms at an angle biased to the fiber direction (Figures 10a and 11a) [34]. The presence of fiber misalignment causes reduced lateral support to the fibers and the formation of kink bands at a lower stress levels [35].

(a)   (b)
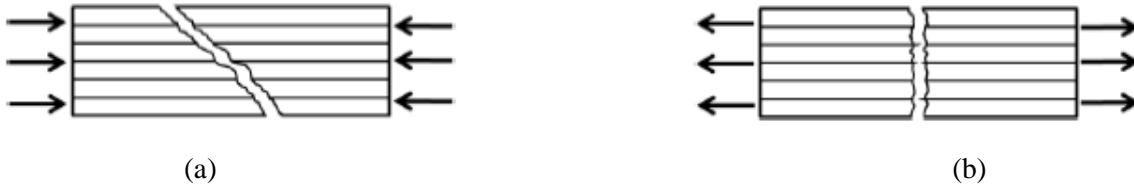
Figure 10. Fiber failure mode for a UD lamina: (a) longitudinal compression (b) longitudinal tension.

(a)   (b)
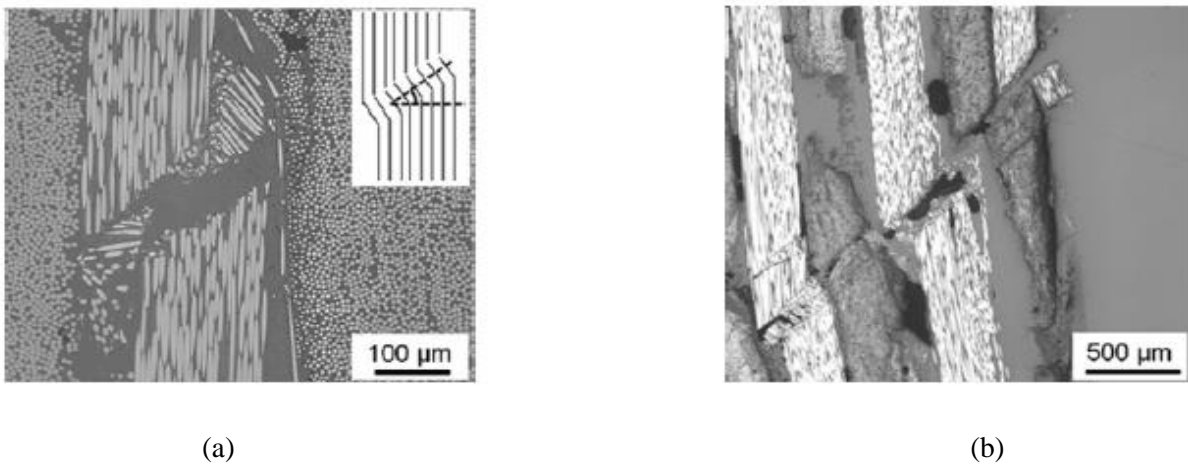
Figure 11. (a) Kink band formation in single UD ply of a laminate, and (b) kink band and matrix crack formation in several plies of a laminate [36].

Alternatively, when the UD lamina is subjected to a longitudinal tensile stress (Figure 10b), the fibers fail in a brittle manner with the fracture plane perpendicular to the loading direction.

2.1.2.3 Delamination

Under various in-service loading conditions laminated composites may be subjected to out-of-plane or interlaminar stresses, which can cause delamination cracks to form at the ply interfaces. The presence of delamination cracks in composite component have been reported to be a significant contributor of absorbed

14

energy [34] . Delamination cracks may form due to out-of-plane loading on the laminate, at the free end of a laminated component where out-of-plane stresses may be high, or caused by interactions with other failure modes. Figure 12 shows the formation of delamination cracks at the tips of through-thickness matrix cracks in composite laminate [37] .
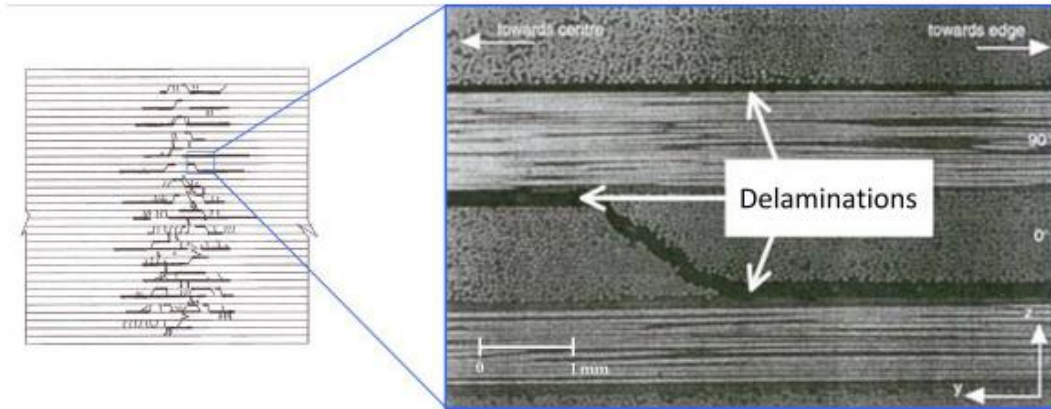
Figure 12. Delamination cracks forming from ply cracks in a cross ply laminate [37].

2.1.2.4 Impact loading of composites

For laminated composite materials subjected to impact loading, several failure modes are typically observed, which further complicates the prediction of damage and failure. Developing corresponding constitutive models that consider the loading rate, initiation and propagation of damage is less developed compared to other materials [38].

As an example, consider the evolution of damage for a flat CFRP cross-ply laminate plate subjected to low energy impact from a small mass as reported in Ref. [39] (Figure 13). At 5 J of impact energy, formation of transverse matrix cracks near the laminate geometric mid-plane induced by vertical bending were observed under the point of impact load. Delamination also formed at the interface of the 0° / 90° plies near the surface opposite from that impacted. Also, at 8 J of impact energy, more transverse matrix cracks were reported at the top and bottom plies of the laminate. Delamination cracks formed at the interface of the 0°/90° plies near the surface opposite from that impacted. Similarly, at 14 J of impact energy, larger cracks formed and extended. The delamination was evident at all the 0°/90° ply interfaces. Finally, at 20 J of impact energy multiple transverse matric cracks was found in the all the 0° plies and wide spread of delamination was evident in the interfaces and fiber breakage arose within all the 90° plies.
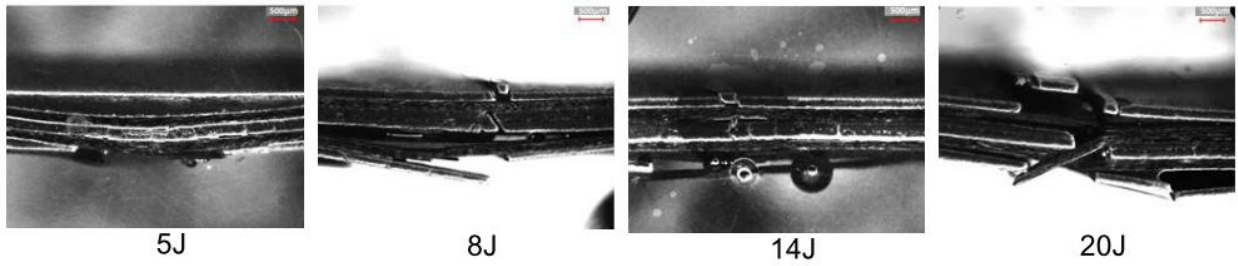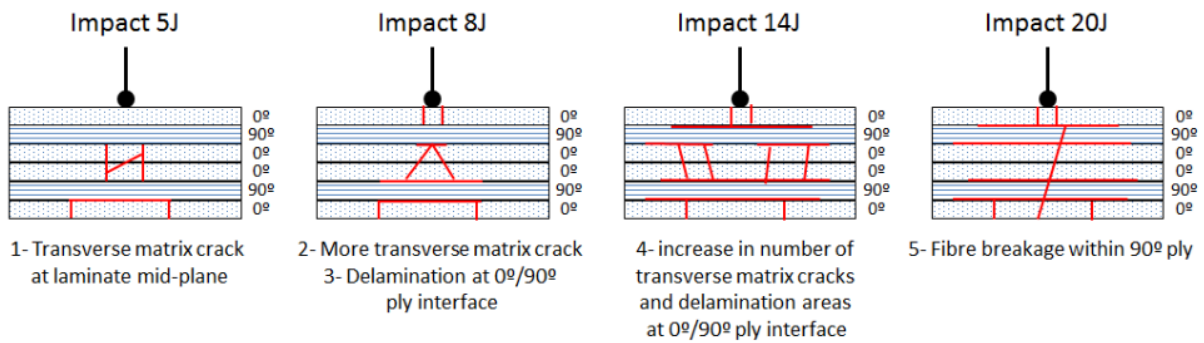
Figure 13. (a) Through-thickness micrographs of impact damage, and (b) schematic of impact damage at impact loading point [39].

2.1.3 Modelling Failure in Composites

Numerous failure criteria have been developed to predict failure of composite materials when subjected to multiaxial stress states, and have been utilized at the lamina level. The failure theories can be classified as interactive or non-interactive, and mode dependent or independent. Mode dependent failure theories consider the intralaminar failure modes that were presented in Section 2.1.2, while mode independent failure theories do not account for these modes of failure. The non-interactive failure theories are mainly stress based and only consider failure based on the stress component along a particular material direction, like the maximum stress and maximum strain theories [38]. The interactive failure theories account for multiaxial stress states, like the Tsai-Wu and Tsai-Hill failure theories. Well-known failure theories such as Hashin, Puck and Chang-Chang are interactive and failure mode dependent.

16

2.1.3.1 Tsai-Wu Failure Criteria

The Tsai-Wu failure theory is the improved form of the Tsai-Hill failure theory, whereby the stress-based polynomial function used distinguishes between tension and compression stresses [40]. For a plane stress condition, the quadratic polynomial is defined as:

$$F_1\sigma_1 + F_2\sigma_2 + F_{11}\sigma_1^2 + F_{22}\sigma_2^2 + F_{66}\sigma_{12}^2 + 2F_{12}\sigma_1\sigma_2 < 1 \tag{2.21}$$

The F_i and F_{ij} components of Equation 2.21 are functions of the lamina strengths and are defined by:

$$F_1 = \frac{1}{X_t} + \frac{1}{X_c} \tag{2.22}$$

$$F_2 = \frac{1}{Y_t} + \frac{1}{Y_c} \tag{2.23}$$

$$F_{11} = \frac{-1}{X_t X_c} \tag{2.24}$$

$$F_{22} = \frac{1}{Y_t Y_c} \tag{2.25}$$

$$F_{66} = \frac{1}{S_c^2} \tag{2.26}$$

$$F_{12} = \frac{-1}{2\sqrt{F_{11}F_{22}}} \tag{2.27}$$

Here, X_t and X_c are the longitudinal tensile and compressive strengths, Y_t and Y_c are the transverse tensile and compressive strengths, and S_c represents the in-plane shear strength. The Tsai-Wu failure surface for a $\sigma_1 - \sigma_2$ stress space is shown in Figure 14. Note, the Tsai-Wu failure criteria does not explicitly account for different failure modes and has no physical basis.
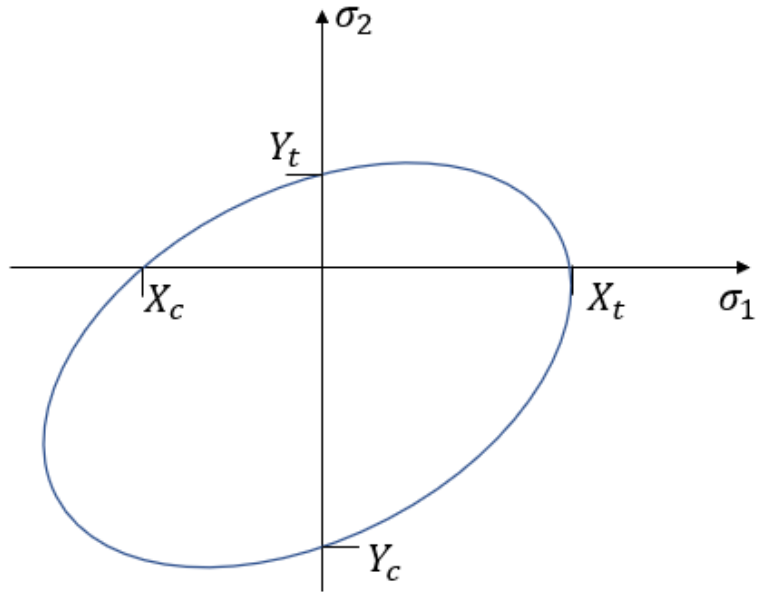
Figure 14. Tsai-Wu failure surface in a $\sigma_1 - \sigma_2$ stress space.

2.1.3.2 Hashin failure criteria

Hashin developed physically based failure criteria for UD lamina that account for different modes of failure, including matrix failure and fiber failure modes that correspond to those shown in Figures 9 and 10, respectively. Assuming plane stress conditions, Equation 2.28 and 2.31 describes the Hashin failure criteria for tensile fiber failure mode, compressive fiber failure mode, tensile matrix failure mode and compressive matrix failure mode, respectively. A piecewise continuous failure surface is defined by each expression.

$$\left(\frac{\sigma_1}{X_t}\right)^2 + \left(\frac{\sigma_{12}}{S_c}\right)^2 = 1 \tag{2.28}$$

$$\sigma_1 = Y_c \tag{2.29}$$

$$\left(\frac{\sigma_2}{Y_t}\right)^2 + \left(\frac{\sigma_{12}}{S_c}\right)^2 = 1 \tag{2.30}$$

$$\left(\frac{\sigma_2}{2S_c}\right)^2 + \left[\left(\frac{Y_c}{2S_c}\right)^2 - 1\right]\frac{\sigma_2}{Y_c} + \left(\frac{\sigma_{12}}{S_c}\right)^2 = 1 \tag{2.31}$$

2.1.3.3 Modified Hashin failure criteria

Hashin's failure criteria are the basis for many failure theories that have been developed. The modified Hashin criteria also considers four failure expressions for fiber and matrix failure modes, and are applicable for different lamina material systems such as woven and unidirectional. The criteria for tensile fiber failure mode, compressive fiber failure mode, tensile matrix failure mode and compressive matrix failure mode are respectively defined by:

$$e_f^2 = \left(\frac{\sigma_1}{X_t}\right)^2 - 1 \tag{2.32}$$

$$e_c^2 = \left(\frac{\sigma_2}{X_c}\right)^2 - 1 \tag{2.33}$$

$$e_m^2 = \left(\frac{\sigma_2}{Y_t}\right)^2 + \left(\frac{\sigma_{12}}{S_c}\right)^2 - 1 \tag{2.34}$$

$$e_d^2 = \left(\frac{\sigma_2}{Y_c}\right)^2 + \left(\frac{\sigma_{12}}{S_c}\right)^2 - 1 \tag{2.35}$$

2.1.3.4 Puck's Failure Criteria

Puck's failure criteria are stress-based criteria for UD lamina that distinguish between fiber failure (FF) and inter-fiber failure (IFF) or matrix modes. The representation of fracture planes for the IFF modes provides failure prediction for UD lamina with combined transverse and in-plane shear stresses [41]-[43].

The tension and compression FF modes were extended from Hashin criteria. It is assumed that a UD lamina fails in tension once the failure strain of the fibers is achieved. In compression, local shearing of the

matrix and fiber kinking is assumed to drive lamina failure. The tensile and compressive FF modes are respectively defined as:

$$\frac{1}{\varepsilon_{1t}^u}\left(\varepsilon_1 + \frac{v_{12f}}{E_{1f}}\, m_{\sigma f}\sigma_2\right) = 1 \tag{2.36}$$

$$\frac{1}{\varepsilon_{1c}^u}\left|\left(\varepsilon_1 + \frac{v_{12f}}{E_{1f}}\, m_{\sigma f}\sigma_2\right)\right| + (10\gamma_{12})^2 = 1 \tag{2.37}$$

where ε_{1t}^u represents the lamina ultimate tensile strength and ε_{1c}^u represents lamina ultimate compressive strength along the fiber direction, $m_{\sigma f}$ represents the stress magnification factor capturing differences in the fiber and matrix transverse stresses, E_{1f} represents the axial modulus of the fiber and v_{12f} represents the fiber Poisson's ratio.

The Inter-Fiber Failure (IFF) modes for UD lamina invoke the modified form of Mohr's failure theory for brittle materials. Three different failure modes are defined based on the combined transverse and shear stress state, with assumed fracture plane orientation as shown in Figure 15.

Mode A: It is invoked when $\sigma_2 > 0$

$$\sqrt{\left(\frac{\sigma_{12}}{S_c}\right)^2 \left(1 - p_{\perp\|}^{(+)} \frac{Y_t}{S_c}\right)^2 \left(\frac{\sigma_2}{Y_t}\right)^2} + p_{\perp\|}^{(+)} \frac{\sigma_2}{S_c} + \left|\frac{\sigma_1}{\sigma_{1D}}\right| = 1 \tag{2.38}$$

Mode B: It is invoked when $\sigma_2 < 0$ and the fracture plane is originated from σ_{12}

$$\frac{1}{S_c}\left(\sqrt{\sigma_{12}^2 + \left(p_{\perp\|}^{(-)}\sigma_2\right)^2} + p_{\perp\|}^{(-)}\sigma_2\right) + \left|\frac{\sigma_1}{\sigma_{1D}}\right| = 1 \tag{2.39}$$

Mode C: It is invoked when $\sigma_2 < 0$ and the fracture plane is originated from σ_2

$$\left[\left(\frac{\sigma_{12}}{2\left(1+p_{\perp\perp}^{(-)}\right)S_c}\right)^2 + \left(\frac{\sigma_2}{Y_c}\right)^2\right]\left(\frac{Y_c}{-\sigma_2}\right) + \left|\frac{\sigma_1}{\sigma_{1D}}\right| = 1 \tag{2.40}$$

Where σ_{1D} denotes the degraded stress and $p_{\perp\|}^{(+)}, p_{\perp\|}^{(-)}, p_{\perp\perp}^{(-)}$ denote empirical constants.
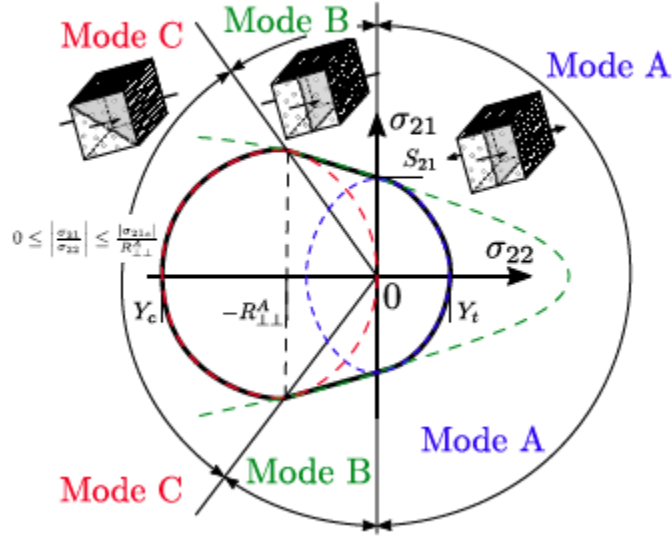
Figure 15. Failure surface for a UD lamina using Puck's IFF modes (Modes A, B and C) when $\sigma_1 = 0$ [41].

2.1.3.5 Chang-Chang failure criteria

The Chang-Chang failure criteria combine progressive damage, failure and degradation of the UD lamina properties beyond failure. For a plane stress condition, the Chang-Chang failure criteria for tensile fiber failure mode, compressive fiber failure mode, tensile matrix failure mode and compressive matrix failure mode are respectively defined by:

$$e_f^2 = \left(\frac{\sigma_1}{X_t}\right)^2 + \beta \left(\frac{\sigma_{12}}{S_c}\right)^2 - 1 \tag{2.41}$$

$$e_c^2 = \left(\frac{\sigma_1}{X_c}\right)^2 - 1 \tag{2.42}$$

$$e_m^2 = \left(\frac{\sigma_2}{Y_t}\right)^2 + \left(\frac{\sigma_{12}}{S_c}\right)^2 - 1 \tag{2.43}$$

21

$$e_d^2 = \left(\frac{\sigma_2}{2S_c}\right)^2 + \left[\left(\frac{Y_c}{2S_c}\right)^2 - 1\right]\frac{\sigma_2}{Y_c} + \left(\frac{\sigma_{12}}{S_c}\right)^2 - 1 \qquad (2.44)$$

Here, e_f, e_c, e_m, e_d represent the distinct failure criteria parameters for fiber and matrix failure modes in tension and compression, and β is the shear stress weighting factor which represents the influence of the shear stress on fiber tensile mode. When $\beta=0$, the expression reduces to the maximum stress criteria, whereas when $\beta=1$ it utilizes the Hashin failure criteria.

2.1.4 Delamination Modelling in Composites

Delamination cracking is considered to be a critical mode of failure when evaluating the performance of composite parts. Delamination cracks are usually represented in a numerical simulation model using either a cohesive zone model (CZM) or a fracture-based approach such as the virtual crack closure technique (VCCT) [44]-[51]. The required Mode I and Mode II traction-separation data for a CZM are obtained by conducting Double Cantilever Beam (DCB) and End-Notched Flexure (ENF) tests, respectively [52]-[53]. To utilize a CZM approach, plies in the laminate must be explicitly modeled and zero-thickness cohesive elements are imbedded at the ply interfaces [46]-[47] . The CZM formulations available in commercial finite element software LS-DYNA are described in the Section 3.5. Note, modelling each ply and the cohesive elements results in a computationally expensive numerical model.

2.1.5 Parameters Effecting Impact Damage

There are several parameters that influence the severity, shape, and distribution of impact-induced damage in laminated composite materials. The fiber and matrix properties, fiber volume fraction and fiber architecture greatly influence the impact damage. Other important parameters include the laminate stacking sequence, laminate thickness, type of loading and the loading rate (dynamic and quasi-static) [54]-[55]. The laminate stacking sequence can be used to tailor the performance and damage evolution of a laminated composite component.

Liu et al. [56] developed a theory to evaluate the effect of the relative angle between adjacent plies in a laminate on the delamination crack size, which compared well to the experiments. When the angle between adjacent plies was higher, the bending stiffness increased and delamination growth increased between those

plies, whereas no delamination was observed between adjacent plies with the same ply orientation. Hitchen et al. [57] suggested that placing ±45° plies on the outer surfaces of the laminate improved the damage tolerance. On increasing the number of dissimilar layers, the occurrence of delamination was reduced and improved the damage resistance of the laminate under compressive loads. However, when stacking a block of similar plies the formation of large cracks increased at the lamina interfaces, which intern enhanced intralaminar cracking in similar plies. Similar results were also represented by Sjogren et al. [58].

Olsson et al. [59] suggested that laminates with larger thickness tend to have delamination in conical distribution initiating from the impact center to the top surface. However, thin laminates tend to delaminate in a barrel pattern. The authors also suggested that increasing the thickness of the composite part increases the impact resistance force and energy absorption capabilities. Moreover, loading the laminate with a slow rate increased the degree of damage, which enhanced the energy absorption of the components. However, the mode of failure was also dependent on the loading rate.

2.1.6 Crashworthiness of FRP Composites

The frontal and rear chassis structure of a vehicle are designed to deform and absorb the kinetic energy by axially crushing, while also preventing intrusion into the cabin of the vehicle [60]to prevent passenger injuries. A typical force-displacement response for a component subjected to an axial crush load is shown in Figure 16. The main zones include initial peak force and the mean or stable crushing zone where the force is almost remains constant. The initial force peak is higher since failure modes are not triggered in component at that stage. The zone between the peak force and stable crush zone is the transition zone, which is highly dependent on the manner that crushing is triggered. The peak force is a critical parameter, which represents the high force experienced during initial crushing. The stable crush force, F_{mean}, is defined as the average force during stable crush over the specimen length l (Equation 2.45). The energy absorption, EA, of a structure is calculated from the total area under the force-displacement curve (Equation 2.46). The specific energy absorption, SEA, is the energy absorbed per unit mass (m) of crushed structure (Equation 2.47).
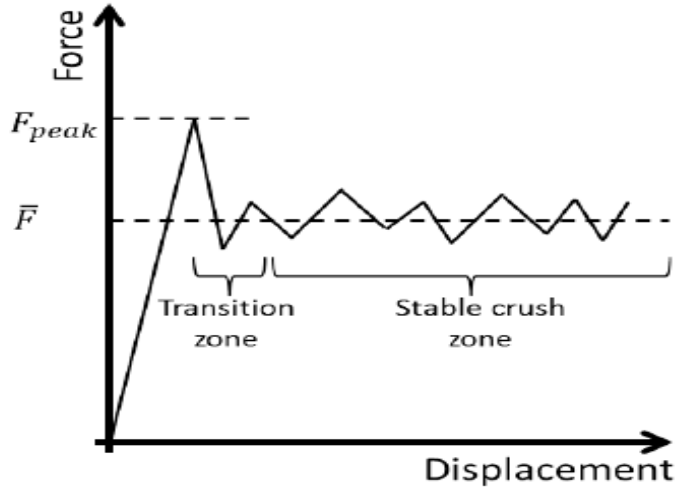
Figure 16. Typical force-displacement response for a component subjected to an axial crush load [61].

$$Mean\ Crush\ Force,\ F_{mean} = \frac{\int Fdl}{l} \tag{2.45}$$

$$Energy\ Absorption,\ EA = \int Fdl \tag{2.46}$$

$$Specific\ Energy\ Absorption,\ SEA = \frac{EA}{m} \tag{2.47}$$

Crashworthiness of a structure is usually measured by the amount of energy absorbed, the peak force and the deceleration of the vehicle. When the *EA* is increased the structural part is safer; however, formation of a higher peak force increases the potential of causing injury to the occupants [62]. It is desirable to reduce the peak force and increase the energy absorption of the component. Conventionally, vehicle metallic structures under axial crush loads absorb energy through two modes, axial collapse and bending mode by plastic folding (Figure 17a). However, many experimental studies have shown that composites have good energy absorbing capabilities during progressive crushing, where energy is absorbed through the formation of several damage mechanisms (Figure 17b). Initiating progressive failure of FRP composites can be challenging since global Euler buckling may occur and notably reduce energy absorption capabilities [63]. To avoid global buckling in composite components, chamfer triggers are used to initiate progressive crushing. Figure 18 shows the different stages of crushing behavior based on the test performed by Hull et al. for a [90/0]$_{2s}$ laminate [64]. During axial crush, the 90° plies were compressed and failed in transverse compression, while the 0° plies exhibited fiber kinking and fragmentation early on. As the crushing proceeded, a debris wedge was formed, which caused both inter and intra laminar cracks along the center

24

of the cross section. This led to the formation of fronds and mode I delamination between the center plies. The splaying mode of failure undergoes extensive buckling instead of fiber fracture which causes mode II delamination in shearing mode [65] (Figure 19).

Figure 17 Comparison of metals and FRP composites under axial crush load: (a) plastic folding in metal component, and (b) brittle fragmentation in an FRP component [66].
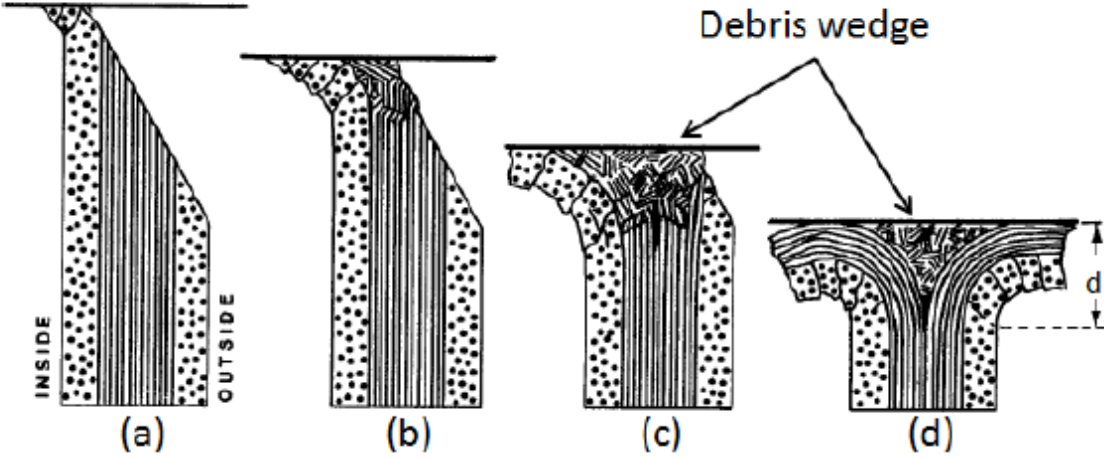
Figure 18. Different stages of composite tube crushing with a chamfer trigger (a-d), representing brittle fragmentation, matrix cracking and a splaying mode of failure [64].

<table>
<tr><td>(a)</td><td>(b)</td></tr>
</table>
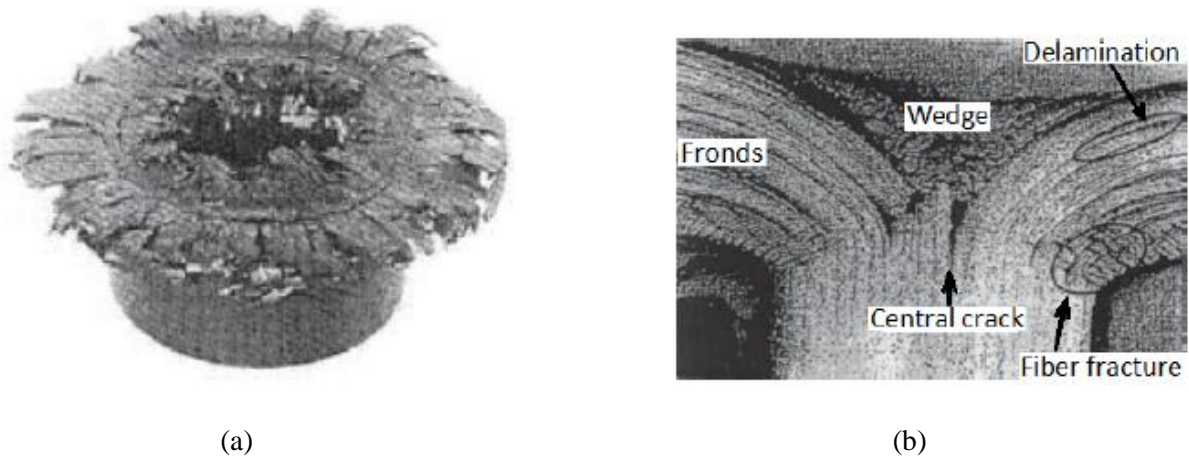
Figure 19. FRP tube axial crush test: (a) tube after axial crush test, and (b) cross-section of crushed tube [67].

2.2 Simulating Axial Crush of FRP Components

On comparison with metallic structures, modelling of FRP composite structures is more complex because of the anisotropic material response and the widespread evolving microscopic damage mechanisms that may form during loading. Finite element methods with continuum-based elements are necessary to simulate the impact behavior of FRP components and structures during vehicle development. Commercially available explicit finite element software are widely used to predict the crash performance of composite components and structures, as is reviewed in following sections. Using continuum-based elements, a layered shell element or single shell element approach may be used. A single shell element approach is widely preferred by industries for modelling crash of FRP structures owing to the high computational efficiency [68], [69]. A multilayered shell element approach is preferred for representing delamination cracking between plies in a laminate, and is regarded as more accurate when compared to the single shell approach [70]-[72]. Many investigations have reported experimental and computational results on CFRP components for side crash structures [73],[74] and [75]. The focus of this thesis is on frontal crash structures where axial crush loading is most relevant. Common cross-sectional geometries for FRP components that have been axially crushed and reported include corrugated, sinusoidal, C-channel [76], angle, square tubes [11], [75], [79]-[86] , circular tubes [87]-[91], conical tubes [85], [92] , open hat channel and closed hat channel. The reported studies where multilayer approaches were used is discussed in Section 2.2.1, while those using single-layer approaches are described in Section 2.2.2.

26

2.2.1 Multilayered Approach

Reuter et al. [93]investigated and simulated the axial crush response of straight CFRP and GFRP tubes with circular cross sections under dynamic loading conditions using LS-DYNA (Figures 20 and 21). Four distinct layers of shell elements were used with tie-breaks to represent groupings of UD plies of the laminates for modeling delamination between predetermined plies (Figures 20c and 21c). The authors calibrated the so-called non-physical material model parameters for the CFRP plies, and subsequently used the same parameters to simulate the axial crush response of the GFRP components. The simulation predictions correlated well with the experimental results, including capturing the observed splaying failure mode (Figures 20 and 21). However, the simulation mode required high rupture strains for fiber compression, matrix, and shear failure modes. Similar studies were reported by several authors [87],[94][95].

(a)   (b)   (c)
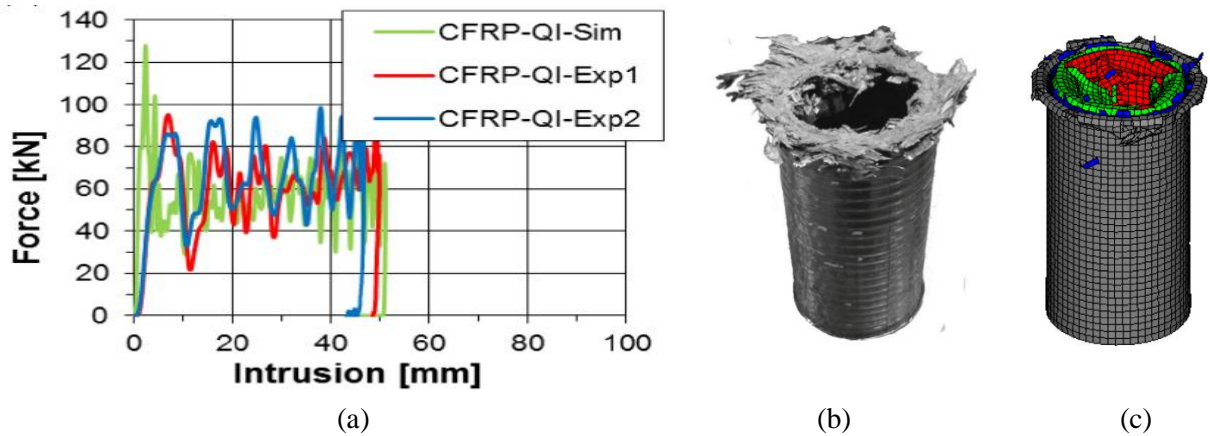
Figure 20. Axial crush response of CFRP composite tube: (a) force-displacement profile, (b) tested tube after crushing, and (c) predicted response [93].
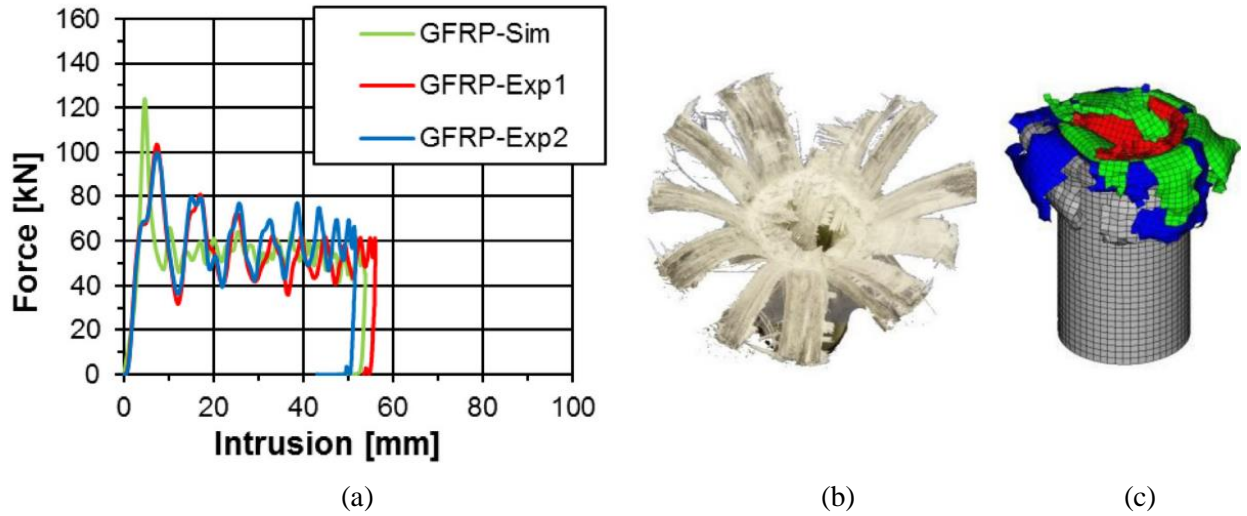
Figure 21. Axial crush response of GFRP composite tube: (a) force-displacement profile, (b) tested tube after crushing, and (c) predicted response [93].

McGregor et al. [96], [97]simulated the axial crush response of square braided CFRP composite tubes under dynamic loading conditions using two-layered and four-layered shell element modelling approaches with the continuum damage based material model CODAM in LS-DYNA (Figures 22). The shell layers were grouped with tie-breaks to model the delamination failure of braided composites. The numerical predictions correlated accurately with the deformation response and experimental results. The material model developed was capable of capturing the damage evolution of composites under different loading conditions
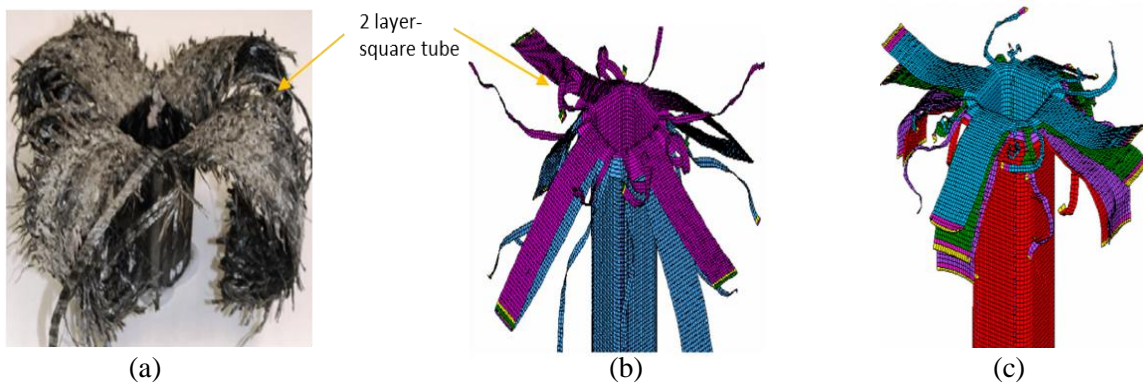
Figure 22. Axial crush response of braided composite tube: (a) tested tube after crushing, (b) 2 ply predicted response, and (c) 4 ply predicted response [96].

Jiang et al. [98]investigated the axial crush response of sinusoidal CFRP component under quasi-static conditions using a non-linear progressive damage model in Abaqus (Figure 23). The multi-layered solid elements were bonded with cohesive elements to simulate the delamination failure. The authors modelled the trigger geometry with 45° chamfer and combination of 45° and 60° chamfer to accurately represent the experimental mode of failure. The predicted response of sinusoidal components correlated well with experimental responses, capturing the splaying failure with some local buckling.

(a)   (b)
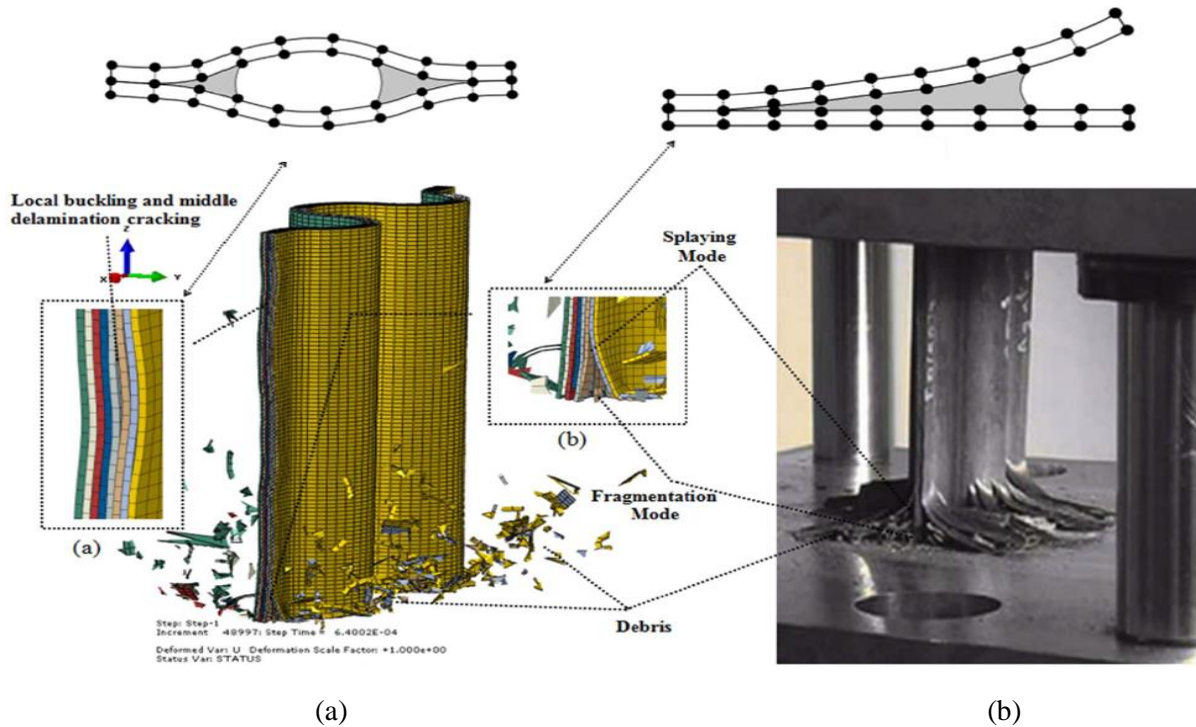
Figure 23. Axial crush response of sinusoidal component: (a) predicted response of multi-layered solid elements, (b) tested component after crushing [98].

Han et al. [99] explored the crash performance of press-molded hat channel and base plate under dynamic conditions using MAT 54 material model in LS-DYNA (Figure 24 and 25). The layered shell elements and base plate were grouped with tie-break connections to capture the damage initiation and crack propagation of CFRP components. The simulated response and crashworthiness metrics were observed to correlate accurately with the experimental data (Figure 25). Joosten et al. [100] used a similar approach to investigate the axial crush of open hat channel using PAMCRASH.
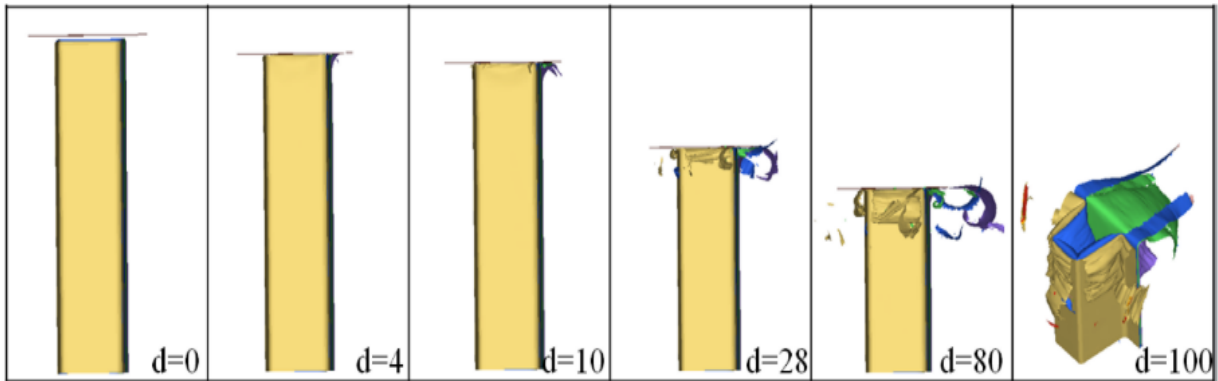
Figure 24. Axial crush response of hat channel and backing plate using LS-DYNA [99]. Images correspond to indicated crush distance during simulation.
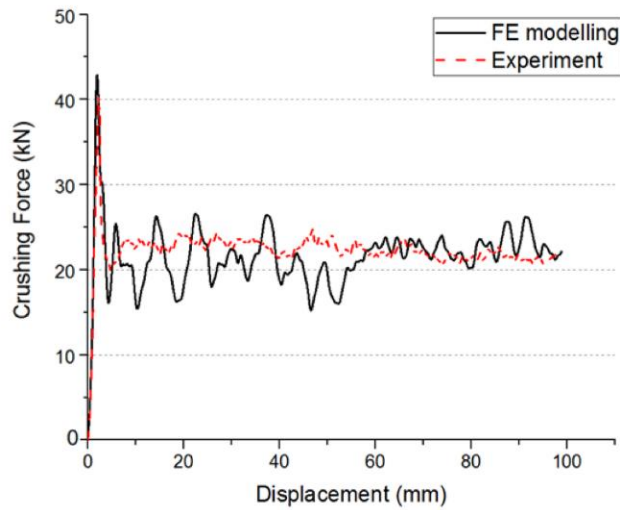
Figure 25. Force-displacement response of hat channel and backing plate compared to the axial crush experimental data [99].

2.2.2 Single Layer Approach

Feraboli et al. [101] evaluated the axial crush response of sinusoidal specimen using MAT 54 material model in LS-DYNA (Figure 26). The composite specimen and trigger geometry were modelled with single layer approach to capture the failure behaviour of UD tape composites . The authors calibrated the values of non-physical and strength parameters to correlate well with experimental results, capturing fragmentation failure mode. The simulation model required a high compressive fiber strength and rupture strains for lamina for calibration.

30

(a)   (b)
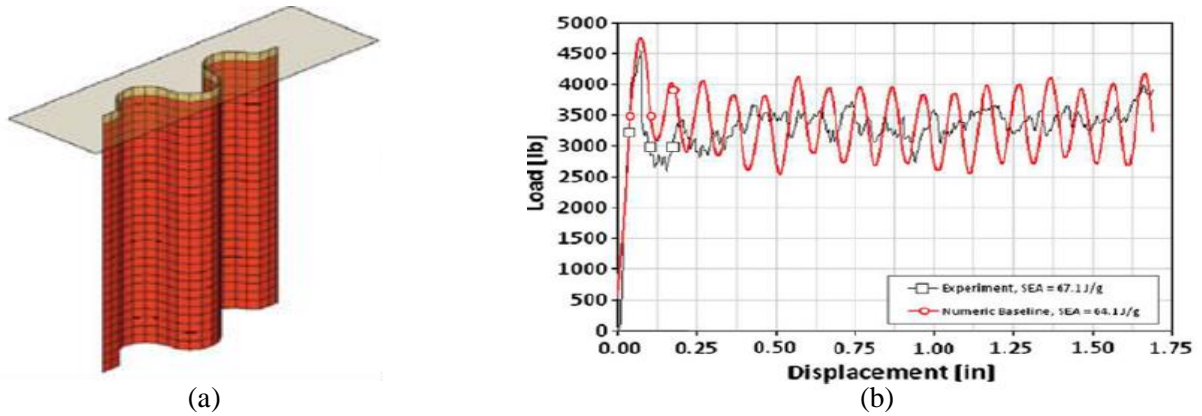
Figure 26. (a) Axial crush response of single layer sinusoidal component (b) force-displacement response compared with numerical response and experimental data [101].

The axial crush response of different geometries namely, large and small C-channel, large and small angles and square tubes were investigated by Deleo et al. [102]. The authors modelled the composites specimens using single layer approach and MAT 54 model in LS-DYNA (Figure 27). The simulated results correlated well with experimental data capturing the fragmentation failure modes. However, the simulation response required high calibration on crash front softening parameter to capture the failure mode of different geometries.

(a)   (b)   (c)

(d)   (e)
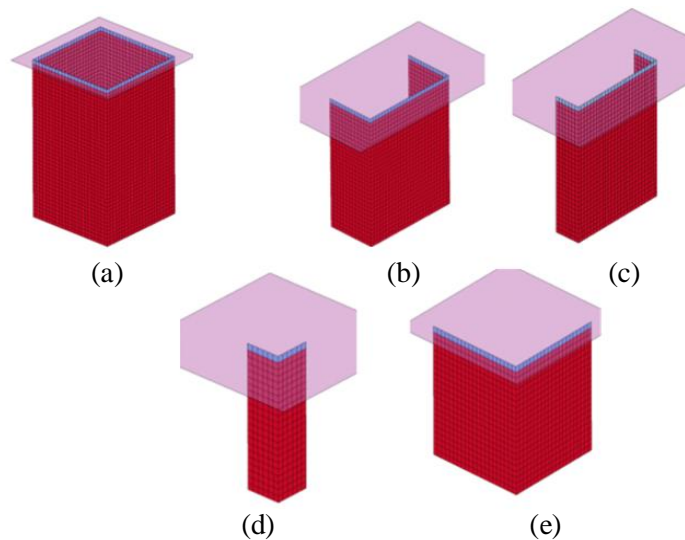
Figure 27. Axial crush of different cross-sectional geometries (a) square tube (b) large channel (c) small channel (d) small corner (e) big corner. [102]

31

Zhang et al. [103]simulated the axial crush response of three GFRP components with circular, conical and square cross-sections. The authors compared the simulated predictions of two distinct layer of shell approach and single layer approach using MAT 54 material model in LS-DYNA (Figure 28). The authors calibrated and simulated the response of different geometrical parameters and subsequently evaluated the axial crush response of foam filled GFRP components.
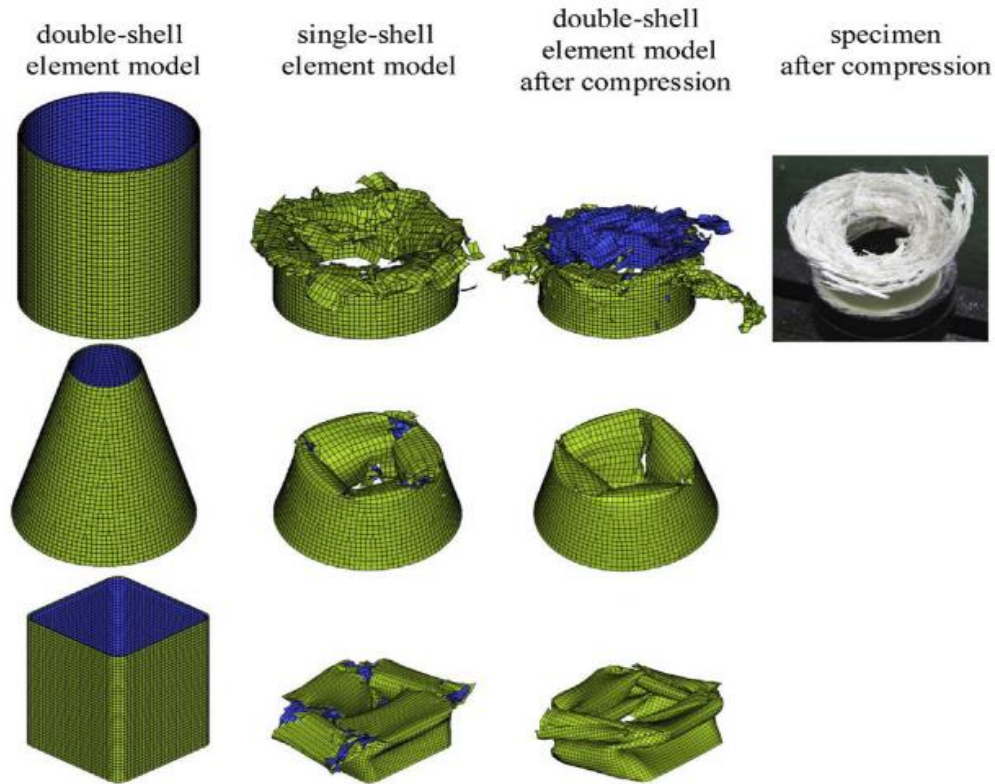
Figure 28. Axial crush response of circular, conical and square tube. Numerical predictions using double shell and single shell approaches were compared to the tested component [103].

Sivakumar et al. [104] investigated the axial performance of UD composites under dynamic conditions using MAT 54 and MAT 58 material model in LS-DYNA (Figure 29). The authors calibrated the non-physical parameters to match the experimental results. However, the simulation required high values for the post-damage parameters to invoke a high mean crush force for the specimens considered. Similarly, Boria et al. [105] evaluated the crush performance of CFRP truncated conical specimens using MAT 54 and MAT 58 model in LS-DYNA. The non-physical parameters of MAT 54 were calibrated, and

subsequently used in MAT 58 to capture the experimental response of CFRP components (Figure 30). The simulation response of both material models correlated well with the experimental results.

(a)

(b)
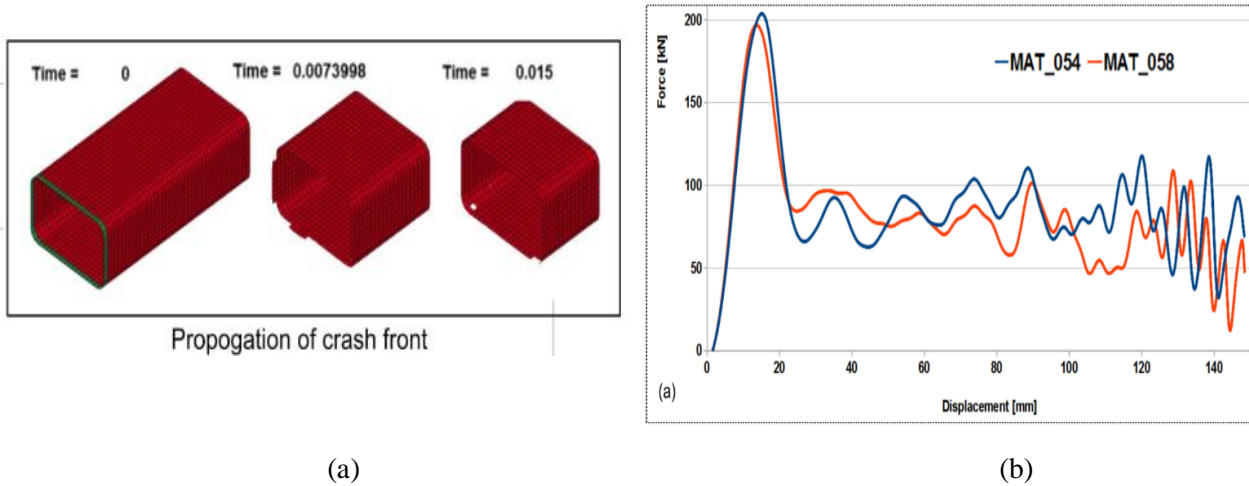
Figure 29. (a) Axial crush response of square tube numerical model (images correspond to indicated crush distance during simulation), and (b) force-displacement response predicted with MAT 54 and MAT 58 material models [104].
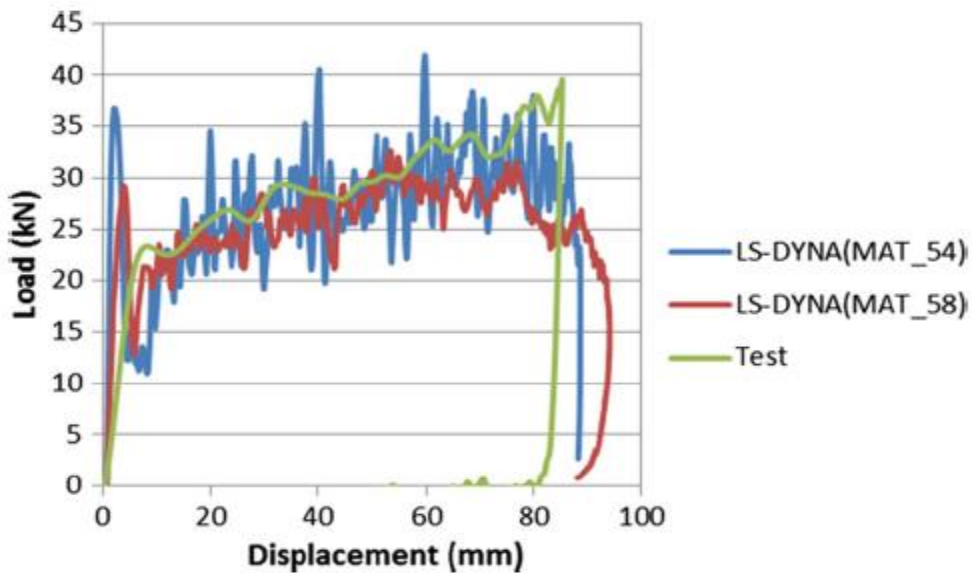
Figure 30. Force-displacement response using MAT 54 and MAT 58 material models compared to the test data [105].

33
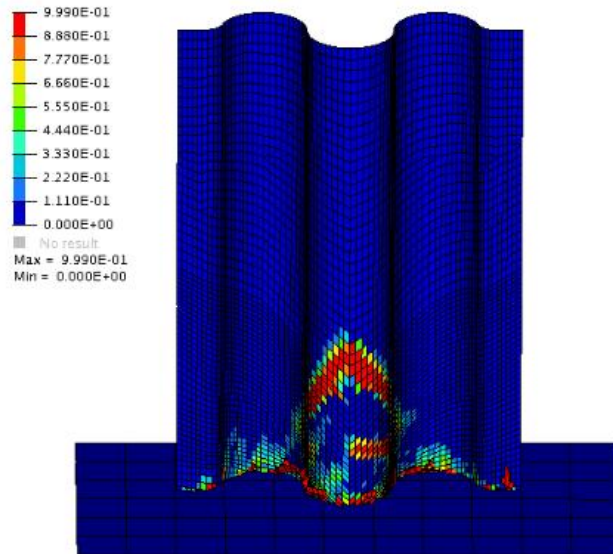
Figure 31. Axial crush response of sinusoidal specimen – structured wave pattern mesh were modelled to establish continuous contact with the impactor [106].

Andersson et al. [106] performed axial crush simulations of CFRP composite components using material models MAT 54 and MAT 262 in LS-DYNA to compare and evaluate the relative predictive capabilities of each material model. For MAT 54 simulation model, predictions were unstable forming many oscillations in force response with a uniform mesh pattern. However, different mesh patterns (Figure 31) led to avoid many oscillations in force response producing a stable result; a similar result was reported by Boria et al. [72]. On the other hand, the MAT 262 simulation model predictions were not mesh dependent, which was deemed to be a result of the physically-based fracture parameters considered by the material model. Nevertheless, the MAT 262 material model requires additional experimental data for calibration compared to MAT 54. Cherniaev et al. [11] investigated the predictive capabilities of MAT 54, MAT 58 and MAT 262 material models in LS-DYNA for a square tubular specimen subjected to axial crush loads (Figure 32). All the three models under predicted the force-displacement response when the default values for the non-physical parameters were used. The non-physical parameters for MAT 54 were subsequently calibrated through a parametric study, which led to good correlation with experimental data (Figure 32.b). Similarly, the MAT 58 and MAT 262 material models were also able produce reasonable results, albeit after extensive calibration. In all cases, the simulation model was able to predict the peak load and mean crush force, as well as the dominant fragmentation mode of failure in the CFRP composite specimen. Additional predictions using the calibrated simulation models for specimens with different

34

stacking sequences, corresponding to a dominant splaying failure mode where delamination was prevalent, led to under predicted force-displacement response due to the single shell element approach used.
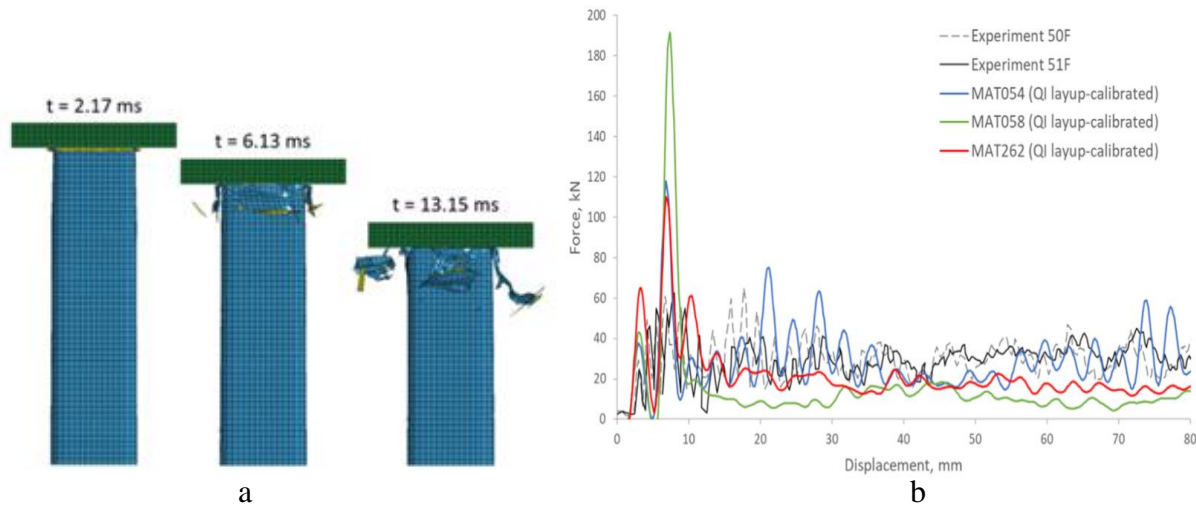
Figure 32. (a) Axial crush response of a square CFRP tube, and (b) experimental and numerical force-displacement data for three material models in LS-DYNA [11].

2.3 Simulating the Impact Response of Energy Absorbing FRP Automotive Structures

Several studies have focused on designing and evaluating the impact performance of FRP composite parts for automotive energy absorbing applications [107]-[113] . Boria et al. [108] investigated the axial performance of a formula SAE vehicle front end attenuator subjected to a 300 kg impact mass under a velocity of 7 m/s. The authors modelled the composite specimens using solid and shell element approach, where cohesive elements were utilized with the former model and MAT 54 was used in latter model. The non-physical parameters of the material model were calibrated using simple straight tube with circular cross-section and subsequently used for the structural simulation models. The single shell element model was able to predict the damage of composite attenuator and correlated well with the experimental results (Figure 33). Similarly, Wang et al. [109] reported the impact attenuator model with ply drop-off method increased the energy absorption and stiffness required for formula SAE racing vehicles.
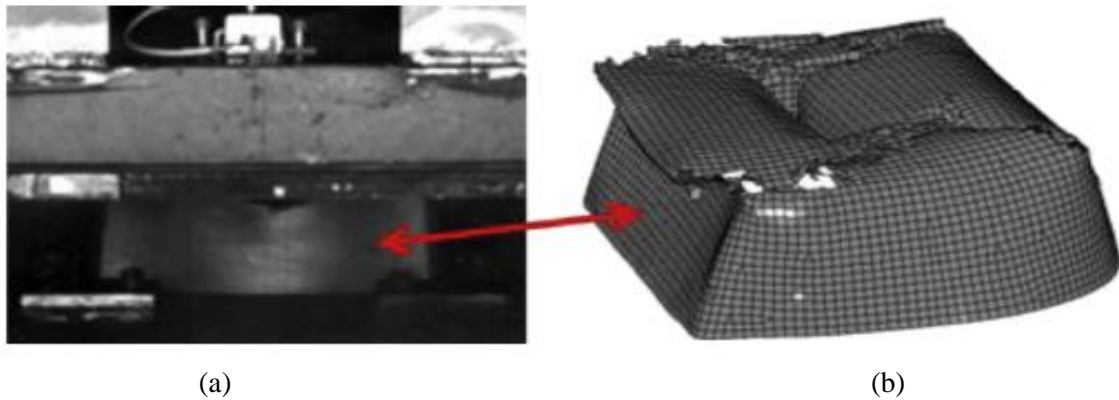
Figure 33. Axial crush of attenuator(a) Experimental image after crushing (b) numerical predictions after crushing using single layer shell approach [108].
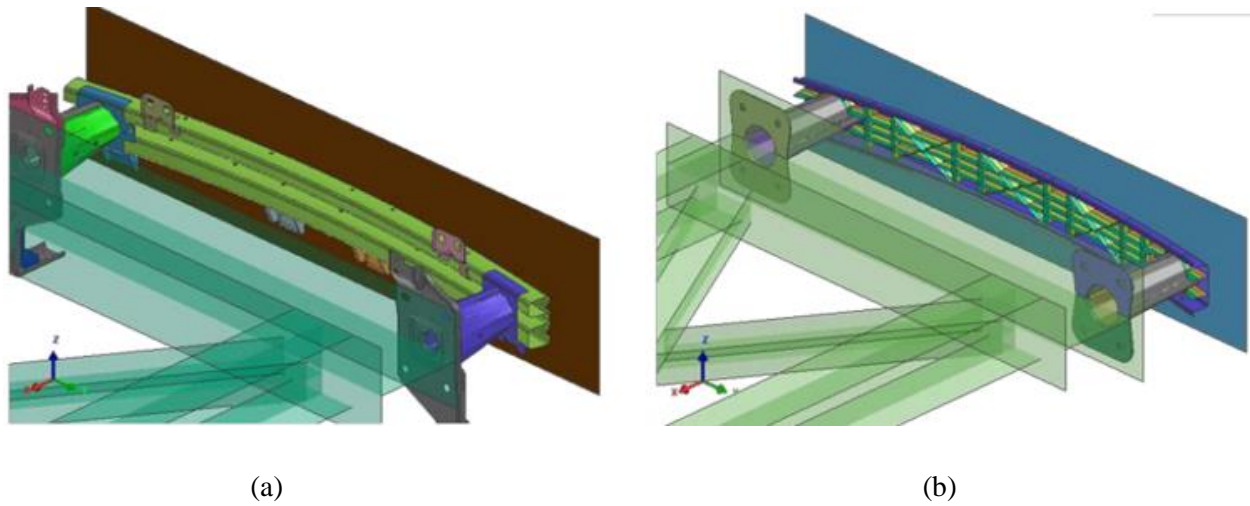
Figure 34. Axial crush of bumper beam: (a) baseline steel bumper beam and crush can, (b) composite bumper beam and crush can [110].

Vto et al. [110] explored the axial crush response of woven CFRP composite bumper beam and crush can under dynamic conditions using MAT 131 material model in PAM-CRASH. The composite components were modelled using a single layer of shell elements (Figure 34). The simulation model was observed to match the crush response and crashworthiness metrics of the experimental data. The authors

reported that composite specimens produced a weight saving of 45% when compared to the baseline steel structures.

(a)   (b)
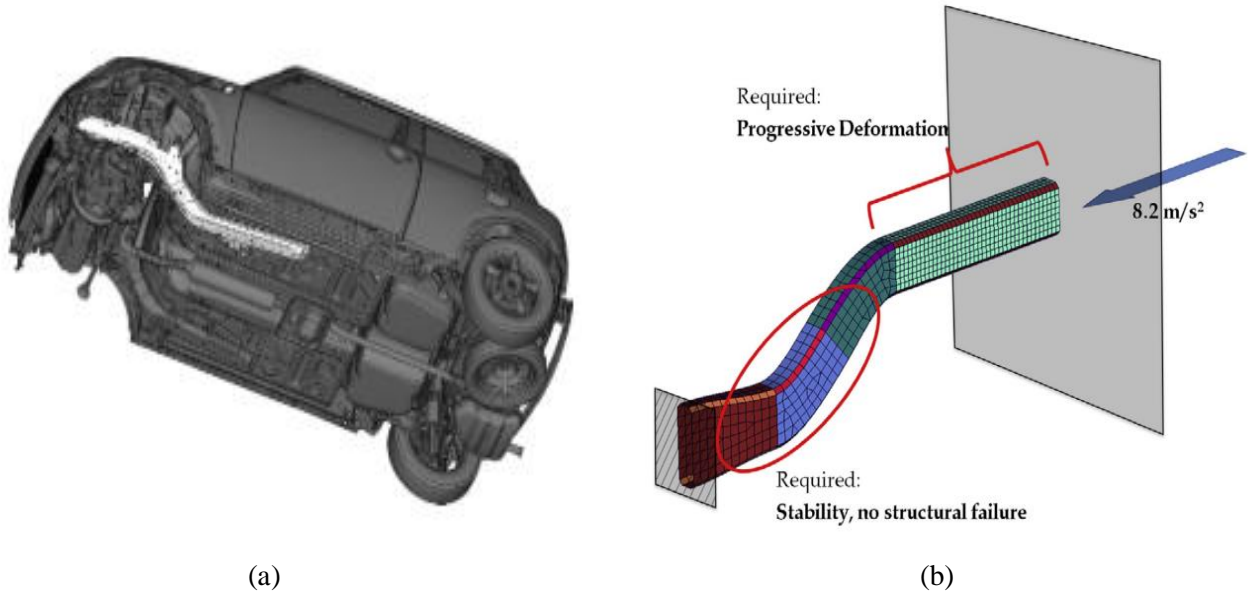
Figure 35. Axial crush response of simplified S-rail: (a) Example of S-rail in a vehicle, (b) simplified composite S-rail modelled for progressive crushing[111].

Hesse et al. [111] simulated the crash performance of a simplified CFRP S-rail using Abaqus FE software (Figure 35). The authors reduced the design complexity and modelled the S-rail with a simplified square cross section for 400 mm of progressive crush in the main rail region, and enlarged the cross section for the S-region. The single shell element model was able to predict continuous progressive failure for high energy absorption and stable intrusion zone matching the criteria for automotive crash applications. Similarly, Dixit et al. [112] performed axial crushing of frontal crash structure to enhance the weight saving and energy absorption for structural components.

Park et al. [113]simulated the performance of composite chassis of the 2007 Chevrolet Silverado under New Car Assessment Program (NCAP) conditions. Two different thickness of braided composites (LMV2 and LMV3) was performed with single shell approach using MAT 58 material model in LS-DYNA (Figure 36). The simulation predictions with thrice the thickness of steel structure correlated well with the baseline structures (Figure 37). Moreover, authors reported a 32% weight savings comparing the steel chassis and 3.2% weight reduced over total vehicle mass using braided composite chassis.

37

<div align="center">(a)   (b)</div>
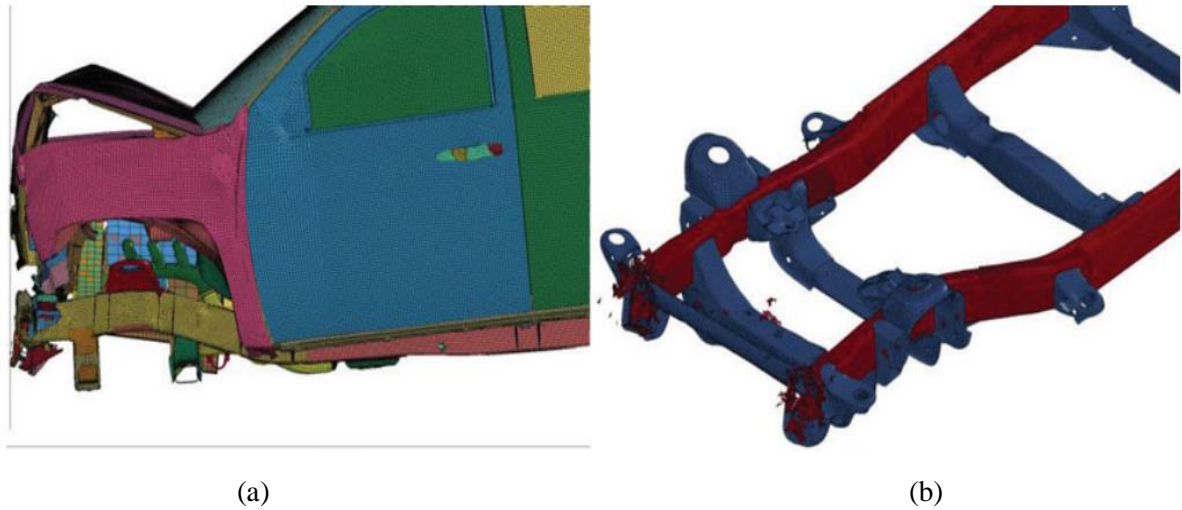
Figure 36. Numerical model of Chevrolet Silverado: (a) frontal impact with composite chassis frame, (b) isolated composite chassis frame [113].
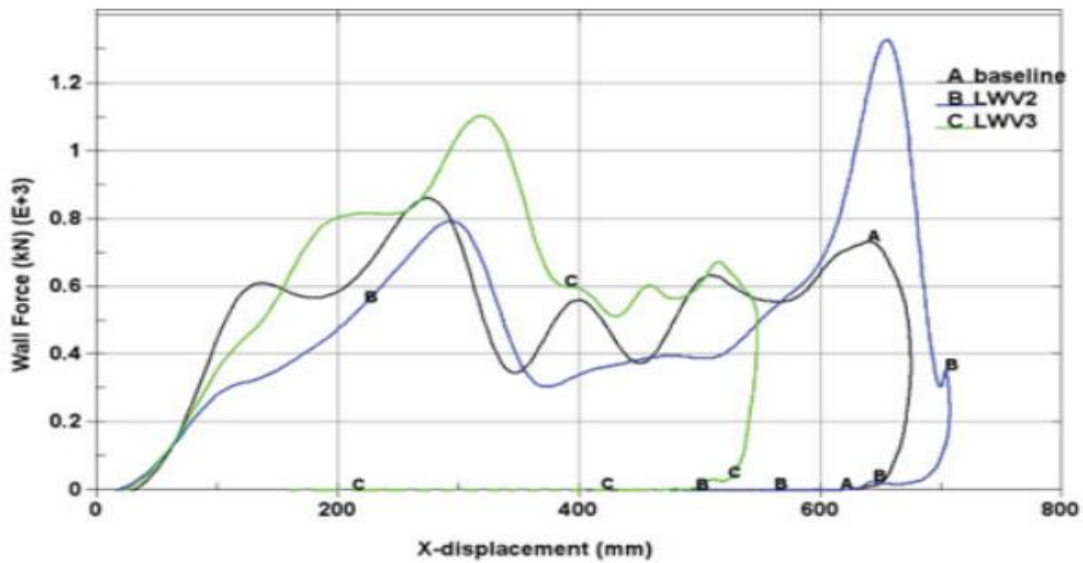
Figure 37. Force vs displacement response of baseline and different thickness composite chassis frame[113].

2.4 Summary

A review of previous studies that focused on the numerical modelling of FRP composites under impact loading has shown the current challenges in accurately predicting this behaviour, and has also revealed the

variety of approaches that have been taken. Both single shell and multiple shell element approaches have their advantages/disadvantages for evaluating the crush performance of FRP composite structures for automotive chassis frame applications. While multilayer shell elements with cohesive elements or tiebreaks is attractive to capture delamination damage propagation, the approach requires a high computational expense and intern increases the complexity for full vehicle crash simulations. Additionally, the macroscale material models currently available in commercial FE software LS-DYNA require significant calibration at the component level before implementation into a structure scale simulation. Furthermore, the studies reported have focused primarily on woven and braided FRP composites, while few studies have considered the NCF composites. Moreover, most studies simulated the impact performance of FRP components with simple geometries where a stable crush behavior was exhibited, while few studies were reported on structure scale impact performance of composites. Additionally, few studies focused on examining the effect of component geometry, laminate thickness and stacking sequence on the energy absorption of FRP composite components.

Chapter 3
FRP Composite Material Models in LS-DYNA

There are several available material models in LS-DYNA for FRP composite materials, which are primarily continuum-based and developed for use with two-dimensional shell elements and/or three-dimensional solid elements. The available material models will be outlined in Section 3.1, while a detailed description of two widely used material models will be described in Sections 3.2 and 3.3. Moreover, the simulation of composite structures requires modelling of the joint between components. Since adhesively bonded joints are preferred for FRP composite components, an overview of available cohesive models is presented in Section 3.4.

3.1 Overview of available material models

Most of the available FRP composite material models in LS-DYNA utilize a continuum damage mechanics-based approach to capture the 'post-peak' lamina response, where the corresponding degradation scheme utilizes strength or fracture mechanics-based terms. The post-peak response, which typically assumes a non-physical response, is used to control the lamina residual stress after failure is predicted and to stabilize the numerical simulation model. Details of the available material models are summarized in Table 1.

Table 1. Composite material models available in LS-DYNA [116].

MATERIAL CARD & NAME	LAMINA RESPONSE	COMPATIBLE ELEMENTS	LAMINA FAILURE CRITERIA	LAMINATE FAILURE SCHEME	COMMENTS
MAT 22 - Composite Damage	Linear Elastic model	Shell, Thick Shell & Solid	Reduced Chang-Chang [114]	Ply discount method.	Simple brittle model. No crash front algorithm
MAT 54/55 Enhanced Composite Damage	Linear Elastic-Plastic model	Shell, Thick Shell & Solid	54 – Chang-Chang [114] 55 – Modified Tsai-Wu [40]	Ply discount approach. when all the plies (Integration Points) are failed.	Improved form of MAT22. Crash front algorithm. Strength reduction parameters.
MAT 58 Laminated Composite Fabric	Elastic-damage model	Shell, Thick Shell & Solid	Modified Hashin Model[115]	All the Plies in the laminate failed.	Same as MAT 54. Smooth stress strain relation. Continuum damage-based model with exponential softening. Crash front algorithm. Non-linear shear behavior
MAT 59 Composite Failure Model	Elastic-Plastic model	Shell, Thick Shell & Solid	Modified Hashin Model[115]	Same as MAT 58	Same as MAT 58. Rate Sensitive.
MAT 116 / 117 / 118	Orthotropic Elastic	Shell	No Failure	No Failure	Elastic response only

Composite Layup					
MAT 158 Rate Sensitive Composite Fabric	Elastic damage model	Shell, Thick Shell & Solid	Modified Hashin Model	Same as Mat 58	Same as 58 but rate sensitive
MAT 161 / 162 Composite MSc Model	Elastic damage model	Solid	Hashin Model[117]	-	Additional license required. MAT 161 offers delamination prediction with solid elements.
MAT 219 CODAM2	Sub laminate-based model.	Shell, Thick Shell & Solid	-	Sub-laminate Model (failed based on equivalent strain measures)	Strain based input formulation (no strength parameter required) No rate sensitivity
MAT 261 Laminated Fracture Daimler Pinho	Continuum damage-based model.	Shell, Thick Shell & Solid	Pinho Model [118][119]	All the Plies in the laminate failed.	Physical based failure criterion. Linear softening based on fracture toughness.
MAT 262 Laminated Fracture Daimler Camanho	Continuum damage-based model.	Shell, Thick Shell & Solid	Camanho Model [120][33]	All the Plies in the laminate failed.	Physical based failure criterion. Bi-linear/linear softening based on fracture toughness.

Based on the available material models, MAT 54 and MAT 58 were considered in this study for evaluating the axial crush performance of composite components. This is owing to their simple framework, reduced number of ply level input parameters and their capabilities to predict the performance of composite structures accurately with a single layer of shell elements at a reduced computational cost. Furthermore, many researchers have utilized MAT 54 and MAT 58 for simulating impact of composite structures [11], [93],[101]-[106], [113], [121]-[125] , and have reported that these material models are simple and robust for predicting the axial crush performance of different composite component geometries.

3.2 Overview of MAT 54 – Enhanced Composite Damage

MAT 54 is one of the most widely used composite material models in LS DYNA, which has been implemented in large-scale structure dynamic crash simulations [108],[109]. Details of the material model is presented in the following sub-sections.

3.2.1 Constitutive & Degradation Model of MAT54

MAT 54 is used to represent the orthotropic stress-strain behaviour of the laminae in a laminated composite material. Deformation of a lamina is assumed to be linear elastic up to failure, which is predicted using the Chang-Change criteria for different modes using Equations 2.41 to 2.44. Once a failure mode is predicted, the corresponding lamina engineering constants are suddenly reduced to zero. The sudden lamina degradation scheme for each failure mode is described below.

For the tensile fiber failure mode, the degradation scheme considers either a fully damaged or undamaged lamina. When $e_f \geq 0$ (Equation 2.41), failure is reached and $E_1, E_2, G_{12}, \nu_{12},$ and ν_{21} are all set to zero. For the fiber compressive fiber failure mode, failure is reached when $e_c \geq 0$ (Equation 2.42), thus E_1, ν_{12}, and ν_{21} are set to zero. Matrix tensile failure occurs when $e_m \geq 0$ (Equation 2.43) and, therefore, the transverse modulus E_2, shear modulus G_{12} and the Poisson's ratio ν_{21} are reduced to zero. Compressive matrix failure occurs when $e_d \geq 0$ (Equation 2.44), therefore, the transverse modulus E_2, shear modulus G_{12} and the Poisson's ratio $\nu_{12},$ and ν_{21} are reduced to zero.

After the sudden reduction of the lamina engineering constants at the peak stress, the subsequent material behavior becomes either perfectly plastic or there is a drop in stress to a residual value followed by a perfectly plastic response (Figure 38). Once the lamina failure strain corresponding to a critical failure mode is attained, the lamina is removed or discounted and the stresses of the laminate are updated.

Subsequent lamina removal continues until all the lamina are removed, leading to failure of the laminate and erosion of the element from the mesh.
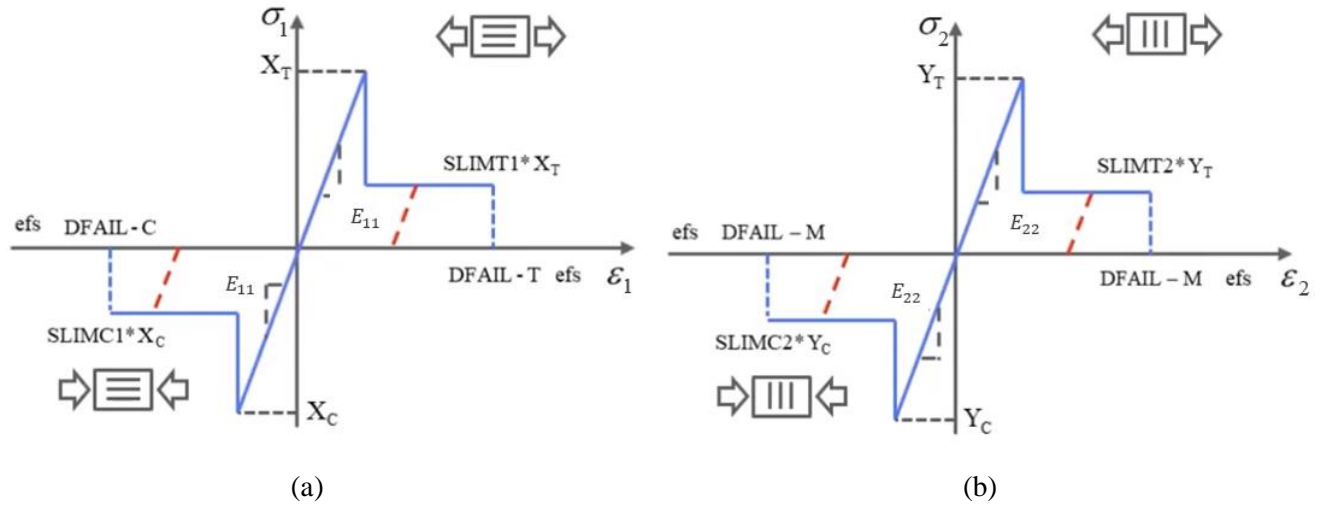
Figure 38. MAT 54 stress-strain model for a lamina: (a) fiber tension and compression, (b) matrix tension and compression.

3.2.2 Parameters of MAT 54 Material Model

Details of all the parameters and material card for MAT 54 are found in Appendix A. There are several non-physical parameters that have been integrated into the MAT 54 material model, which require a parametric study for calibration. The DFAIL parameters define the failure strains for elemental deletion (Figure 38), and are larger in magnitude compared to the strain at peak stress that would be measured during mechanical characterization testing. DFAILT and DFAILC correspond to the maximum longitudinal tension and compression strains, respectively. DFAILM is the maximum transverse tension and compression strain, which are assumed to be equal.

The SLIM parameters control the magnitude of the post-peak residual stress of the composite lamina, which can be defined as a fraction of the associated strength for all in-plane directions. SLIMT1, SLIMC1, SLIMT2, SLIMC2, and SLIMS correspond to fiber tension, fiber compression, matric tension, matrix compression and shear, respectively. The SLIM parameter values may range from zero to one .

The SOFT parameter defines the softening reduction factor that scales down the lamina strength for the elements in the immediate crash front. Elements with common nodes have one of the deleted

elements with reduced strength. The value of the SOFT parameter ranges from zero (full strength reduction) to one (no strength reduction).

The PFL variable controls the percentage of layers in the lamina within an element (integration point) that must fail to allow transfer the reduced strength (controlled by SOFT) to the neighboring elements. For instance, a value of PFL = 100 represents that 100% of the layers must fail in an element to transfer the softening strength parameter to adjacent elements.

The TFAIL parameter offers an additional option for elemental deletion. In a numerical model were elements that cannot carry any load and are not deleted using the DFAIL parameters may be controlled by this variable. In general, TFAIL is a time dependent parameter were the value represent the time beyond which the elements are eroded.

A general flowchart summarizing the solution scheme for the material model MAT 54 is shown in Figure 39.
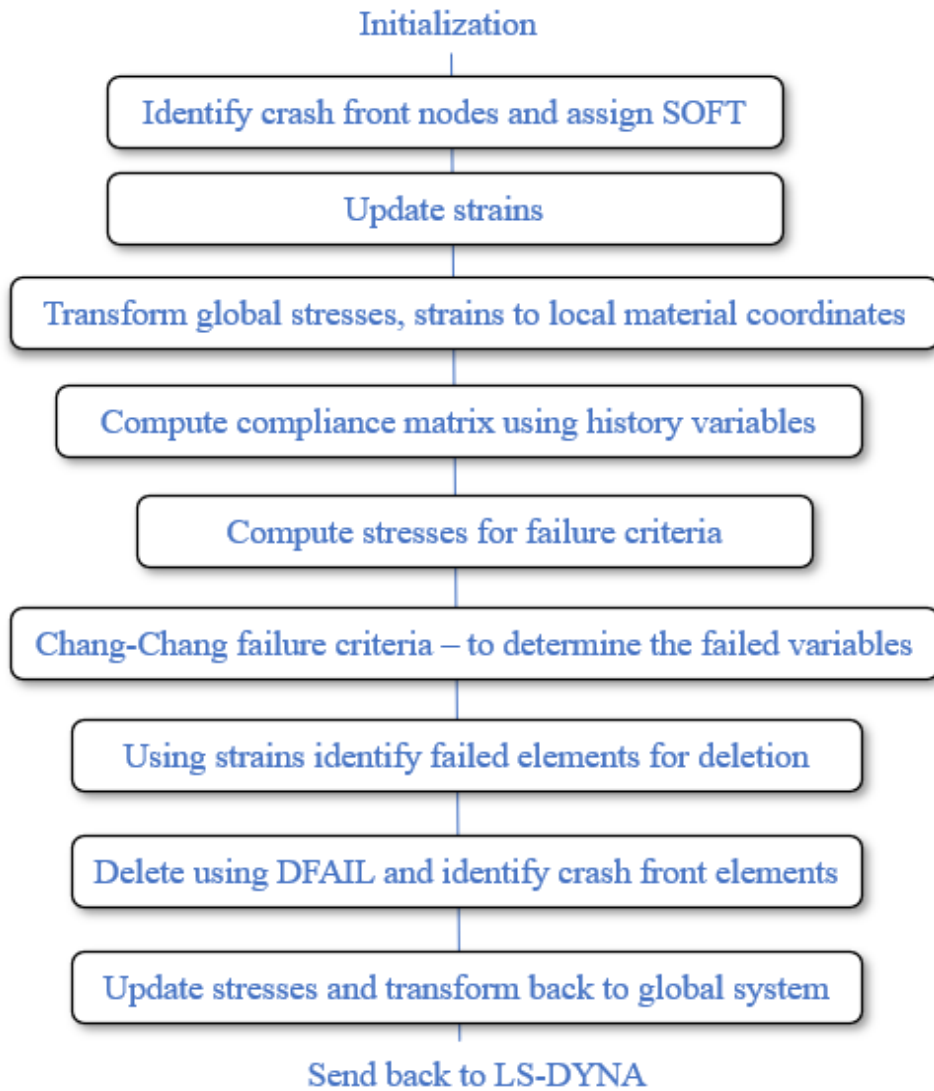
Figure 39. A simplified general flow chart for the MAT 54 material model in LS-DYNA.

3.3 Overview of MAT 58 – Laminated Composite Fabric

MAT 58 is also a widely used material model for performing impact simulations of large-scale structures [113]. The simplicity of the model is similar to the MAT 54, and it also utilizes ply properties to evaluate the properties of the laminates. Details of the material model are presented in the following sub-sections.

3.3.1 Constitutive and Degradation Model of MAT 58

MAT 58 is similar to MAT 54 in that linear elastic behaviour is assumed initially for a lamina, and a post-peak residual stress scheme is also invoked with subsequent perfectly plastic behaviour until a defined failure strain is reached (Figure 40). The main difference is that MAT 58 uses the Matzenmiller-Lubliner-Taylor (MLT) [115]continuum damage mechanics-based model to degrade the engineering constants of a lamina once failure is predicted (i.e., post-peak). Note, failure in each direction is defined using the modified Hashin failure criteria described by Equations 2.32 to 2.35.

The MLT model uses the concept of effective stresses to predict the effects of damage evolution along each lamina direction on the elasticity tensor. The effective stresses ($\bar{\sigma}_{ij}$) are defined by:

$$[\bar{\sigma}] = \begin{bmatrix} \overline{\sigma_1} \\ \overline{\sigma_2} \\ \overline{\sigma_{12}} \end{bmatrix} = \begin{bmatrix} \frac{1}{1-d_1} & 0 & 0 \\ 0 & \frac{1}{1-d_2} & 0 \\ 0 & 0 & \frac{1}{1-d_{12}} \end{bmatrix} \begin{bmatrix} \sigma_1 \\ \sigma_2 \\ \sigma_{12} \end{bmatrix} \tag{3.1}$$

where d_1, d_2 and d_{12} are the damage parameters corresponding to the longitudinal fiber, transverse matrix and in-plane shear directions. The evolution of the damage parameters with increasing strain magnitude is assumed to be:

$$d_{ij} = 1 - \exp\left[-\frac{1}{m}\left(\frac{\epsilon}{\epsilon_f}\right)^m\right] \tag{3.2}$$

where ϵ, ϵ_f and m are lamina strain, strain at maximum directional stress and a parameter that controls the profile of the stress-strain curve, respectively.

The components of constitutive tensor C(d) for a lamina are represented as a function of the damage parameters and undamaged layer engineering constants as:

$$C(d) = \frac{1}{D}\begin{bmatrix} (1-d_1)E_1 & (1-d_1)(1-d_2)v_{21}E_2 & 0 \\ (1-d_1)(1-d_2)v_{12}E_2 & (1-d_2)E_2 & 0 \\ 0 & 0 & D(1-d_{12})G_{12} \end{bmatrix} \tag{3.3}$$

where $D = 1 - (1-d_1)(1-d_2)v_{12}v_{21} > 0$.

The damage parameters d_1 & d_2 are assumed to have different values for fiber tension and compression and matrix tension and compression. The effective stresses defined by Equation 3.1 were used in Equations 2.32 – 2.35 for predicting failure, where failure occurs when $e_f, e_c, e_m, e_d \geq 0$. Subsequent degradation of lamina properties was gradual (Equation 3.3) until the residual stress was attained, which initiated perfectly plastic deformation until a predetermined failure strain (Figure 45). On reaching the lamina failure strains, the lamina is removed and laminate stresses are updated. This process is repeated until all the lamina are failed in the laminate, after which elements were removed.
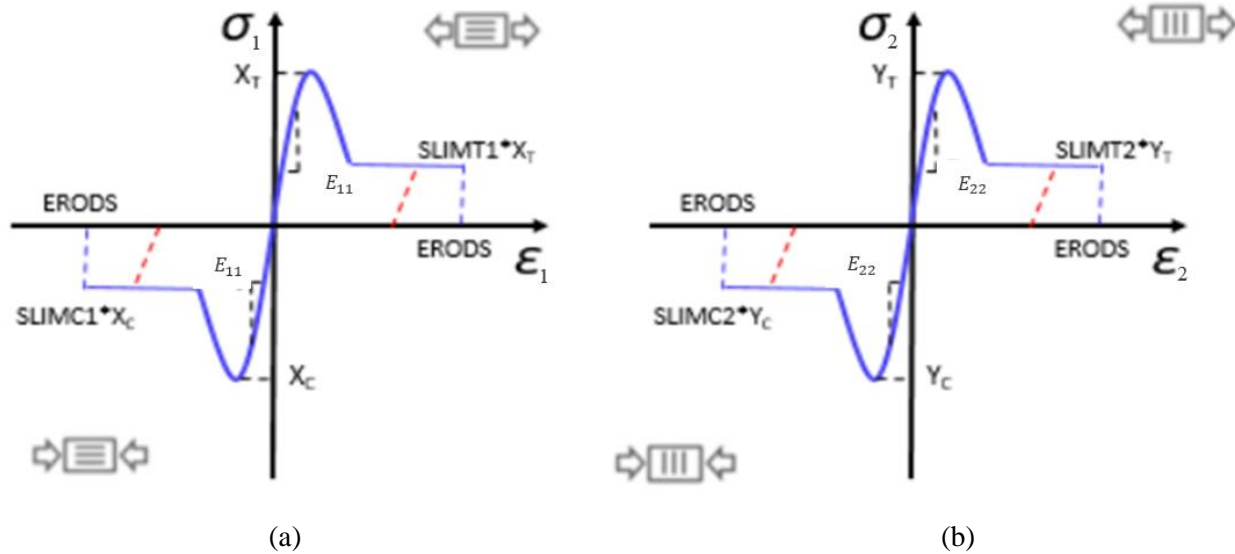
Figure 40. MAT 58 stress strain model for a lamina: (a) fiber tension and compression, and (b) matrix tension and compression.

3.3.2 Parameters of MAT 58 Material Model

Details of the MAT 58 material card parameters are found in Appendix B. Similar to the MAT 54 material model, there are several non-physical parameters that have been integrated into the MAT 58 material model. The FS parameter defines the chosen set of failure criteria. When FS = 1 an interaction between normal and shear stresses are assumed for the evolution of damage in the 1-2 directions; however, when FS = -1 it is assumed that damage is independent of any the other stresses in the lamina. The ERODS defines the effective plastic strain that controls the maximum strain of a lamina for elemental erosion.

The SLIM parameters control the magnitude of the post-peak residual stress of the composite lamina, with SLIMT1, SLIMC1, SLIMT2, SLIMC2, and SLIMS (defined previously). The SLIM parameter values range from zero to one, which scale the residual stress.

TFAIL defines the time dependent parameter for elemental erosion and SOFT defines the softening factor to reduce the lamina strength of crash front elements. The functionality of two parameters are same as the MAT 54 material model (defined in Section 3.2.2).

A general flowchart summarizing the solution scheme for the material model MAT 58 is shown in Figure 41.

Initialization

Identify crash front nodes and assign SOFT

Update strains

Transform global stresses, strains to local material coordinates

Compute compliance matrix using history variables

Compute effective stresses for failure criteria

Modified Hashin failure criteria – to determine the failed variables

Using strains identify failed elements for deletion

Delete using ERODS and identify crash front elements

Update stresses and transform back to global system

Send back to LS-DYNA

Figure 41. A simplified general flow chart for the MAT 58 material model in LS-DYNA.

3.4 Cohesive Modelling in LS-DYNA

Cohesive zone models were widely used to numerically model failure of adhesively bonded composite joints [126],[127] which are important for simulating the performance of composite structures comprised of assembled components, as well as delamination between plies in laminates [46],[50]. The cohesive zone models available in LS-DYNA are based on traction-separation laws (Figure 42). Some material models can capture the strain rate and temperature dependency on delamination crack growth. The models are described in the subsequent paragraphs.

MAT_COHESIVE_ELASTIC (MAT 184) uses simple bilinear traction-separation laws for both Mode I and Mode II crack propagation. Peak traction, initial stiffness and the displacement at failure are required as input parameters for the material model [116].

MAT_COHESIVE (MAT 185) is a trilinear cohesive model developed by Hutchinson et al. [128]. The material model is completely reversible based on loading and unloading following same path[116]. The traction-separation law for the material model is shown in Figure 42b.

MAT_COHESIVE_GENERAL (MAT 186) is material model developed by Khaled et al.[129] to numerical predict the ballistic impact response of composite plates. It is observed that the interaction between Mode I and Mode II are modelled for three mixed mode interaction. The damage is modelled as irreversible when loading and unloading from the same path [116]. The normalized traction separation of the material model is shown in Figure 42.

MAT_COHESIVE_MIXED_MODE (MAT 138) is a simplified form of MAT 186 model with linear softening. The delamination is modelled as bilinear with damage evolution and mixed mode delamination criteria [116]. Figure 42 shows the bilinear traction separation curve that T and S represent the peak traction in units of stress in normal and tangential direction.

MAT_COHESIVE_MIXED_MODE_ELASTOPLASTIC_RATE (MAT 240) is like MAT_185 model which additionally includes rate and plasticity models. Figure 42 shows the traction separation curve developed by Marzi et al.[130]. It is observed from the traction separation curves due to ideal plastic behavior the loading and unloading paths are different in this model. The failure behavior is modelled as plastic no brittle fracture are modelled in the material model [116].
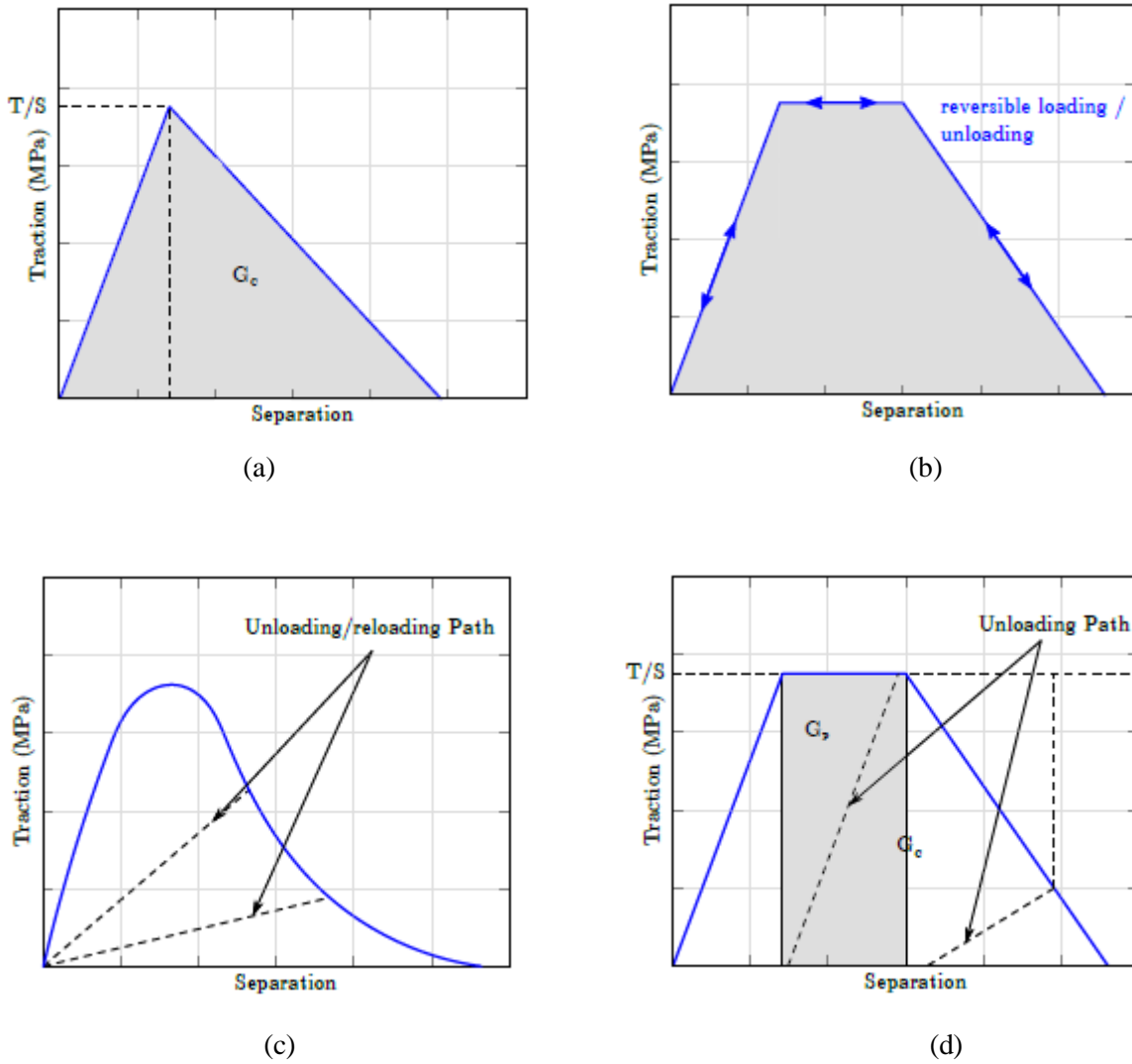
Figure 42. Traction-separation laws for available cohesive zone material Models in LS-DYNA[131]: (a) MAT 138, (b) MAT 185, (c) MAT 186, and (d) MAT 240.

Chapter 4

Hat Channel Component Axial Crush: Experimental and Numerical Model Details

As a first step in a development of the technology demonstrator, hat channel component comprised of UD-NCF carbon fiber/epoxy laminates were utilized to calibrate the material models (MAT 54 and MAT 58) used in the axial crush numerical simulation models. The mechanical properties of the CFRP material and details of the fabrication process are outlined in Section 4.1, while a detailed description of the experimental procedures are described in Section 4.2. Details of the numerical modelling strategy used for composites in LS-DYNA as well as the developed numerical simulation model for the hat channel components are presented in Sections 4.3 and 4.4, respectively.

4.1 CFRP Composite Material and Hat Channel Components
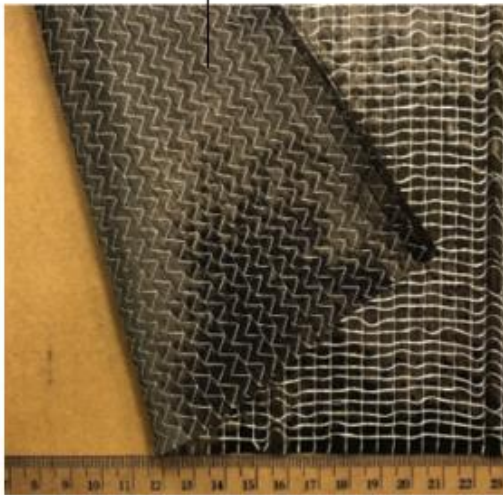
Figure 43. (a) ZOLTEK™ PX35 UD300 UD-NCF, and (b) HP-RTM manufacturing equipment [28][29].

Table 2. Ply properties of cured UD-NCF ply with a fiber volume fraction of $V_f = 53\%$ obtained from quasi-static tests [78]

MECHANICAL PROPERTIES	
Density, g/cm^3	1.46
Longitudinal Young's modulus E_1, GPa	123.39
Transverse Young's modulus E_2, GPa	8.41
Major in-plane Poisson's ratio ν_{12}	0.37
In-plane shear modulus G_{12}, GPa	3.55
Longitudinal tensile strength X_t, MPa	1765
Transverse tensile strength Y_t, MPa	60.31
Longitudinal compressive strength X_c, MPa	1000
Transverse compressive strength Y_c, MPa	144.9
In-plane shear strength S_L, MPa	89.77
Longitudinal strain at failure ε_{1f}, %	1.30
Transverse strain at failure ε_{2f}, %	0.66
Longitudinal strain at failure ε_{1c}, %	0.80
Transverse strain at failure ε_{2c}, %	2.42
In-plane shear strain at failure γ_{12f} , %	8.88

The reinforcement and matrix materials used to fabricate the CFRP composite components used in this study were ZOLTEK™ PX35 UD300 UD-NCF and HEXION EPIKOTE™ TRAC 06150 snap-cure epoxy resin, respectively [28][29]. The fabric was produced from aligned tows comprised of 50k continuous carbon fibers, supported by transversely oriented glass fibers, and stitched with a polyester yarn in a tricot pattern (Figure 43). An HP-RTM process was used to fabricate flat plates for materials characterization testing, as well as hat channel components that were used to calibrate the numerical simulation model for

predicting the axial crush response. Details of the setup and the cure cycle used can be found in Ref. [28] The ply properties of the cured CFRP composite material were extracted from Ref. [78] and used in the numerical model (Table 2).

4.2 Hat Channel Component Axial Crush Experimental Setup

The axial crush experiments for the hat channel components under quasi-static and dynamic loading rates were performed by Harvey [77], and used in this study to validate the developed numerical models. The hat channel component specifications, experimental setup, and testing conditions are described in the following paragraphs.

The fabricated CFRP hat channel components comprised of a constant cross-section with an approximate length of 800 mm (Figure 44). The hat channel was trimmed and cut to length to extract both quasi-static and dynamic test specimens (Figure 44.b). All test specimens were approximately 2.7 mm thick and comprised of 8 layers of the UD-NCF with either a $[0/\pm45/90]_s$ or a $[\pm45/0_2]_s$ stacking sequence. A chamfer trigger was machined on one end of all hat channel specimens to promote axial crushing during testing (see Section 4.4.4).

(a)   (b)
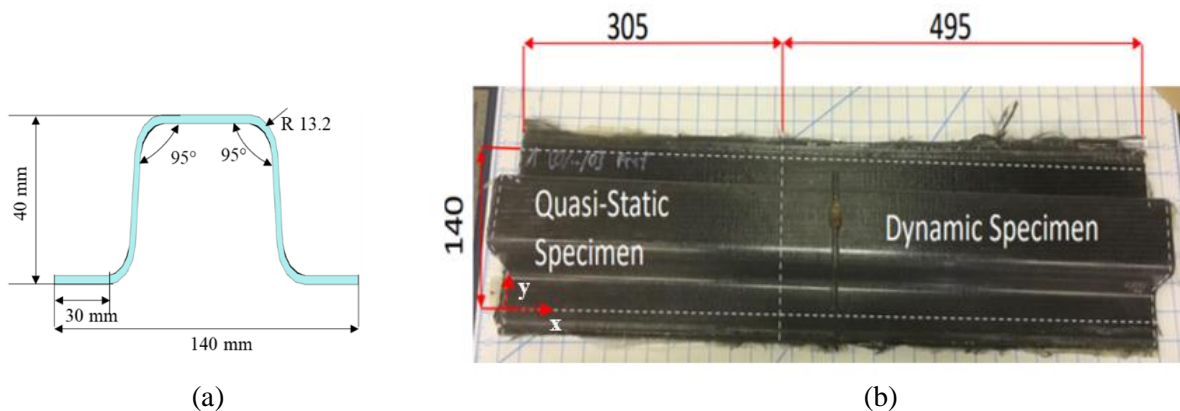
`**Figure 44.** (a) Cross-section of hat channel, (b) quasi-static and dynamic specimens from a fabricated hat channel [77].

A 600 kN hydraulic test frame was used to perform the quasi-static axial crush tests with a constant crosshead speed of 1 mm/s (Figure 45). A fixture was used to clamp a 50 mm section of the channel on the opposite end (Figure 45).
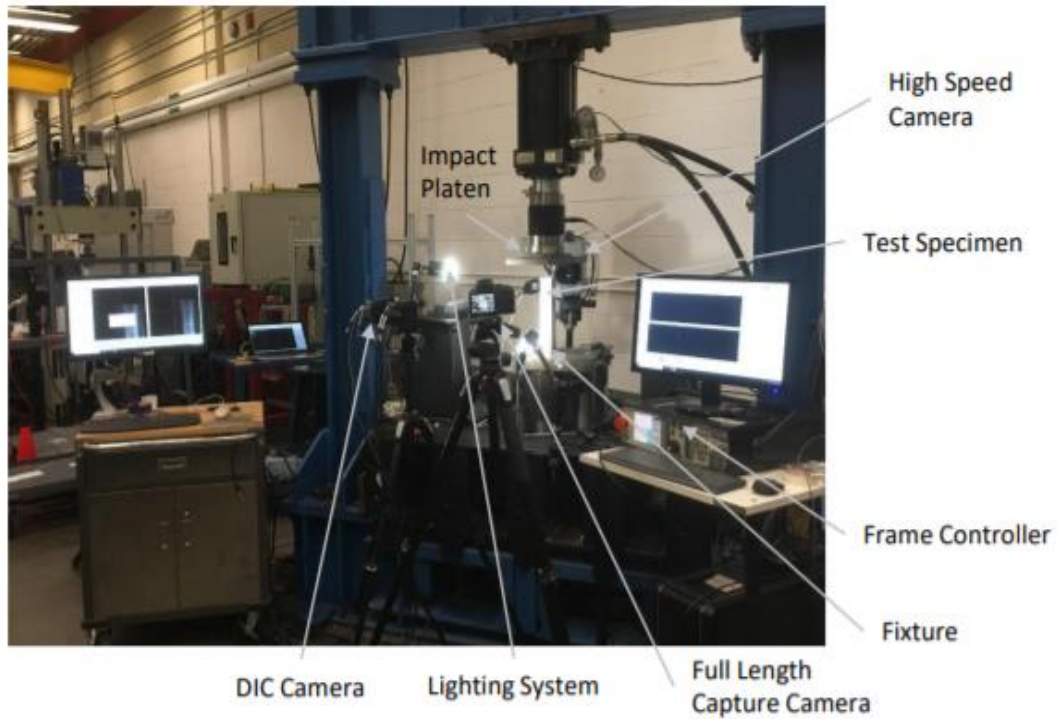
Figure 45. Experimental setup for quasi-static axial crush tests [77].

A crash sled was used to perform the dynamic tests [77], where the sled impact velocity and mass were 7.5 m/s and 855 kg, respectively (Figure 46). The same clamping fixtures used for the quasi-static tests were used for the dynamic experiments. The impact force was measured from three piezo-electric load sensors located at the impactor end, and used to establish the force-displacement response.
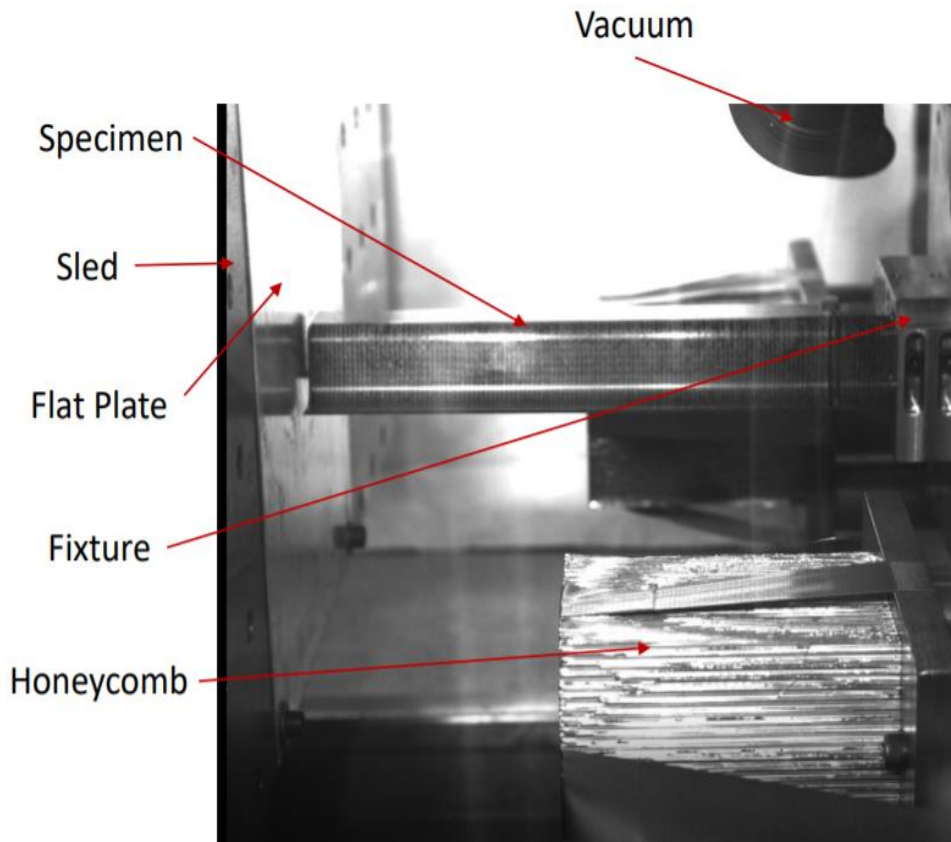
Figure 46. Experimental setup for dynamic axial crush tests [77].

4.3 Overview of Composite Modelling in LS-DYNA

Composite materials can exhibit different intralaminar and interlaminar failure modes (Chapter 2), which are dependent on the specific loading conditions, structural geometries, and ply stacking sequences. The intralaminar failure modes and damage mechanisms were considered through failure criteria in the material models. Interlaminar delamination was not considered in this study since a single shell element approach was followed, which is detailed in the subsequent paragraphs.

4.3.1 Single Shell Element Approach

A single-layer shell element modelling approach implicitly accounts for the plies of the laminated composite, where a single integration point is used for each ply through the thickness of the laminate (see Figure 47). Effective material properties for the laminated shell elements are based on the selected lamination theory. This approach was used in this study to simulate the axial crush behavior of CFRP hat

channel components. Note, the single shell element approach cannot capture the inter-ply delamination failure mode.
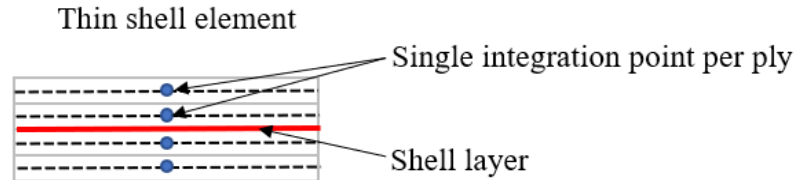
Figure 47. Shell element representation of a laminate with integration points per ply in LS-DYNA.

Additional options in the simulation model were required to use a single layer model approach, including definition of the primary laminate directions (Figure 47) and the laminate stacking sequence. The CONTROL_SHELL card was used to define the laminate theory and to control the warpage and orientation of the shell elements. The LAMSHT parameter controls the type of laminate theory used, such as CLPT or other plate deformation theories that consider the out-of-plane shear strain through the thickness of the laminate plies. The LAMSHT parameter was set to 1 for this study, which allows for out-of-plane shear strains through the thickness of the laminate plies. Generally, the results predicted tend to be stiffer if the correction flag is not used [116].

The CONTROL_ACCURACY card was used to set the accuracy of the numerical predictions. As the simulation progresses the shell elements deform and rotate, and the material coordinate system orientation changes. Changes in the material coordinate orientation may affect the shell element node numbering. This intern affects the in-plane shearing response and may lead to element hourglassing. Thus, to minimize unwanted element hourglassing by controlling the distortion of the elements, the INN option was set to 2.

4.3.2 Uniaxial Simulations with Single Element Model

Uniaxial single element simulations were performed on single plies of the UD-NCF CFRP material to understand the orthotropic stress-strain behavior captured by the material models MAT 54 and MAT 58, and to investigate the influence of the non-physical parameters (Figure 48). Prescribed displacements were applied to one side of the single element along the fiber or transverse fiber direction, with symmetry boundary conditions applied to the opposite side. Both tension and compression loading were considered.
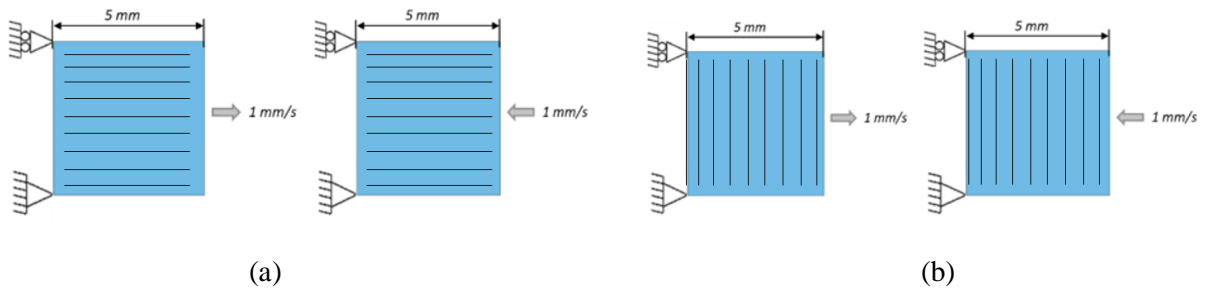
Figure 48. Uniaxial single element model: (a) Tension and compression along the UD lamina fiber direction, and (b) Tension and compression along the UD lamina transverse direction.

4.4 Hat Channel - Axial Crush Model

The material models MAT 54 and MAT 58 were both considered for simulating axial crush of the hat channel components (Figure 49), while the single shell element approach (Section 4.3.1) with the available quasi-static lamina properties (Table 2) was used. Note, the same lamina properties were used for both the quasi-static and dynamic simulations. The setup of the simulation model comprised of four main parts: geometry, material orientation, crush trigger representation, and application of boundary conditions. In this study, the following system of units was used: force in [N], distance in [mm], energy in [J], and time in [s].

4.4.1 Elemental Formulation and Mesh for Hat Channel

The axial crush simulation models for the hat channel component were developed to replicate the corresponding experiments. For simplification, only the fixture mounting plate and the flat impactor were modelled, without considering the entire quasi-static or dynamic test setup. The elements used to mesh the hat channel components were fully integrated BELYTSCHKO-TSAY shell elements (Type 16), which were generated using the commercially available mesh generator tool ANSA Version 20.0.0 (BETA CAE Systems International AG, Root, Switzerland). Three types of mesh patterns were studied: uniform structured quad mesh, V-patterned structured quad mesh, and non-structured triangular mesh with triangular shell elements (Figure 49). The V-patterned mesh was suggested by Boria et al. [105] and Andersson et al. [106] to avoid substantial oscillations in the force-displacement response when using MAT 54 for simulating axial crush of components. To investigate the effect of element mesh size, the hat channel components were meshed using five different element sizes (i.e., 2 mm, 3 mm, 4 mm, 5 mm, and 6 mm).
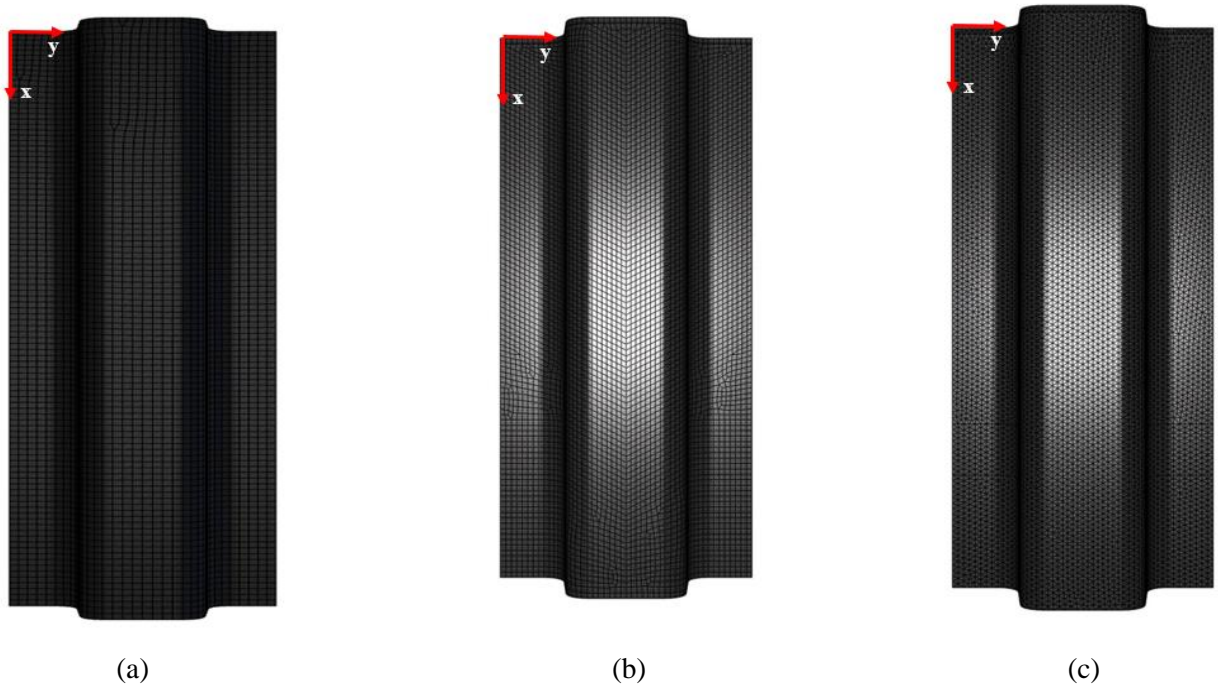
Figure 49. Hat channel components meshed with different patterns: (a) uniform structured quad mesh, (b) V-patterned structured quad mesh, and (c) non-structured triangular mesh.

The steel impactor for all performed simulations was modelled using a refined mesh of shell elements and treated as a rigid body (Figure 50.a). The friction coefficient for the composite specimen and impactor was maintained at 0.2 as per recommendations from Refs. [100],[121], [132],[133]. Furthermore, the fixed-end steel mounting plate was modeled using solid elements with rigid material properties (Figure 50).
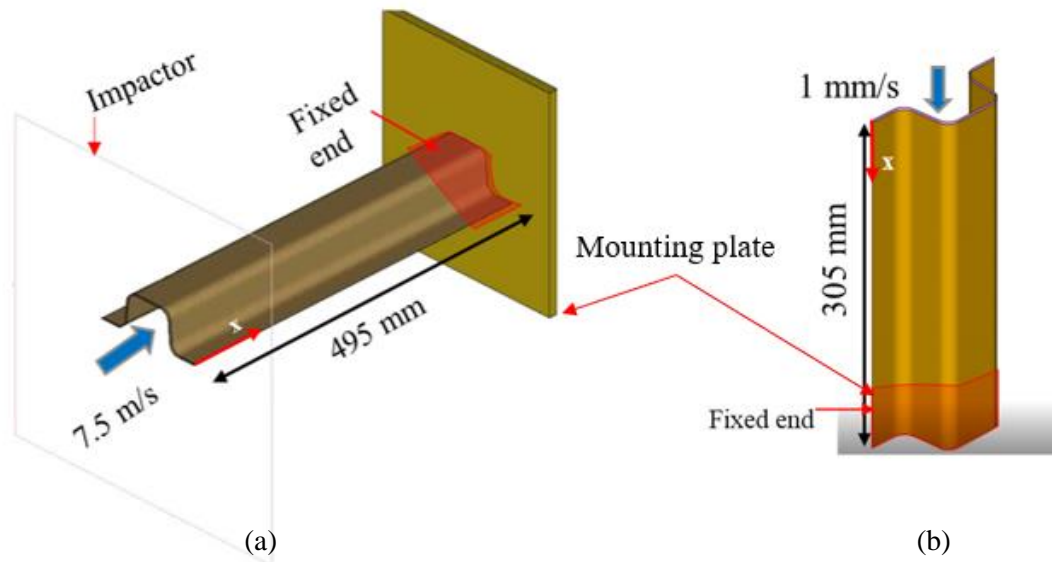
Figure 50. Boundary conditions for axial crush simulations of the hat channel specimen: (a) dynamic loading condition, and (b) quasi-static loading condition.

4.4.2 Defining Local Material and Laminate Coordinate System Orientations

Since laminated composite materials are orthotropic, it is crucial to properly define the local material directions for the plies (i.e., directions 1, 2, 3 in Figure 7) and the primary directions for the laminate (i.e., directions *x*, *y*, *z* in Figure 7) in the numerical model. The directions for the laminate (i.e., principal a-b-c coordinate system in LS-DYNA) were defined by the material orientation option in ANSA. The principal laminate axis were mapped using a guide curve along the laminate *x*-direction (Figure 51), which rearranged the node numbering according to the mapped direction. Also, there are five material axes options (AOPT) for the MAT 54 and 58 material models. For this study, AOPT was set to zero for the shell elements, which assigned the laminate *x*-direction using three elemental nodes (i.e., N1, N2, and N4). If the a-b-c coordinate system is defined by the AOPT options in the material model, the laminate *x*-direction can be offset with respect to the global coordinate system for the FE model.
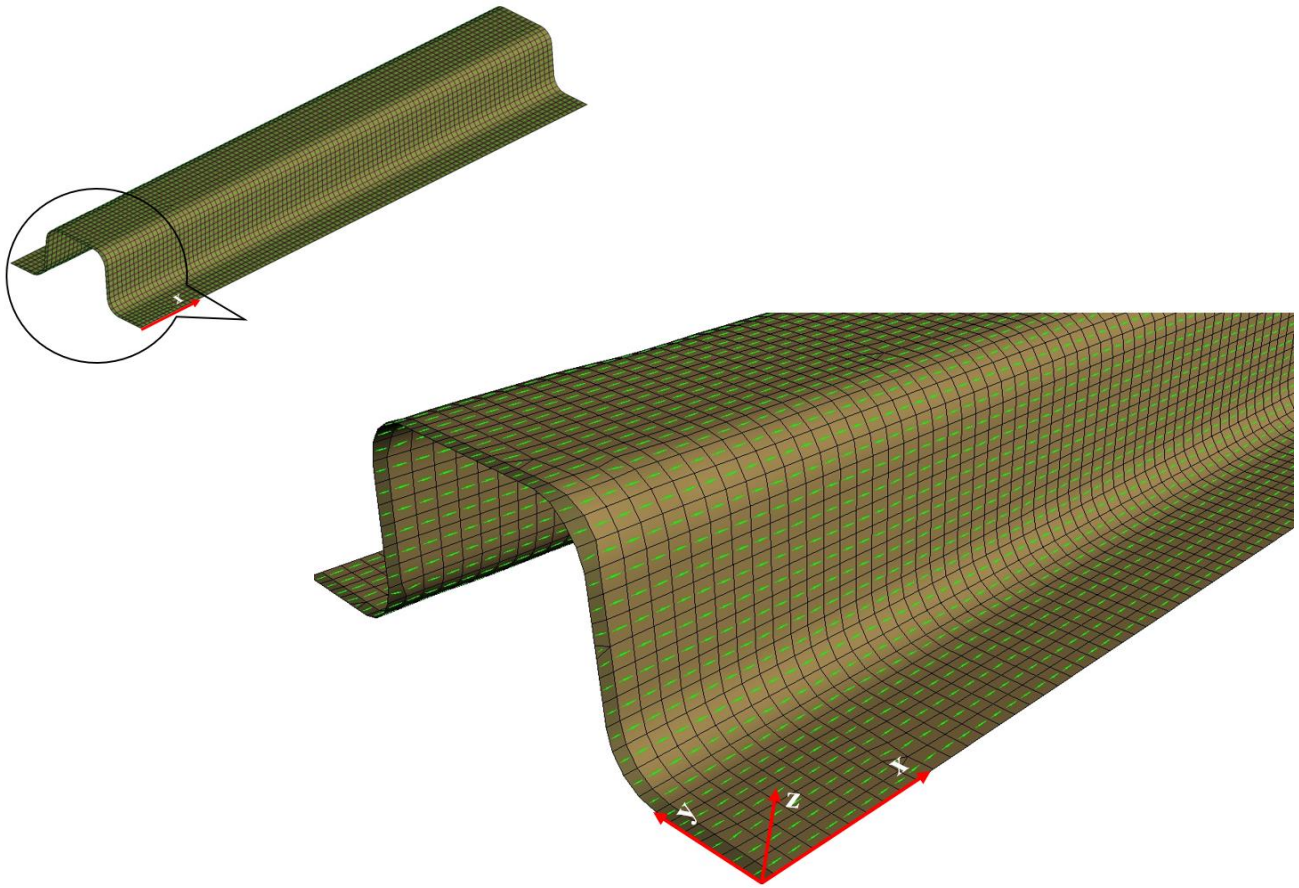
Figure 51. Principal laminate coordinate system for the hat channel component.

4.4.3 Modelling of Stacking Sequence

The LAMINATE TOOL in ANSA was utilized to define the laminate stacking sequence for the 2D shell elements. The number of plies was defined, as well as the orientation, material, and thickness of each ply. Two different stacking sequences (i.e., $[0/\pm45/90]_s$ and $[\pm45/0_2]_s$) were considered for the hat channel component (Figure 52). In the ANSA property card, the output type for the hat channel and trigger components are set to the PART_COMPOSITE keyword to define the stacking sequence and thickness for the LS-DYNA solver (Figure 53).

Angle= 0
Angle= 45
Angle= -45
Angle= 90
Angle= 90
Angle= -45
Angle= 45
Angle= 0
Layup 1 – [0/±45/90]$_s$

Angle= 45
Angle= -45
Angle= 0
Angle= 0
Angle= 0
Angle= 0
Angle= -45
Angle= 45
Layup 2 - [±45/0$_2$]$_s$
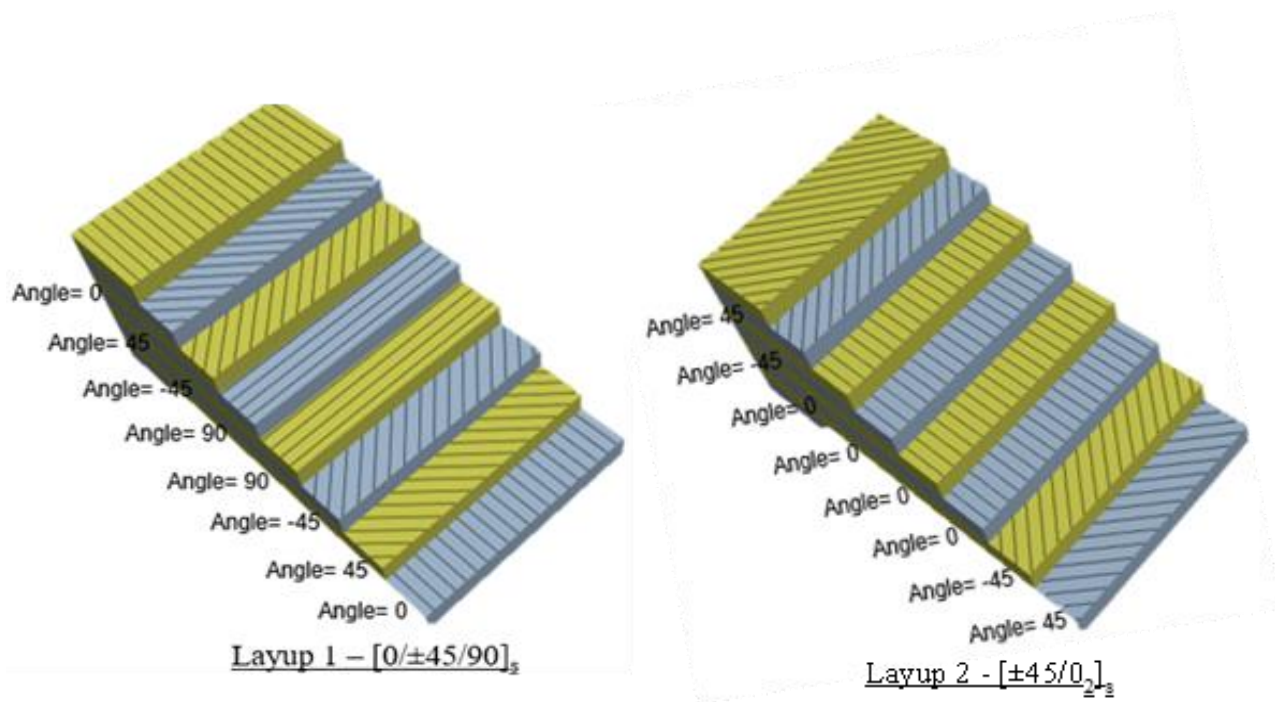
(a)   (b)

Figure 52. Ply orientation for: (a) layup 1, and (b) layup 2.
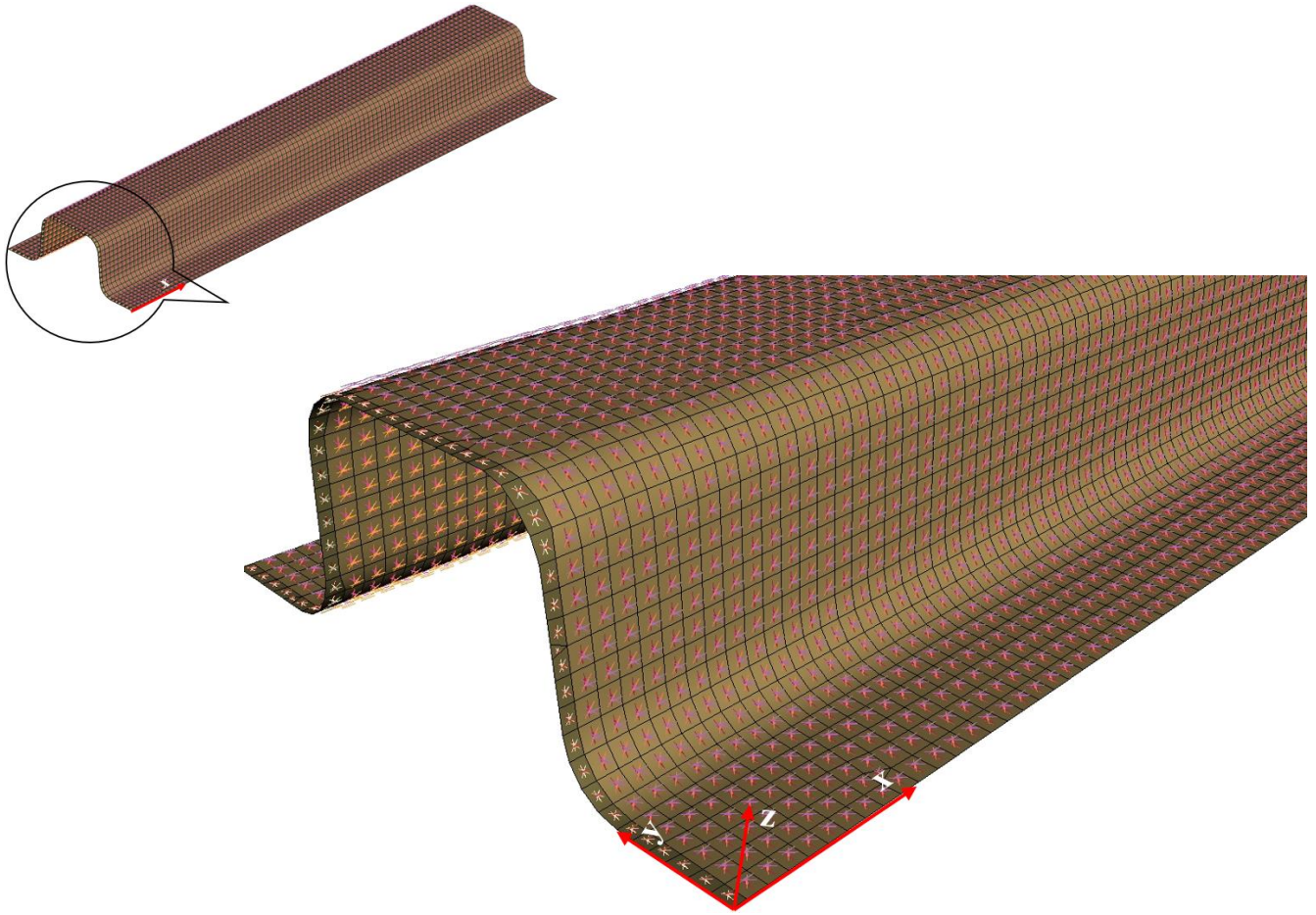
Figure 53. PART_COMPOSITE option where a single integration point is defined for each ply in the laminate for the shell elements.

4.4.4 Trigger – Crush Initiator

Due to the challenge with modeling the chamfer trigger in the hat channel specimens with shell elements, a reduced shell element thickness was introduced to the nodes in the trigger region (Figure 54). The geometry was partitioned over a 3mm length from the impactor end of the specimen. The region was assigned with the same material properties and number of plies, with a ply thickness reduced to half (Figure 54). Although this approach fails to consider the local failures in the trigger region, it simplified the development of the simulation model and provided the geometric discontinuity needed to initiate progressive failure.
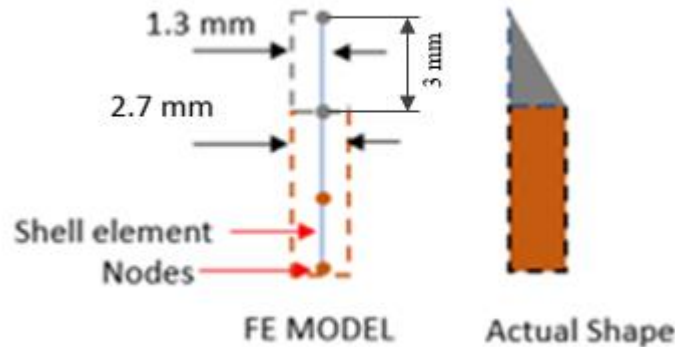
Figure 54. Representation of chamfer trigger for the hat channel component for a single shell element layer approach.

4.4.5 Boundary Conditions – Dynamic Simulations

For the dynamic test simulations, the fixed end of the hat channel specimen (i.e., the region clamped by the fixture shown in Figure 50) was modelled by constraining the total clamped length of 50 mm in all six degrees of freedom. The TIED_SURFACE_TO_SURFACE contact algorithm in LS-DYNA was defined between the specimen and the rigid mounting plate (Figure 50a).

The rigid impactor plate was assigned a mass of 855 kg (i.e., the sled mass) and an initial velocity of 7.5 m/s along the channel axis to match the experimental conditions (Figure 50.a). The AUTOMATIC_SINGLE_SURFACE contact algorithm was defined between the hat channel specimen and impactor, which also considered self-contact for the hat channel and impactor. The dynamic crash simulations were run for 0.03 s, and the simulation time step was defined using the Friedrichs-Levy condition to maintain numerical stability. It should be noted that the honeycomb material used in the experiments to decelerate the sled was not considered in the numerical model, and crushing was only simulated for the free crush length prior to engagement of the honeycomb.

4.4.6 Boundary Conditions – Quasi-Static Simulations

For the quasi-static test simulations, the same boundary conditions on the fixed end of the hat channel specimen used for the quasi-static simulations were defined (Figure 50.b). The rigid impacting

plate was assigned a constant prescribed velocity of 1 mm/s along the channel axis to match the test conditions. Furthermore, time-scaling was employed for the quasi-static simulations. The prescribed impact velocity was scaled by a factor of 500 to attain a value of 500 mm/s. The time scaling on the prescribed velocity was imposed to reduce the total run time of the quasi-static models.

Chapter 5

Hat Channel Component Axial Crush Results

In this chapter the existing experimental results that were used for calibrating the material models MAT 54 and MAT 58 are presented (Section 5.1). The results of uniaxial single element simulations using MAT 54, including the effect of the residual stress parameters, are outlined in the Section 5.2. A parametric study that was performed to calibrate key non-physical parameters in MAT 54 material model are described in Section 5.3. Similarly, single element model simulation results and the outcome of a parametric study for MAT 58 material model are described in the Sections 5.4 and 5.5. Finally, the axial crush prediction results using the two calibrated material models for the hat channel with two different stacking sequences ($[0/\pm45/90]_s$ and $[\pm45/0_2]_s$) and two different loading conditions are presented (Section 5.6).

5.1 Experimental results for numerical calibration

The hat channel with a $[0/\pm45/90]_s$ stacking sequence subjected to dynamic loading conditions was selected for calibration of two material models. The experimental force-displacement results [77] (Figure 55) were utilized to compare with the results of the numerical predictions for calibration (see Sections 5.3 and 5.5). The load-displacement profiles for each tested hat channel were repeatable, with a high initial peak force (82.3 kN) and a sudden drop to a stable mean crush force (40 kN) through a 200 mm crush distance.
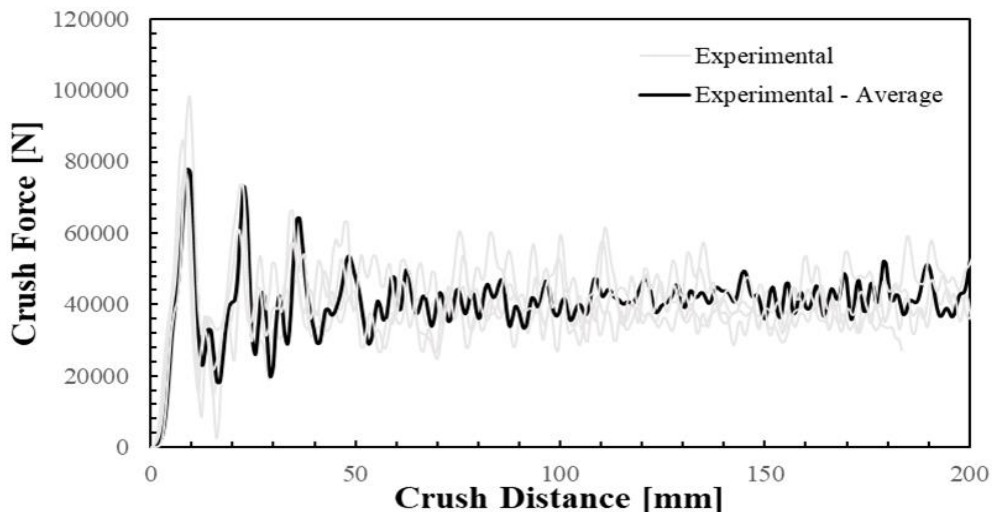
Figure 55. Experimental force vs displacement plots for hat channel specimens with a $[0/\pm45/90]_s$ stacking sequence under dynamic axial crush loading [77].

66

5.2 MAT 54 - Uniaxial Simulations with Single Element Model

The single element models were used to characterize the material model and adjust the non-physical parameters for the UD-NCF composite plies. The stress-strain behavior of a UD lamina in tension and compression along both the fiber and transverse directions are shown in Figure 56 for the case when the SLIM parameters were set to zero. Without the post-peak residual stresses, the UD lamina response along the direction was perfectly plastic material after failure, where the level of stress remained constant until the defined maximum failure strains were achieved.
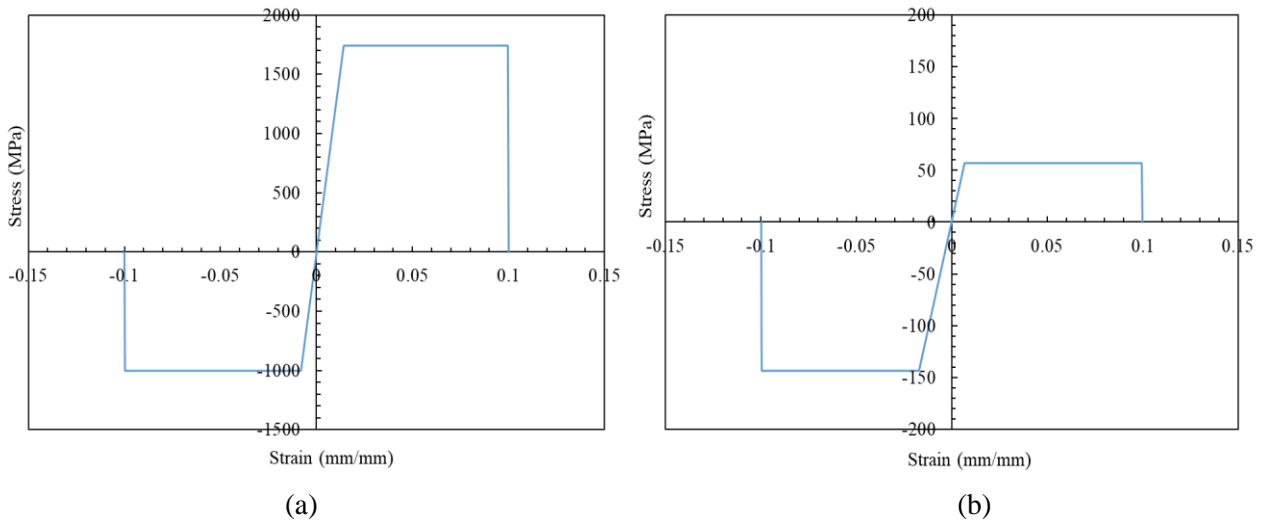
Figure 56. Single element model predicted uniaxial stress-strain behavior (SLIM parameters set to zero): (a) fiber tension and compression, and (b) transverse tension and compression.

For the case when the residual stress is considered through non zero SLIMT1, SLIMC1, SLIMT2, and SLIMC2 parameters, the stress level suddenly dropped after the peak stress was attained to a value that was a fraction of the peak stress as defined by the SLIM parameter (Figure 57). The stress remained constant until the maximum failure strain were achieved.
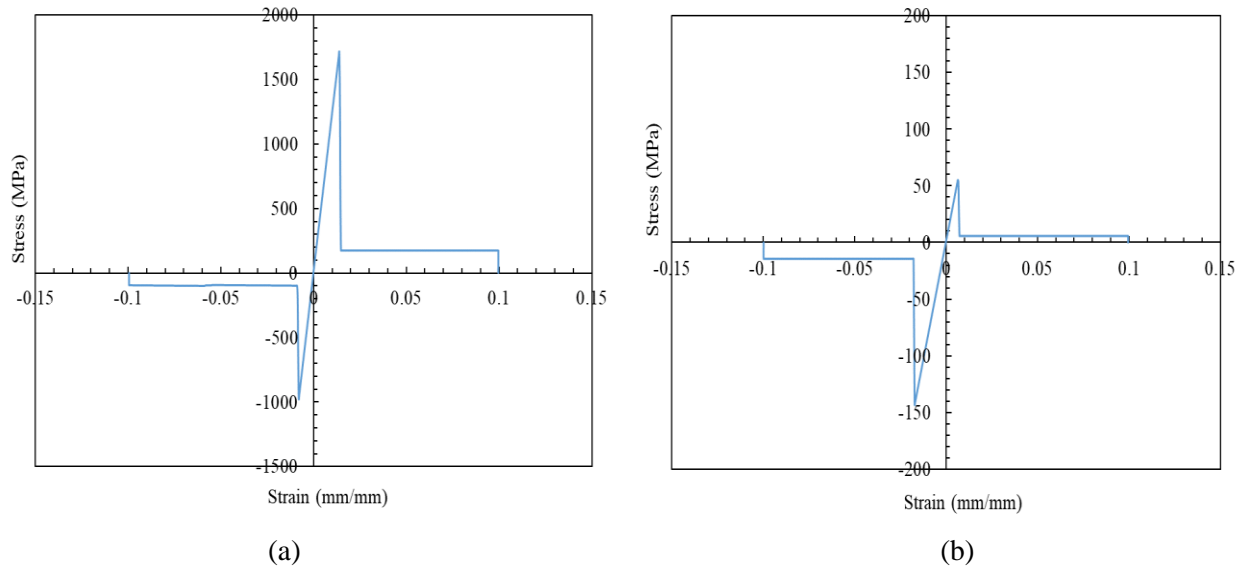
Figure 57. Single element model predicted uniaxial stress-strain behavior (SLIM parameters set to 0.1): (a) fiber tension and compression, and (b) transverse tension and compression.

5.3 Calibration of MAT 54 Material model

The hat channel component with a [0/±45/90]$_s$ stacking sequence under dynamic loading conditions was numerically modelled for calibration of the non-physical parameters in the material model. The effect of mesh shape and size the axial crush performance of the hat channel was also evaluated. Each non-physical parameter in the material model was calibrated through a parametric study.

5.3.1 Effect of Mesh shape

Axial crush simulations were performed on the hat channel specimens for all three mesh patterns, namely uniform structured quad mesh, V-patterned structured quad mesh, and non-structured triangular mesh. The simulation with the uniform structured quad mesh predicted progressive crushing behavior with many force oscillations, as evidenced by the force-displacement response (Figure 58). After the deletion of the trigger elements, the strength reduction parameter (SOFT) reduced the strength of the next row of elements that were in contact with the impactor plate. This resulted in a progressive row-by-row element erosion and the observed force oscillations (Figure 58). In other words, the force reached a peak value when the impactor was in contact with the hat channel and suddenly dropped to a near zero value once the elements were deleted, which is not a physically accurate response. The simulations with the V-patterned structured quad mesh and non-structured triangular mesh resolved the row-by-row element erosion issue.

68

For both simulations, the impactor established continuous contact with the hat channel, while progressive crushing was observed after the initial peak force (Figure 58). A higher mean crush force was observed with the non-structured triangular mesh when compared with the V-patterned structured quad mesh, while the peak force was approximately constant for both. The high sensitivity of the simulation model to the mesh pattern may be due to the post-peak response considered in the MAT 54 material model.
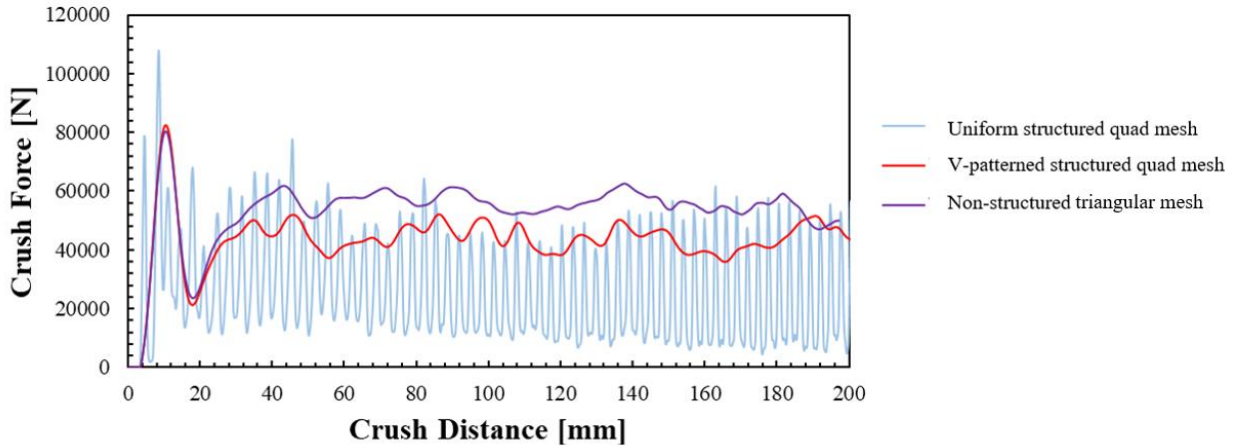
Figure 58. MAT 54 - Force vs displacement response of hat channel specimen with [0/±45/90]$_s$ stacking sequence under dynamic loading conditions for different mesh patterns.

5.3.2 Effect of Mesh size

To further evaluate the mesh dependency of the developed simulation model, axial crush of the hat channels for the V-patterned structured quad mesh with five different element sizes were performed. Simulations with element sizes in the range of 3-6 mm produced similar force-displacement responses, with progressive crushing under a mean crush force of approximately 48 kN (Figure 59). The corresponding energy absorption was also similar for these simulations (Figure 60). It was observed that the force-displacement response for simulations with 2 mm elements dropped to zero force and created numerical instabilities during the simulation. During stable crushing, the force response for the simulations with the 6 mm element size exhibited more substantial oscillations and higher value of average crushing force, whereas the simulations with the other element sizes produced lower magnitude force oscillations. An element size of 5mm was selected for subsequent simulations to balance computational efficiency and accuracy, which was close to element sizes used for vehicle crash simulations [108][113].

69
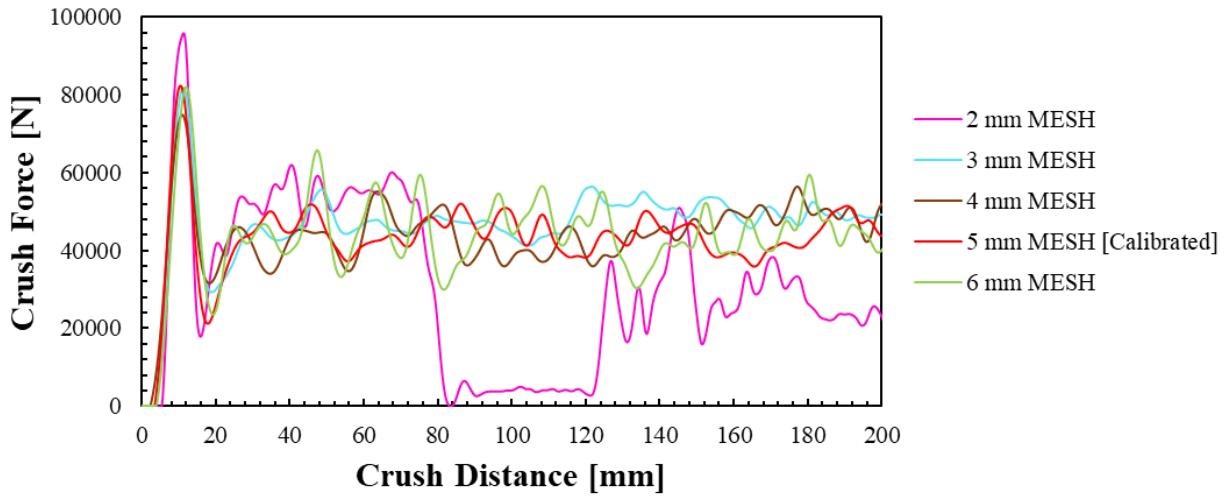
Figure 59. MAT 54 - Force vs displacement response of hat channel specimen with [0/±45/90]$_s$ stacking sequence under dynamic loading conditions for different mesh sizes.
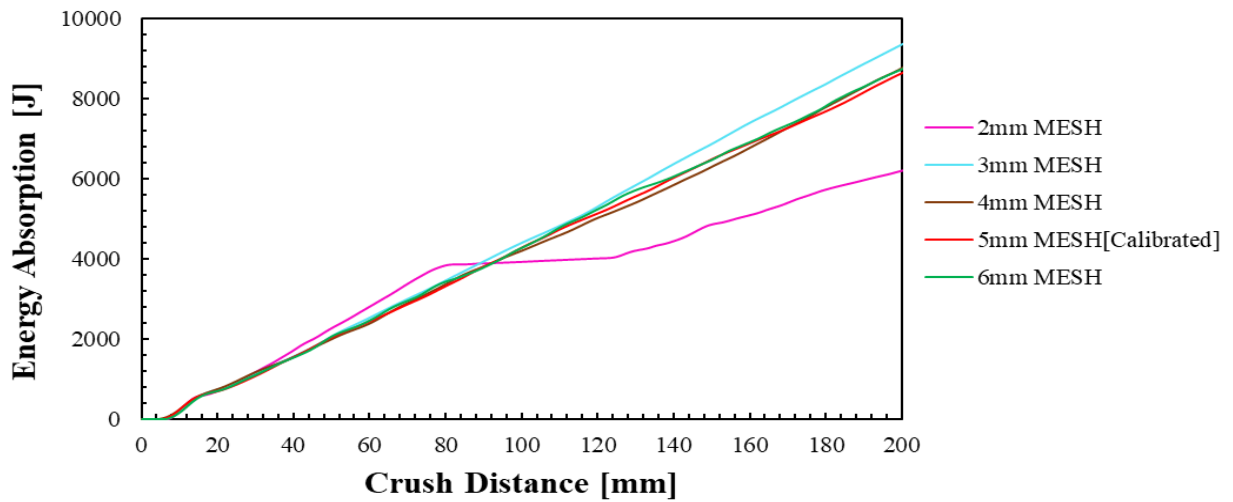
Figure 60. MAT 54 – Energy absorption response of hat channel specimen with [0/±45/90]$_s$ stacking sequence under dynamic loading conditions for different mesh sizes.

5.3.3 Effect of Non-physical parameters

In addition to the mesh dependency, the various non-physical parameters in the material card that cannot be experimentally defined were calibrated through a parametric study. The effects of each parameter on the axial crush response of the hat channel component are discussed below. A parametric study was conducted for a group of non-physical parameters in the MAT 54 material model, including DFAIL, SLIM and SOFT parameters. A V-patterned structured quad mesh with an element size of 5 mm was used for all simulations.

5.3.3.1 DFAILT

DFAILT parameter is the maximum strain to failure for the fiber tensile failure mode of a lamina, beyond the peak stress. A parametric variation was performed by considering values ranging from 0 to 1. The force-displacement response (Figure 61) and energy absorption data (Figure 62) for the hat channel were consistent for all DFAILT values considered, with some slight variation during stable crushing at the mean crushing load. This is not surprising since the fiber tensile failure mode was not the primary mode of failure for the lamina. The results corresponding to a value of DFAILT = 0.15 force response was similar to the experimental data (Figure 55).
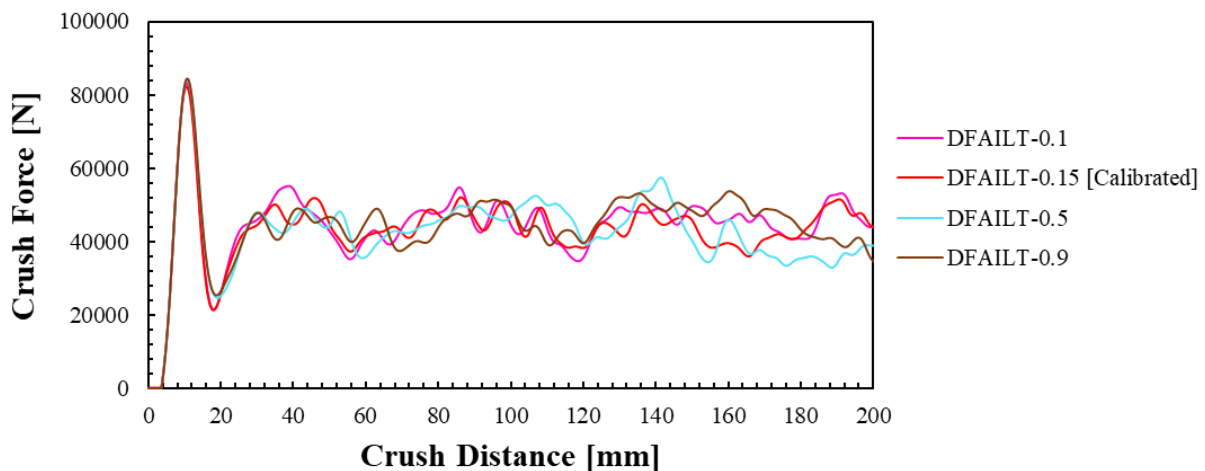
Figure 61. MAT 54 - Force vs displacement response of hat channel specimen with $[0/\pm45/90]_s$ stacking sequence under dynamic loading conditions for different values of DFAILT.
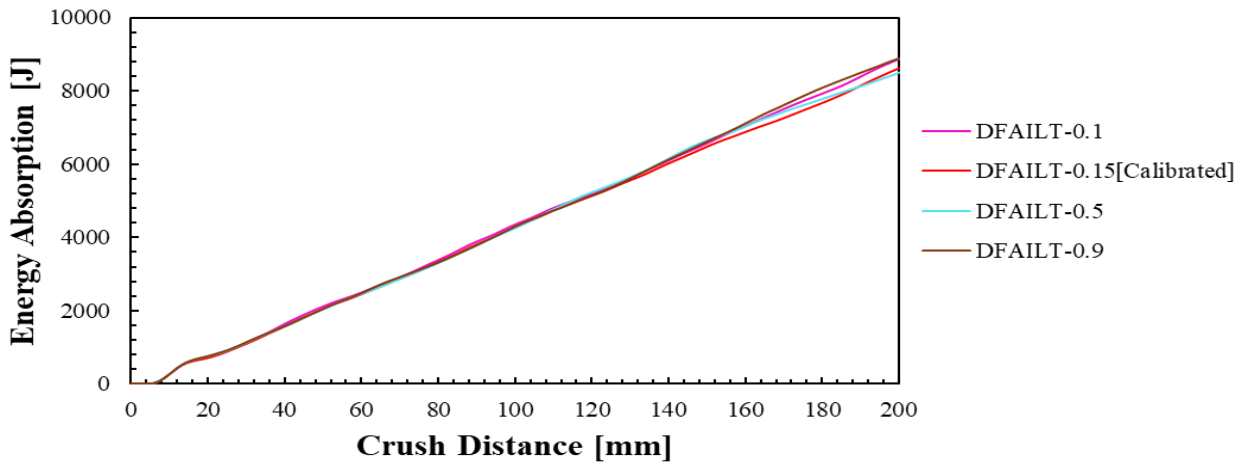
Figure 62. MAT 54 – Energy absorption response of hat channel specimen with [0/±45/90]ₛ stacking sequence under dynamic loading conditions for different values of DFAILT.

5.3.3.2 DFAILC

DFAILC parameter is the maximum strain to failure for the fiber compressive failure mode of a lamina, beyond the peak stress. Values ranging from -1 to 0 were considered. The initial peak force and mean crush force (Figure 63) and energy absorption (Figure 64) were greatly influenced by the values of DFAILC, which is not surprising since the 0° plies were subjected to compressive stresses. The predicted initial peak force and mean crush force decreased with decreasing DFAIL values. The results for a value of DFAILC = 0.28 produced a force-displacement response that was similar to the experimental data (Figure 55).
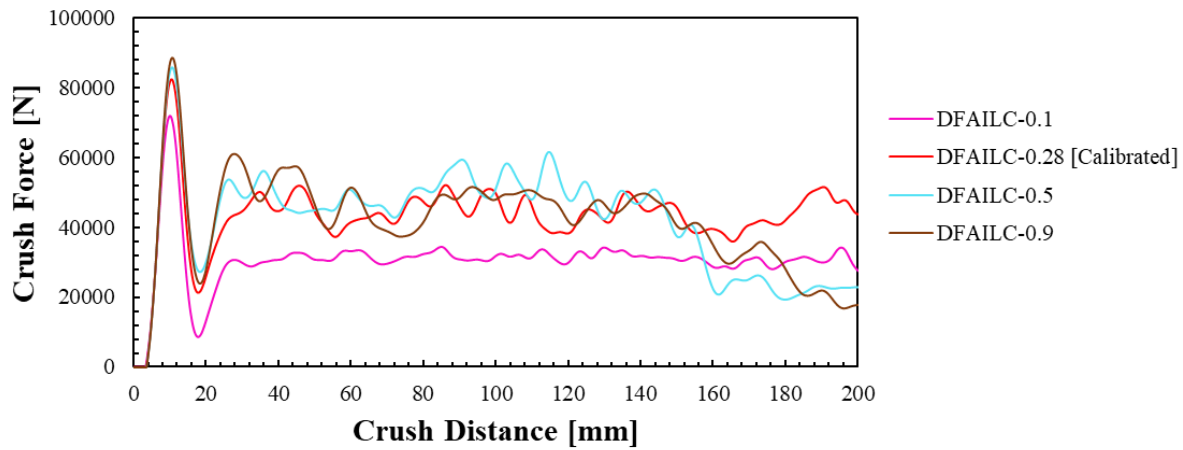
Figure 63. MAT 54 - Force vs displacement response of hat channel specimen with [0/±45/90]ₛ stacking sequence under dynamic loading conditions for different values of DFAILC.

Figure 64. MAT 54 – Energy absorption response of hat channel specimen with [0/±45/90]ₛ stacking sequence under dynamic loading conditions for different values of DFAILC.

5.3.3.3 DFAILM

DFAILM parameter is the maximum strain to failure for both the matrix tension and compression failure mode of a lamina, beyond the peak stress. A parametric variation was performed by considering

values ranging from 0 to 1. The force-displacement response (Figure 65) and energy absorption (Figure 66) were increased for increasing DFAILM values. The numerical prediction corresponding to a value of DFAILM=0.28 produced a force-displacement response corresponding to the experimental data (Figure 55). For higher values of DFAILM, numerical models were computationally expensive.

Figure 65. MAT 54 - Force vs displacement response of hat channel specimen with [0/±45/90]ₛ stacking sequence under dynamic loading conditions for different values of DFAILM.
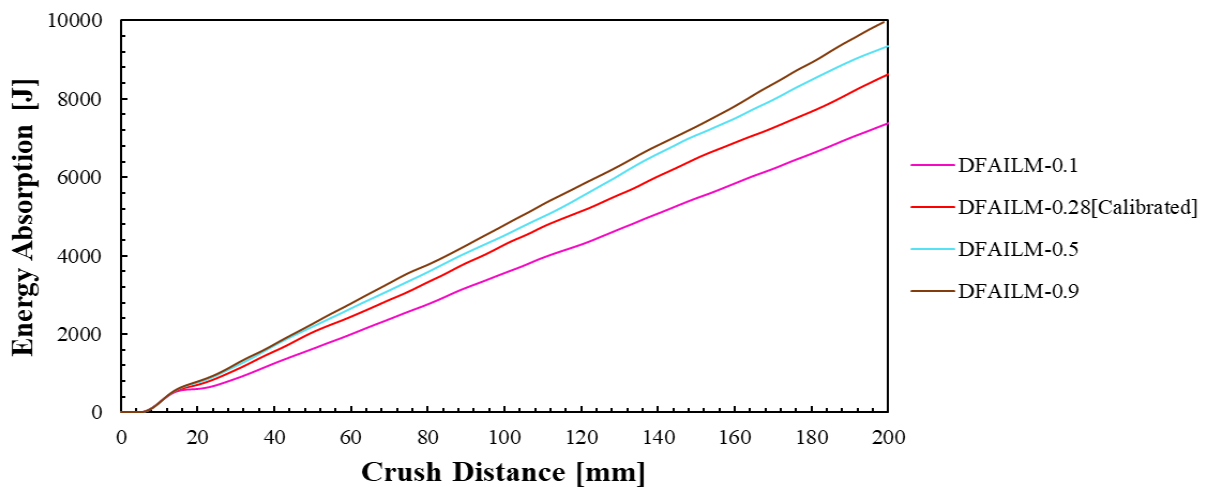
Figure 66. MAT 54 – Energy absorption response of hat channel specimen with [0/±45/90]ₛ stacking sequence under dynamic loading conditions for different values of DFAILM.

74

5.3.3.4 DFAILS

DFAILS parameter is the maximum strain to failure for shear failure mode of a lamina, beyond the peak stress. Values ranging from 0 to 1 were considered. The mean crush force (Figure 67) and energy absorption (Figure 68) were greatly influenced until value of 0.28. However, for increased values of DFAILS the force-displacement response and energy absorption data were consistent, with some slight variations in mean crush force. The results for the value of DFAILS = 0.28 force response was same as the experimental data (Figure 55).

Figure 67. MAT 54 - Force vs displacement response of hat channel specimen with [0/±45/90]$_s$ stacking sequence under dynamic loading conditions for different values of DFAILS.

Figure 68. MAT 54 – Energy absorption response of hat channel specimen with $[0/\pm45/90]_s$ stacking sequence under dynamic loading conditions for different values of DFAILS.

5.3.3.5 SLIMT1

SLIMT1 parameter defines the magnitude of post-peak residual stress for the fiber tensile failure mode of a lamina. A parametric study was performed by considering values ranging from 0 to 1. The initial peak force (Figure 69) and energy absorption data (Figure 70) for the hat channel were consistent for all the values of SLIMT1 considered, with some slight variations for mean crush force. The results corresponding to a value of SLIMT1 = 0.3 force response was correlated well with experimental data (Figure 55).

Figure 69. MAT 54 - Force vs displacement response of hat channel specimen with $[0/\pm45/90]_s$ stacking sequence under dynamic loading conditions for different values of SLIMT1.

Figure 70. MAT 54 – Energy absorption response of hat channel specimen with [0/±45/90]ₛ stacking sequence under dynamic loading conditions for different values of SLIMT1.

5.3.3.6 SLIMT2

SLIMT2 parameter defines the magnitude of post-peak residual stress for the transverse tensile failure mode of a lamina. Values ranging from 0 to 1 were considered. The force-displacement (Figure 71) and energy absorption (Figure 72) were constant for all values of SLIMT2, with some slight variations for average crush force. The results for a value of SLIMT2 = 0.3 produced force response that was same as the experimental data (Figure 55).

Figure 71. MAT 54 - Force vs displacement response of hat channel specimen with [0/±45/90]ₛ stacking sequence under dynamic loading conditions for different values of SLIMT2.

Figure 72. MAT 54 – Energy absorption response of hat channel specimen with [0/±45/90]$_s$ stacking sequence under dynamic loading conditions for different values of SLIMT2.

5.3.3.7 SLIMC1

SLIMC1 parameter defines the magnitude of post-peak residual stress for the fiber compressive failure mode of a lamina. A parametric study was performed for values ranging from 0 to 1. The initial peak force and average crush force (Figure 73) and energy absorption (Figure 74) were greatly influenced by the values of SLIMC1. The predicted force response and energy absorption data increased with increasing SLIMC1 values. The force-displacement response predicted for a value of SLIMC1 = 0.8 was similar to the experimental data (Figure 55).

Figure 73. MAT 54 - Force vs displacement response of hat channel specimen with [0/±45/90]$_s$ stacking sequence under dynamic loading conditions for different values of SLIMC1.

Figure 74. MAT 54 – Energy absorption response of hat channel specimen with [0/±45/90]$_s$ stacking sequence under dynamic loading conditions for different values of SLIMC1.

5.3.3.8 SLIMC2

SLIMC2 parameter controls the magnitude of post-peak residual stress for the transverse compressive failure mode of a lamina. Values ranging from 0 to 1 were considered. The initial peak force for the hat channel were consistent for all values of SLIMC2 considered. However, the mean crush force (Figure 75) and energy absorption data (Figure 76) were influenced by increasing values of SLIMC2. The

results for the value of SLIMC2 = 0.8 produced force-displacement response that was same as the experimental data (Figure 55).

Figure 75. MAT 54 - Force vs displacement response of hat channel specimen with [0/±45/90]$_s$ stacking sequence under dynamic loading conditions for different values of SLIMC2.
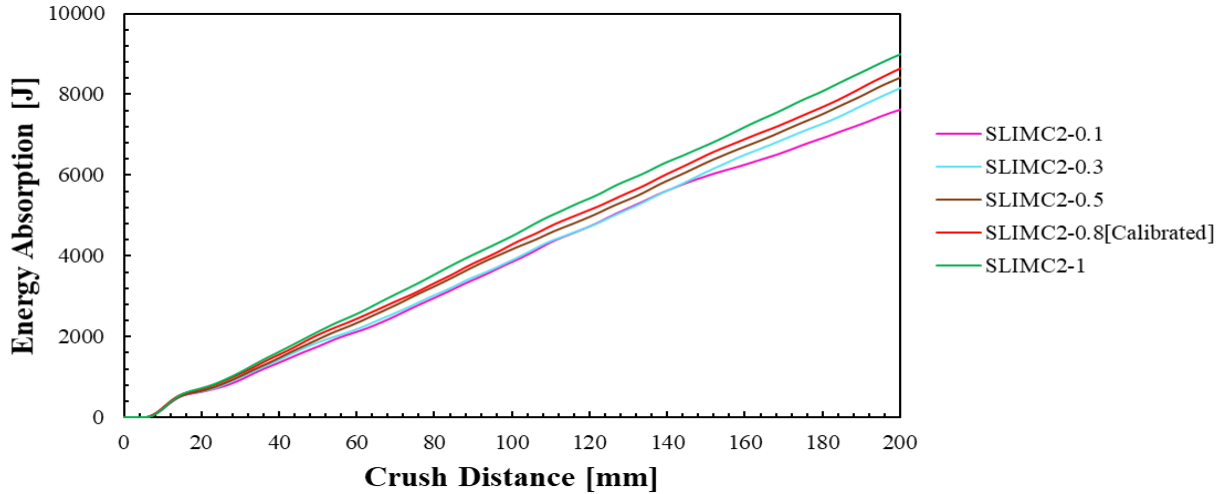
Figure 76. MAT 54 – Energy absorption response of hat channel specimen with [0/±45/90]$_s$ stacking sequence under dynamic loading conditions for different values of SLIMC2.

5.3.3.9 SLIMS

SLIMS parameter defines the magnitude of post-peak residual stress for the shear failure mode of a lamina. A parametric variation was performed by considering values ranging from 0 to 1. The force-displacement response (Figure 77) and energy absorption data (Figure 78) were consistent for all SLIMS values considered, with some slight variations with average crushing load. The results corresponding to a value of SLIMS = 0.8 force response was same as the experimental data (Figure 55).

Figure 77. MAT 54 - Force vs displacement response of hat channel specimen with [0/±45/90]$_s$ stacking sequence under dynamic loading conditions for different values of SLIMS.

Figure 78. MAT 54 – Energy absorption response of hat channel specimen with [0/±45/90]$_s$ stacking sequence under dynamic loading conditions for different values of SLIMS.

5.3.3.10 SOFT

Figure 79. MAT 54 - Force vs displacement response of hat channel specimen with [0/±45/90]ₛ stacking sequence under dynamic loading conditions for different values of SOFT.

Figure 80. MAT 54 – Energy absorption response of hat channel specimen with [0/±45/90]ₛ stacking sequence under dynamic loading conditions for different values of SOFT.

SOFT parameter is the crash front algorithm that scales down the lamina strength for the elements in the immediate crash front. Values ranging from 0 to 1 were considered. The initial peak force and average crush force (Figure 79) and energy absorption data (Figure 80) were highly influenced by values of SOFT. The predicted peak force and average crush force decreased with decreasing SOFT values. However, the results corresponding to SOFT = 0 and 0.98 was consistent capturing the small influence of the parameter.

The results corresponding to a value of SOFT = 0.98 force response was observed to similar to the experimental data (Figure 55).

5.3.3.11 MAT 54 - Calibration Summary

The sensitivity analysis presented in previous sections led to the calibration of each non-physical parameter, which is summarized (Table 3).

Table 3. Calibrated non-physical parameters for MAT54 material model.

Parameter	Calibrated Value	Parametric Variations Considered
DFAILT	0.15	0.1, 0.15, 0.5, 0.9
DFAILC	-0.28	-0.1, -0.28, -0.5, 0.9
DFAILM	0.28	0.1, 0.28, 0.5, 0.9
DFAILS	0.3	0.1, 0.28, 0.5, 0.9
SLIMT1	0.3	0.1, 0.3, 0.5, 0.8, 1.0
SLIMT2	0.3	0.1, 0.3, 0.5, 0.8, 1.0
SLIMC1	0.8	0.1, 0.3, 0.5, 0.8, 1.0
SLIMC2	0.8	0.1, 0.3, 0.5, 0.8, 1.0
SLIMS	0.8	0.1, 0.3, 0.5, 0.8, 1.0
SOFT	0.98	0.0, 0.25, 0.5, 0.75, 0.98

5.4 MAT 58 – Uniaxial Simulations with Single Element Model

Most of the non-physical parameters for the material model MAT 58 are common to those considered in MAT 54. A similar sensitivity study was performed using the single element models to assess the effect of each non-physical parameter on the lamina response.

The stress-strain behavior of the UD lamina in tensile and compression along both the fiber and transverse directions are shown in Figure 81 for the case when the SLIM parameters were set to zero. The pre-peak response was linear elastic until just prior to the peak stress, where a nonlinear response was

predicted based on the damage model (Section 3.3.1). Without the residual stresses defined the lamina post-peak non-linear response was continuous and reduced to zero, which was maintained until the defined maximum failure strain was achieved.

(a)   (b)
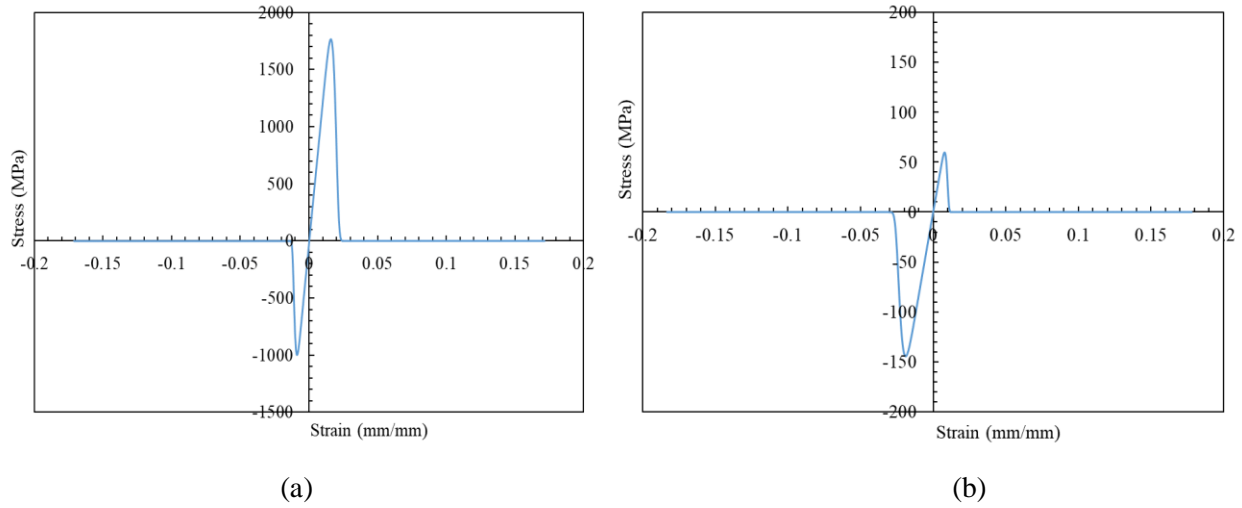
Figure 81. Single element model predicted uniaxial stress-strain behavior (SLIM parameters set to zero): (a) fiber tension and compression, and (b) matrix tension and compression.

For the case when the residual stress was considered through non-zero SLIMT1, SLIMC1, SLIMT2, and SLIMC2 parameters, the UD lamina post-peak non-linear response was continuous and gradually reduced to the residual stress level with a value that was fraction of the peak stress (Figure 82). The residual stress was maintained until the defined maximum failure strain for the lamina was achieved.

(a)   (b)
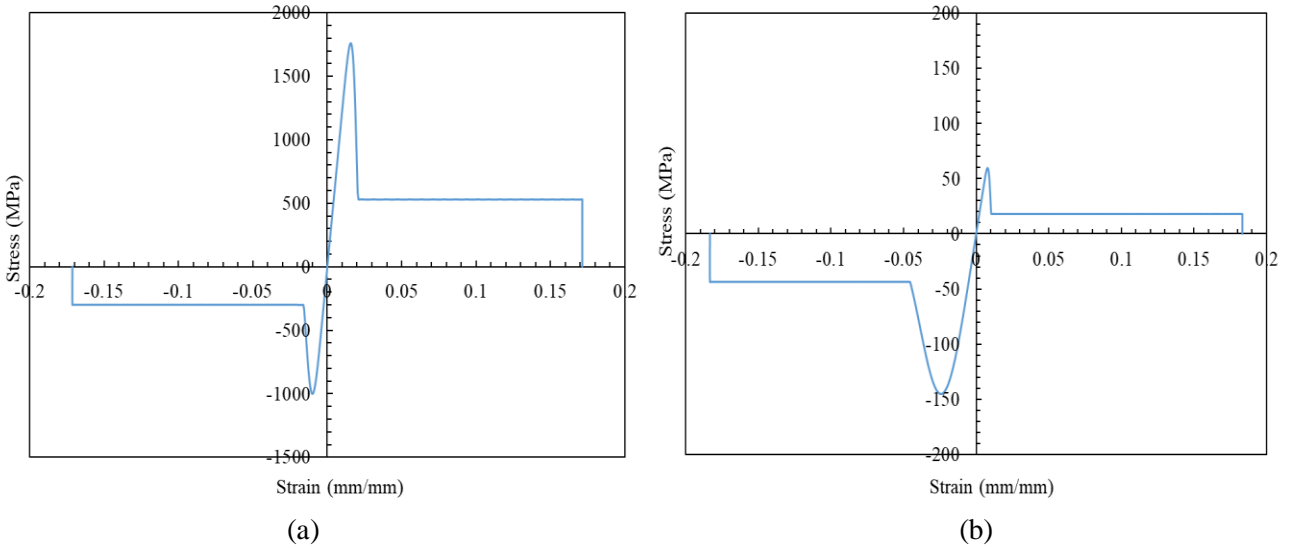
Figure 82. Single element model predicted uniaxial stress-strain behavior (SLIM parameters set to 0.3): (a) fiber tension and compression, and (b) matrix tension and compression.

5.5 Calibration of MAT 58 Material model

The same numerical model and loading condition discussed in Section 5.2 were utilized to calibrate the non-physical parameters of the MAT 58 material model, which are fewer in comparison to MAT 54. First, the effect of mesh shape and size on the axial crush performance of the hat channel was evaluated. Each non-physical parameter was subsequently calibrated through a parametric study.

5.5.1 Effect of Mesh shape

Axial crush of the hat channel specimens was simulated using three different mesh patterns, uniform structured quad mesh, V-patterned structured quad mesh and non-structured triangular mesh (Figure 49). The simulation with a uniform structured quad mesh simulation resulted in progressive crushing of the hat channel with notable oscillations in the force-displacement response (Figure 83). However, simulations with the V-patterned structured quad mesh and non-structured triangular mesh simulations predicted failure of the hat channel by unzipping at the corners, where fronds formed. A similar unzipping failure mode predicted using MAT 58 for FRP channels under axial crush loading was reported in Refs. [96][97][133]. For these simulations, progressive crushing was predicted after the initial peak force without severe oscillations (Figure 83). A higher mean crush force was predicted with the non-structured

triangular mesh when compared with the V-patterned structure quad mesh, and the initial peak force was almost constant for both simulations.
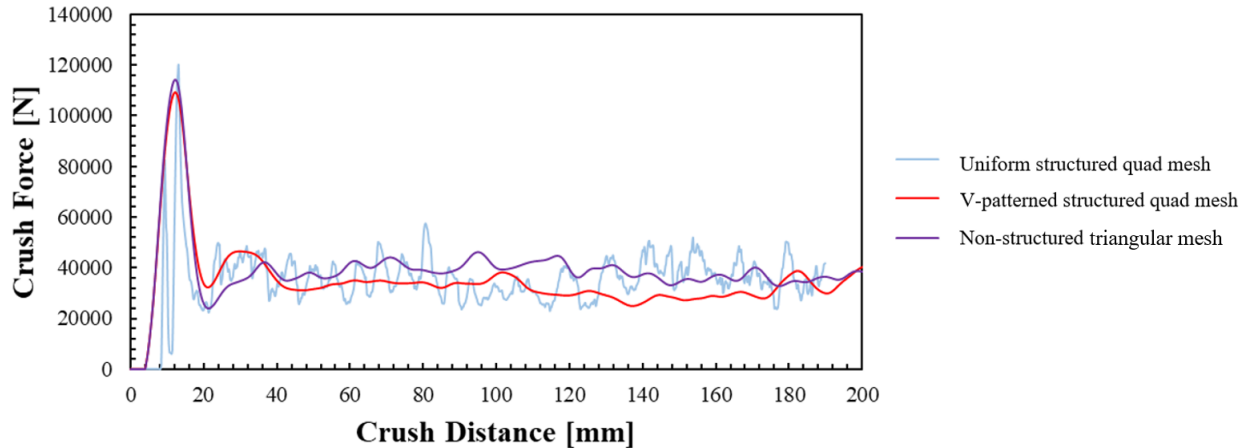
Figure 83. MAT 58 - Force vs displacement response of hat channel specimen with $[0/\pm45/90]_s$ stacking sequence under dynamic loading conditions for different mesh patterns.

5.5.2 Effect of Mesh size

To further investigate the effect of mesh sensitivity on the predictions of the developed simulation model, axial crush of the hat channel specimens with the V-patterned structured quad mesh was performed using five different element sizes. Simulations with element sizes ranging from 2-6 mm produced distinct force-displacement (Figure 84) and energy absorption (Figure 85) responses. Predicted force-displacement responses using element sizes of 2-4 mm resulted in a lower mean crush force (<30 kN) and lower total energy absorption. Simulations using 5 and 6 mm element sizes predicted stable crushing with a constant peak force and higher average crush force. An element size of 5 mm was selected for further simulations based on accuracy and computational efficiency.
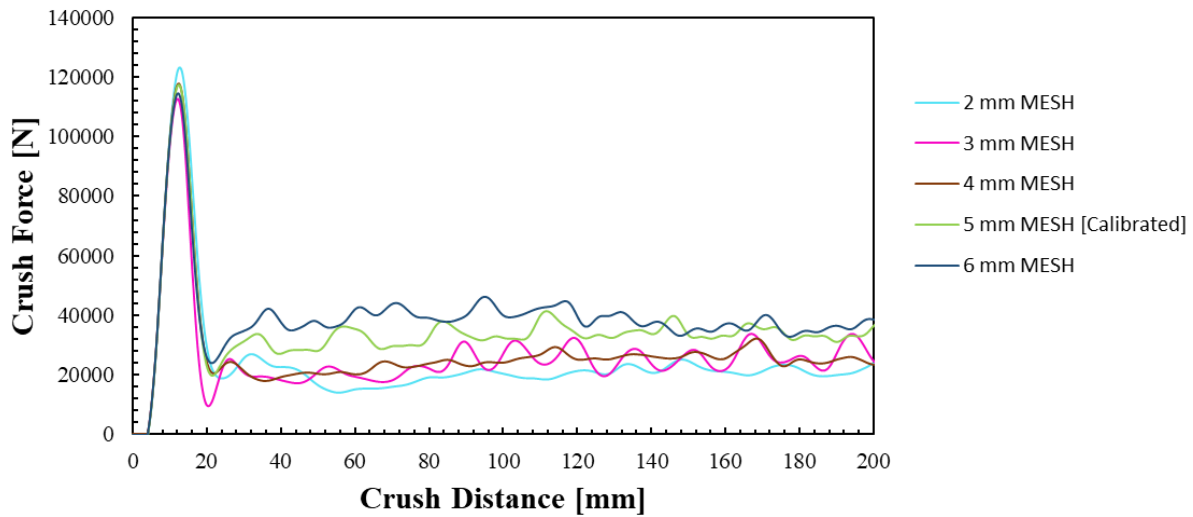
Figure 84. MAT 58 - Force vs displacement response of hat channel specimen with [0/±45/90]$_s$ stacking sequence under dynamic loading conditions for different mesh sizes.
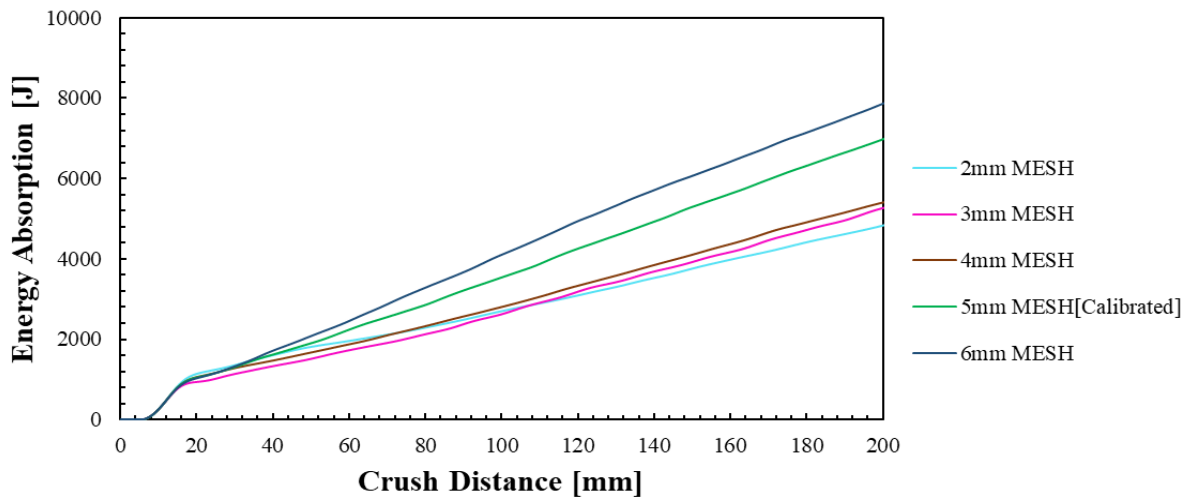
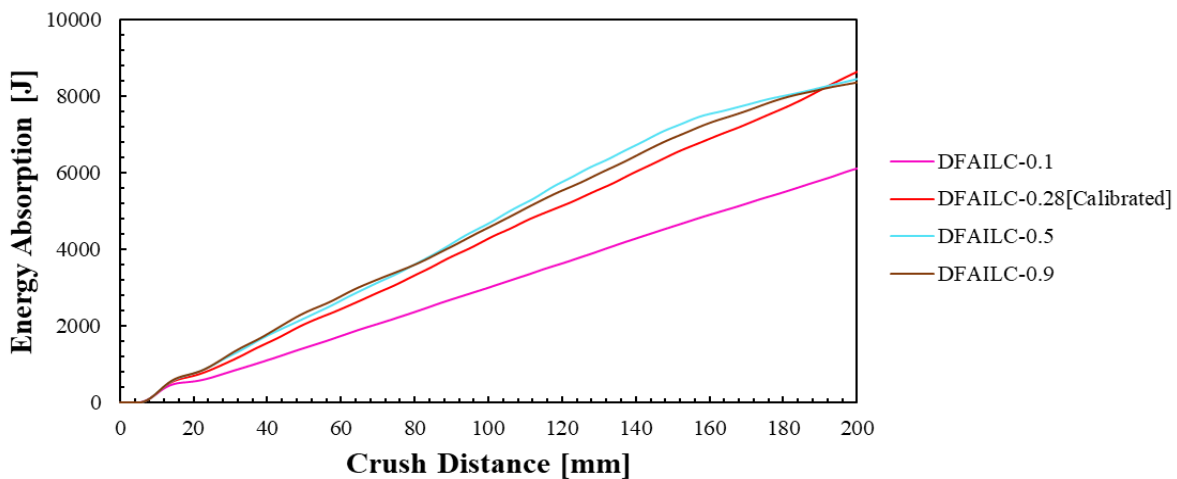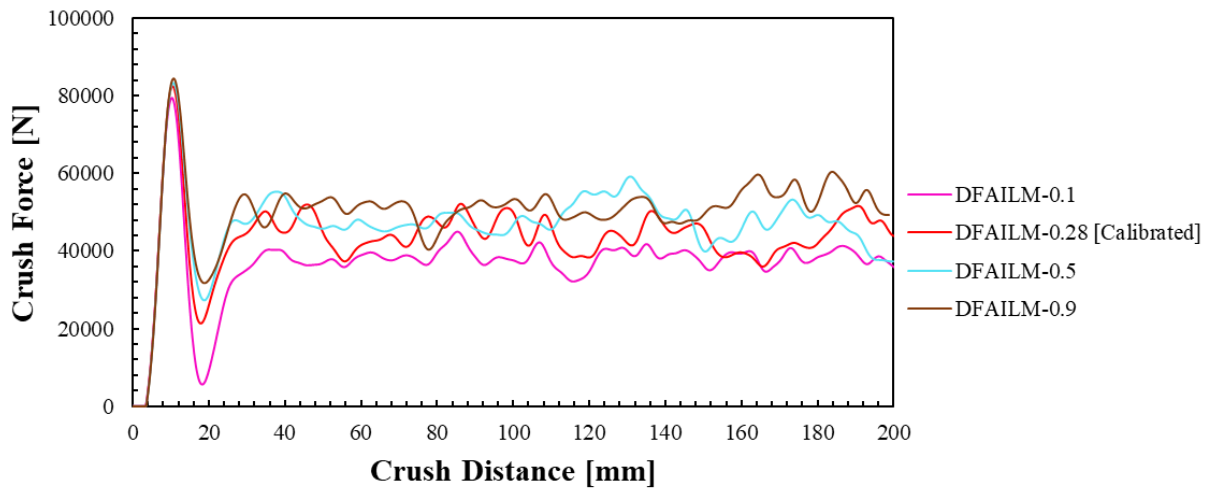**Figure 85.** MAT 58 – Energy absorption response of hat channel specimen with [0/±45/90]$_s$ stacking sequence under dynamic loading conditions for different mesh sizes.

5.5.3 Effect of Non-physical parameters

The various non-physical parameters in the material model, including SLIM, SOFT and ERODS, were calibrated through a parametric study. The effects of each parameter on the axial crush response of the hat channel component are discussed below. A V-patterned structured quad mesh with an elemental size of 5 mm was considered for all simulations.

87

5.5.3.1 SLIMT1

SLIMT1 parameter defines the magnitude of post-peak residual stress for the fiber tensile failure mode of a lamina. A parametric study was performed by considering values ranging from 0 to 1. The initial peak force (Figure 86) and energy absorption data (Figure 87) for the hat channel were consistent for the values of SLIMT1 ranging between 0.3 to 1, with some slight variations for mean crush force. However, the initial peak force and mean crush force predicted for the value of SLIMT1 = 0.1 was lower comparing the range of values considered. The results corresponding to a value of SLIMT1 = 0.3 force response was correlated well with experimental data (Figure 55).
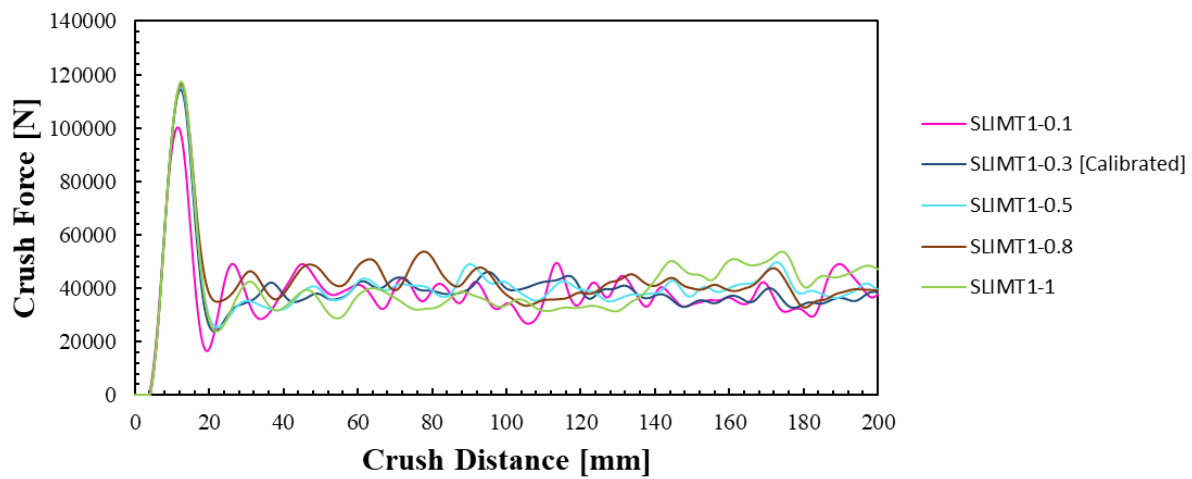
Figure 86. MAT 58 - Force vs displacement response of hat channel specimen with [0/±45/90]$_s$ stacking sequence under dynamic loading conditions for different values of SLIMT1.
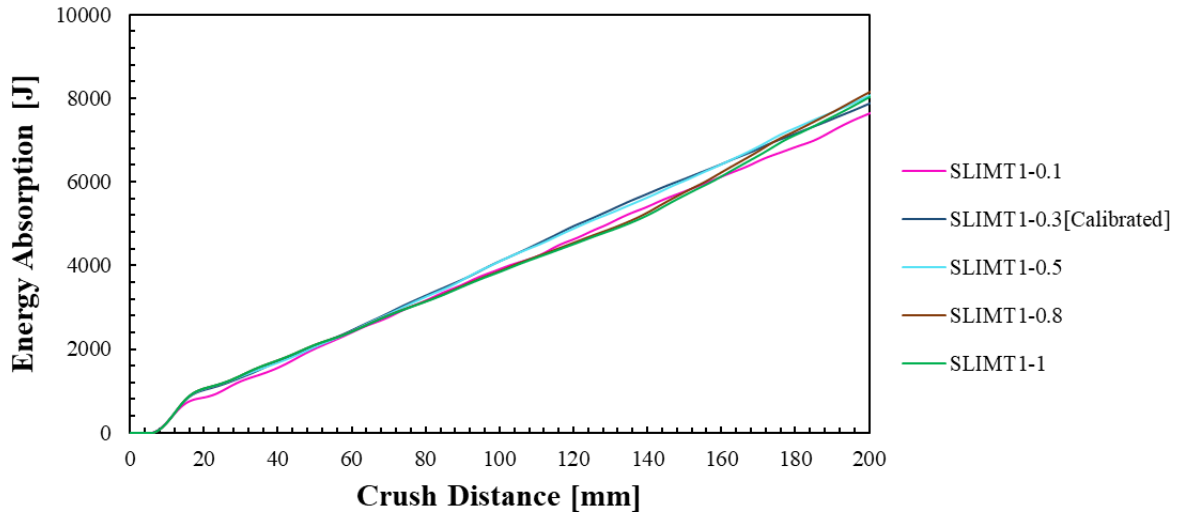
Figure 87. MAT 58 – Energy absorption response of hat channel specimen with $[0/\pm45/90]_s$ stacking sequence under dynamic loading conditions for different values of SLIMT1.
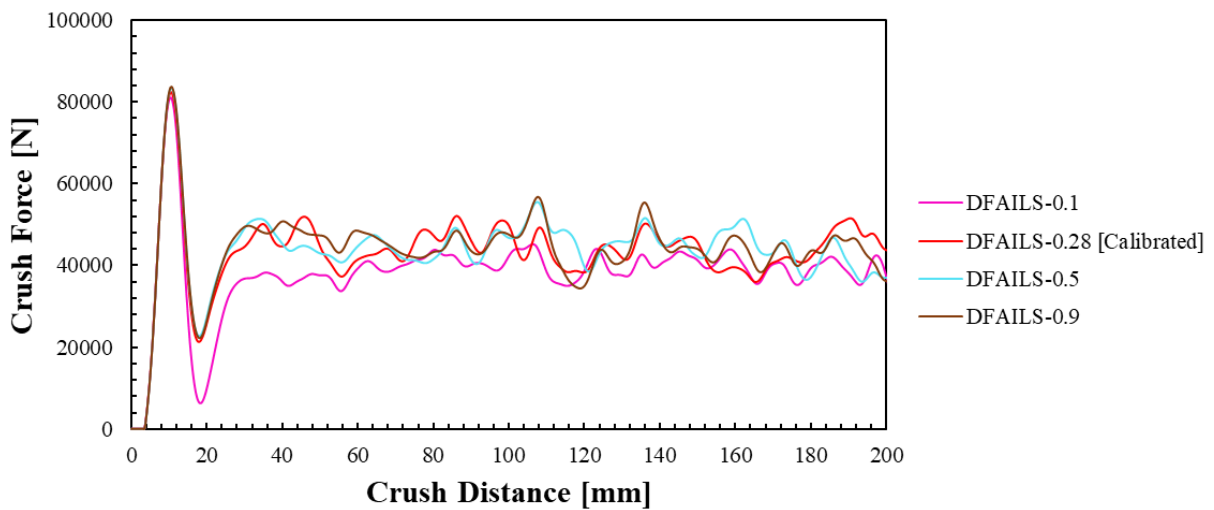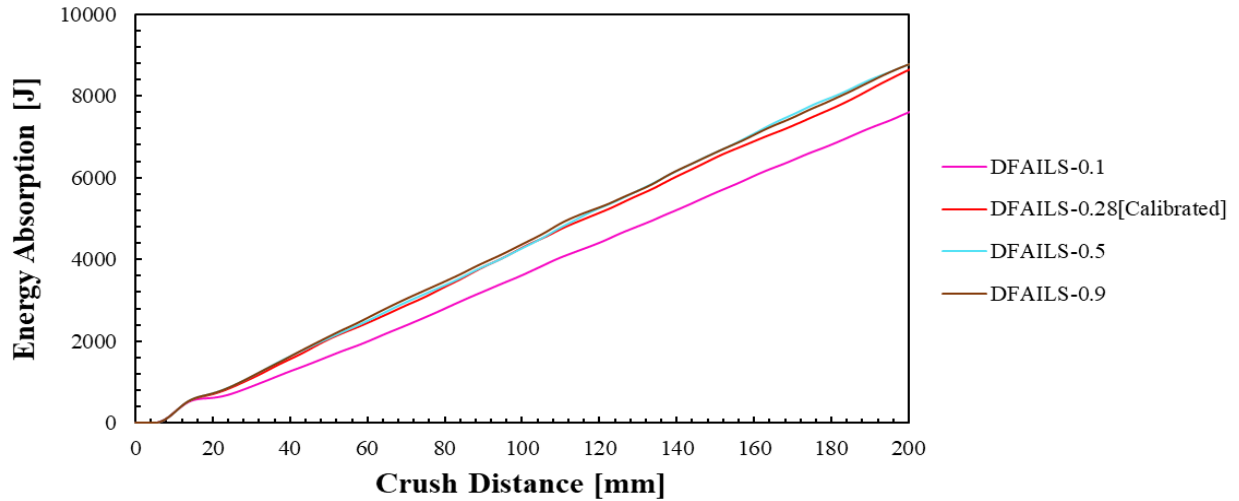
5.5.3.2 SLIMT2

SLIMT2 parameter defines the magnitude of post-peak residual stress for the transverse tensile failure mode of a lamina. Values ranging from 0 to 1 were considered. The force-displacement response (Figure 88) and energy absorption data (Figure 89) were constant for all the values of SLIMT2, with some slight variations for average crush force. The results for a value of SLIMT2 = 0.3 produced force response that was same as the experimental data (Figure 55).
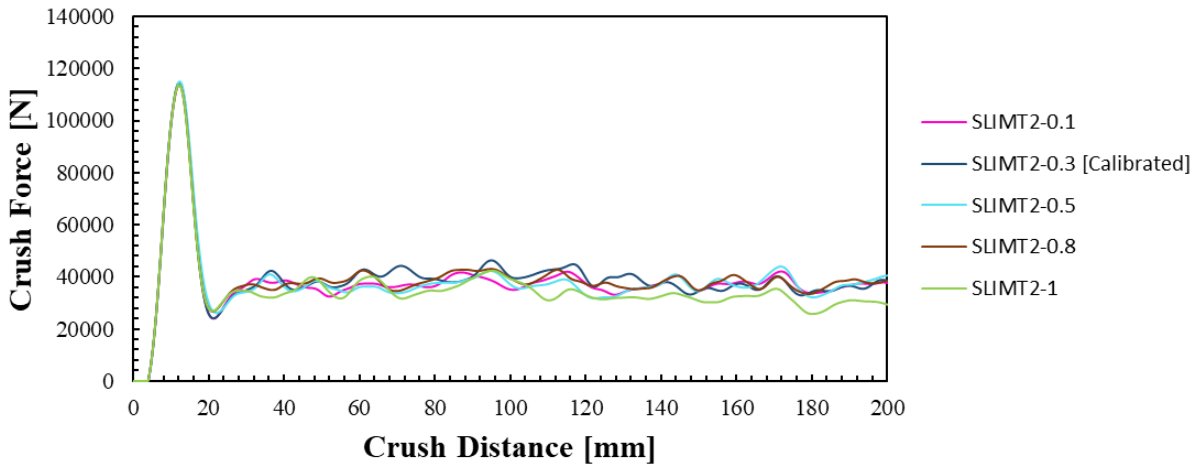
Figure 88. MAT 58 - Force vs displacement response of hat channel specimen with $[0/\pm45/90]_s$ stacking sequence under dynamic loading conditions for different values of SLIMT2.
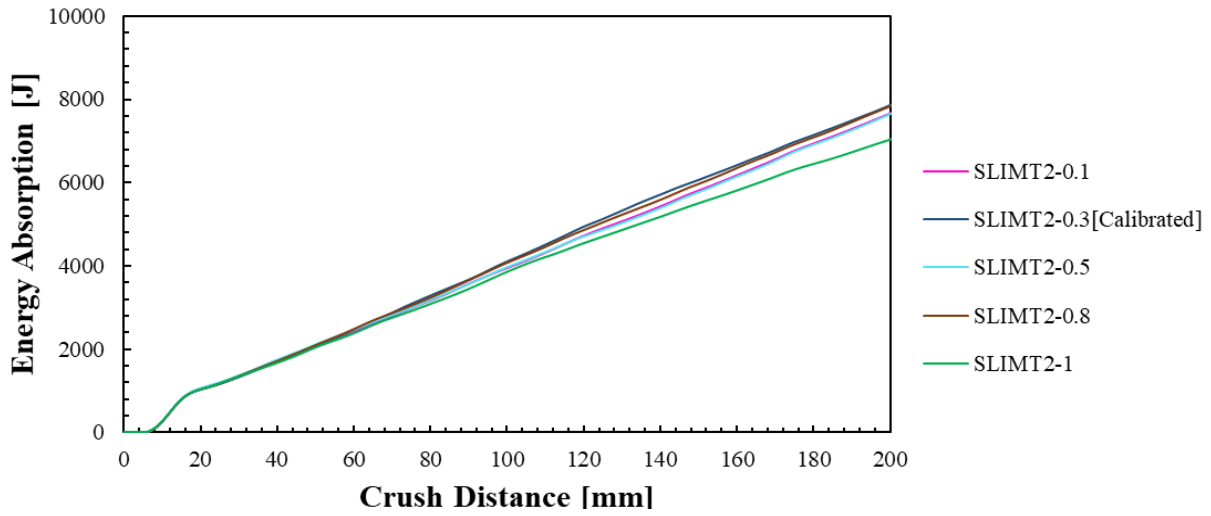
Figure 89. MAT 58 – Energy absorption response of hat channel specimen with [0/±45/90]$_s$ stacking sequence under dynamic loading conditions for different values of SLIMT2.
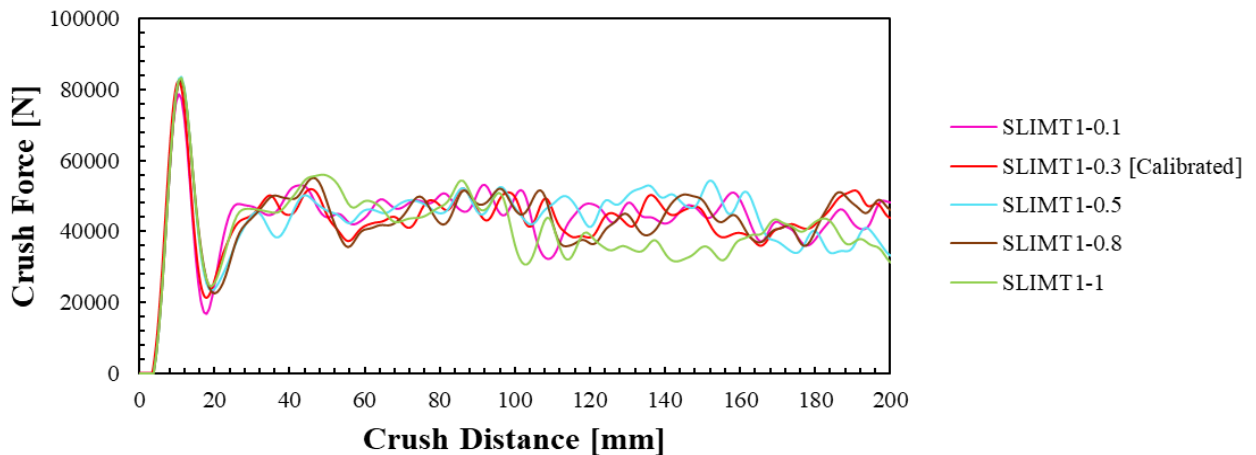
5.5.3.3 SLIMC1
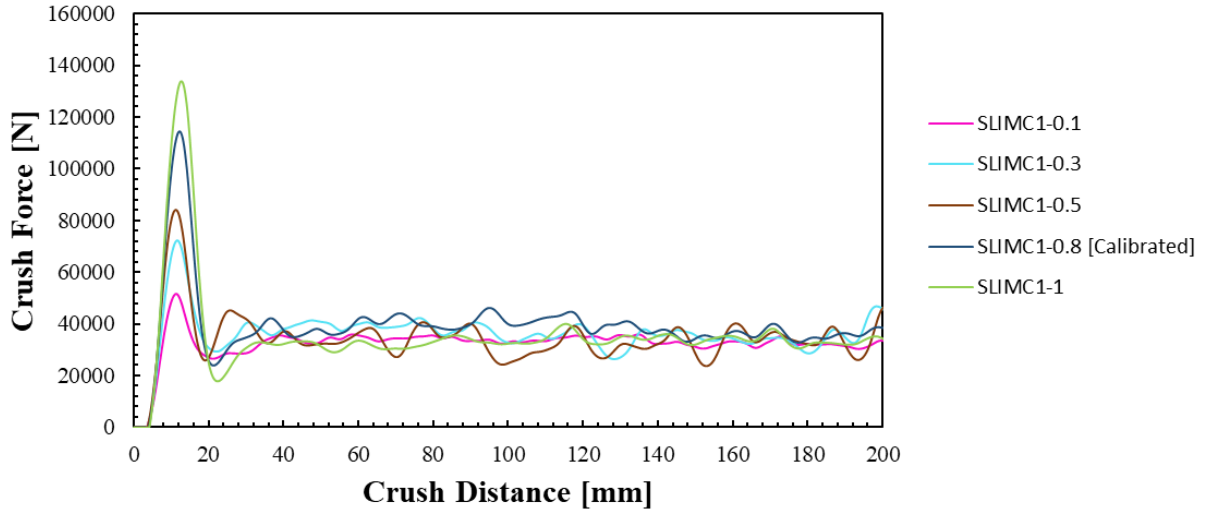
Figure 9091. MAT 58 - Force vs displacement response of hat channel specimen with [0/±45/90]$_s$ stacking sequence under dynamic loading conditions for different values of SLIMC1.
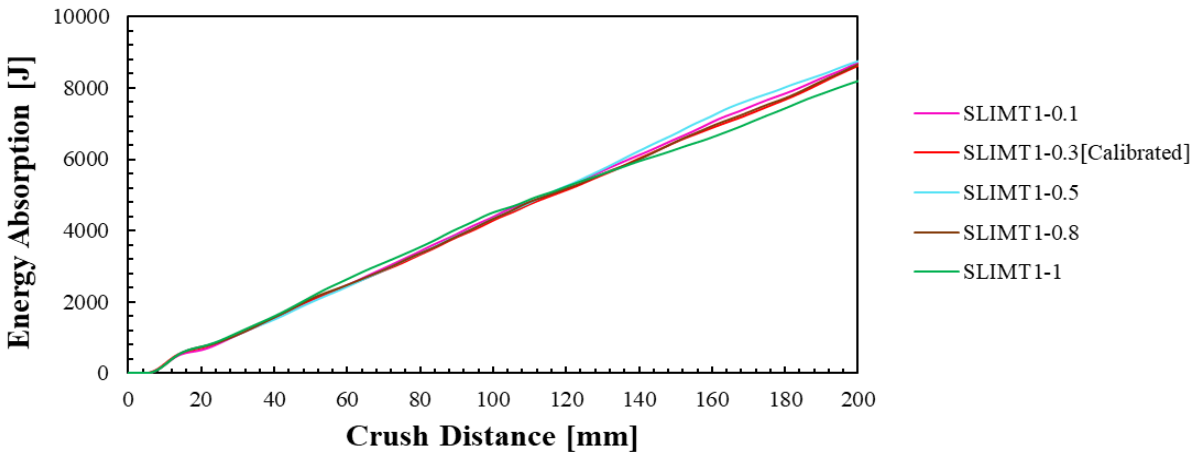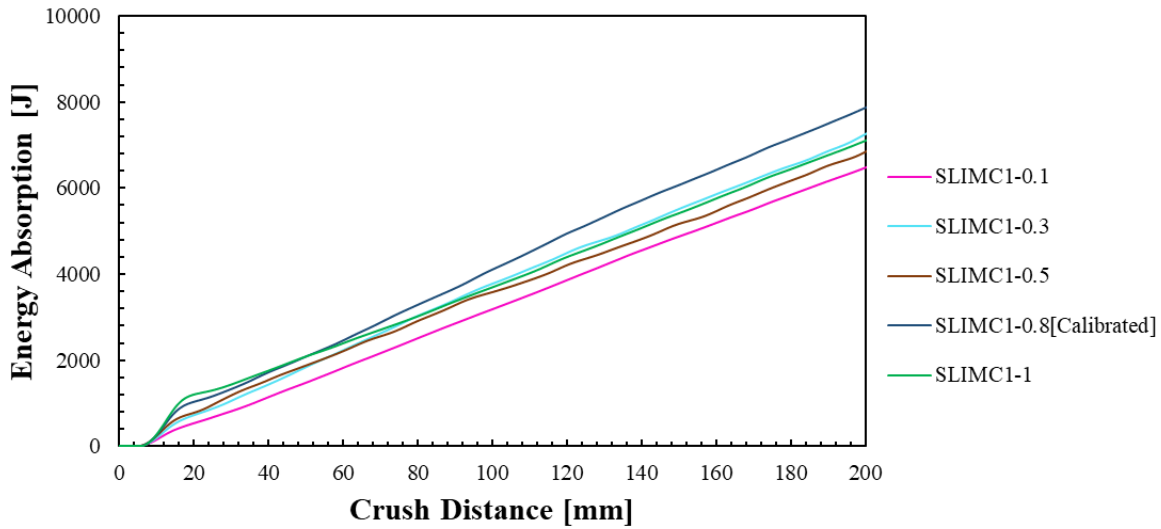
Figure 91. MAT 58 – Energy absorption response of hat channel specimen with [0/±45/90]ₛ stacking sequence under dynamic loading conditions for different values of SLIMC1.

SLIMC1 parameter controls the magnitude of post-peak residual stress for the fiber compressive failure mode of a lamina. A parametric study was performed for the values ranging from 0 to 1. The initial peak force and average crush force (Figure 90) and energy absorption data (Figure 91) were greatly influenced by the values of SLIMC1. The predicted force response and energy absorption data increased with increasing SLIMC1 values. The force-displacement response predicted for a value of SLIMC = 0.8 was similar to the experimental data (Figure 55).

5.5.3.4 SLIMC2

SLIMC2 parameter defines the magnitude of post-peak residual stress for the transverse compressive failure mode of a lamina. Values ranging from 0 to 1 were considered. The initial peak force for the hat channel were consistent for all values of SLIMC2. However, the mean crush force (Figure 92) and energy absorption data (Figure 93) were influenced by increasing values of SLIMC2. The results for the value of SLIMC2 = 0.8 produced the force-displacement response that was same as the experimental data (Figure 55).
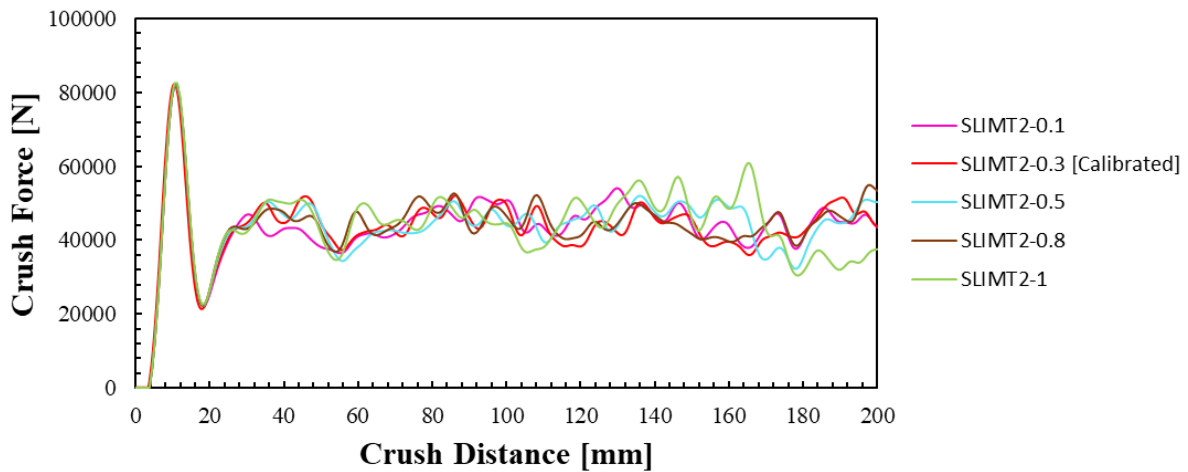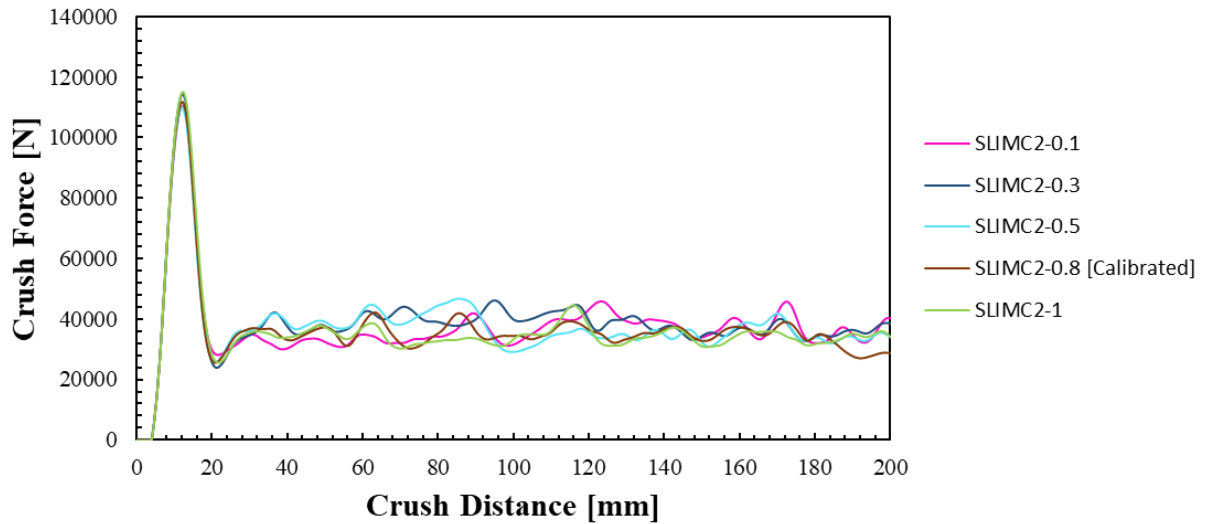
Figure 92. MAT 58 - Force vs displacement response of hat channel specimen with [0/±45/90]ₛ stacking sequence under dynamic loading conditions for different values of SLIMC2.
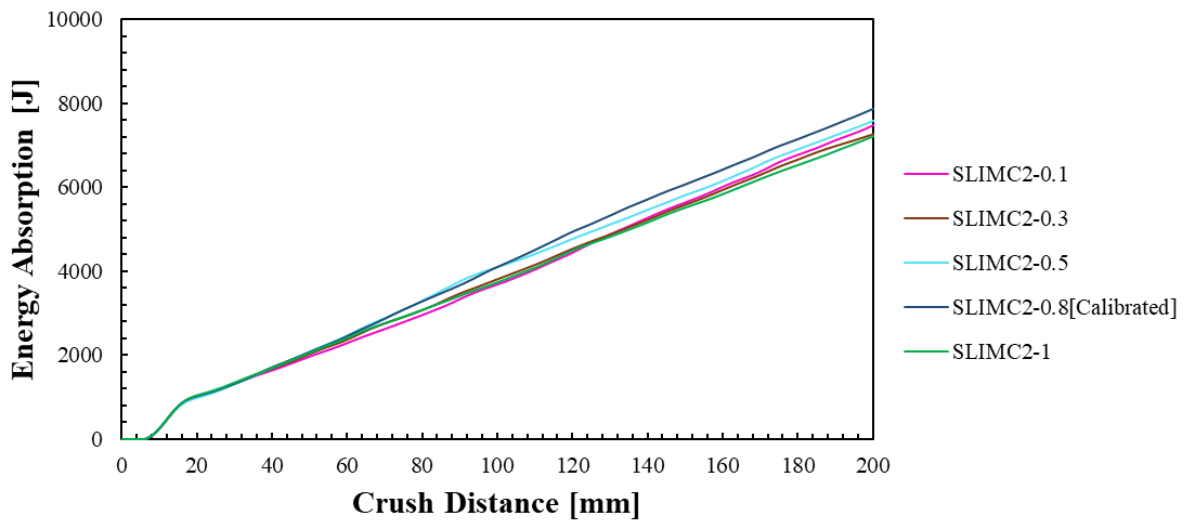
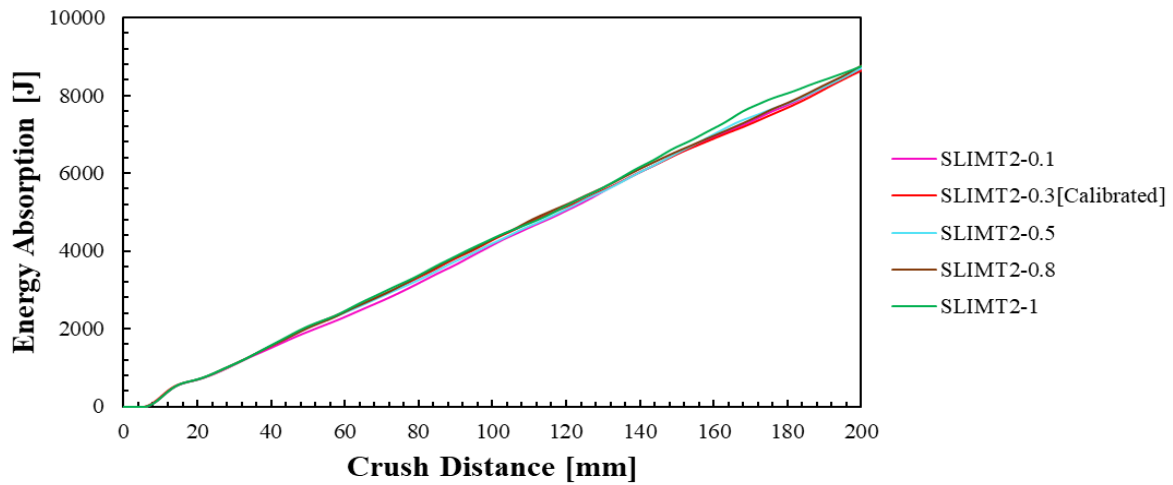**Figure 93.** MAT 58 – Energy absorption response of hat channel specimen with [0/±45/90]ₛ stacking sequence under dynamic loading conditions for different values of SLIMC2.

5.5.3.5 SLIMS

SLIMS parameter defines the magnitude of post-peak residual stress for the shear failure mode of a lamina. A parametric variation was performed by considering values ranging from 0 to 1. The mean crush force (Figure 94) and energy absorption data (Figure 95) were greatly influenced by increasing values of

SLIMS. However, the numerical predictions of peak force were consistent for all the values of SLIMS considered. The results corresponding to a value of SLIMS = 0.8 force response was same as the experimental data (Figure 55).
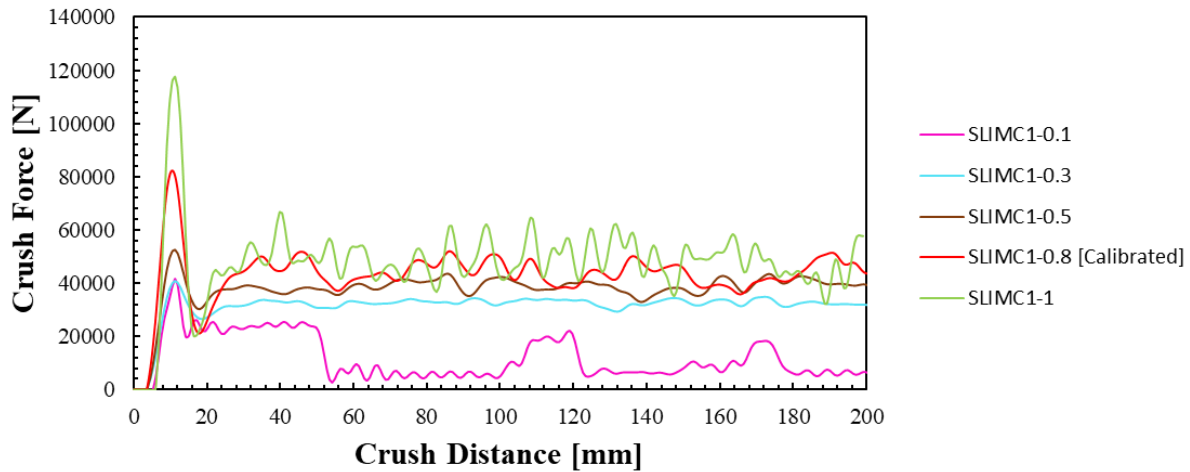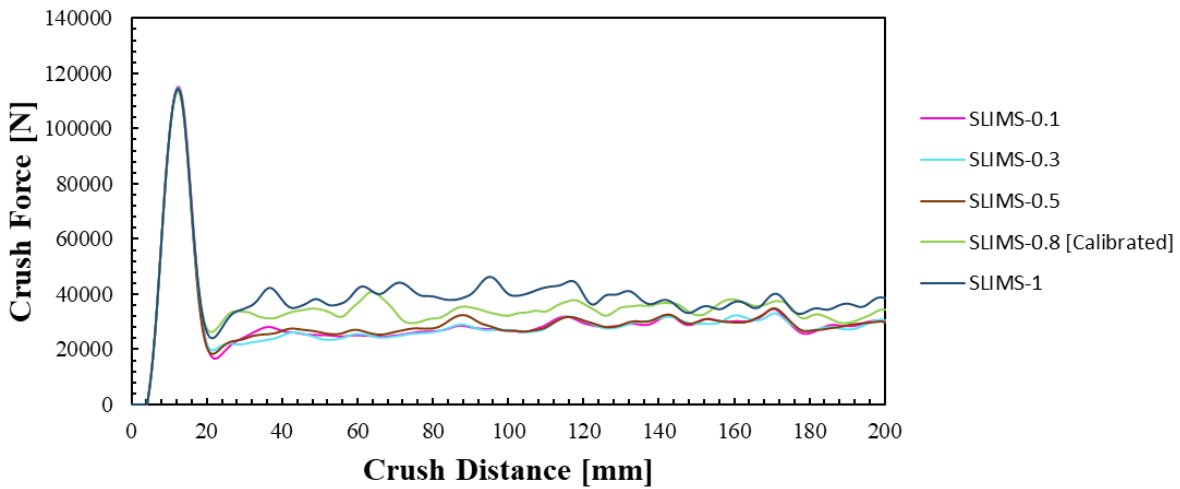

Figure 94. MAT 58 - Force vs displacement response of hat channel specimen with [0/±45/90]$_s$ stacking sequence under dynamic loading conditions for different values of SLIMS.
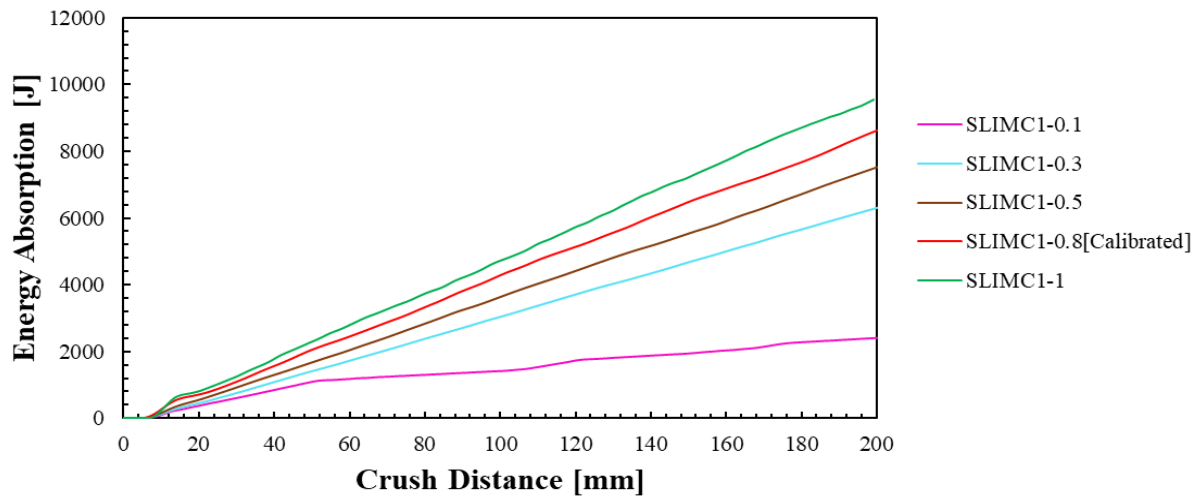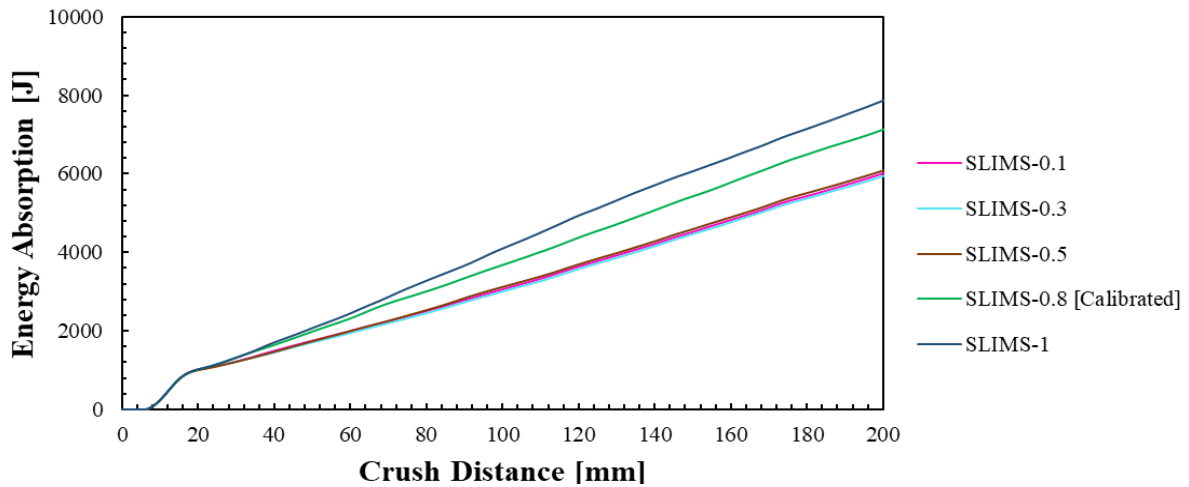

Figure 95. MAT 58 - Energy absorption response of hat channel specimen with [0/±45/90]$_s$ stacking sequence under dynamic loading conditions for different values of SLIMS.

5.5.3.6 SOFT

SOFT parameter is for the crash front algorithm and scales the lamina strength for the elements in the immediate crash front. Values ranging from 0 to 1 were considered. The force-displacement response (Figure 96) and energy absorption data (Figure 97) were constant for all the values of SOFT considered. The SOFT parameter was not crucial for the simulations performed using the MAT 58 model.
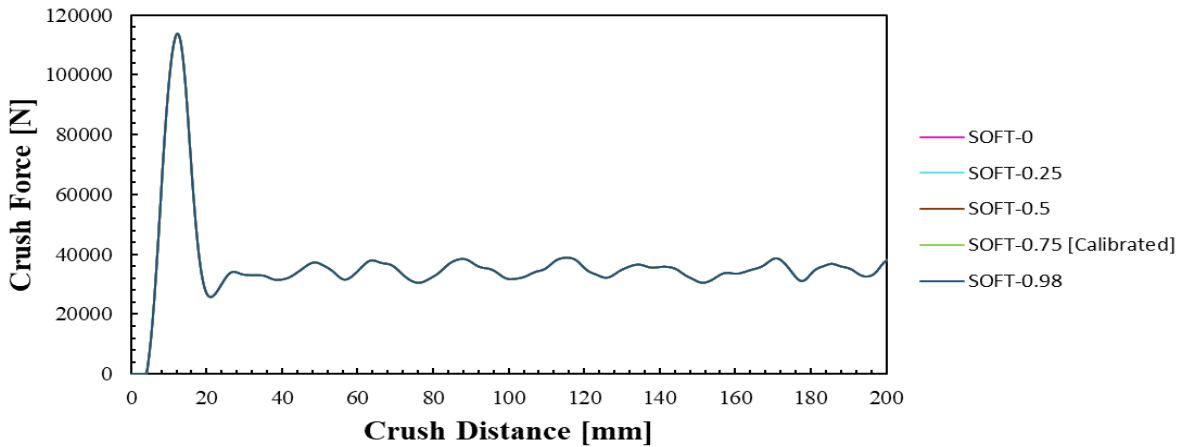
Figure 96. MAT 58 - Force vs displacement response of hat channel specimen with $[0/\pm45/90]_s$ stacking sequence under dynamic loading conditions for different values of SOFT.
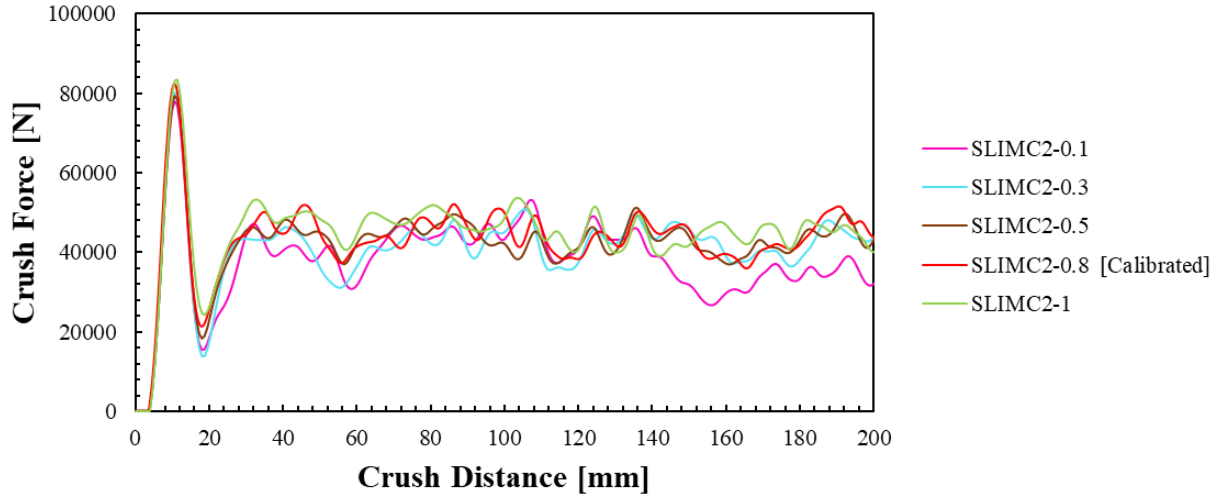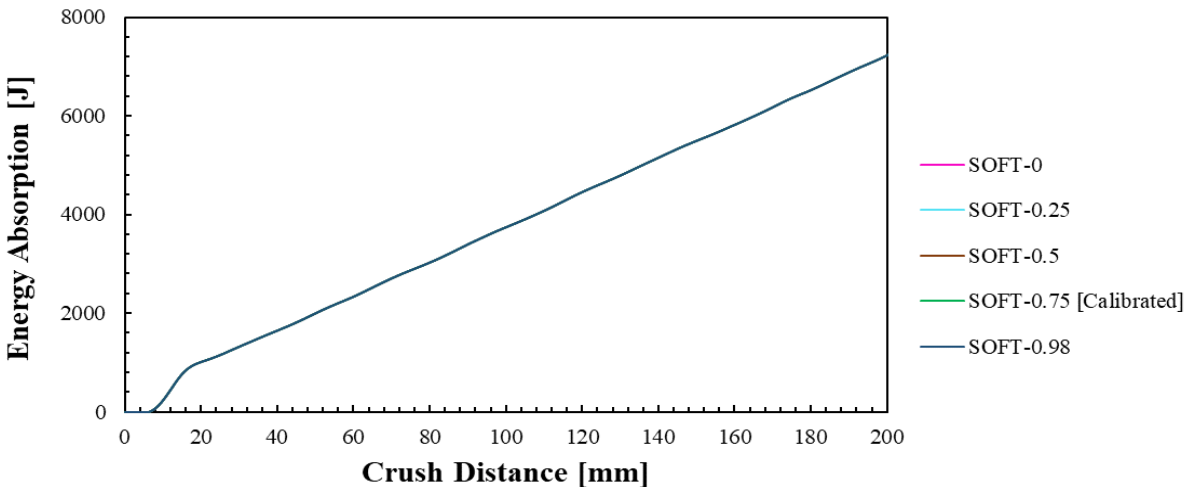

Figure 97. MAT 58 – Energy absorption response of hat channel specimen with $[0/\pm45/90]_s$ stacking sequence under dynamic loading conditions for different values of SOFT.

94

5.5.3.7 ERODS

ERODS is defined as the maximum effective failure strain (EFS) for a lamina. A parametric study was performed by considering values ranging from 0 to 1. The force-displacement response (Figure 98) and energy absorption data (Figure 99) were greatly influenced by the values of ERODS. The predicted initial peak force and mean crush force decreased with increasing ERODS values. The results for a value of ERODS = 0.6 produced a force-displacement response that was similar to the experimental data (Figure 55).
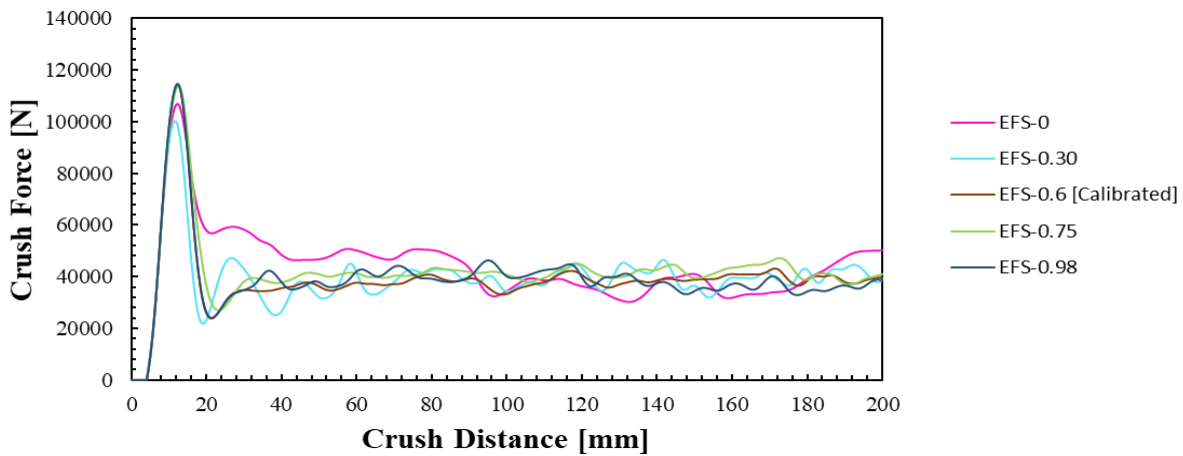
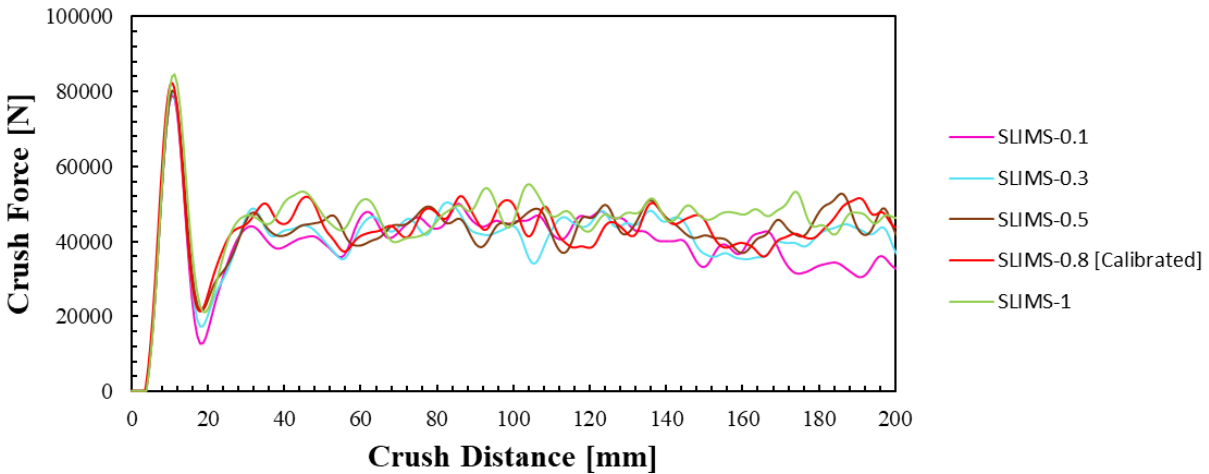**Figure 98.** MAT 58 - Force vs displacement response of hat channel specimen with $[0/\pm45/90]_s$ stacking sequence under dynamic loading conditions for different values of ERODS.
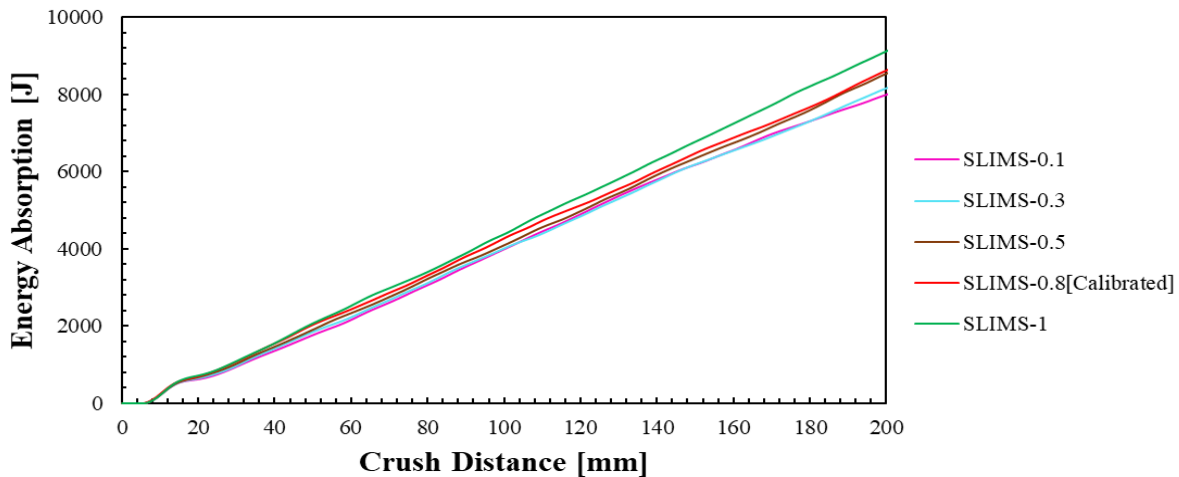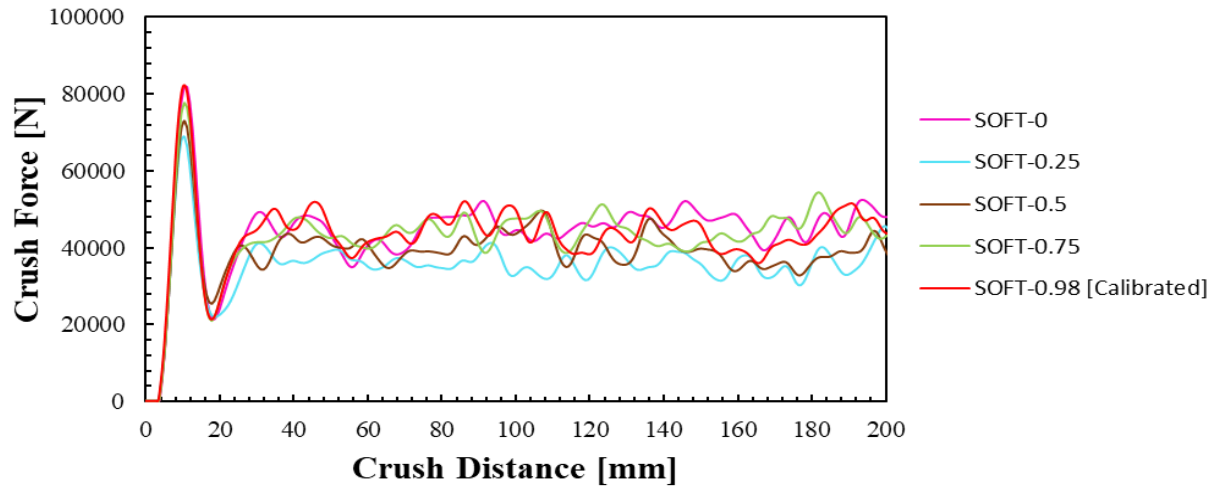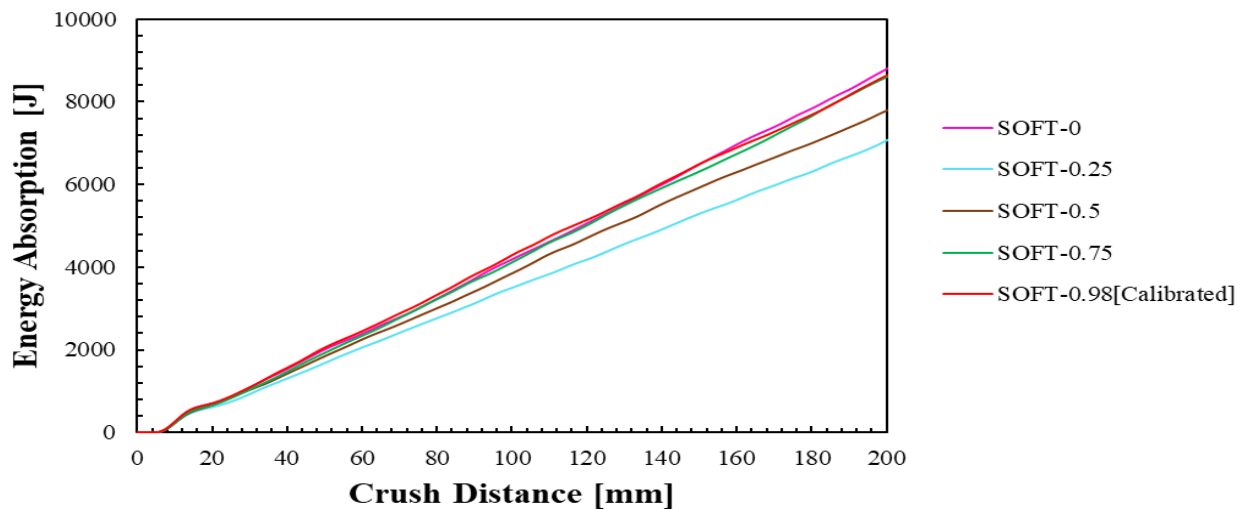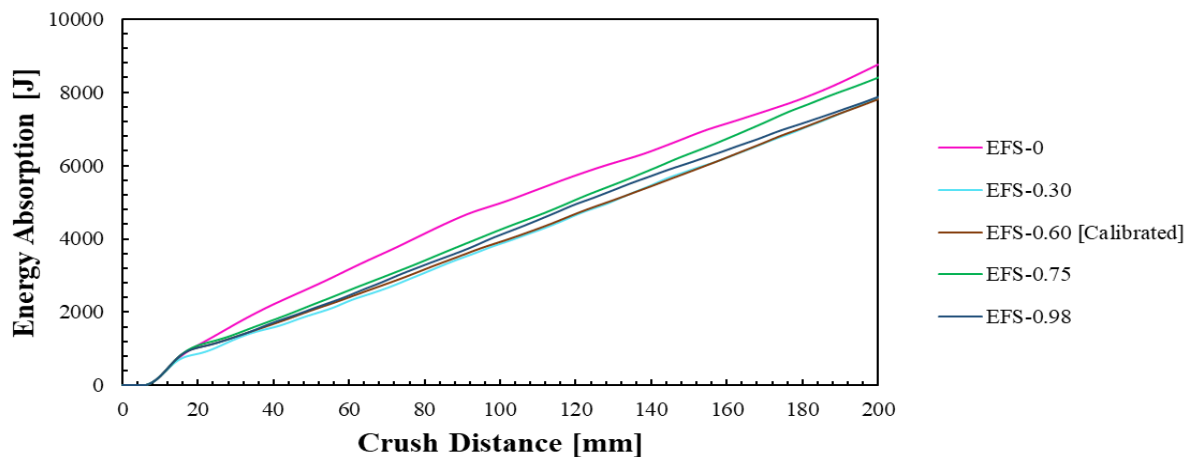
Figure 99. MAT 58 – Energy absorption response of hat channel specimen with $[0/\pm45/90]_s$ stacking sequence under dynamic loading conditions for different values of ERODS.

5.5.3.8 Calibration Summary

The sensitivity analysis presented in the previous sections led to the calibration of each non-physical parameter, which is summarized (Table 4).

Table 4. Calibrated non-physical parameters for MAT 58 material model.

Parameter	Calibrated Value	Parametric Variations Considered
SLIMT1	0.3	0.1, 0.3, 0.5, 0.8, 1.0
SLIMT2	0.3	0.1, 0.3, 0.5, 0.8, 1.0
SLIMC1	0.8	0.1, 0.3, 0.5, 0.8, 1.0
SLIMC2	0.8	0.1, 0.3, 0.5, 0.8, 1.0
SLIMS	0.8	0.1, 0.3, 0.5, 0.8, 1.0
SOFT	0.98	0.0, 0.25, 0.5, 0.75, 0.98
EFS	0.6	0.0, 0.3, 0.6, 0.75, 0.98

5.6 Crash Performance Evaluation for Hat Channel Component

The axial crush performance of the hat channel components under two different loading conditions and two stacking sequences was numerically predicted using the calibrated material model parameters (Tables 3 and 4), and compared with available experimental data in the following sub-sections. Note that all results presented correspond to simulation models with an element size of 5 mm and a V-patterned structured quad mesh.

5.6.1 Dynamic Simulation with Layup 1: $[0/\pm45/90]_s$

It was observed that the hat channel specimen in the MAT 54 model progressively folded and failed locally through a brittle fragmentation mode (Figure 100), which was observed experimentally [77]. The initial buckling tendency of hat channel flanges was also captured, and the stable progressive crush response was simulated. However, the hat channel specimen for the MAT 58 model initially failed through fragmentation, and after 30 mm of crushing an unzipping mode of failure at all the corners of the hat channel was predicted (Figure 100).
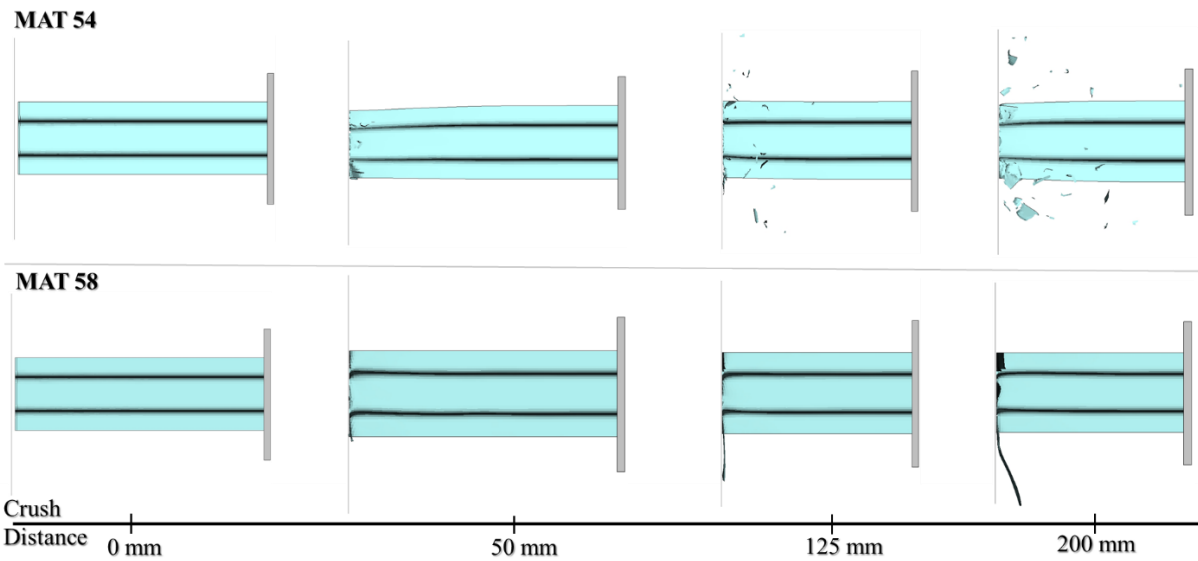
Figure 100. Axial crush response of hat channel specimens under dynamic loading condition with layup 1 $[0/\pm45/90]_s$ for both MAT 54 and MAT 58 material models. Images correspond to the indicated crush distance during the simulation.

The predicted load-displacement response (Figure 101) and cumulative energy absorption (Figure 102) were compared to the average experimental results. The initial peak force was over predicted by the MAT 58 model (114.4 kN or 37% higher than the experimental value), whereas the peak force predicted by the MAT 54 model was similar compared to the experimental data (82.3 kN). After the initial peak, the sudden drop in crush force was well captured by both the models, as was the mean crushing force. Also, the predicted energy absorption by both the MAT 54 and MAT 58 models, respectively 8.6 kJ and 7.9 kJ, correlated well with the experimental value of 8.3 kJ (Figure 102). The overall crush force-displacement response was predicted reasonably well for both models, which was expected since the MAT 54 and MAT 58 material model non-physical parameters were calibrated for these simulation models.
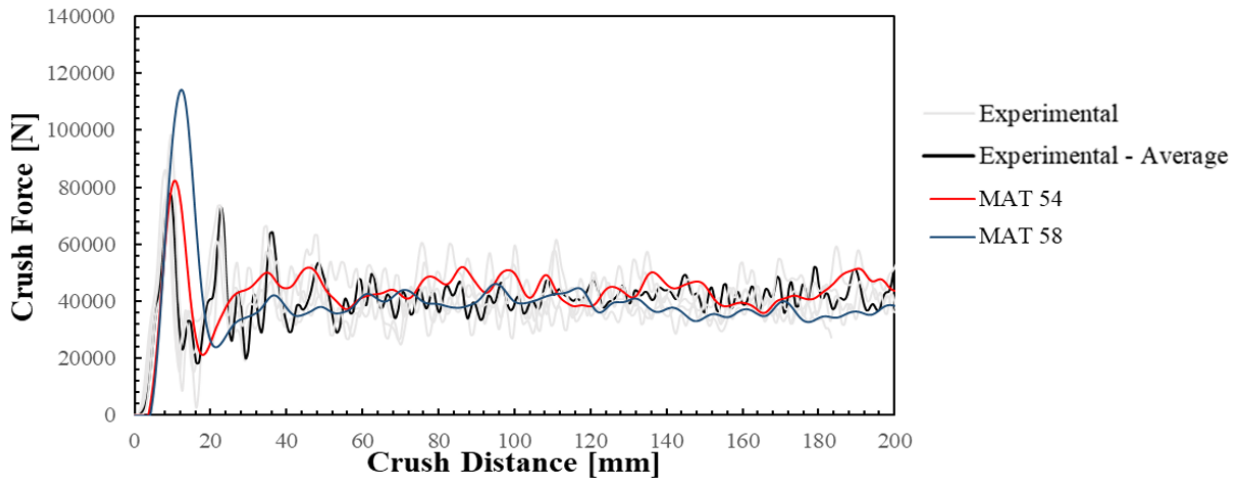
Figure 101. Force vs displacement response of hat channel specimens under dynamic loading condition with layup 1 [0/±45/90]ₛ for both MAT 54 and MAT 58 material models.
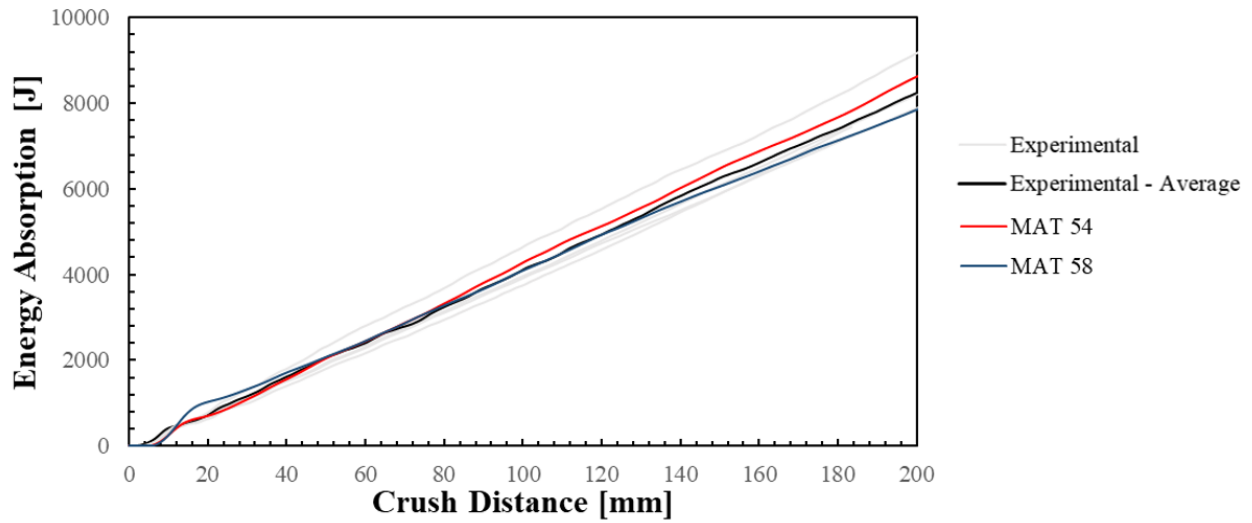
Figure 102. Energy absorption response of hat channel specimens under dynamic loading condition with layup 1 [0/±45/90]ₛ for both MAT 54 and MAT 58 material models.

5.6.2 Quasi-static Simulation with Layup 1: [0/±45/90]ₛ

Fragmentation was the major failure mode observed for the quasi-static hat channel specimens [77]. For the MAT 54 model the hat channel specimen flanges initially buckled and fracture folds developed during progressive crushing (Figure 103). The presence of constrained 90° layers at the center of the laminate may have led to transverse compressive failure in these layers and subsequent failure of the

adjacent layers. For the MAT 58 model the hat channel specimen formed fronds due to tearing of the channel at the corners w (Figure 103). Overall, stable progressive crushing was captured by both models.

MAT 54
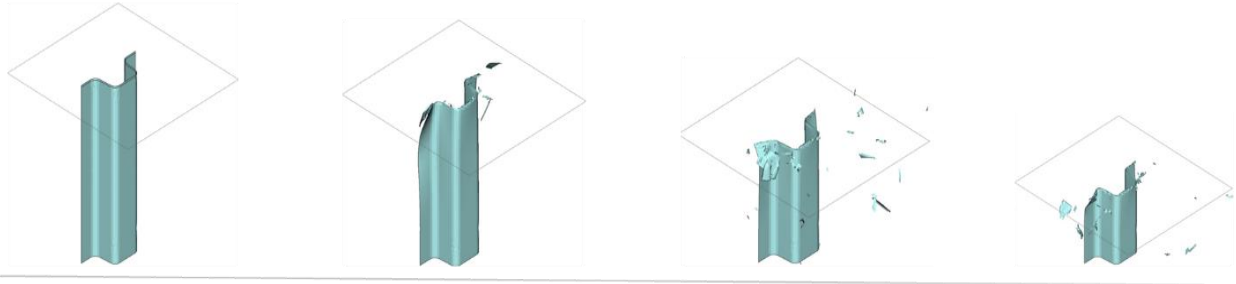
MAT 58
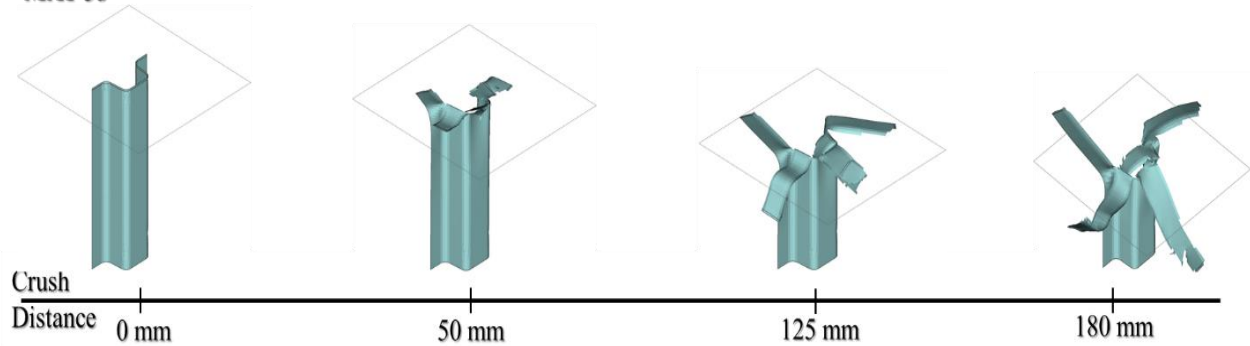
Figure 103. Axial crush response of hat channel specimens under quasi-static loading condition with layup 1 [0/±45/90]$_s$ for both MAT 54 and MAT 58 material models. Images correspond to the indicated crush distance during the simulation.

The force-displacement response (Figure 104) and cumulative energy absorption (Figure 105) revealed that the initial peak force was over predicted by approximately 65% by both models. Overprediction of the peak force may be due to time scaling of the numerical model for quasi-static applications. After this first force peak, a good correlation between the model and experiments was observed. The average crush force (48 kN) and total energy absorption (8.75 kJ) predicted by the MAT 54 model were close to the experimental data of 50.7 kN and 9.2 kJ. Though, MAT 58 underpredicted the mean force (39 kN) and energy absorption (7 kJ). The underprediction of energy absorption may also be due to time scaling, as well as the inability to predict the mode of failure observed in the experiments.

99
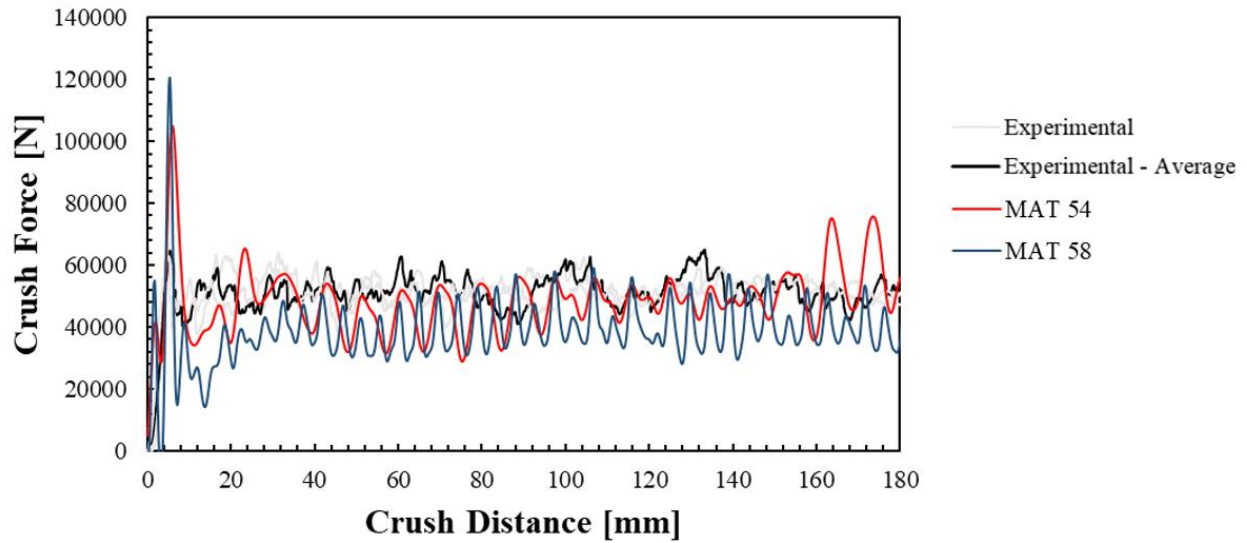
Figure 104. Force vs displacement response of hat channel specimens under quasi-static loading condition with layup 1 [0/±45/90]ₛ for both MAT 54 and MAT 58 material models.
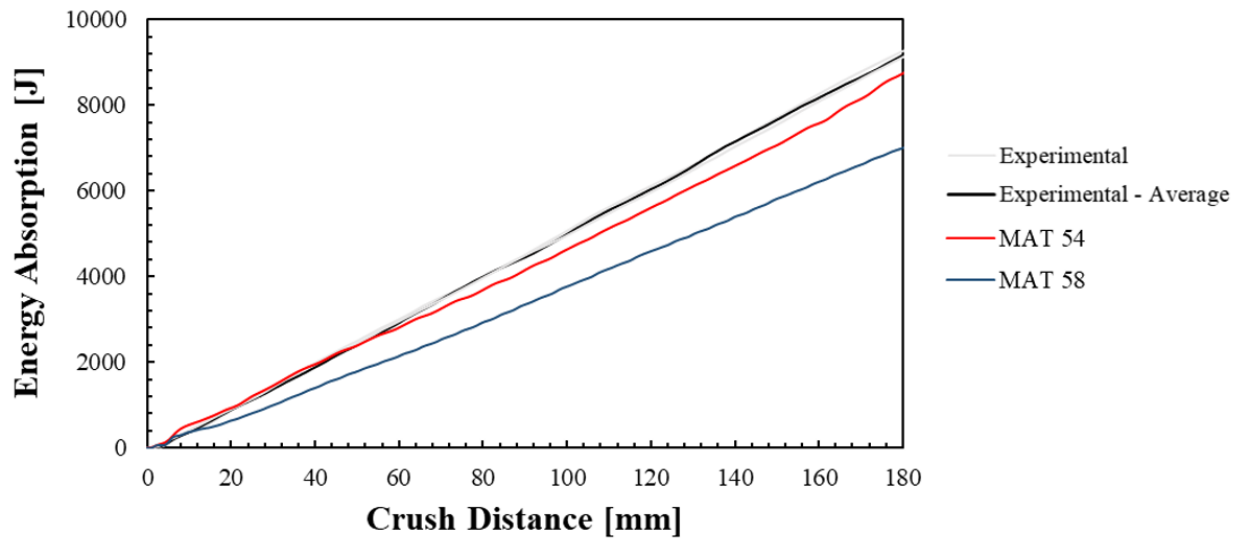
Figure 105. Energy absorption response of hat channel specimens under quasi-static loading condition with layup 1 [0/±45/90]ₛ for both MAT 54 and MAT 58 material models.

5.6.3 Dynamic Simulation with Layup 2 : [±45/0₂]ₛ

The predictions for the hat channel component using MAT 54 resulted in stable progressive failure through brittle fragmentation (Figure 106), which was observed experimentally [77]. During stable crushing fronds formed as petals due to the dominant number of $0°$ plies at the laminate center (Figure 106.a). However, for the MAT 58 model predictions the hat channel component deformed initially by fragmentation and unzipping failure occurred at all the radius corners of the hat channel (Figure 106.b).
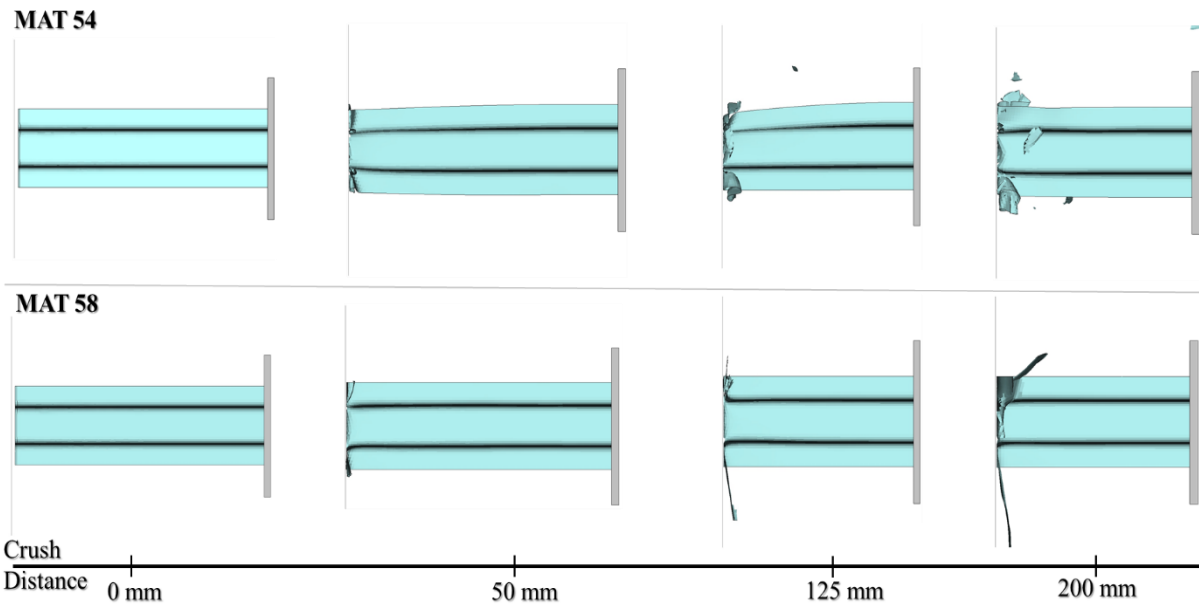
Figure 106. Axial crush response of hat channel specimens under dynamic loading condition with layup 2 [±45/0₂]ₛ for both MAT 54 and MAT 58 material models. Images correspond to the indicated crush distance during the simulation.

The predicted load-displacement (Figure 107) and cumulative energy absorption (Figure 108) response correlated well with the average experimental results for the MAT 54 model. The predicted initial peak force was similar to the experimental value (104 kN), while the average crush force (60 kN) and total energy absorption (12 kJ) weres close to the test data of 68.8 kN and 13 kJ, respectively. For the MAT 58 model, the initial peak force was overpredicted (143 kN or 33.5% higher than experimental value) and the average crush force (44 kN) and energy absorption (8.8 kJ) were underpredicted.

101
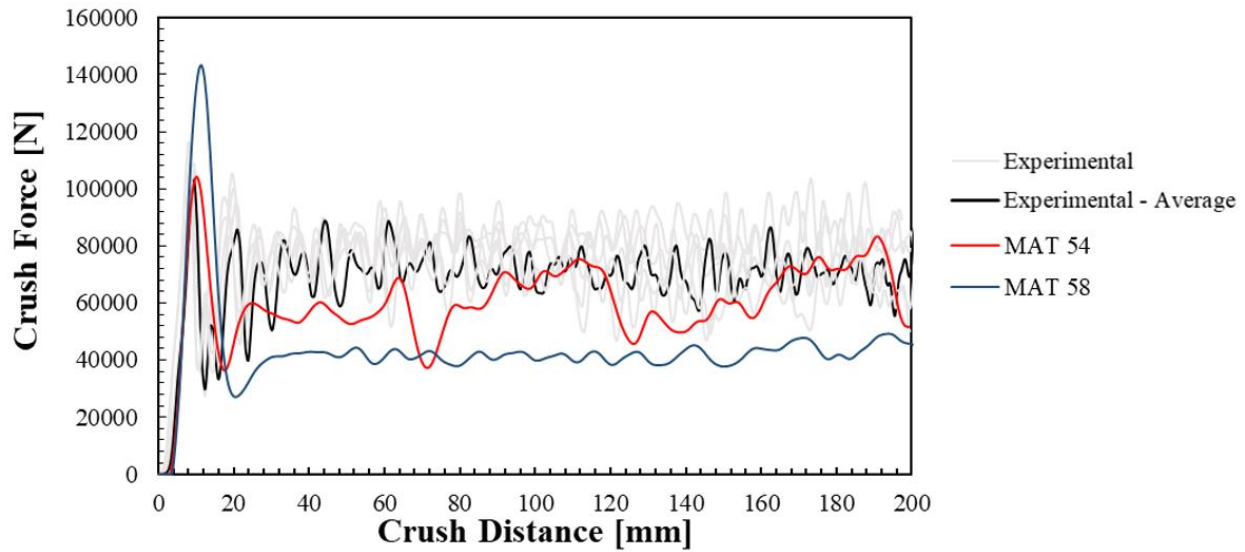
Figure 107. Force vs displacement response of hat channel specimens under dynamic loading condition with layup 2 [±45/0$_2$]$_s$ for both MAT 54 and MAT 58 material models.
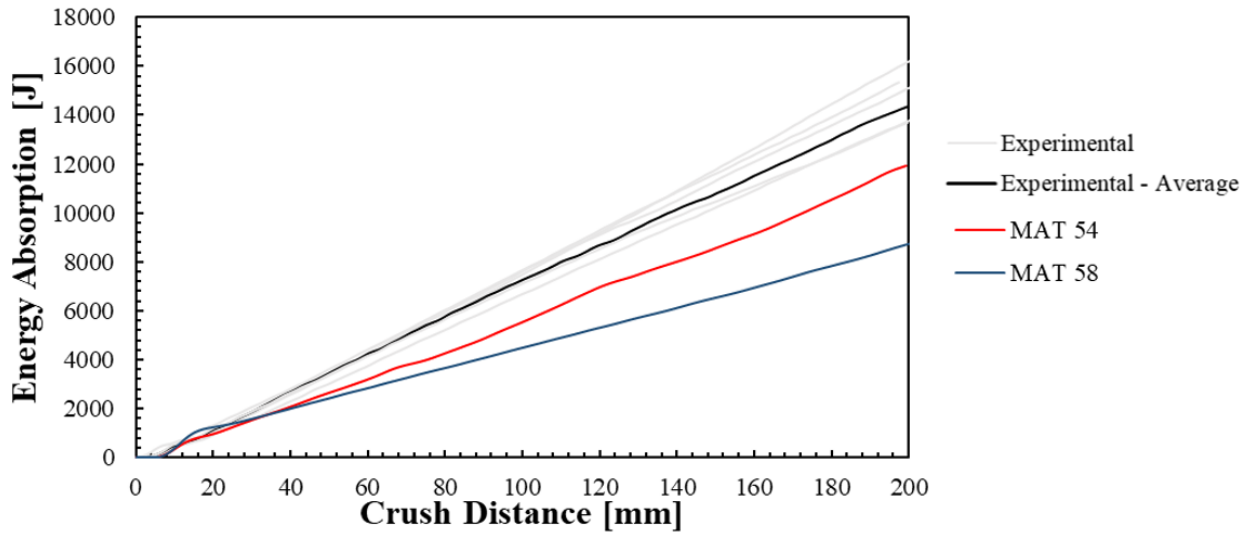
Figure 108. Energy absorption response of hat channel specimens under dynamic loading condition with layup 2 [±45/0$_2$]$_s$ for both MAT 54 and MAT 58 material models.

5.6.4 Quasi-static Simulation with Layup 2: [±45/0$_2$]$_s$

Splaying was the major failure mode observed for the quasi-static hat channel specimens with a [±45/0$_2$]$_s$ stacking sequence [77], and was attributed to the presence of several 0° plies at the center of the laminate.

102

However, the single shell element modelling approach used in this study could not capture the splaying mode of failure. For the MAT 54 model the hat channel specimen flanges rotated and petals formed during progressive crushing (Figure 109.a). The MAT 58 model predicted unzipping failure (Figure 109b) in all the corners of the channel due to inward/outward movement of the flanges. Overall, stable crushing was predicted by both models.
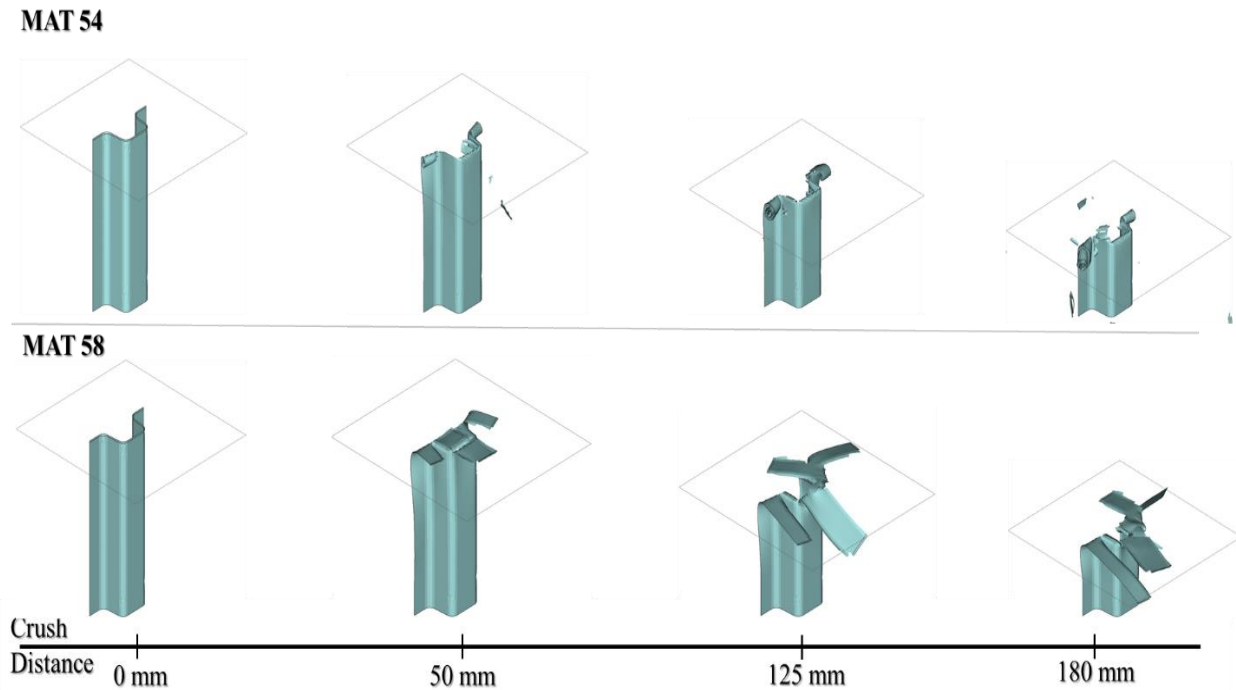
Figure 109. Axial crush response of hat channel specimens under quasi-static loading condition with layup 2 $[\pm45/0_2]_s$ for both MAT 54 and MAT 58 material models. Images correspond to the indicated crush distance during the simulation.

The predicted load-displacement response (Figure 110) and cumulative energy absorption (Figure 111) revealed that the initial peak force was over predicted by both models, while the subsequent drop in crush force was also not well captured. For both models, the predicted average crush force up to 80 mm of crush distance deviate from the experimental data. The average crush force (44 kN) and total energy absorption (8.4 kJ) predicted by the MAT 54 model were close to the experimental data of 53 kN and 10 kJ. However, the MAT 58 model underpredicted the mean crush force (46 kN) and total energy absorption (7.7 kJ). The overprediction of initial peak load and underprediction of energy absorption may be due to the inability of the model to predict the splaying mode of failure.

103
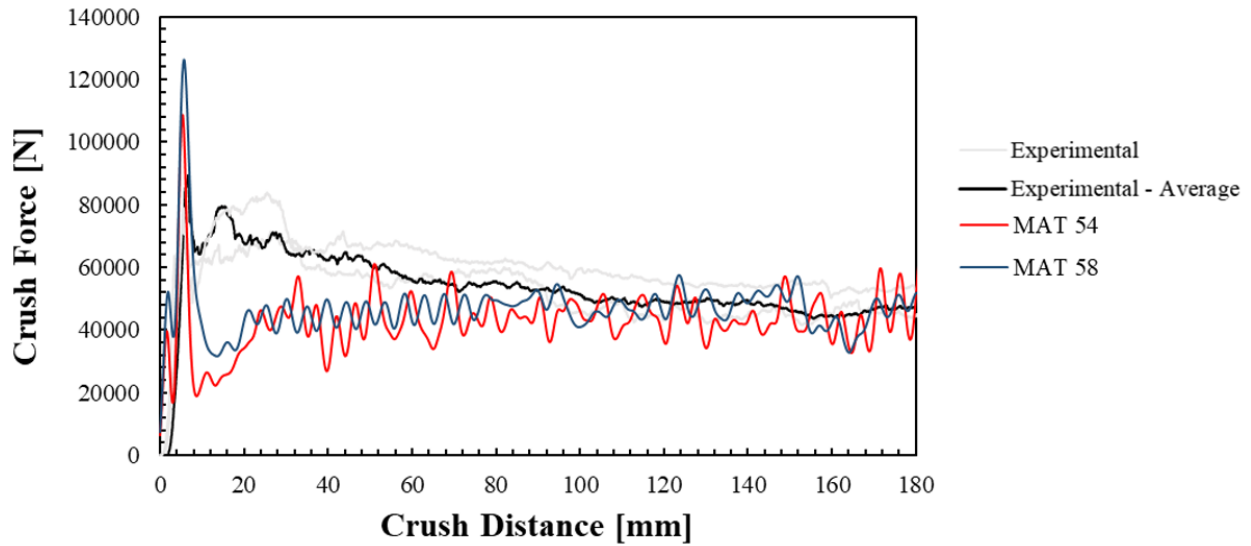
Figure 110. Force vs displacement response of hat channel specimens under quasi-static loading condition with layup 2 [±45/0_2]$_s$ for both MAT 54 and MAT 58 material models.
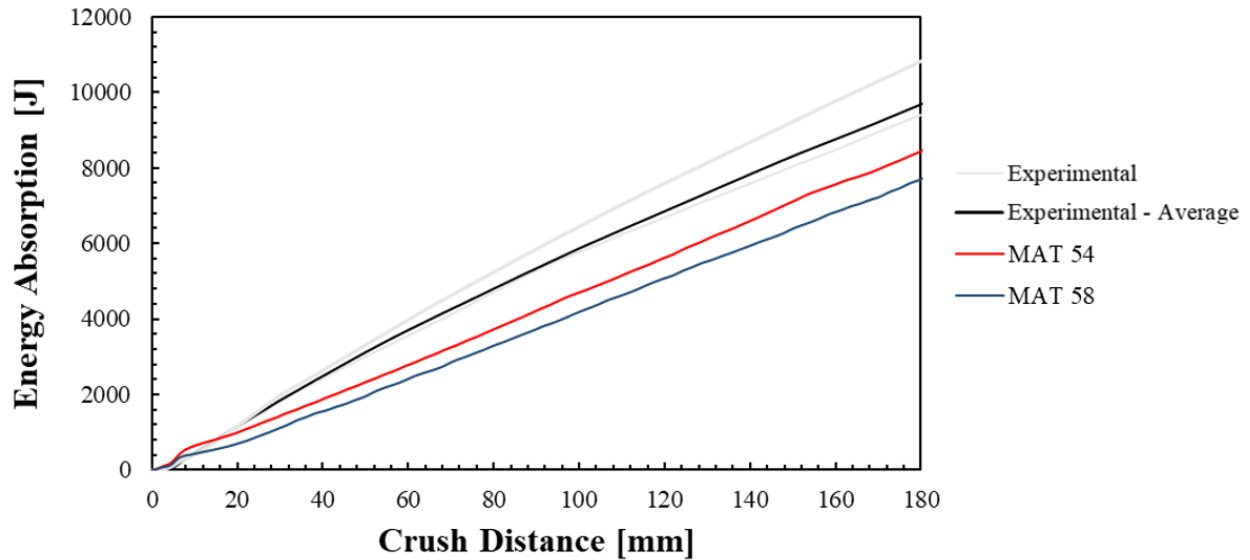
Figure 111. Energy absorption response of hat channel specimens under quasi-static loading condition with layup 2 [±45/0_2]$_s$ for both MAT 54 and MAT 58 material models.

5.6.5 Evaluation Summary

The main results for axial crush of the hat channel specimen with two different laminate stacking sequences under dynamic loading conditions are summarized in Figure 112. The total energy absorption for the hat channel with layup 2 ([±45/0_2]$_s$) was 82% higher when compared to layup 1 ([0/±45/90]$_s$). The

peak force and average crush force for the hat channel with layup 2 were 30% higher than with layup 1. Overall, the prediction of peak force, average crush force, and energy absorption for the MAT 54 model under dynamic loading rates correlated well with the experimental data. Although for the MAT 58 model the initial peak force was over predicted compared to the experiments, the mean crush force and energy absorption were slightly under predicted.

The main results for the quasi-static loading condition are summarized in Figure 113. Similar to the dynamic tests, for the quasi-static tests hat channels with layup 2 exhibited a higher energy absorption compared to layup 1. The peak force and average crush of layup 2 are also superior to layup 1. Both MAT 54 and MAT 58 models over predicted the initial crush force compared to the experiments. However, the mean crush force and energy absorption were lower in magnitude when compared to the test data.

(a)   (b)
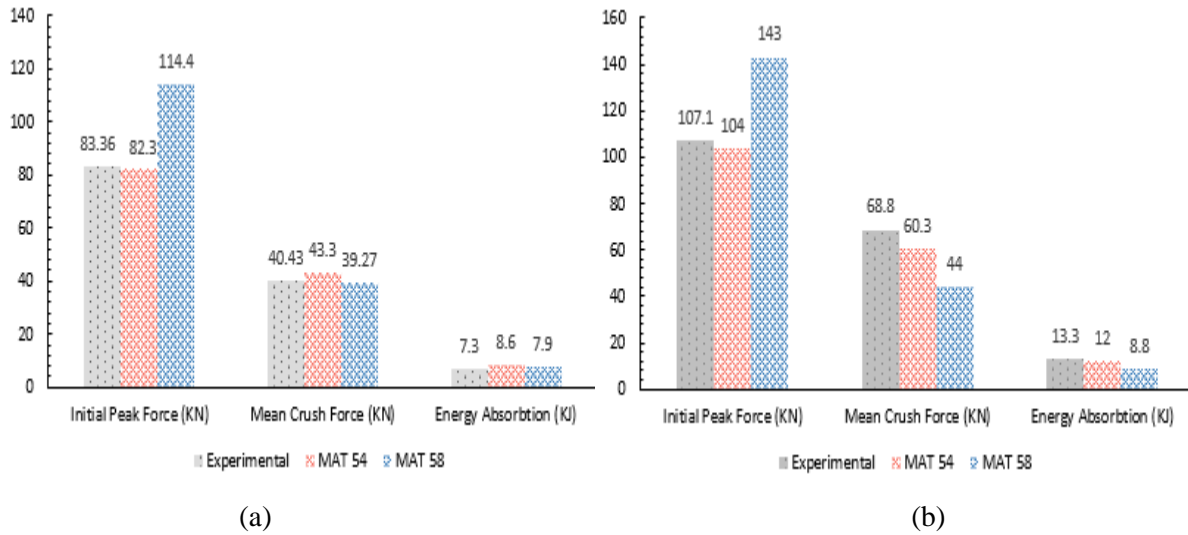
Figure 112. Comparison of the crush performance for the hat channel under dynamic loading conditions: (a) Layup 1, and (b) Layup 2.
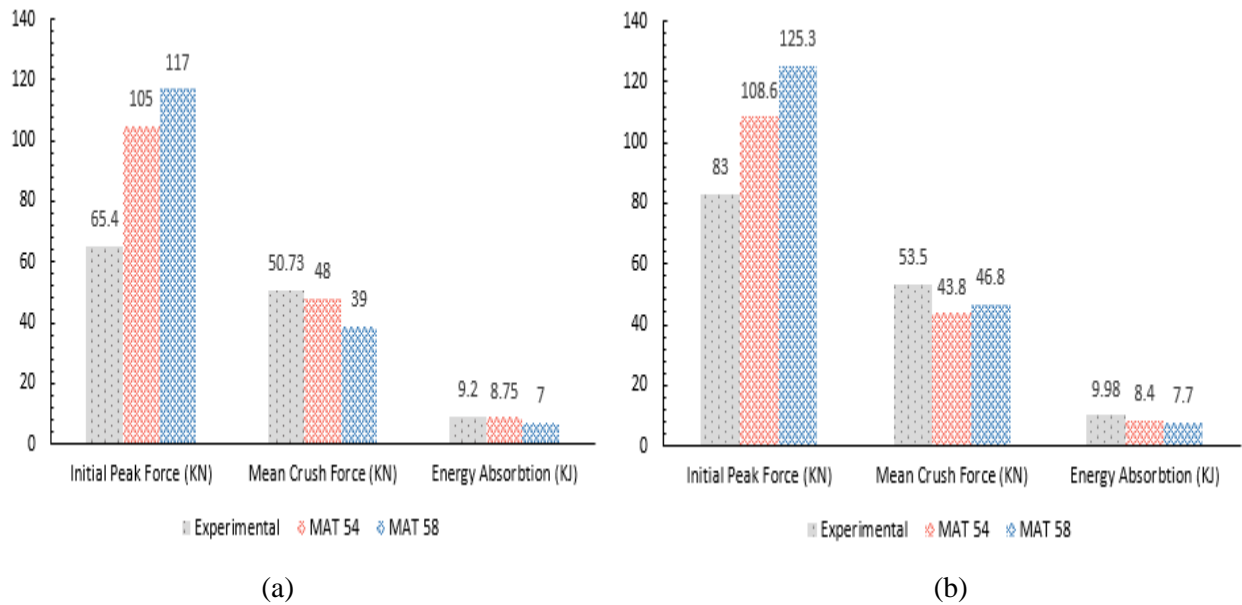
Figure 113. Comparison of the crush performance for the hat channel under quasi-static loading conditions: (a) Layup 1, and (b) Layup 2.

The results summary revealed that the numerical model using MAT 54 was able to predict the axial crush response of the studied CFRP composite hat channel components more accurately when compared to the numerical model using MAT 58. When using MAT 58, the numerical model over-predicted the initial peak force and under-predicted the average crush force and energy absorption. Thus, the MAT 54 material model was selected to evaluate the performance of the designed CFRP technology demonstrator for frontal crash applications.

Chapter 6
CFRP Technology Demonstrator Design

The calibrated material model MAT 54 from Chapter 5 was used in the virtual development of a new lightweight energy absorbing CFRP frontal crash automobile structure. The side frame member of a baseline JAC 590R steel frontal crash BIW structure from a LDV (Figure 114) was redesigned using the NCF CFRP composite material (Chapter 4), with the goal of improving performance and reducing the weight of the structure. The frontal crash structure is required to safely absorb the kinetic energy during a full-frontal crash, while preventing intrusion within the vehicle occupant zone, to meet vehicle certification standards [107][111]. In this study, a reduced-scale technology demonstrator of the side frame member was designed, with the requirement to be manufacturable using a lab-scale HP-RTM process for a possible future testing program. The designed side frame member was required to be seamlessly integrated within the frontal crash BIW structure of the LDV, replacing the baseline JAC 590R steel side frame member (Figure 115).
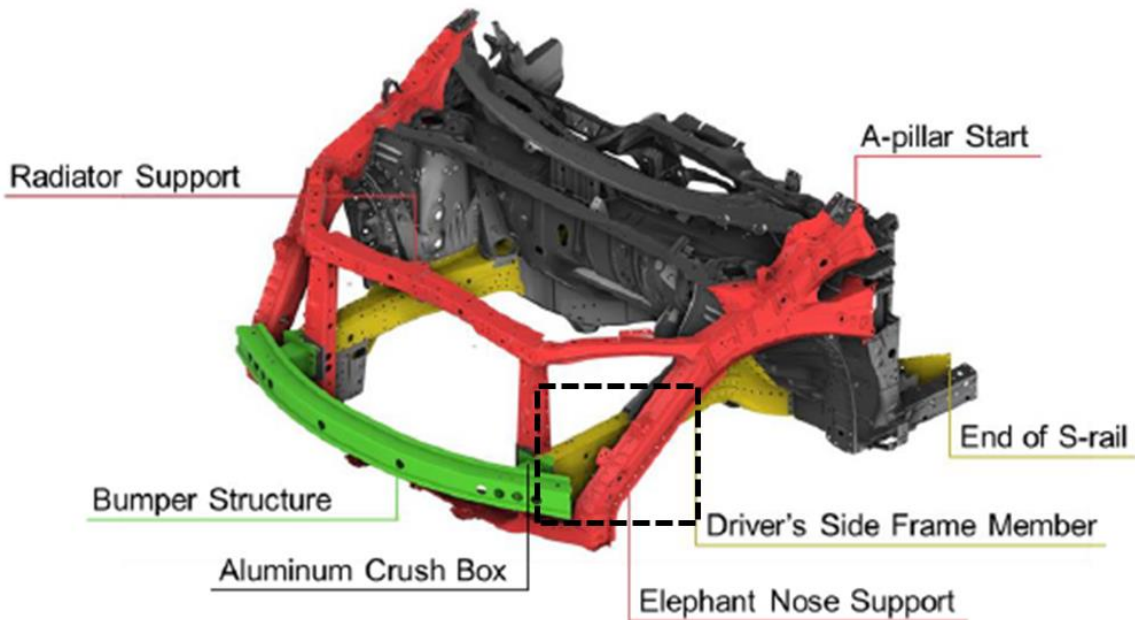
Figure 114. Frontal BIW structure of an LDV with surrounding production structures [16].

A simulation-based design approach was used to design the reduced-scale side frame member CFRP technology demonstrator. The main crush channel cross-sectional profile was first designed, prior to the development of several design concepts for the technology demonstrator assembly. Subsequently,

the effect of ply stacking sequence, total laminate thickness and ply transitions (i.e., drop-off) on the impact performance were studied to optimize the technology demonstrator design. An overview of the reduced-scale technology demonstrator is presented in Section 6.1, while a detailed description of the associated channel component cross-section and demonstrator design concepts are outlined in Sections 6.2 and 6.3. The reduced-scale technology demonstrator assembly with surrounding components and joining details are presented in Sections 6.4 and 6.5, respectively. Moreover, the details of the numerical model used to assess the performance of the technology demonstrator are outlined in Section 6.6.

6.1 Reduced-Scale Technology Demonstrator – Overview

The crush tip and middle region of a baseline steel side frame member with variable sheet thickness was considered for evaluating the crashworthiness performance of a replacement UD-NCF carbon fiber/epoxy member. FRP composites parts cannot be designed using similar approaches as sheet metal parts. This is primarily due to the distinct manufacturing processes, which are governed by the nature of the material, and the limitation these processes may impose on the part geometry and thickness. Furthermore, FRP laminates can be tailored for a specific application by considering the ply stacking sequence and placement in the part, which can be exploited to control progressive failure and energy absorption capabilities of the structure.
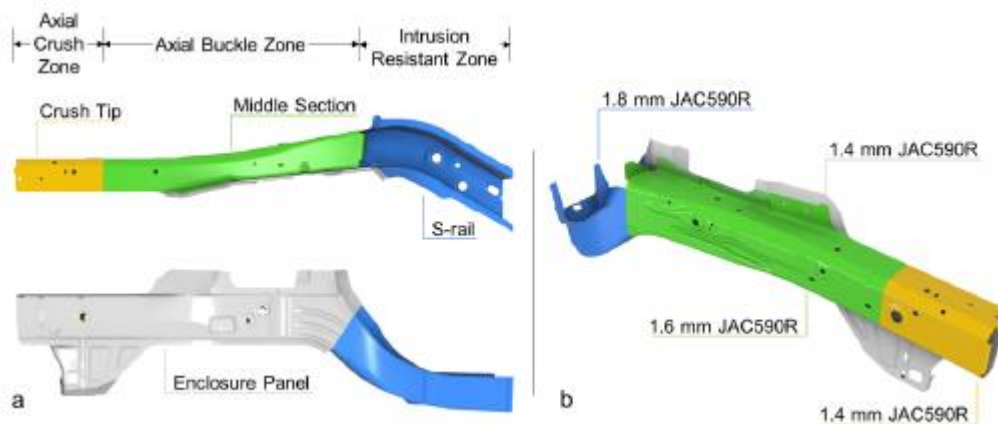
Figure 115. Primary chassis side frame member showing the production material and thickness along with the JAC590R steel sheet thickness[16][89].

In the study by Peister [89], a reduced-scale conventional JAC 590R chassis structure was tested in the laboratory under dynamic impact conditions. The author considered a 340 mm length portion of the chassis structure side frame member, including the crush region of (220 mm) and the middle region (120 mm). Additionally, Tummers [16] tested a similar reduced-scale hot-stamped ductibor steel chassis structure with overall length of 491 mm, allowing for 250 mm of free crush distance. The results produced by Tummers [16]will be used as baseline data for this study.

In this thesis, the middle region of the CFRP technology demonstrator from the crush tip back to the shock tower support along with the crush tip were considered, resulting in a total length of 525 mm (Figure 116). At this length, the CFRP reduced-scale technology demonstrator comprised of a crush region with a length of 200 mm, which was considered to evaluate the crash performance.

(a)   (b)
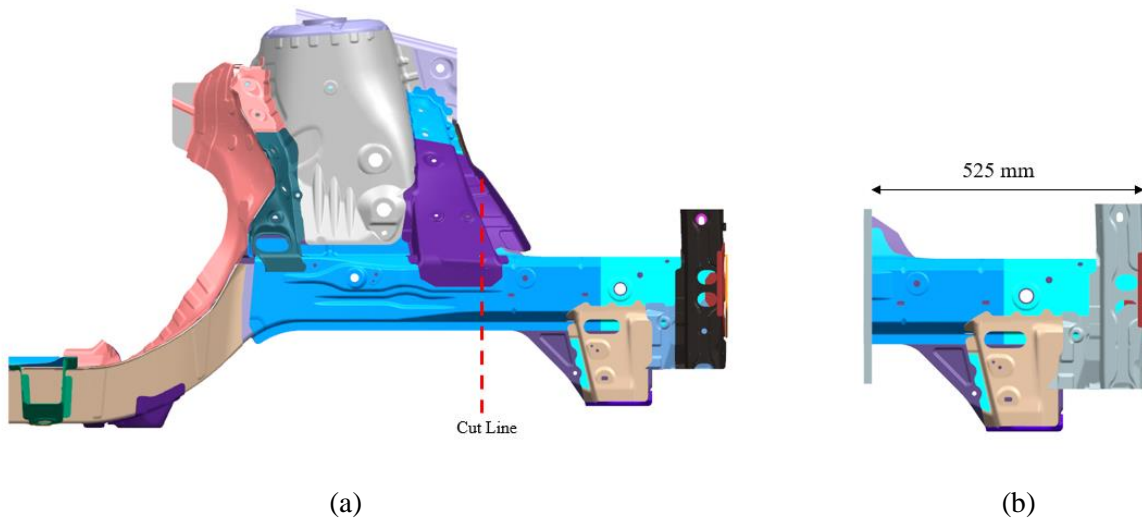
Figure 116. Technology demonstrator: (a) production scale full-length chassis side frame member, and (b) reduced-scale front-end structure.

6.2 Reduced-Scale Technology Demonstrator – Channel Cross Sectional Profile

The energy absorption capabilities of FRP composite parts under axial crush loads are largely dependent on the cross-sectional profiles. Conventional crush structures have two main components, namely a channel and backing plate (Figure 117) [134]. The conventional cross-section of the channel for the baseline steel structure is a half octagonal along the length of the crush tip and middle region, comprised of a horizontal flange on the top and small vertical flange on the bottom (Figure 118.a). The backing plate

is a relatively flat component used to close-off the channel. The backing plate consists of four radii to aid in stiffening the structure (Figure 118.a). To accommodate manufacturing of the CFRP channel using an HP-RTM process while maintaining the overall dimensions of the channel, several topological changes were required for the conventional channel cross-section. The top flange was modified to allow for a vertical flange orientation, while the dimensions of the sharp corner radii were increased. The transition angle on the vertical wall face was moved upwards as highlighted (Figure 118.b). Also, a draft of 5° was added to the vertical sidewalls to improve the quality of fabrication of the channel component and allow for part demolding.
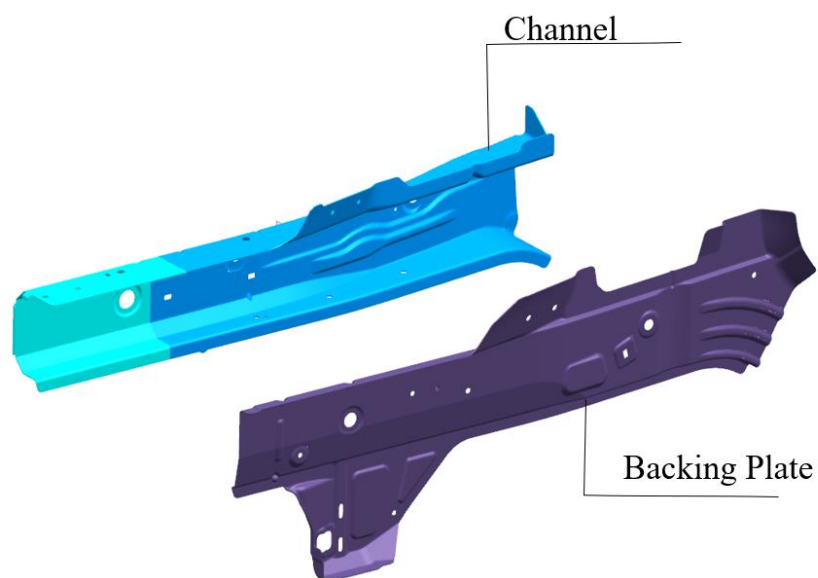
Figure 117. Exploded view of conventional channel and back plate
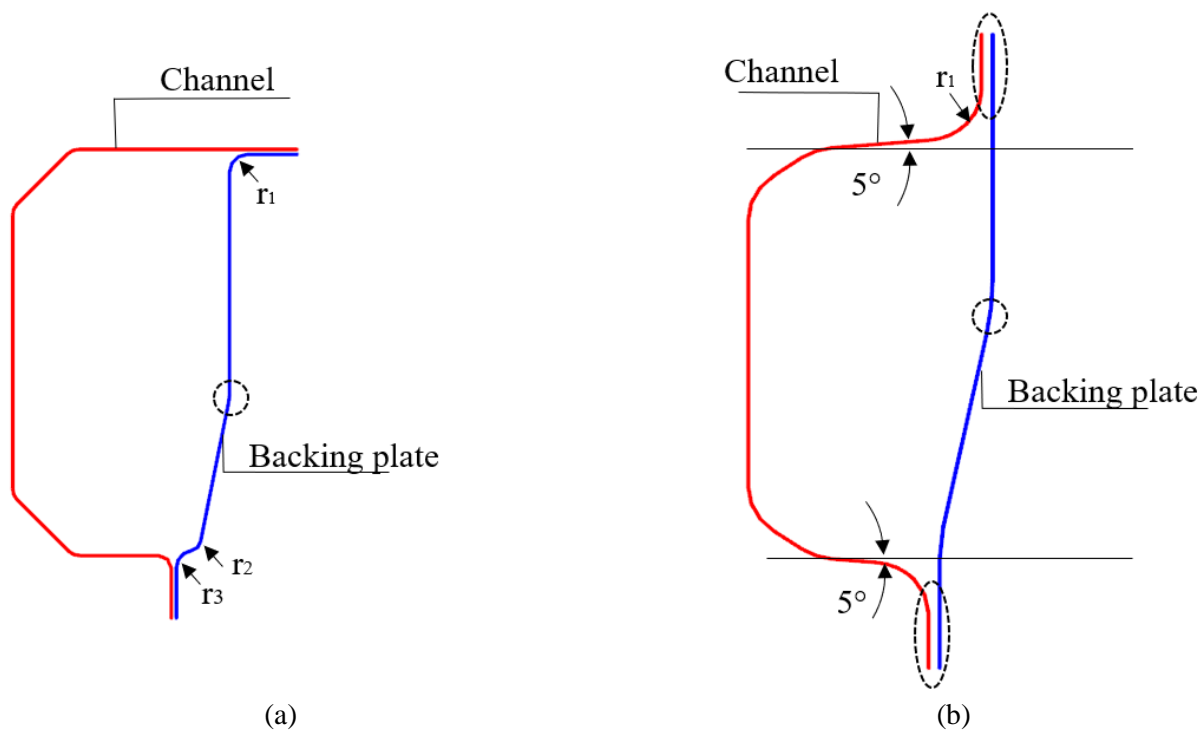
Figure 118. Cross-sectional profile: (a) baseline steel channel cross-section, and (b) proposed CFRP composite channel cross-section with modified radius and extended mating flanges.

6.2.1 Design of different cross-sectional profile for composite chassis frame

Along with the modified channel cross-section, three additional profiles, namely a hat profile, B profile, and W profile (Figure 119), were benchmarked and considered for the technology demonstrator. The additional radii and geometric changes may lead to a change in the section stiffness and energy absorption capabilities when compared to the conventional channel. These changes were paramount to eliminate the additional bulkheads and reinforcing panels in the composite structure. The hat channel (Figure 119a) was the simplest profile, and was developed by removing the chamfers on the vertical side walls of the channel. The B profile (Figure 119b) was designed with a large dimple along the length of the vertical side wall to increase the channel stiffness. The W profile was intentionally developed with an increased number of side walls and radii to mimic the conventional metallic structure that comprises inner reinforcement panels. The W channel was incorporated with three joining regions with back plate (Figure 119c). The backing plate geometry was constant for all the cross-sectional profiles considered.

The developed numerical simulation modeling framework with the calibrated MAT 54 material model were used to evaluate the axial crush performance of channels with the different profiles (Figures 118 and 119). The channel with the best performance characteristics was selected as a basis for the reduced-scale CFRP technology demonstrator design.
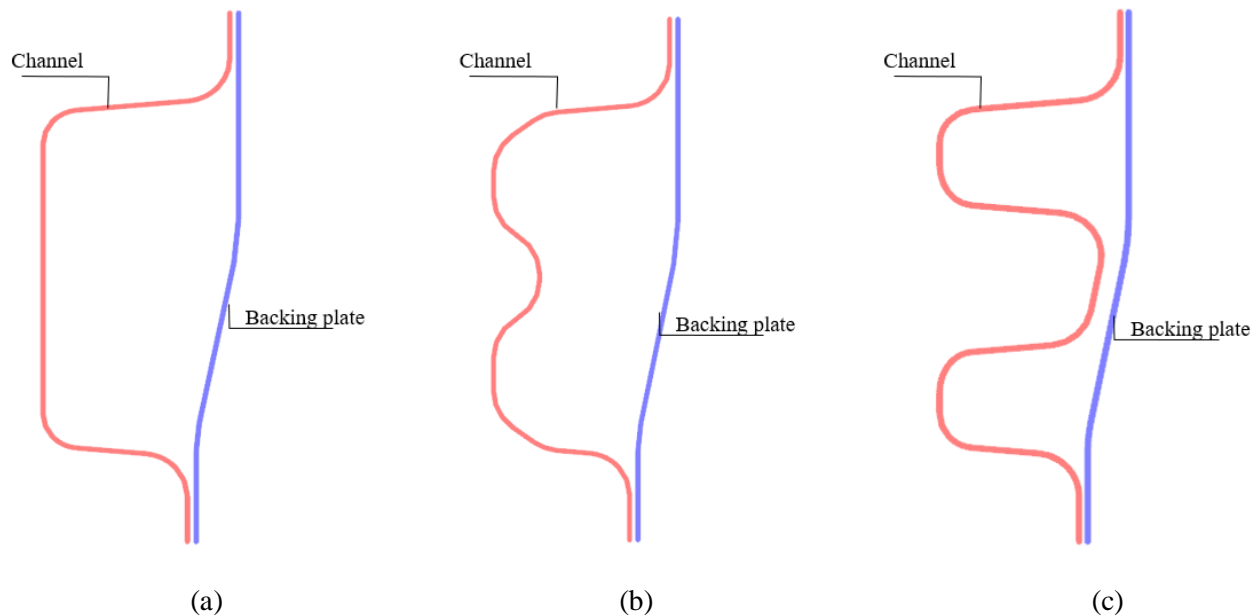
Figure 119. Different cross sections considered for the CFRP composite channel: (a) hat profile, (b) B profile, and (c) W profile.

6.2.2 Adhesively Bonded Joint Modelling

The CFRP composite channel and backing plate were adhesively joined. The adhesive was numerically modelled by a single layer of solid cohesive elements with bond line thickness of 0.2 mm. A predefined gap was maintained between the mid-plane of the composite shell elements and the solid adhesive layers to account for the thickness of the composite material, which varied depending on the number of plies in the laminate (Figure 120). The solid cohesive elements (type 19) chosen account for through-thickness deformations, while the cohesive zone material model (MAT 240) was used to define the traction-separation law for the adhesive. The adhesive properties are reported by Watson et al.[126],[127],[134] for the bond line thickness of 0.2 mm, which was considered throughout this study. An offset contact algorithm in LS-DYNA

(TIED_SHELL_EDGE_TO_SURFACE_CONSTRAINED_OFFSET) was used to account for the connection between the composite flanges shell elements and the solid adhesive elements. The three adhesive regions modeled for the W profile channel with backing plate are shown in Figure 121.
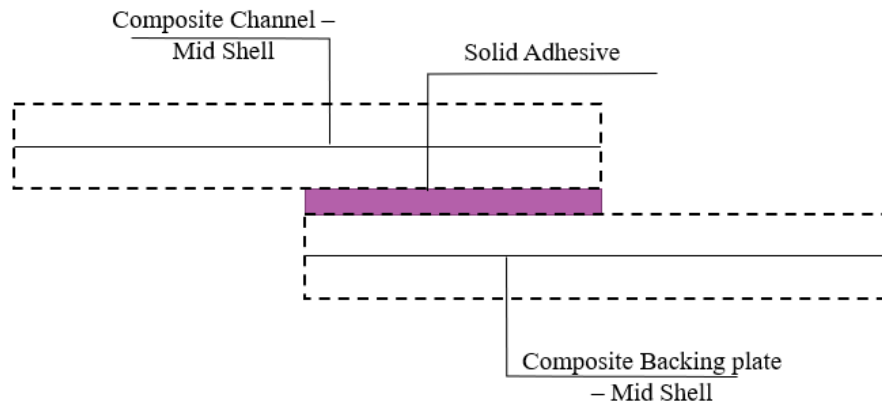
Figure 120. Modeling of adhesively bonded composite joints using shell elements and solid cohesive elements.
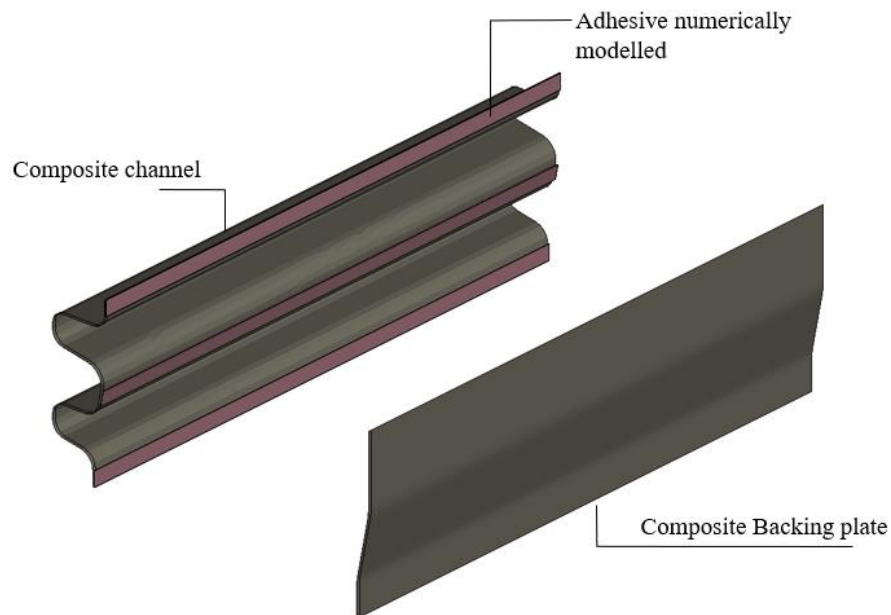
Figure 121122. Exploded view of CFRP channel with W profile showing locations of the modeled adhesive.

6.3 Reduced-Scale Technology Demonstrator – Design

The UD-NCF carbon fiber/epoxy composite side frame member was designed as two components to reduce part count (i.e., assembly time) and tooling cost (Figure 122). The reinforcement parts from the conventional baseline side frame member structure were combined with the CFRP crush channel and backing plate that were both comprised of multiple UD-NCF plies. The initial design concept was developed by making the mating flanges of the CFRP channel vertical and combining the lower reinforcement with the channel as a single part (Figure 123).
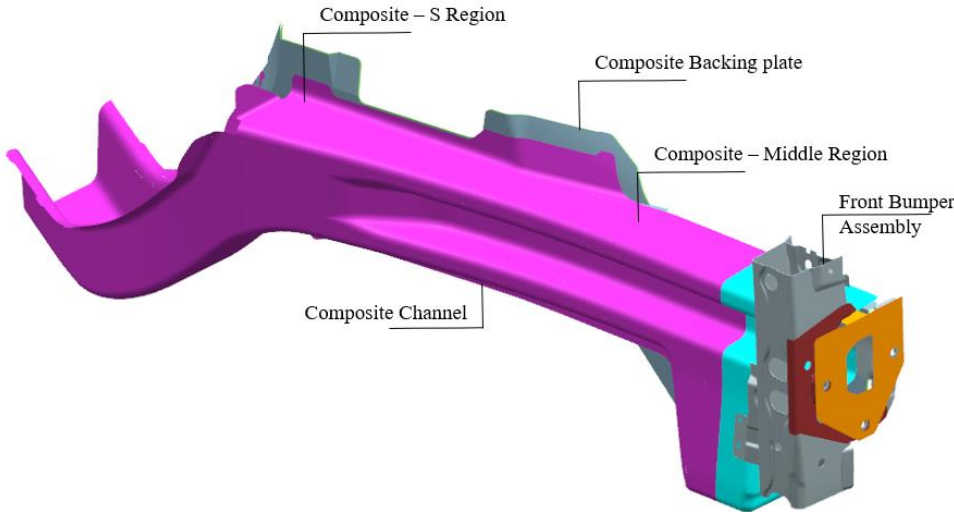
Figure 122. Isomeric view of isolated front-end chassis side frame member.
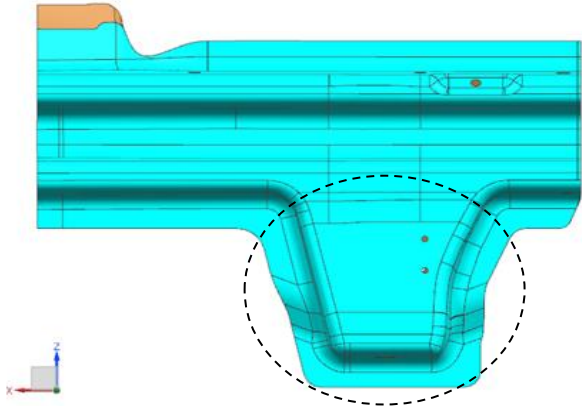
Figure 123. Reduced-scale composite chassis structure - initial design concept with combined lower reinforcement part.

114

6.3.1 Design Concept 1

The initial technology demonstrator design was modified to improve manufacturing feasibility and part quality (Figure 124). A more gradual transition was included for the channel-to-lower reinforcement region and for the side walls to ensure component demolding during fabrication. Also, the corner radii were enlarged to limit the potential for local fiber thinning and fiber breakage, as well as to ensure resin flow in the corners during resin transfer into the mold (Figure 124).

(a)   (b)
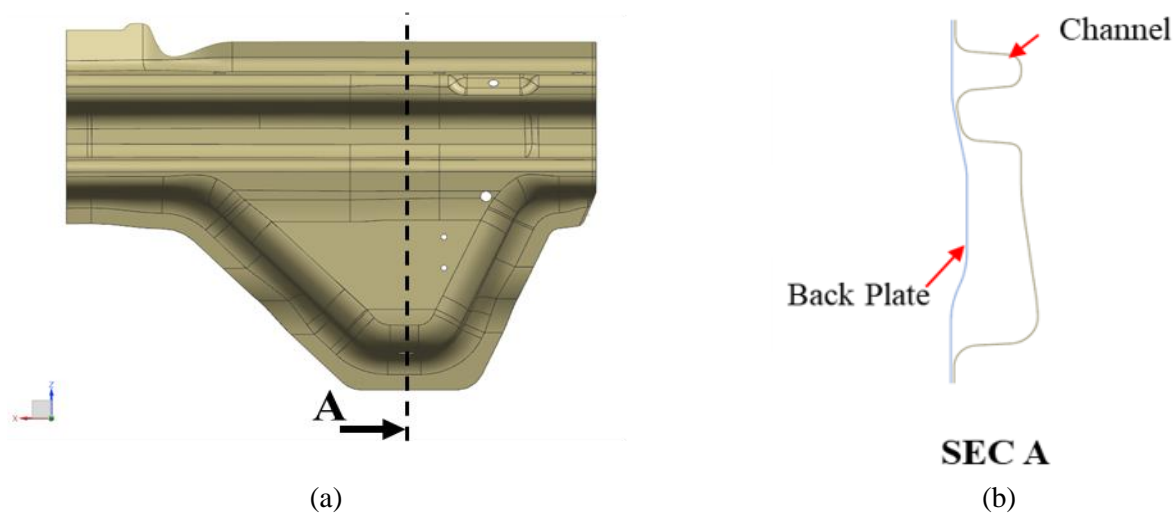
Figure 124. Design concept 1: (a) side view of technology demonstrator, (b) sectional view of technology demonstrator.

6.3.2 Design Concept 2

The gradual channel-to-lower reinforcement transition adopted in design concept 1 created a 350 mm gap in the channel profile. This profile gap may negatively affect the energy absorption capacity of technology demonstrator. To address this potential performance reduction, a separate composite plate was mechanically fastened to the channel to span the gap (Figure 125). The laminate stacking sequence of the plate followed that of the channel.
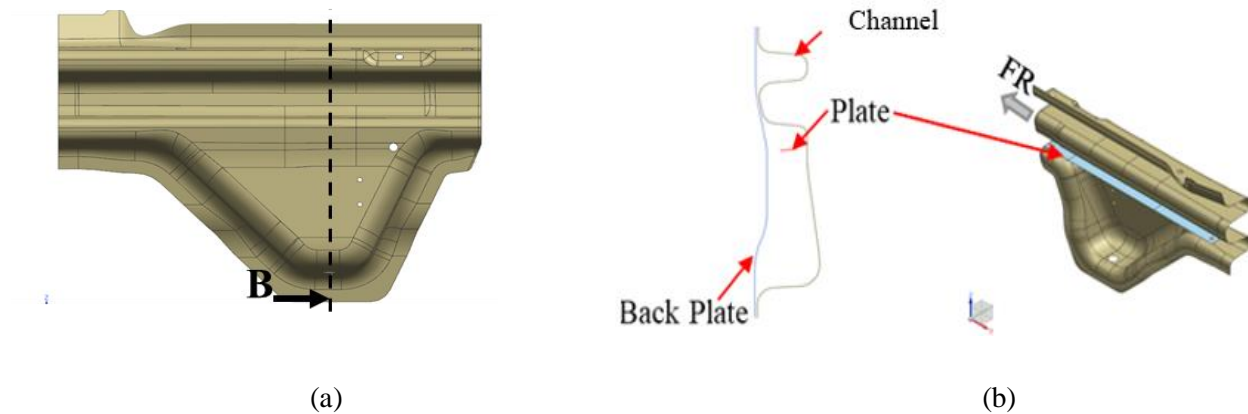
Figure 125. Design concept 2: (a) side view of technology demonstrator, (b) sectional and isomeric views of technology demonstrator showing addition of reinforcement plate.

6.3.3 Design Concept 3

This design iteration substituted the flat composite plate with an L-angle component to span the gap in the channel (Figure 126). The mounted-angle was joined to both the channel flange and the backing plate using mechanical fasteners. The same stacking sequence as channel and backing plate were assumed for the L-angle.
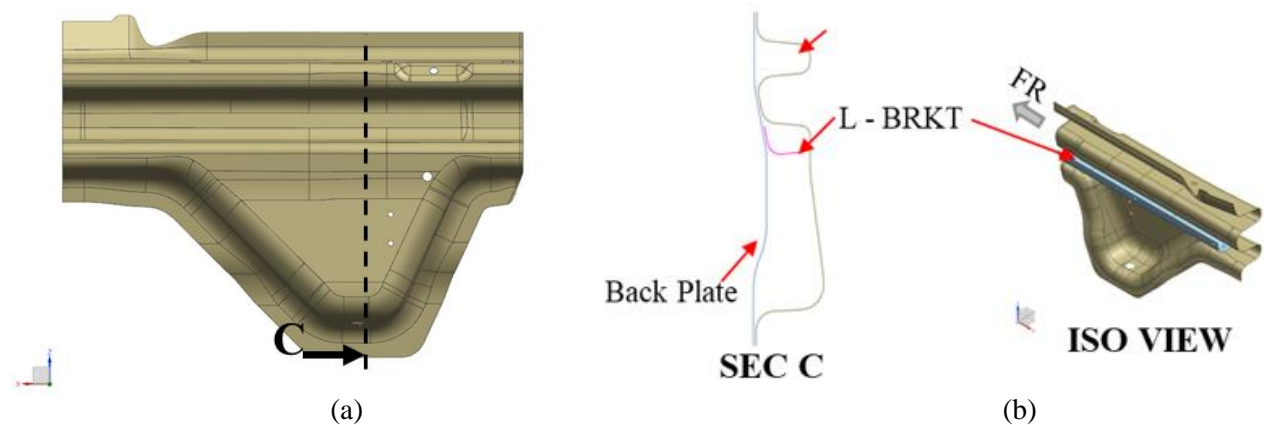
Figure 126. Design concept 3: (a) side view of technology demonstrator, (b) sectional and isomeric views of technology demonstrator showing addition of L-angle component.

6.3.4 Design Concept 4

| (a) | (b) |
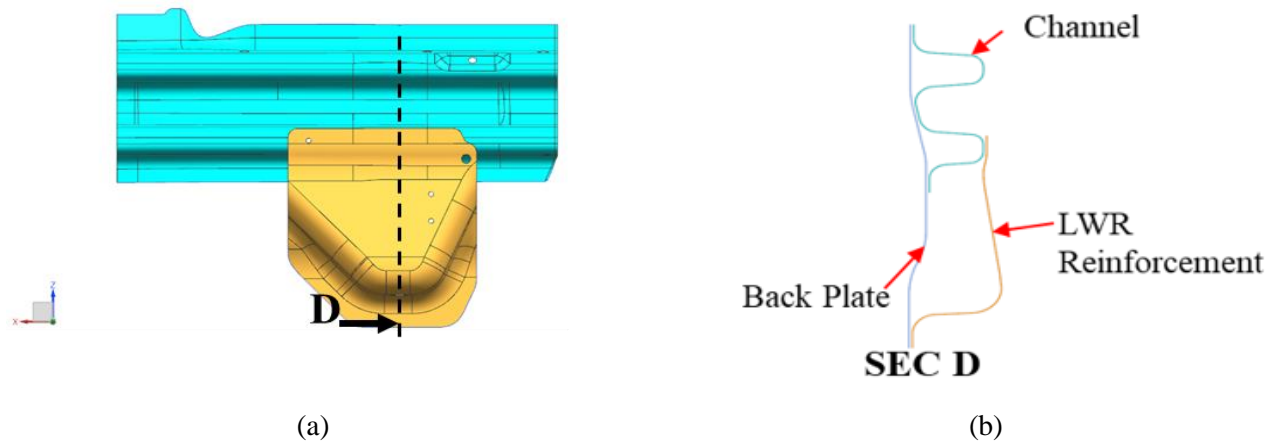
Figure 127. Design concept 4: (a) side view of technology demonstrator, (b) section view of technology demonstrator showing a separate lower part.

For this design concept the main channel part was separated into two components, a straight channel and lower reinforcement component, to reduce the complexity of the channel geometry (Figure 127). The lower reinforcement component comprises the same ply mechanical properties and stacking sequence as the channel and backing plate. The lower reinforcement component was mechanically fastened to the channel and back plate.

6.4 Reduced-Scale Technology Demonstrator – Assembly

Several production components from the side frame member structure, such as the front bumper assemblies (Figure 128), were considered for the reduced-scale technology demonstrator design. The end of the technology demonstrator opposite the bumper assembly was mounted onto a steel plate, which represents the support during a physical test.
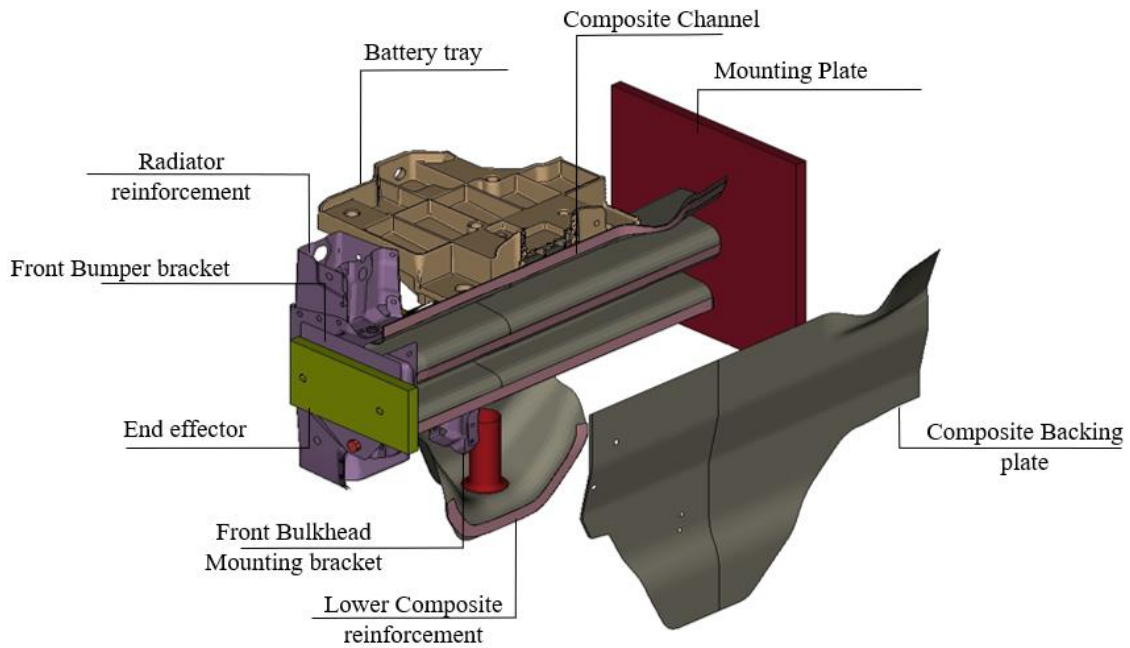
Figure 128. Exploded view of reduced-scale technology demonstrator, showing production components with all surrounding structures.

Several modifications were made to the production components to account for the changes in the cross-section, flange orientation, draft angle and profile of the CFRP channel and backing plate components for each design concept. Consequently, all the production components were mechanically fastened to the channel and backing plate. The changes made to each component were described below.

6.4.1 Parts modified to accommodate the Composite rail

In the front region of the reduced-scale demonstrator, an interference was observed between the top flange of the front bumper bracket and the CFRP backing plate (Figure 129). Additionally, a gap between the front bumper bracket side flange and backing plate, which are mating surfaces, was observed. The front bumper bracket was redesigned to remedy these issues (Figure 130), with minor changes made. The top flange of the bracket was removed to avoid interference with the backing plate and the bracket feature lines were removed to aid with joining of two parts.

118

(a)   (b)
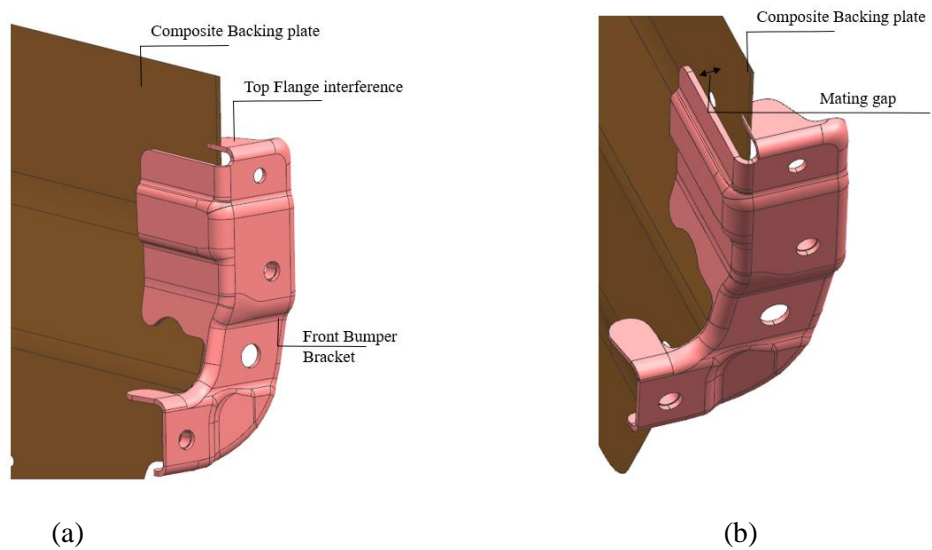
Figure 129. Composite backing plate: (a) interference with production front bumper bracket, (b) gap between the bracket and backing plate.
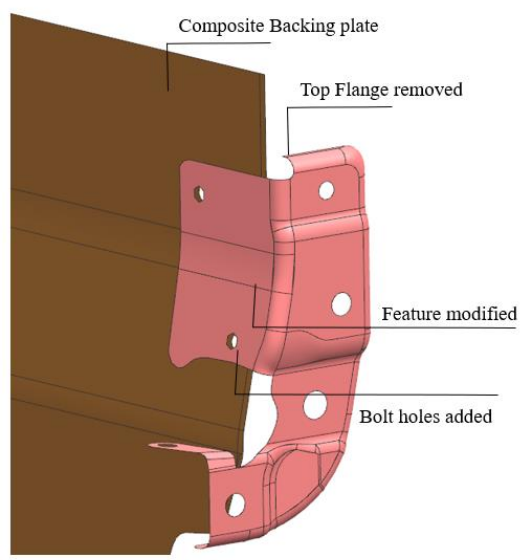
Figure 130. Re-designed front bumper bracket to accommodate composite backing plate.

Additionally, the front bumper plate extension interfered with the vertical flange of channel and backing plate (Figure 131.a). The interference region of the bumper plate was trimmed to mitigate the problem (Figure 131.b).

119

(a)   **(b)**
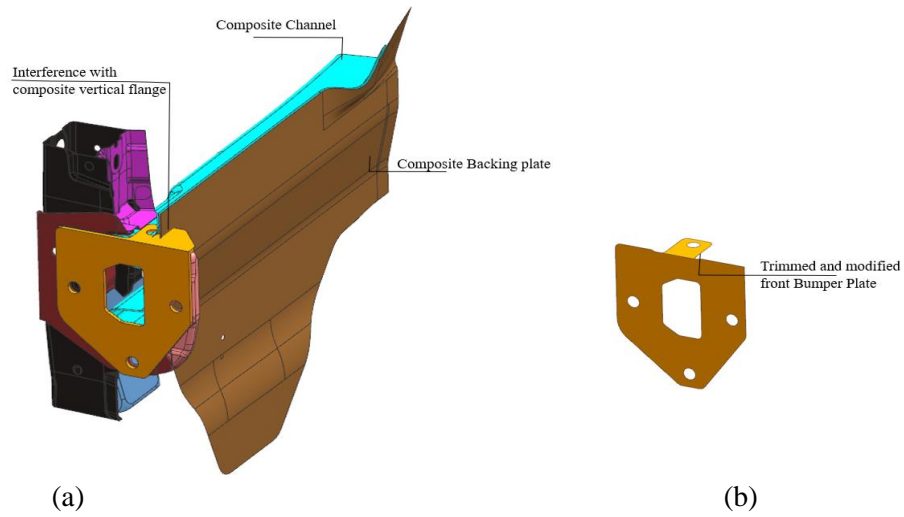
Figure 131. (a) Bumper plate interference with composite backing plate vertical flange, (b) trimmed and modified front bumper plate.

6.4.2 Part Modifications to accommodate Side Wall Draft Angle

The consequence of modifying the draft angle for composite channel resulted in incompatible mating surfaces with some of the production components . To ensure compatibility of components, the front bracket, radiator support reinforcement and front bulkhead mounting collar were redesigned (Figure 132).
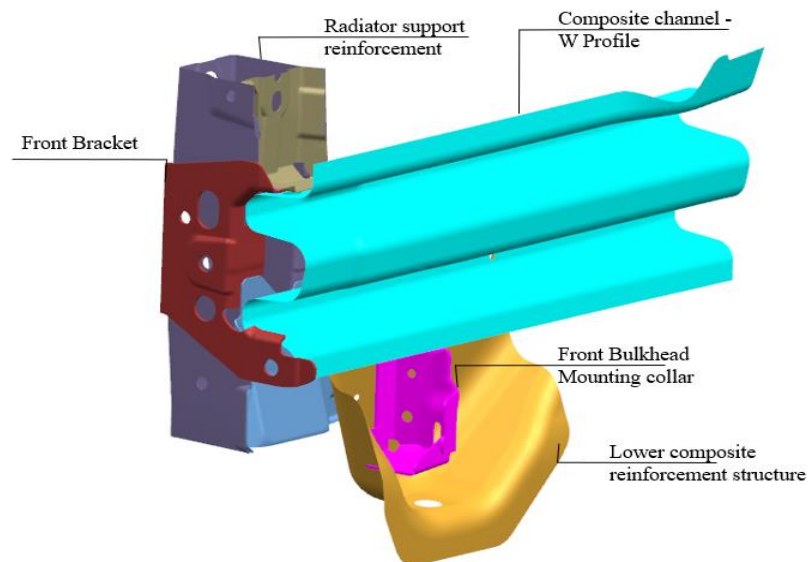
Figure 132. Production components modified to accommodate composite assembly.

6.4.2.1 Front Bulkhead Mounting Collar

Several flanges of the production front bulkhead mounting collar were modified (Figure 133). The spot flange on the top of the mounting collar was modified to avoid interference with the channel. The mounting flanges on the upper and lower regions of the collar were reshaped and tapered to match the draft angle of the channel. Two mounting holes were designed on either side of the mounting collar to mount the component to the composite channel and back plate assembly.
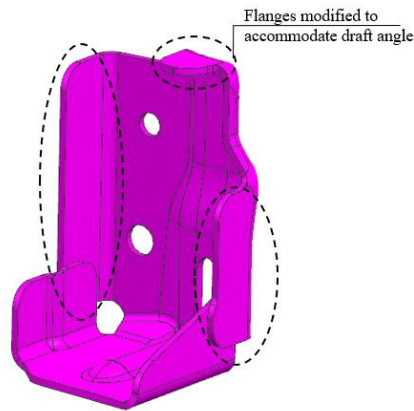
Figure 133. Production front bulkhead mounting collar – modified region highlighted with dashed lines.

6.4.2.2 Front Bracket

The front bracket mounting features, especially the top flange (Figure 134), were redesigned. The front vertical flange was opened to match the draft angle of the channel and the side flanges were designed to add sufficient clearance to accommodate the new cross section.
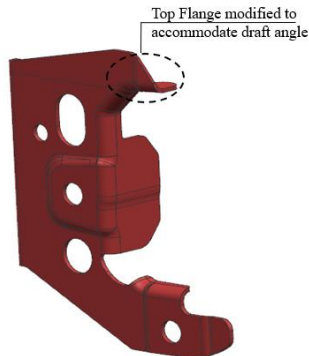
Figure 134. Production front bracket – modified regions highlighted with dashed lines.

6.4.2.3 Radiator support Reinforcement

The lower spot flange of the radiator reinforcement was re-shaped (Figure 135). The flange was bent to accommodate the draft angle changes of the composite channel, to ensure a proper mating surface.
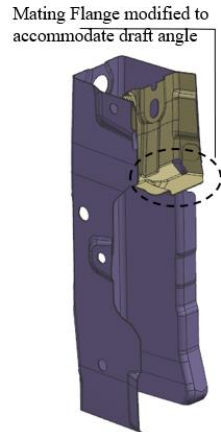
Figure 135. Front radiator support reinforcement – production component highlighting modified region.

6.5 Reduced-Scale Technology Demonstrator – Joining of Components

The production components and designed CFRP components were joined using three different techniques, including spot welds for metal to metal connections, adhesive for composite to composite connections, and mechanical fasteners (bolts) for metals to composite connections. Each modelling technique is described below.

6.5.1 Spot welding

Front bumper steel parts were modelled as shell elements and connected using MAT 100 (MAT_SPOTWELD_DAMAGE_FAILURE) a spot weld material card available in LS-DYNA. The spot weld material model used isotropic hardening plasticity coupled with the failure model that was used for the baseline demonstrator structure models [16]. As recommended by Malcolm and Nutwell [136], the spot weld was represented using eight-sided hexagonal pattern solid elements with single integration points (type 1). The steel parts were re-meshed to ensure that their nodes coincided with the spot weld element nodes. The solid elements filled the gap between the two sheets. The spot weld elements were evaluated based on the modelled true thickness value of $1E^{-6}$ mm which was important for shear loading. A visualization of the mesh dependent spot weld (Figure 136) modelled in LS-DYNA are represented by hexagonal solid element.
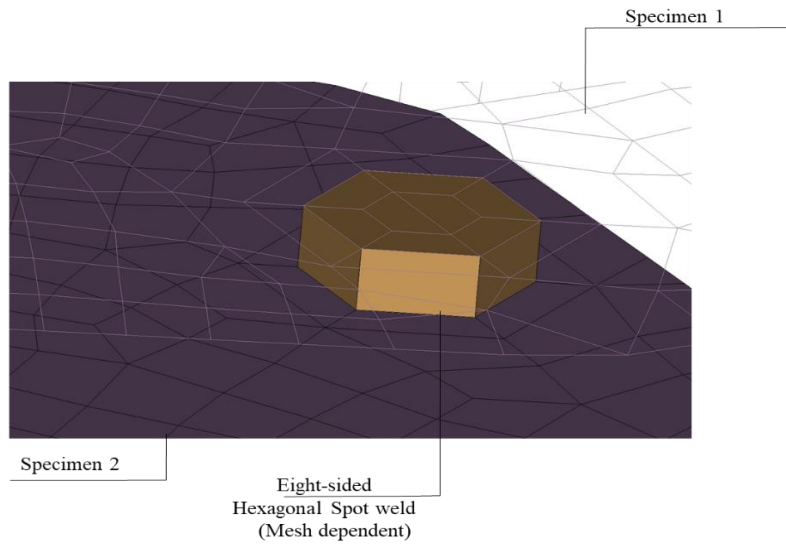
Figure 136. Hex spot weld with mesh dependent model.

The front bumper brackets, side radiator reinforcement and front bumper extension bracket were connected using the spot weld solid elements (Figure 137, red regions) with the two or three stack combinations.

(a)

(b)
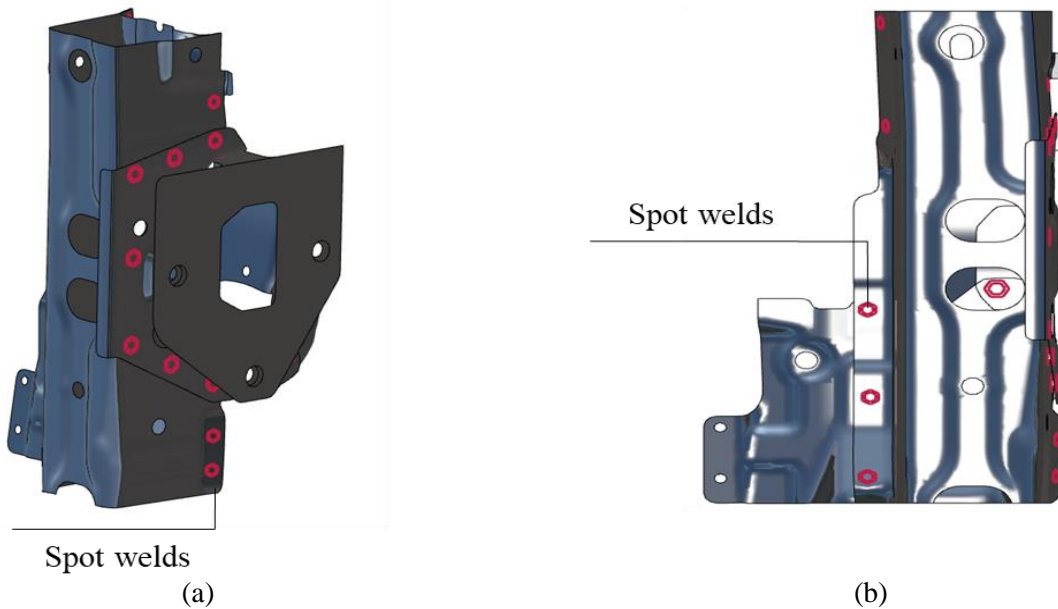
Figure 137. Reduced scale front bumper assembly – red region denotes the spot welds modelled (a) isomeric view, and (b) side view.

6.5.2 Adhesive modelling

The composite parts and adhesives are modelled in the same way as described in Section 6.2.2, thus for brevity they will not be explained again.

6.5.3 Bolt modelling

The secondary components modelled for the reduced scale technology demonstrator include the base battery plate, brace front bulkhead, and front-end plates. Each of these components were bolted to the composite structures in various locations.

The battery base holds the battery in an automobile and is manufactured using reinforced plastics. Solid tetrahedral elements with type 13 formulations was implemented for the numerical models. The failure strains of 0.3 mm/mm was assigned using the kinematic hardening material model in LS-DYNA. The battery base was connected to the composite structures using bolts connections (Figure 138), where steel bolts without pretension were modelled using 10 mm cross sectional diameter Hughes-Liu beam elements. The beam elements were connected to the channel and battery base using the constrained nodal rigid bodies. The failure of bolts was modelled using the constraint spot weld definition. The normal and shear force failure for bolt beam elements were assumed to be 9 kN [16].
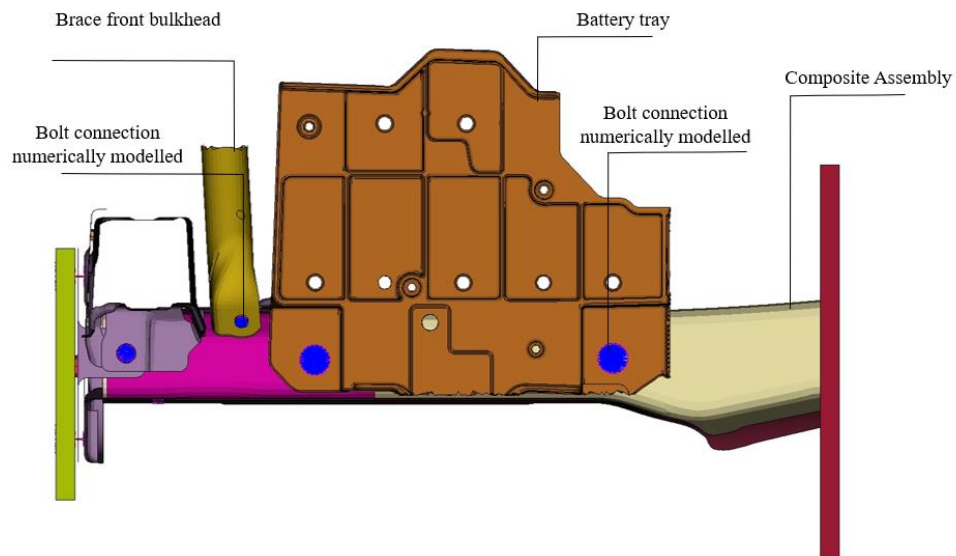
Figure 138. Battery tray and brace front bulkhead bolt connection to the composite channel.

For the purposes of the numerical model, the brace front bulkhead was reduced to 180 mm of length and the unnecessary length connecting the radiator support was not considered (Figure 138). The brace

front bulkhead was bolted onto the composite channel using 8 mm cross-sectional diameter Hughes-Liu beam elements with constrained nodal rigid bodies.

The aluminium 6061 end plate was modelled using single integration point solid elements with material data taken from Ambriz and Jaramillo [137]. The aluminium end plate was connected to the bumper brackets using type 9 spot weld beam elements (axial preload of 29.2 kN) with constrained nodal rigid bodies (Figure 139).

The bulkhead mounting collar and other front bumper brackets were attached to the composite technology demonstrator using M8 bolt connections. The bolts were modelled using the same spot weld Hughes-Liu beam elements (Type 1) without any pretension applied to beam elements. The normal and shear failure for the beam elements are assigned to be 9 kN.
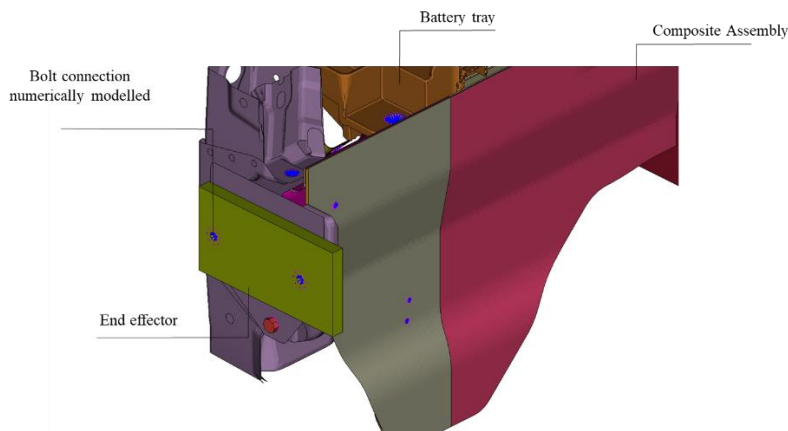
Figure 139. Bolt connection modelled for reduced-scale composite assembly.

6.6 Reduced-Scale Technology Demonstrator – Numerical Model

The overall length of the assembled reduced-scale technology demonstrator was 525 mm, which comprised of 2.7 mm thick laminated CFRP channel and backing plate, and several redesigned production components. Multi-thickness CFRP components were also considered in the design of the technology demonstrator.

A standard Seattle safety crash sled with a mass of 855 kg and a speed of 51 km/hr was used to simulate the energy absorbing capabilities of the demonstrator structure (Figure 140). The fixed end of the channel and backing plate was mounted to a 0.5 inch thick steel plate using a fixture that closely conformed to the

hat channel (Section 4.3.5). A wood pine board was mounted to the impacting end of the crash sled to control the noise in the load cell data.
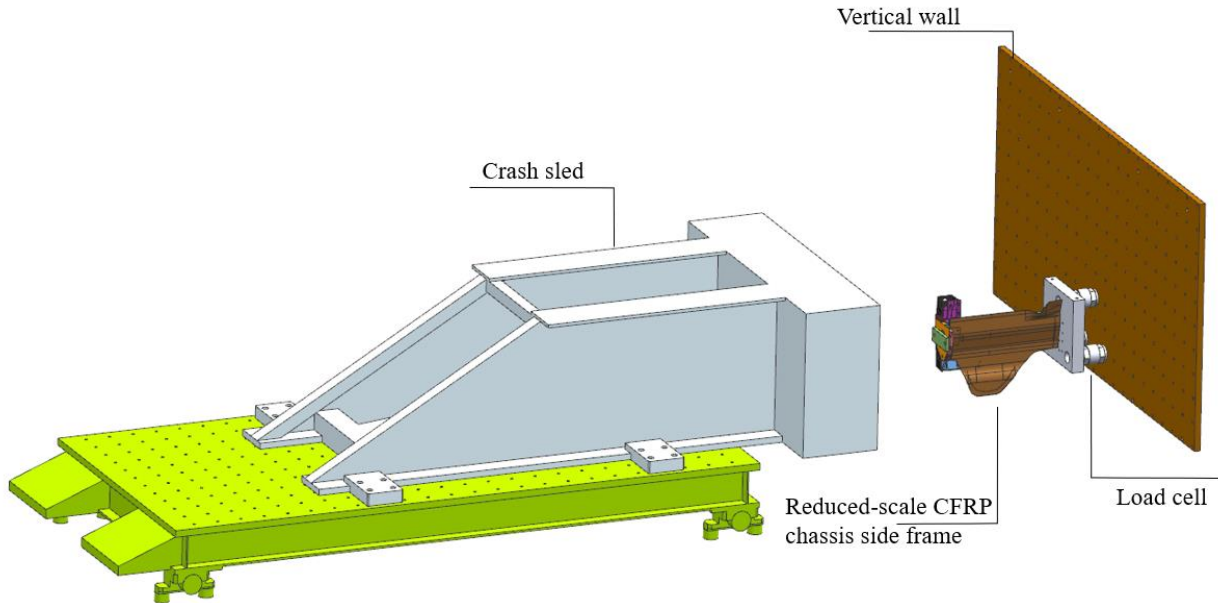
Figure 140. Experimental setup for dynamic crash of Reduced scale CFRP chassis side frame.

The reduced scale composite technology demonstrator was numerically modelled to account for all the physical boundary conditions (Figure 141). Many of the modelling parameters, material properties, and joining methods remain the same as those described in Chapter 4 and Section 6.5; only the additional boundary conditions are described hereafter.

The boundary conditions at the fixed end of reduced-scale structure and the steel plate was modelled using the TIED_NODES_TO_SURFACE_OFFSET contact algorithm in LS-DYNA. The steel plate (Figure 141) was modelled as a linear elastic material and solid elements were used. The rigid wall face of the steel plate was fixed in all degrees of freedom using the single point constraint (SPC) option.

The crash sled was numerically modelled as a rigid plate, with type 16 BELYTSCHKO-TSAY shell elements. A prescribed mass of 855 kg and an initial velocity of 51 km/hr (14.167 m/s) was assigned to the sled elements. The wood pine was modelled as a southern pine wood material with properties from Ref. [16] and meshed using solid elements and tied to the rigid sled using TIED_SURFACE_TO_SURFACE_OFFSET contact algorithm. A free crush distance of 250 mm was achieved with the reduced-scale technology demonstrator.
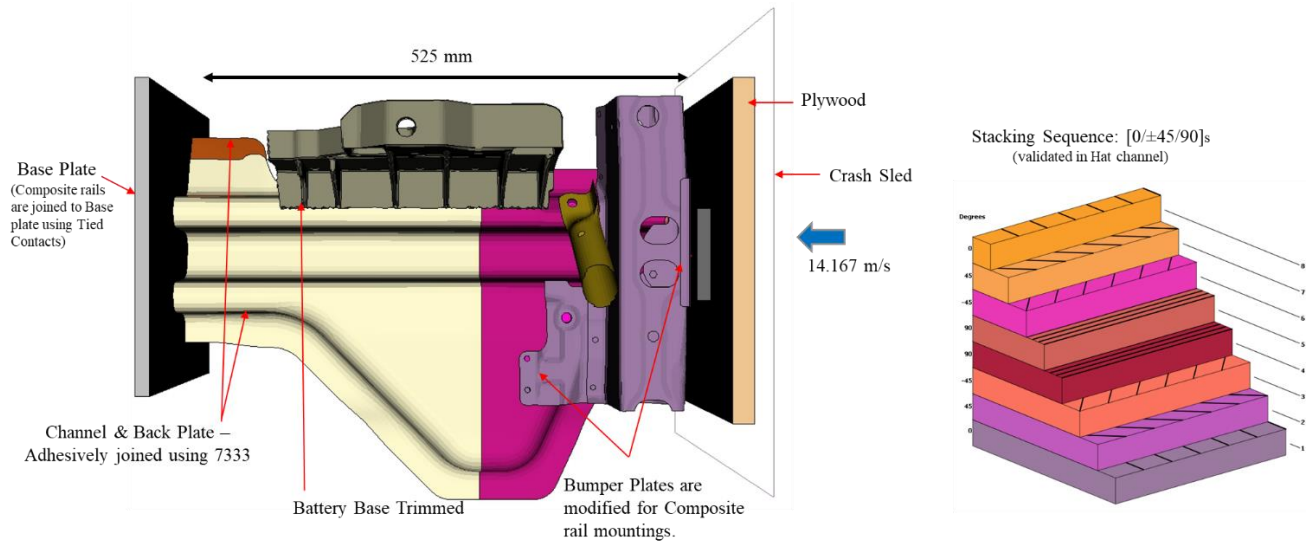
Figure 141. Boundary conditions for reduced-scale technology demonstrator (design concept 1 shown).

Chapter 7

Reduced-Scale Technology Demonstrator Numerical Results

In this chapter, the performance assessment of the different cross-sectional geometries developed for the main channel of the reduced-scale composite technology demonstrator (Section 6.2) is presented in Section 7.1. The axial crush response of straight channels for each cross-sectional geometry were assessed numerically. The crash performance and energy absorbing capabilities for all technology demonstrator design concept (Section 6.3) was numerically predicted, and will be presented in Section 7.2 along with a comparison to a baseline tailor-welded hot stamped steel structure [16]. Finally, the results of a parametric study focused on assessing the effect of ply stacking sequence (Section 7.3), laminate thickness variation (Section 7.4), and variable laminate thickness (Section 7.5) on the crash performance of the CFRP technology demonstrator are presented.

7.1 Numerical results for channel cross-sectional profile development

Axial crush of 500 mm long straight channel components was simulated using the same numerical modeling strategy described in Chapter 4 under dynamic loading conditions. A distinct simulation model was developed for each channel with different cross-sectional geometry (Section 6.2). The UD-NCF ply stacking sequence considered for all channels was $[0/\pm45/90]_s$, and the ply properties were reported in Table 2. The calibrated material model MAT 54 was used for all simulations, while a V-patterned structured shell element quad mesh was used for the channels. In addition, a flat CFRP backing plate with the same stacking sequence and lamina properties was adhesively bonded to the straight CFRP channel flanges. The backing plate was meshed using structured quad elements, and the adhesive bond was represented in the numerical model using the same method described in Section 6.2.2. The aim of the numerical simulations was to evaluate the energy absorption capabilities of each channel.

A stable progressive crushing response was predicted for all four channel geometries up to 60 mm of crush distance, where a fragmentation failure mode with frond formation over the straight areas and shearing in all corners of the channel was predicted (Figure 142). Through to a crush distance of 200 mm, channels with the hat, half octagonal and W profiles continued to fragment and form progressive fronds; however, the B profile channel eventually buckled causing a reduction in the loading bearing stiffness of the channel cross section. The channel with the W profile, designed with an increased number of edges and high cross-sectional rigidity, formed more brittle fragments and with notable shear deformation around the corners.

128

(a) Half Octagonal Profile

(b) Hat Profile

(c) B Profile

(d) W Profile

Crush
Distance   40 mm   150 mm   200 mm
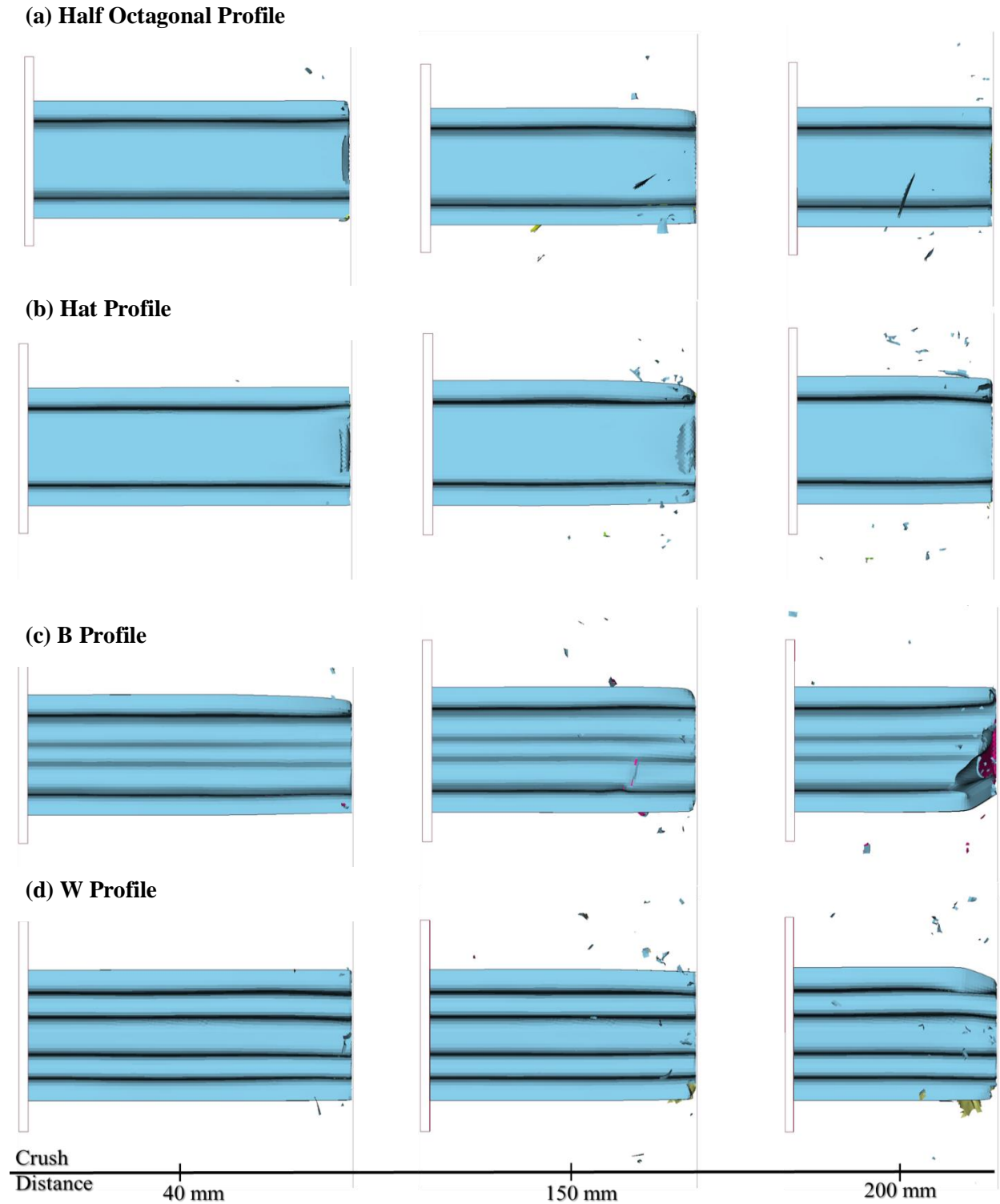
Figure 142. Dynamic axial crush response of straight CFRP channels (stacking sequence of [0/±45/90]s) with different cross-sectional profiles at specified crush distances.

129

The initial peak force for the hat, B and W profile channels was approximately 200 kN, which occurred at 20 mm of crush distance (Figure 143). The initial peak force for the channel with a half octagonal profile was lower at approximately 150 kN. A subsequent drop in the force response in the transition region was followed by an average crushing force during stable crush. The mean crushing force for the channels with hat profile, B profile, and half octagonal profile were 53 kN, 54 kN, and 56 kN, respectively (Figure 143). The hat and half octagonal profile channels exhibited stable crushing, while the B profile channel exhibited a drop in force level after 150 mm of sled displacement due to buckling. The W profile channel exhibited a higher mean crush force of 87 kN, with stable crushing until the considered 200 mm crush distance.
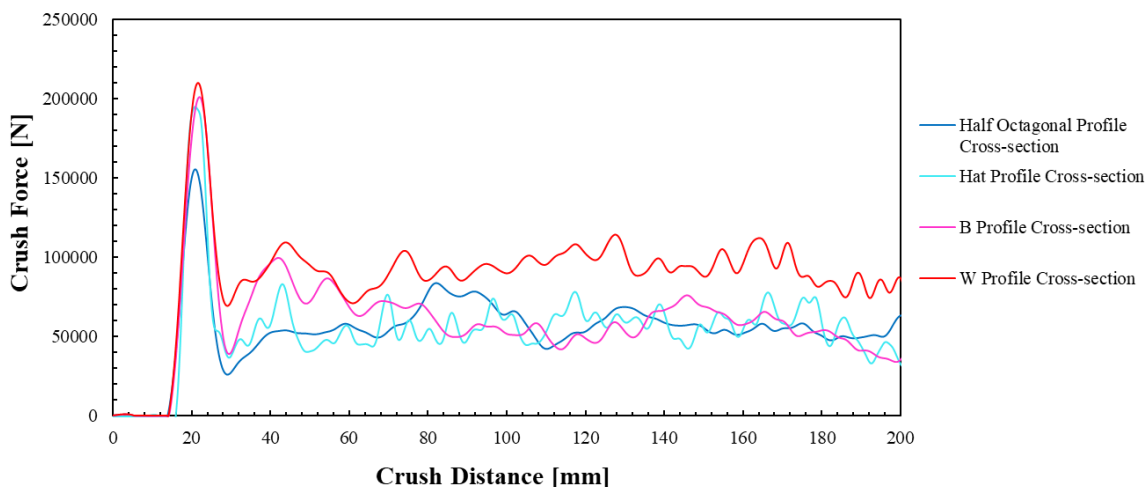
Figure 143. Force vs displacement response for CFRP hat channels (stacking sequence of [0/±45/90]s) with different cross-sectional profiles under dynamic axial crush loading.

The channels with hat and half octagonal profiles absorbed approximately 10 kJ of total energy and 33 J/g of specific energy absorption after a crush distance of 200 mm. The B profile channel absorbed slightly more energy, although a gradual drop in the energy absorption rate was observed after 160 mm of crush distance due to buckling. The channel with a W profile absorbed the most total energy at 18 kJ (Figure 144a) and higher specific energy absorption of 45 J/g (Figure 144b). Increasing the number of radius and edges in the W profile tended to cause more damage in the flanges and corners of cross-section, which improved the energy absorption capabilities. Thus, the W profile was used for the main channel in the

130

reduced-scale technology demonstrator. It should be noted that the W profile channel geometry was designed to be manufacturable using an HP-RTM process.
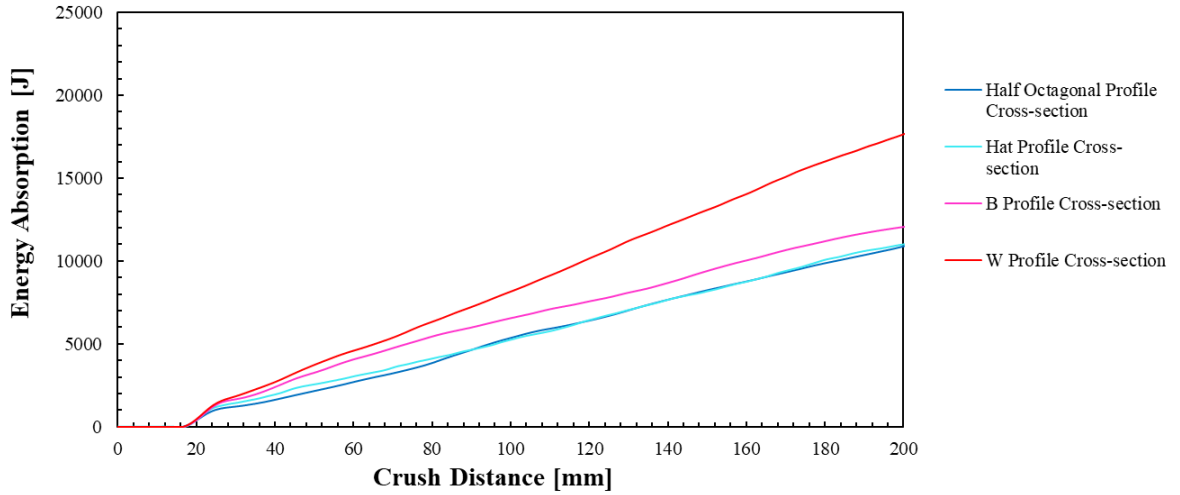
(a)
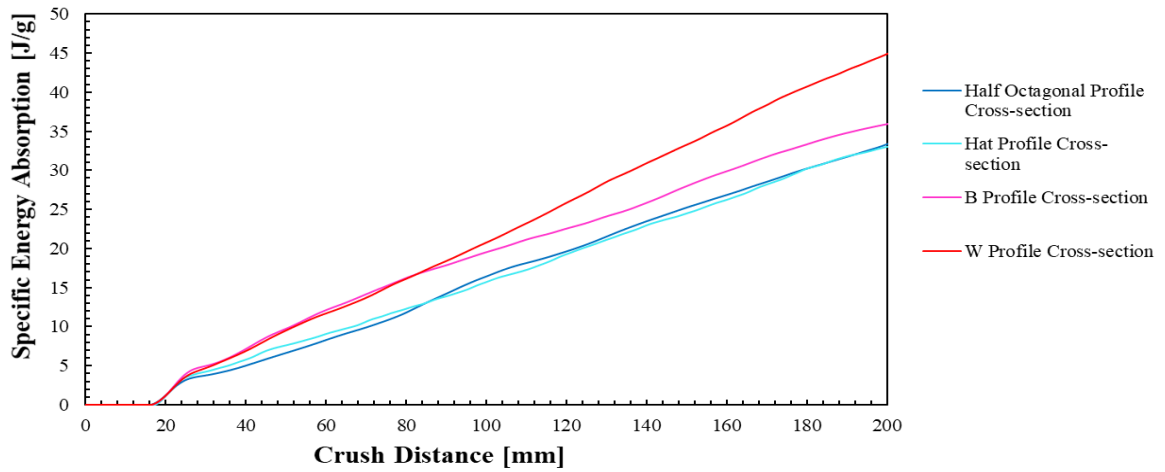
(b)

Figure 144. (a)Energy absorption and (b) specific energy absorption responses for CFRP hat channels (stacking sequence of [0/±45/90]s) with different cross-sectional profiles under dynamic axial crush loading.

7.2 Numerical Results for Technology Demonstrator Design Concepts

The crash performance of the different reduced-scale technology demonstrator design concepts (Section 6.3) are presented in this section. The numerical model described in Sections 6.3-6.6 was utilized for each design concept. The CFRP main channel (W profile) and backing plate (Figure 128) comprised of a laminate stacking sequence of $[0/\pm45/90]_s$ with UD-NCF lamina properties defined in Table 2. For design concept 4 (Figure 127), the lower reinforcement had the same stacking sequence. The calibrated material model MAT 54 was used for all simulations. Dynamic crushing was the only loading condition considered for the technology demonstrator (Figure 141).

7.2.1 Overall Crush Response

For all design configurations, progressive failure of the CFRP main channel and backing plate was predicted until a crush distance of 80 mm (Figure 145). The dominant failure mode in the CFRP components was brittle fragmentation, where element debris was formed upon the sequential progression of the impactor.

At a crush distance of 150 mm, the main channel for design concept 1 failed in shear at the rear end (Figure 145.a). However, for design concepts 2 and 3 shear failure was apparent in the composite channel and backing plate (Figure 145.b and 145.c). Shear failure for design concepts 1-3 was attributed to the lack of load transfer across the lower channel feature and reduced section stability. On the other hand, stable crushing was observed for the main channel and backing plate in design concept 4. The improved crushing response in design concept 4 was attributed to the stable crushing of the straight channel since the lower reinforcement was modelled as a separate part.

At 250 mm of crush distance, the formation of a shear hinge point over the lower area of the channel near the back end transition led to global buckling and shearing in the middle region of the channel for concepts 1-3 (Figure 145.c). The CFRP channel and backing plate for concept 4 continued to undergo stable crushing without any buckling or shear deformation through the entire considered crush distance of 250 mm. The deformation behavior beyond 250 mm of crush distance was not considered since during physical testing of the baseline metallic structure the sled would begin to engage with the arresting honeycomb.

(a) Design Concept 1
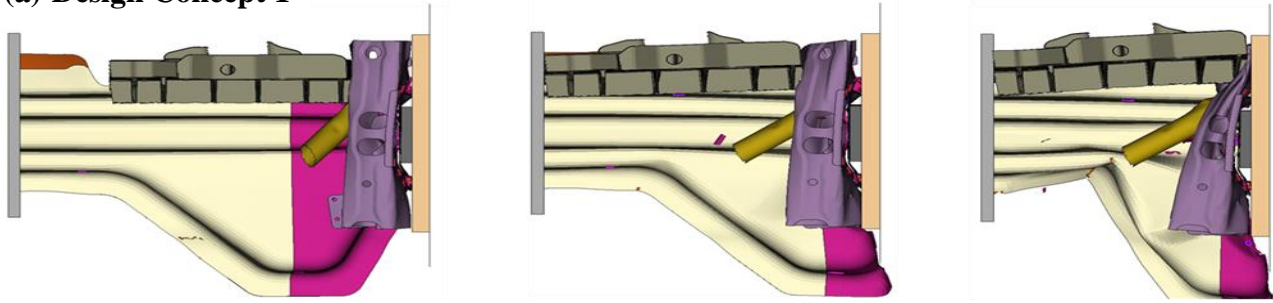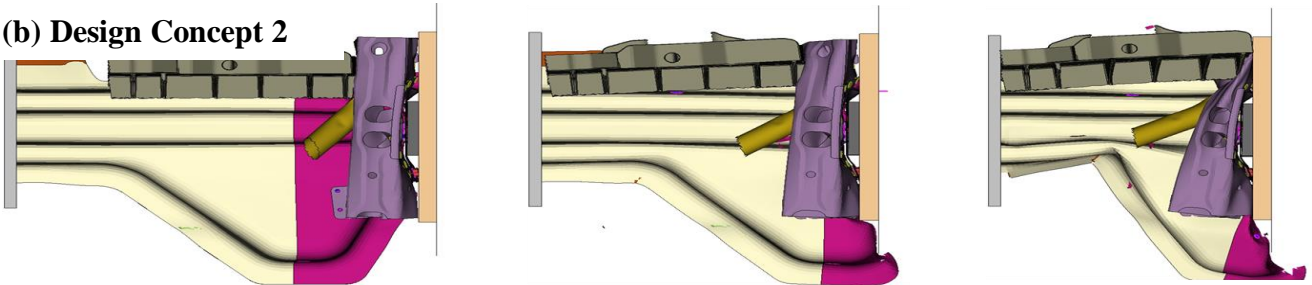
(b) Design Concept 2

(c) Design Concept 3

(d) Design Concept 4

Crush
Distance

80 mm   150 mm   250 mm
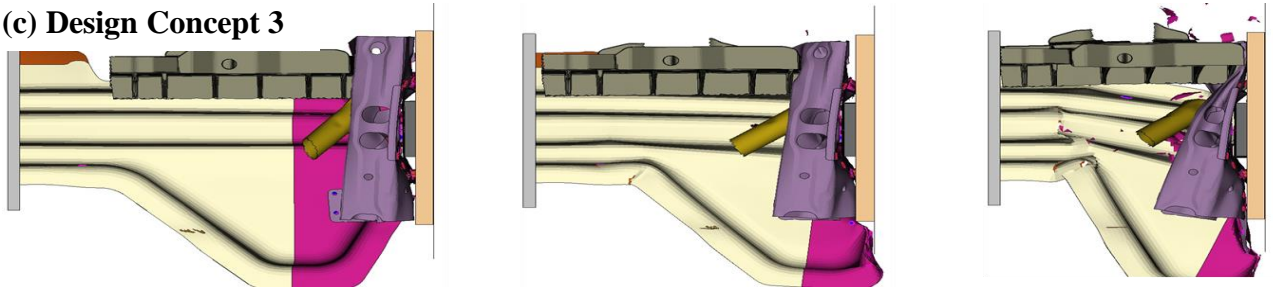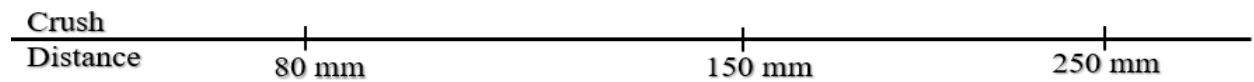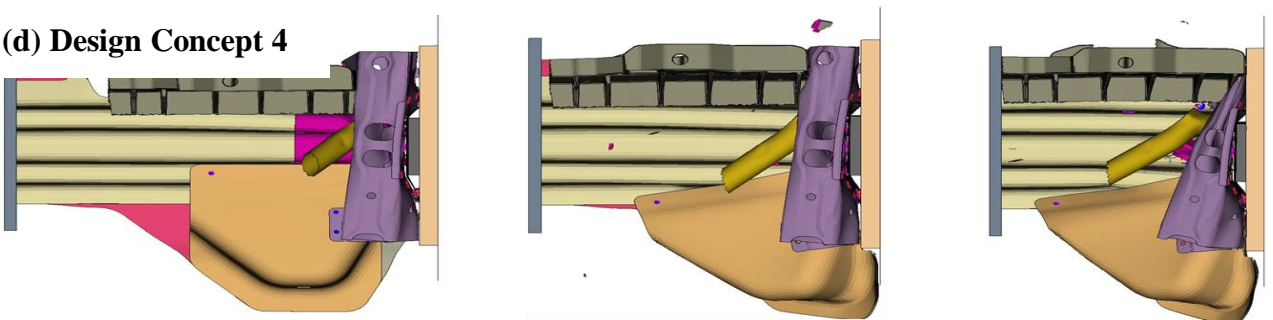
Figure 145. Crush response for different reduced-scale technology demonstrator design concepts, where a side view is shown at different crush distances: (a) design concept 1, (b) design concept 2, (c) design concept 3, and (d) design concept 4.

133

7.2.2 Crush Force-Displacement Response

The crush force from the numerical model was established from the reaction force at the single point constraint (SPC) located at the non-impacting end of the mounting plate. The crush forces predicted for the different design concepts were compared to that of the baseline hot-stamped steel structure (Figure 146). The initial peak force (120 kN) was found to be virtually identical for all demonstrator design concepts as well as the metallic baseline structure. After 30 mm of sled displacement, the CFRP demonstrators exhibited a second peak (180 kN) that was notably higher in magnitude compared to that of the metallic structure, which occurred after 110 mm of crush distance due to plastic folding. The second peak for the composite structures occurred sooner as a result of the interaction between the main CFRP structure and surrounding components forming onset of damage initiation before stable crushing. Beyond the second peak up to a crush distance of 150 mm, the composite demonstrators underwent stable crushing with a fragmentation mode of failure. The magnitude of the average crush force for the composite demonstrators was 115 kN for design concept 4, 99 kN for design concept 2, and 97 kN for design concepts 1 and 3. The variation of magnitude was dependent on the failure behavior of the CFRP components in the demonstrator structures. The average crush force for design concept 4 was 32% higher than the baseline metallic structure (87 kN). In addition, after 250 mm of crush distance, for design concepts 1-3 there was a gradual drop in the reaction forces owing to the formation of shear hinge points over the lower area of the channel near the back end transition. For design concept 4, stable crushing failure was predicted without any drop of reaction forces.
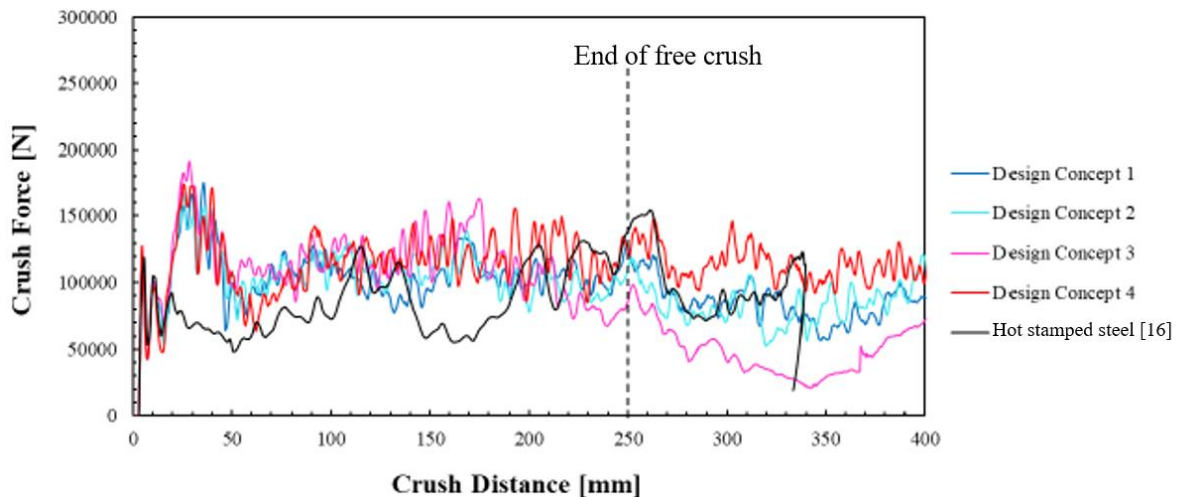
Figure 146. Force vs displacement response for various CFRP reduced-scale technology demonstrators and the baseline hot stamped steel structure.

134

7.2.3 Energy Absorption

The cumulative energy absorption values up to 250 mm of crush distance were calculated for each demonstrator design concept and compared to that of the hot-stamped steel structure (Figure 147). Design concept 4 absorbed the highest amount of energy (28.5 kJ), followed by the design concept 3 (28 kJ) and design concepts 1 and 2 with the same magnitude of energy absorption (26.3 kJ). the total energy absorption for design concept 4 was 34% higher than the metallic structure. Considering the trend of the curves beyond 250 mm of crush distance, concept 1- 3 tends to observe less energy because of buckling and shear whereas utilizing design concept 4 the maximize the energy absorption (45.5 kJ) at 400 mm of crush distance. The design concept 4 demonstrator was regarded as a suitable alternative for replacing the baseline steel structure and was considered for subsequent parametric studies.
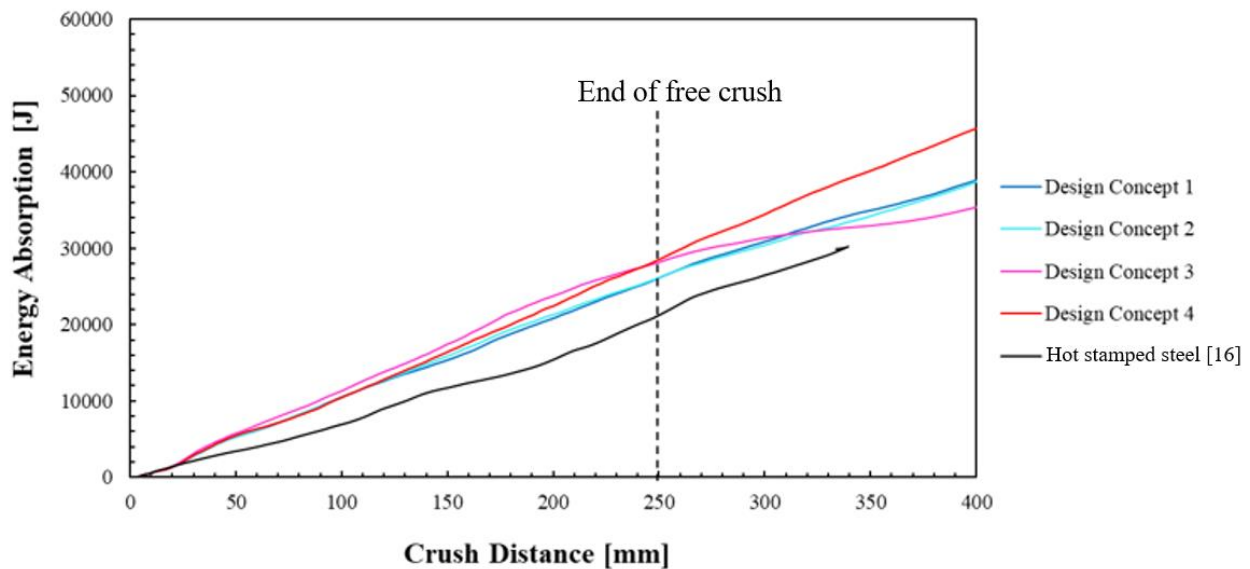
Figure 147. Energy absorption plots for various CFRP reduced-scale technology demonstrators and the baseline hot stamped steel structure.

7.3 Effect of stacking sequence on technology demonstrator performance

The effect stacking sequence on the energy absorbing capabilities of the reduced-scale technology demonstrator was considered to further enhance the impact performance. Variation in the stacking sequence for a laminate under mechanical loading is known to affect the type and sequence of damage mechanisms [138], and thus will also influence the energy absorption characteristics for a laminated structure. The same

numerical model from Section 7.2 was used for design concept 4 with a W profile main channel, where only the stacking sequence was varied. In total, 11 stacking sequences with 8 plies each were considered:

Table 5. Various stacking sequence considered for reduced scale CFRP technology demonstrator.

S. No	Stacking sequence considered
1	$[0/\pm45/90]_s$
2	$[0/90/\pm45]_s$
3	$[\pm45/0_2]_s$
4	$[\pm45_2/0_4]$
5	$[\pm60/0_2]_s$
6	$[\pm55_2/0_4]$
7	$[\pm55/0_2]_s$
8	$[\pm15/\pm45]_s$
9	$[90/\pm15/0]_s$
10	$[0/\pm60/90]_s$
11	$[90/\pm60/0]_s$

7.3.1 Crush Force-Displacement Response

The force-displacement response for the reduced-scale technology demonstrator with different stacking sequences was predicted. The overall profile was similar to that described in Section 7.2 (Figure 148). The average crush force for the demonstrator with a $[0/90/\pm45]_s$ stacking sequence was 9.5% higher (126 kN) than that of the demonstrator with a $[0/\pm45/90]_s$ stacking sequence, while the initial peak force was constant (120 kN). Also, the mean crush force for a demonstrator with a $[90/\pm60/0_2]_s$ stacking sequence was 22% higher (117 kN) than that of the demonstrator with a $[0/\pm60/90]_s$ stacking sequence. A change in the position of 90° plies away from the center of the laminate reduced the effective 90° ply thickness, which influenced the laminate failure process. Placing dominant 0° plies at center of the laminate, instead of at either end, triggered different modes of failure in the composite laminates. The average crush force for the demonstrator with a $[\pm45/0_2]_s$ stacking sequence was 28% higher (137 kN) than that of the demonstrator with a $[\pm45_2/0_4]$ stacking sequence. Placing plies with orientation higher than 45° in the laminate reduced the average crush force of the demonstrator. The average crush force of the demonstrator modeled with a $[\pm45/0_2]_s$ stacking sequence was 13% and 24% higher (137 kN) than that of the demonstrator with $[\pm55/0_2]_s$ and $[\pm60/0_2]_s$ stacking sequences, respectively.

136
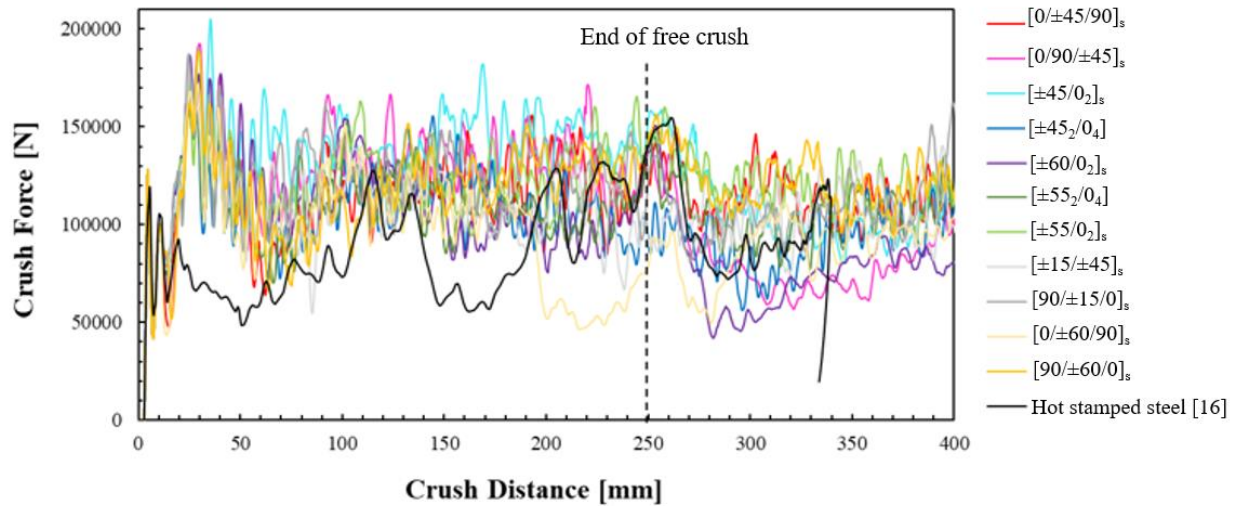
Figure 148. Crush force vs displacement plots for the CFRP reduced-scale technology demonstrator with various stacking sequences and the baseline hot stamped steel structure.

The demonstrator stacking sequence yielding the highest average crush force of 137 kN was $[\pm45/0_2]_s$, which was 57% higher when compared to that of the hot stamped steel structure (87 kN).

7.3.2 Energy Absorption

The energy absorption curves for the demonstrator with each stacking sequence were compared to the hot stamped metal structure (Figure 149). The position of 90° plies greatly influence the energy absorption capabilities of composite laminate. The energy absorbed for the demonstrator with a $[0/90/\pm45]_s$ stacking sequence was 10.5% higher (31.5 kJ) than that of the demonstrator with a $[0/\pm45/90]_s$ stacking sequence. Additionally, the amount energy absorbed for a demonstrator with a $[90/\pm60/0_2]_s$ stacking sequence was 20.5% higher (29.2 kJ) than that of the demonstrator with a $[0/\pm60/90]_s$ stacking sequence. The position of 0° plies at the center increases the laminate stiffness and energy absorption capabilities. The energy absorbed for the demonstrator with a $[\pm45/0_2]_s$ stacking sequence was 28% higher (34.3 kJ) than that of the demonstrator with a $[\pm45_2/0_4]$ stacking sequence. Placing the plies higher than 45° for a stacking sequence reduces the amount of energy absorption with a composite laminate. The energy absorbed for the demonstrator modeled with $[\pm45/0_2]_s$ stacking sequence was 13.5% and 23% higher (34.3 kJ) than that of the demonstrator with a $[\pm55/0_2]_s$ and $[\pm60/0_2]_s$ stacking sequences.

137
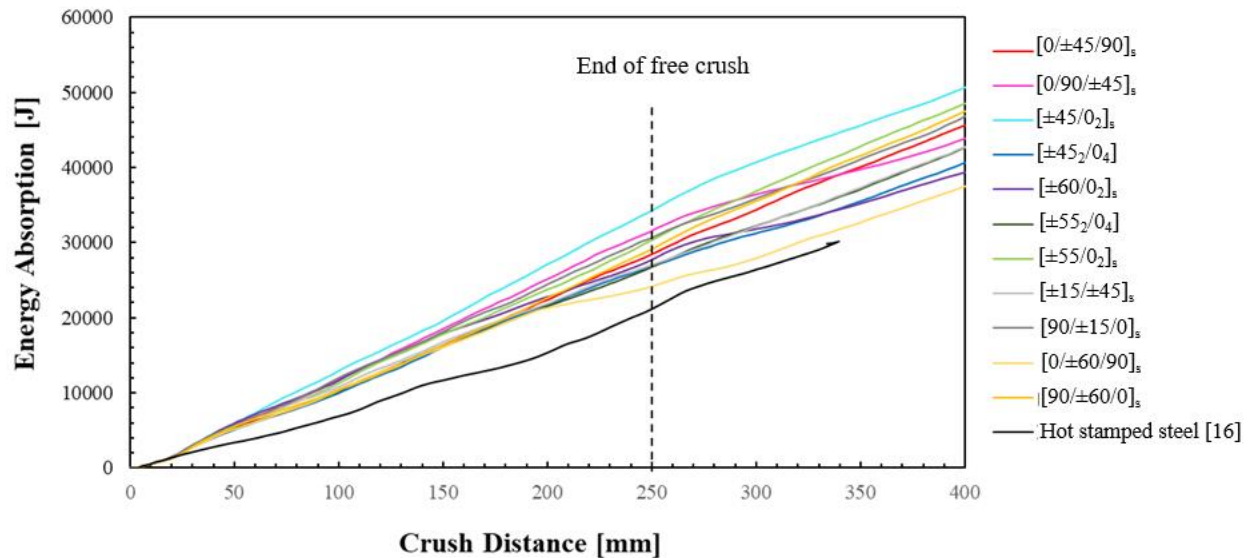
Figure 149. Energy absorption plots for the CFRP reduced-scale technology demonstrator with various stacking sequences and the baseline hot stamped steel structure.

For the stacking sequences considered, the highest and lowest total energy absorbed were 34.3 kJ for the demonstrator with a $[\pm45/0_2]_s$ laminate and 24.2 kJ for with a $[0/\pm60/90]_s$ laminate, respectively (Figure 150). These laminates produced a total absorbed energy for the demonstrator that were 14% and 60% greater than the hot stamped steel structure, respectively. In general, the crash performance of the composite technology demonstrator can be improved by using more plies in the laminate with orientation angles less than 45°, and by placing the 0° layers at the center of the laminate. Placing plies with orientations greater than 45° at the center of laminate sequence increases the damage formation and decreases the overall stiffness of the laminate. Consider the $[0/\pm60/90]_s$ laminate, by placing 60° and 90° layers at the center of the laminate led to low energy absorption prediction when compared to the demonstrator with other stacking sequences.
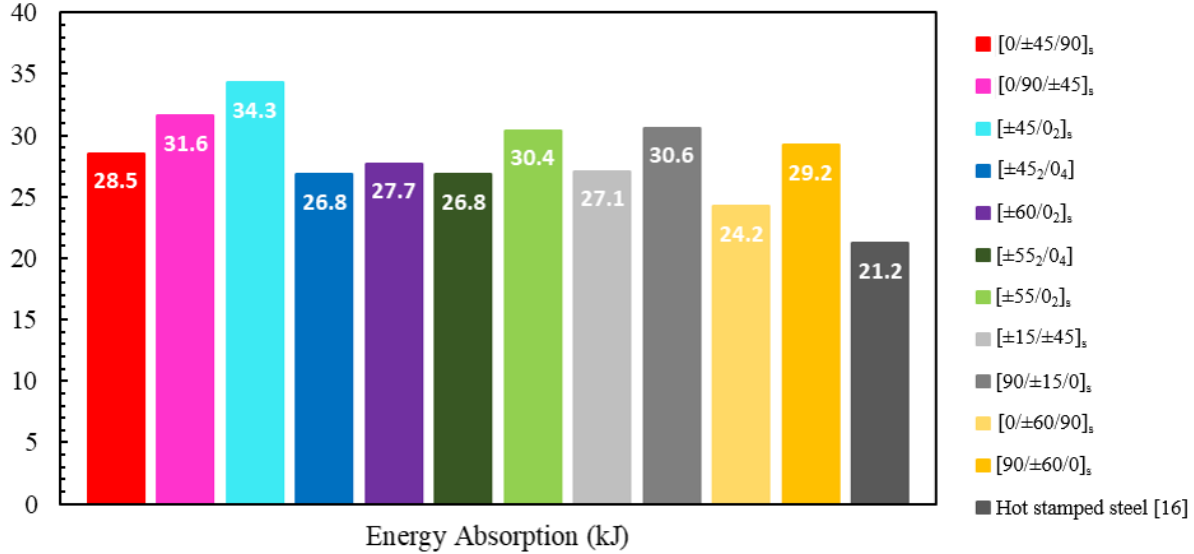
Figure 150. Comparison of total energy absorption for the CFRP reduced-scale technology demonstrator with various stacking sequences and the baseline hot stamped steel structure.

7.4 Effect of laminate thickness on technology demonstrator performance

In this Section, the numerical study on the effect of increasing total laminate thickness on the impact performance of the reduced-scale technology demonstrator is presented. The same numerical model from Section 7.3 was used, where only the total laminate thickness (and possibly the stacking sequence) was varied for the main hat channel, and backing plate.

7.4.1 Effect of laminate bending stiffness

Bending stiffness is an important parameter to consider while designing the thickness and stacking sequence of the laminate for a component. Charles et al.[139]reported that the bending stiffness of a laminated composite material used for a side frame member should be maintained more than 960 Nmm to prevent intrusion in the occupant region. The longitudinal bending stiffness (D_{11}) values for the laminates considered were calculated using Equation 2.15 (Table 5).

139

Table 6. Calculated laminate bending stiffness values.

Simulation Number	Number of layers	Laminate Thickness (mm)	Laminate stacking sequence	Laminate bending stiffness, D_{11} (Nmm)
Sim-1	8 Layers	2.7	$[0/\pm45/90]_s$	147.1
Sim-2	8 Layers	2.7	$[\pm45/0_2]_s$	208.4
Sim-3	12 Layers	4.0	$[0/90/\pm30/\pm60]_s$	394.2
Sim-4	12 Layers	4.0	$[90/0_2/\pm60/0]_s$	423.2
Sim-5	14 Layers	4.7	$[90/\pm25/\pm45/0_2]_s$	658.4
Sim-6	16 Layers	5.4	$[\pm15/\pm60/\pm15_2]_s$	1101

7.4.2 Overall Crush Response

Images of the reduced-scale technology demonstrator at different crush distances for simulations with the different stacking sequences considered are shown in Figures 151 and 152. An increase in the number of plies in the laminate for the CFRP parts increased the structural rigidity of the demonstrator. Until a crush distance of 150 mm, stable crushing behavior was observed for all the laminate configurations. Progressive crushing with a brittle fragmentation mode occurred in the crush region of the main channel. At 250 mm of displacement, the predicted crush response notably varied for demonstrators with different laminate stacking sequences (i.e., different laminate bending stiffness). For Sim-1 and Sim-2 (8 Plies) and Sim-3 and Sim-4 (12 Plies), a stable crush behavior propagating to the middle region was predicted beyond 250 mm of displacement. For Sim-5 (14 Plies), the structure was more rigid compared to the demonstrators with the other stacking sequences, which resulted in arresting of the impactor and complete kinetic energy absorption after 280 mm. For Sim-6 (16 Plies), the rigidity of the demonstrator was higher and complete kinetic energy absorption occurred after 238 mm of sled displacement. The presence of high laminate bending stiffness and impact resistance by the demonstrators in Sim-5 and Sim-6 resulted in severe compression of the plywood in the front region. Finally, it was deemed that the laminate stacking sequences considered in Sim-5 and Sim-6 resulted in a structure that resisted force and may be suitable for the intrusion resistance zone of the chassis frame member.
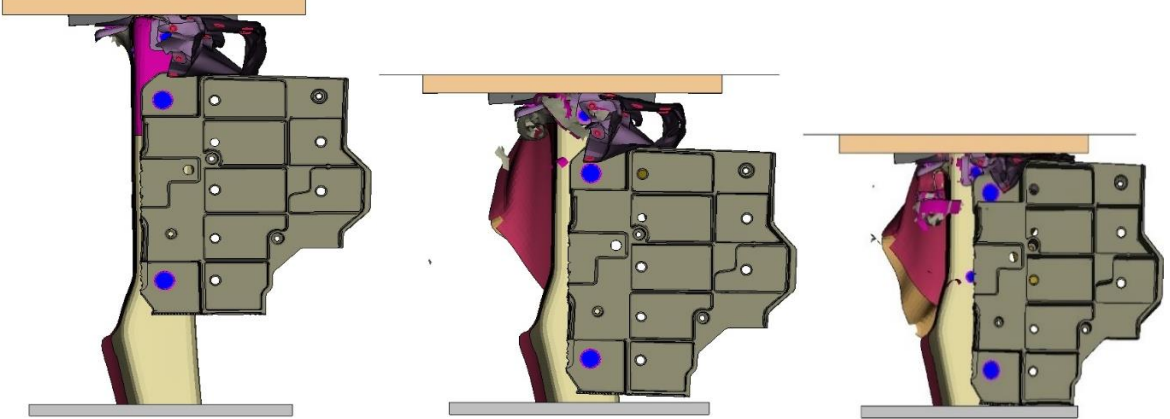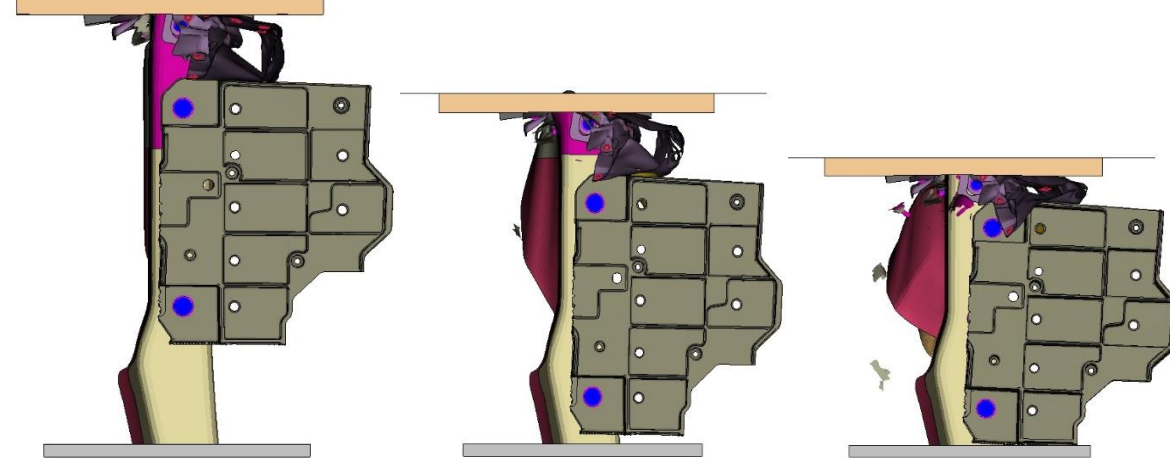
Figure 151. Crush response of reduced-scale technology demonstrator with different laminate thicknesses shown at different crush distances: (a) Sim 1, (b) Sim 2, (c) Sim 3.

Sim – 4 : 12 Plies
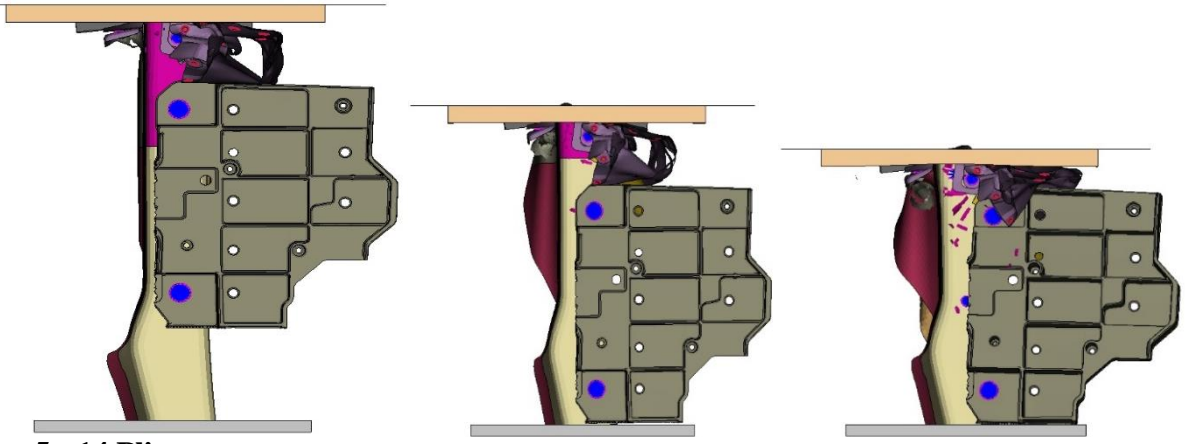
Sim – 5 : 14 Plies

Sim – 6 : 16 Plies

Crush
Distance

80 mm   150 mm   250 mm
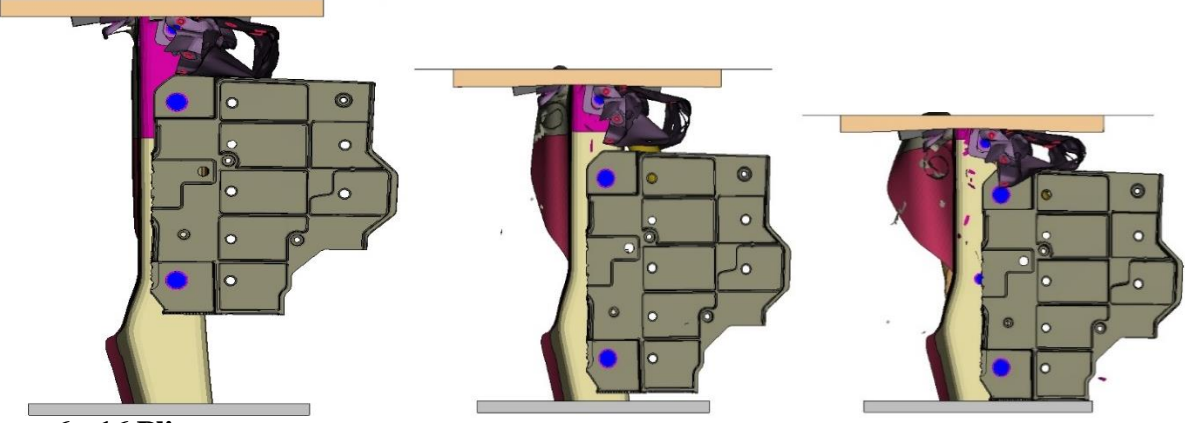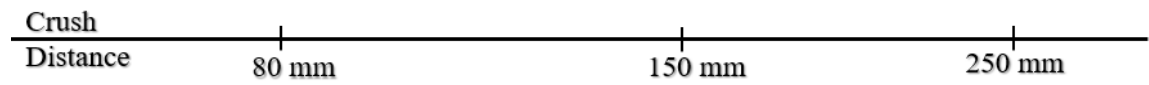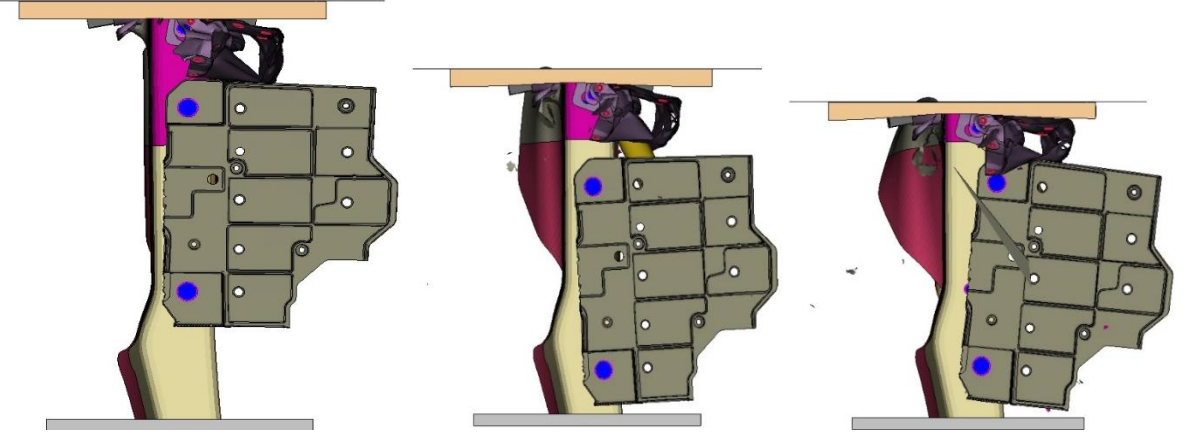
Figure 152. Crush response of reduced-scale technology demonstrator with different laminate thicknesses shown at different crush distances: (a) Sim 4, (b) Sim 5, (c) Sim 6.

142

7.4.3 Crush Force-Displacement Response

The force-displacement response revealed that for technology demonstrators with increasing laminate thickness an increase in the average crush force was predicted (Figure 153). The initial peak of the demonstrators remained unchanged with increasing the laminate thickness or number of plies in composite specimens. A significant difference was observed with the second peak, which increased as the laminate thickness increased. The 12-layer composite structure was observed to form second peak (~ 300 kN) between 20 and 50 mm of sled displacement, while the second peak load for the 14-layer and 16-layer composite structure were 410 kN and 550 kN, respectively (Figure 153). Also, the predicted average crush force for the 16-layer (305 kN) and 14-layer (275 kN) demonstrators were notably higher than the other demonstrators. These results are not surprising, since an increase in laminate thickness increases the strength and stiffness of the composite structure.
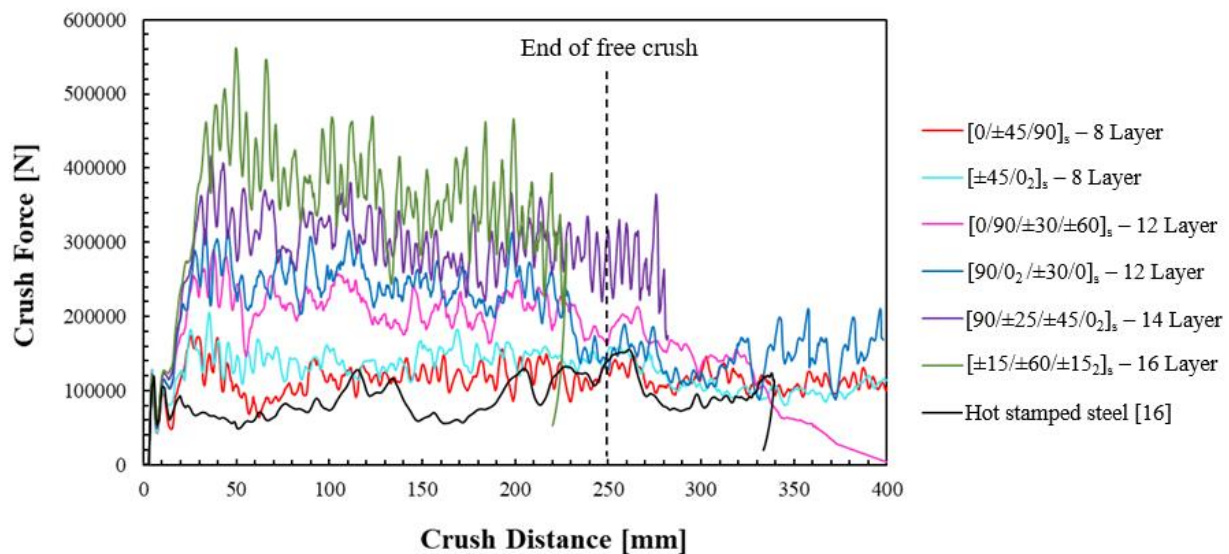
Figure 153. Crush force vs displacement plots for the CFRP reduced-scale technology demonstrator with various laminate thicknesses and stacking sequences and the baseline hot stamped steel structure.

7.4.4 Energy Absorption

The predicted cumulative energy absorption was also found to increase with increasing laminate thickness (Figure 154). The total absorbed energy for the composite technology demonstrator after 250 mm of crush distance was 79.2 kJ for 16-layers (after 238 mm of crush distance), 71.8 kJ for 14-layers, 51 or

56 kJ for 12-layers, and 34.3 or 28.5 kJ for 8-layers (Figure 154). The predicted energy absorption of all the configurations was higher than the baseline metallic structure.
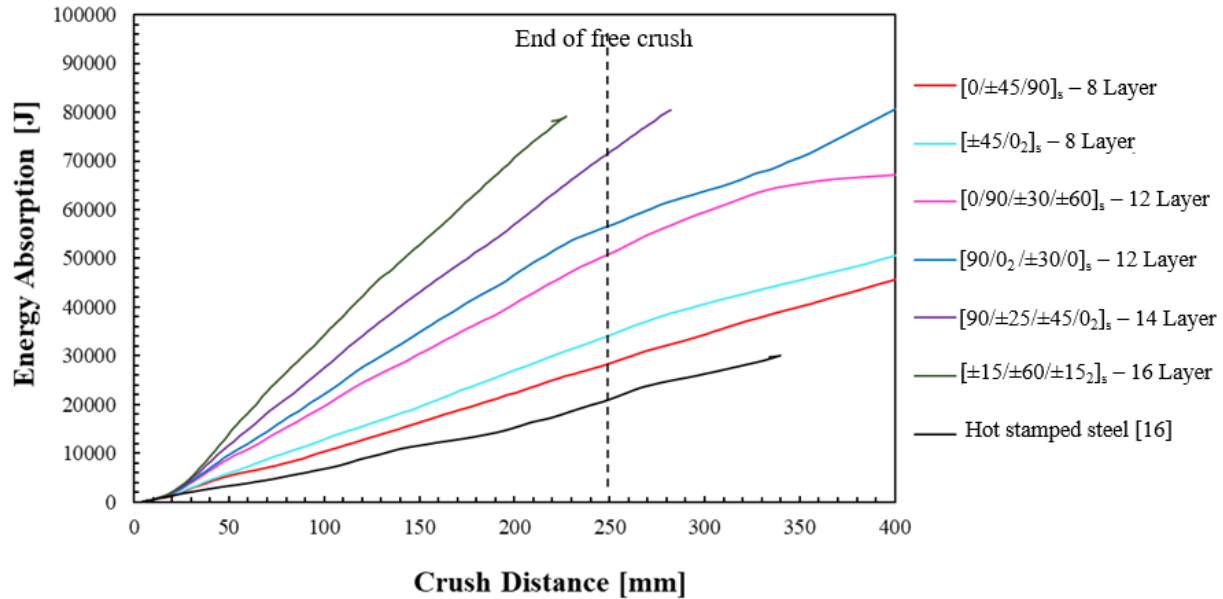
Figure 154. Energy absorption plots for the CFRP reduced-scale technology demonstrator with various laminate thicknesses and stacking sequences and the baseline hot stamped steel structure.

7.4.5 Deceleration Profile

The deceleration profile of the crash sled during impact with the composite technology demonstrator was compared to that of the hot stamped metal structure (Figure 155). Overall, there was a notable difference in the deceleration profile for the composite and metallic structures. However, after 250 mm of crush distance the kinetic energy for the metallic structure significantly reduced due to contact of the sled with the honeycomb structure. Recall, for the composite demonstrator models the honeycomb was not represented, which led to a higher predicted crush force and slower deceleration profile after 250 mm of sled displacement. It was observed that the deceleration profile for the composite structure with a laminate comprised of 8 layers was consistent up to 250 mm of displacement. The composite structures with the stiffer 16 layers and 14 layers decelerated to zero after 238 mm and 280mm of sled displacement, respectively, which was sooner than the metallic structure (Figure 155).

144
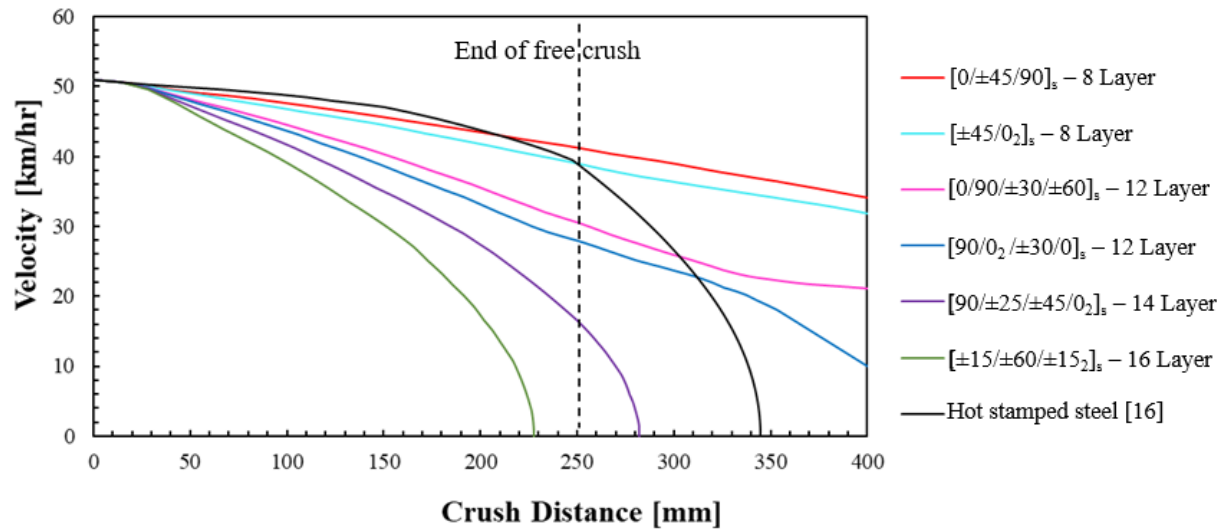
Figure 155. Deceleration profile for the CFRP reduced-scale technology demonstrator with various laminate thicknesses and stacking sequences and the baseline hot stamped steel structure.

7.5 Numerical results for the variable thickness demonstrator

Recall that a chassis side frame member functions as an energy absorbing component as well as an intrusion resistant component to protect the occupants from injury. Thus, the crush tip of the side frame member must undergo stable crush and absorb energy, while the middle section and rear end (i.e., S-rail) must have a high structural rigidity to prevent displacement of the chassis component beyond the automotive firewall region. In this study, a ply drop-off method was utilized to develop composite technology demonstrator concepts to achieve the desired response. The crush zone of the technology demonstrator CFRP main channel and backing plate was modelled with 8 plies over a length of 200 mm, while and the middle region was modelled with 14 or 16 plies (Table 6). The lower reinforcement was modeled with 8 plies and laminate stacking sequences of $[0/\pm45/90]_s$. The same numerical model from Section 7.3 was used, where only the total laminate thickness (and possibly the stacking sequence) was varied.

145

Table 7. Stacking sequence in both regions of the main hat channel and backing plate components.

Simulation Number	Number of layers - crush zone	Number of layers - intrusion zone	Stacking sequence - crush zone	Stacking sequence – intrusion zone
Ply drop off #1	8 Layers	14 Layers	$[0/\pm45/90]_s$	$[0_2/\pm45/90/0_2]_s$
Ply drop off #2	8 Layers	16 Layers	$[0/\pm45/90]_s$	$[0_2/\pm45/90/0_3]_s$
Ply drop off #3	8 Layers	16 Layers	$[0/\pm45/90]_s$	$[0/\pm45/90/\pm15_2]_s$

7.5.1 Overall Crush Response

The crush behavior of the composite technology demonstrator structures was numerically evaluated. It was observed that progressive crushing (Figure 156) with fragmentation mode of failure was achieved for each configuration.

146

Ply drop off #1 : 8 + 14 Plies
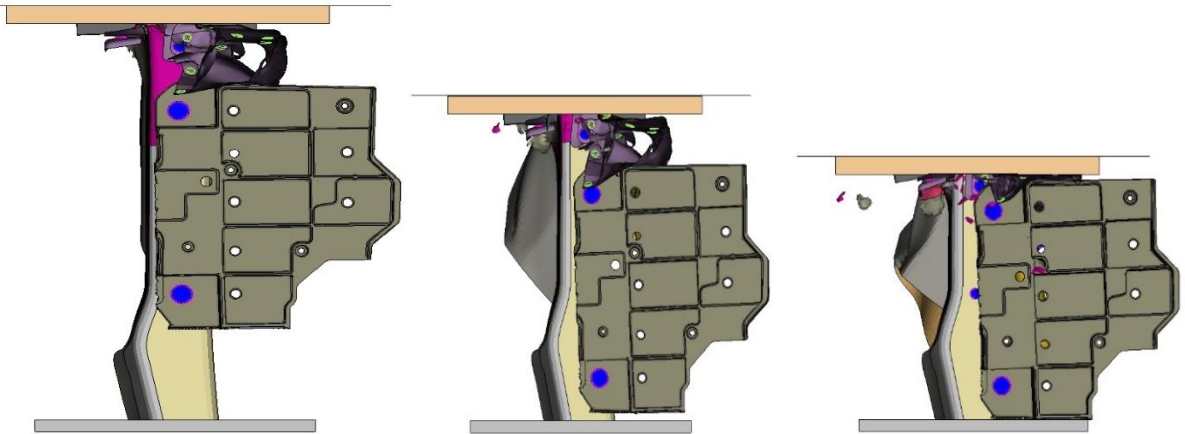
Ply drop off #2 : 8 + 16 Plies
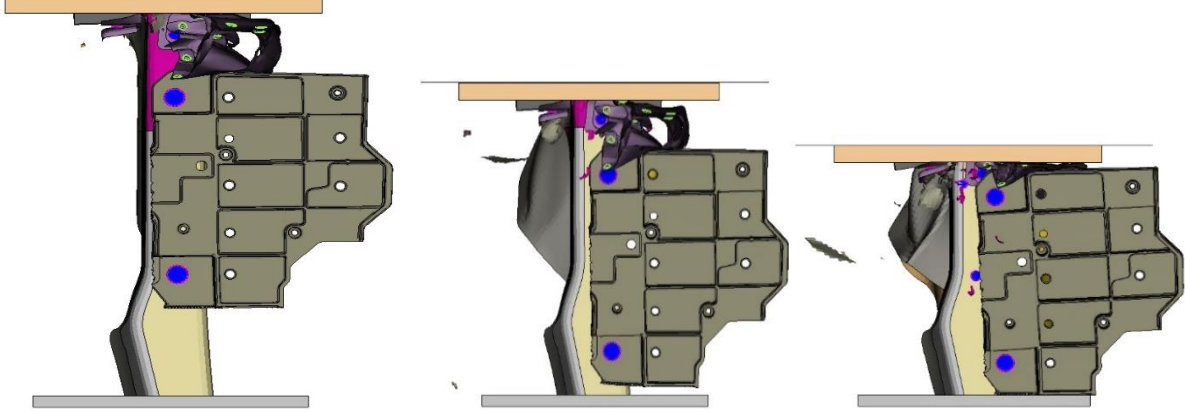
Ply drop off #3 : 8 + 16 Plies

Crush
Distance   80 mm   150 mm   250 mm

Figure 156. Crush response for the CFRP reduced-scale technology demonstrator with different ply drop-off configurations, shown from top view: (a) ply drop off #1, (b) ply drop off #2, (c) ply drop off #3.

147

7.5.2 Crush Force-Displacement Response

The composite technology demonstrator structures exhibited three peak reaction forces (Figure 157). The initial peak and the second peak, which was predicted at 30 mm of sled displacement (185 kN) during crushing of the 8-layer channel region, were consistent for all configurations. The third peak was consistently observed at 200 mm of sled displacement (i.e., middle zone) where the transition from 8 layers to increased laminate thickness was implemented. The magnitude of the third force peak was > 440 kN and caused by the increased laminate stiffness and part rigidity. The average crush force for the ply drop off models was notably higher when compared to the hot-stamped steel structures.
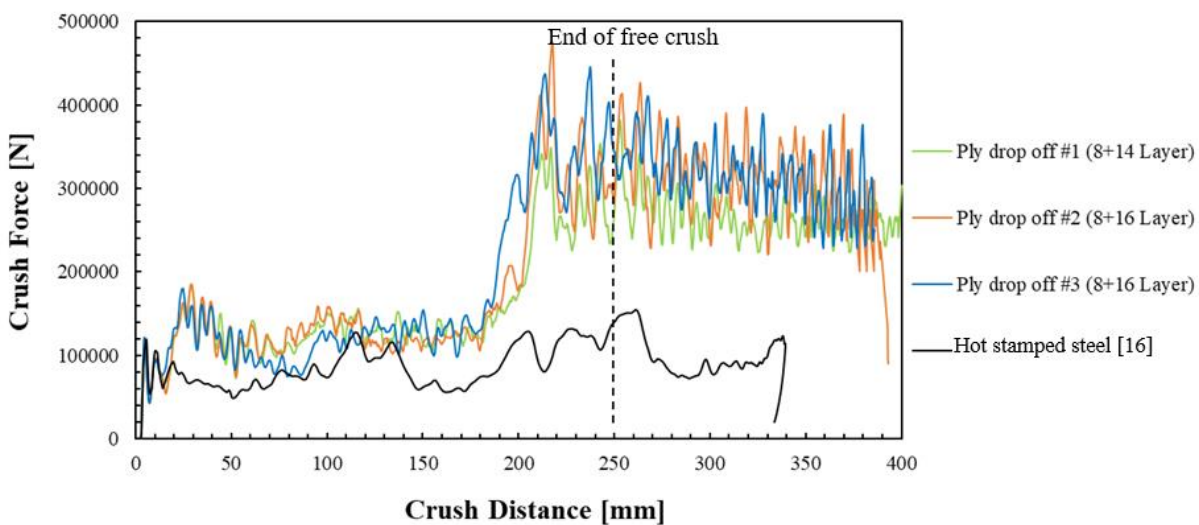
Figure 157. Crush force vs displacement for the CFRP reduced-scale technology demonstrator with different ply drop-off configurations and the baseline hot stamped steel structure.

7.5.3 Energy Absorption

Energy absorption curves for the ply drop off technology demonstrator models were compared to that of the hot stamped steel structure (Figure 158). The major transition point for all ply drops off models occurred at 200 mm of crush distance, which corresponded to the ply transition location. The predicted total energy absorption after 200 mm of crush distance was 40 kJ for the ply drop-off models, which is more than double that of the baseline metallic structure.

148
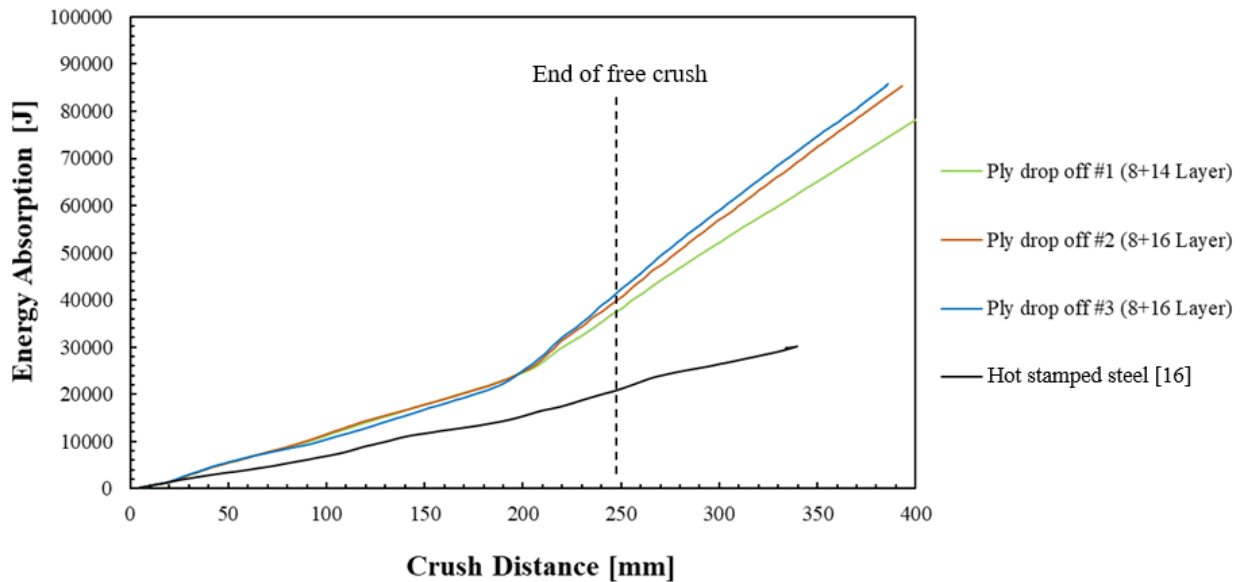
Figure 158. Energy absorption for the CFRP reduced-scale technology demonstrator with different ply drop-off configurations and the baseline hot stamped steel structure.

7.5.4 Deceleration Profile

The predicted deceleration profile of the sled during crushing of the composite demonstrator was compared to the hot stamped steel structure (Figure 159). With 8 plies in the crush region, the deceleration profile for the composite structures up to 250 mm of displacement was almost identical to that of the metallic structure (within 10%). Beyond 250 mm, the deceleration profile of the composite structures deviated from the metallic structure due to honeycomb activation (not modeled for the composite structures). This variation led to the prediction of a slower deceleration profile for the composite demonstrator. The functionality of composite crush rail of the chassis structure beyond 250 mm was qualitatively assessed and compared to the data of the baseline steel structure reported in Ref.[16]. The baseline steel structure model predicted full deceleration between 420 to 430 mm of sled distance. Nevertheless, the composite ply drop-off models #2 and model #3 was able to decelerate the sled kinetic energy to zero between 380 to 400 mm of sled displacement.

149
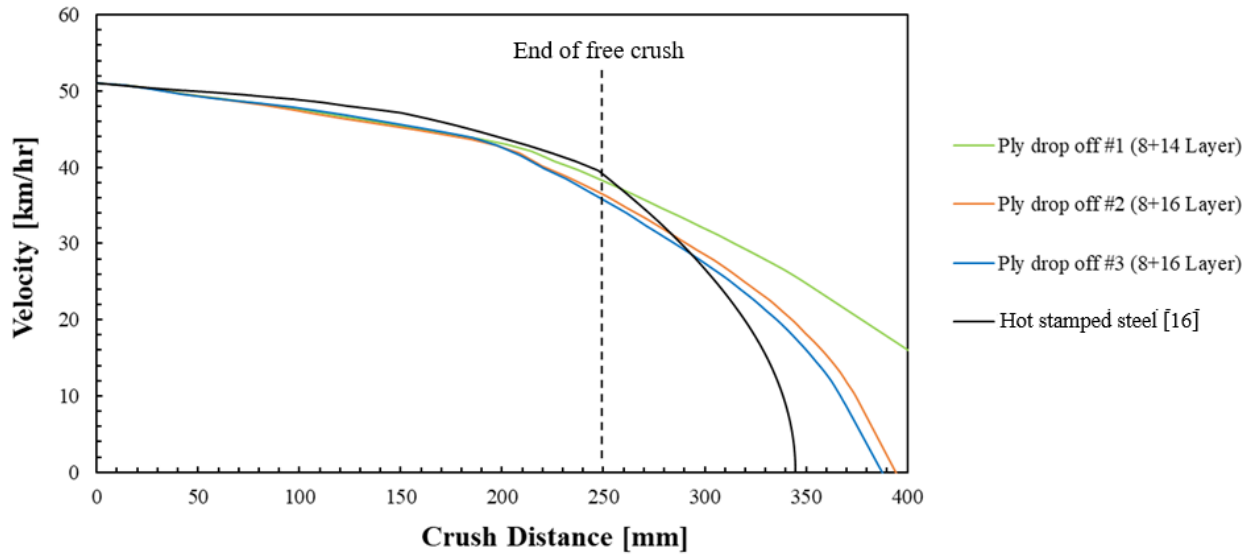
Figure 159. Deceleration profile for the CFRP reduced-scale technology demonstrator with different ply drop-off configurations and the baseline hot stamped steel structure.

Overall, the results indicate that the multilayered NCF composite laminate is a promising substitution for the conventional steel structure in terms of velocity history and energy absorption capabilities. By utilizing a reduced thickness laminate for the crush zone of the hat channel and higher thickness for intrusion zone, composite components can be tailored for automotive frontal crash applications.

Chapter 8

Discussions

8.1 Material models for numerical simulation of hat channel components

The non-physical parameters for two lamina-level material models considered in the developed single shell element numerical simulation model were calibrated using existing axial crush data for a CFRP hat channel component with $[0/\pm45/90]_s$ laminate stacking sequence under dynamic loading conditions [77]. It is important to note that although MAT 54 and MAT 58 have few calibration parameters and are relatively simple to use, the requirement to calibrate the non-physical parameters using component level test data is a main limitation. The predictions of the numerical simulation models are highly sensitive towards the selection of the material card non-physical parameter values (Chapter 5). The calibrated models were subsequently validated using additional axial crush test data for the same hat channel components with a different laminate stacking sequence ($[\pm45/0_2]_s$) under dynamic loading, and further for the case of quasi-static loading conditions for both stacking sequences [77]. Since validation of the material model was performed using the same part geometry and loading case (i.e., axial crush), the calibrated material model non-physical parameters may not be suitable for other cases. It has been reported that several existing material models must be recalibrated for different part geometries, loading cases and laminate stacking sequences [101].

Furthermore, recall that a single layer of shell elements was used in the numerical model to represent the thin laminates for computational efficiency, without considering delamination cracking. This led to discrepancies in the force-displacement response for the axial crush simulation under quasi-static loading for the hat channel with $[\pm45/0_2]_s$ stacking sequence (Figure 110). The experimentally observed splaying failure mode that is driven by delamination cracking was not modeled. Another consequence of using shell elements to model the laminate was that the representation of the trigger geometry using a reduced thickness shell element was not representative of the hat channel components (Figure 54). This may have caused the trigger elements to fail later than expected providing higher resistance than the actual trigger geometry. This limitation allows the delayed onset of damage and progressive crushing with high initial peak force.

Despite the identified limitations, when using the calibrated material models the developed numerical simulation models predicted the overall deformation response and cumulative energy absorption profile of the NCF CFRP laminated hat channels under axial crush loads (Section 5.6). The prediction accuracy for simulations using MAT 54 was highly dependent on mesh pattern and element size (Section 5.3), which is

likely due to the fact that the material model does not account for damage evolution and instead uses a simplified 'residual stress' approach for laminae. On the other hand, MAT 58 is a continuum damage mechanics-based model that models pre-peak and post-peak damage evolution for laminae. The predictions for the hat channel geometry using MAT 58 were not dependent on mesh pattern and somewhat dependent on the element size (Section 5.5). Furthermore, the MAT 54 simulations model was able to capture the brittle fragmentation failure mode that was experimentally observed for the hat channel specimens under dynamic axial crushing loads, while the MAT 58 simulation model predicted an unzipping behaviour (Figure 160). This may be due to deficiency in the modulus reduction law implemented in MAT 58 to capture the post-peak response, as well as the elemental erosion scheme, which influenced the load distribution and the deformation modes. This led to an over estimation of the initial peak force and underpredicted energy absorption capacity for the MAT 58 simulation model. However, under dynamic loading rates, the numerical model using MAT 54 was able to predict the axial crush behavior and energy absorption with good accuracy. Under quasi-static rates, the MAT 54 simulation model predicted failure of the component and the crashworthiness parameters with improved accuracy compared to the MAT 58 simulation model. Overall, MAT 54 was a more suitable material model for the studied hat channel components when compared to MAT 58. A similar conclusion was previously reported in the literature [11],[105][108].
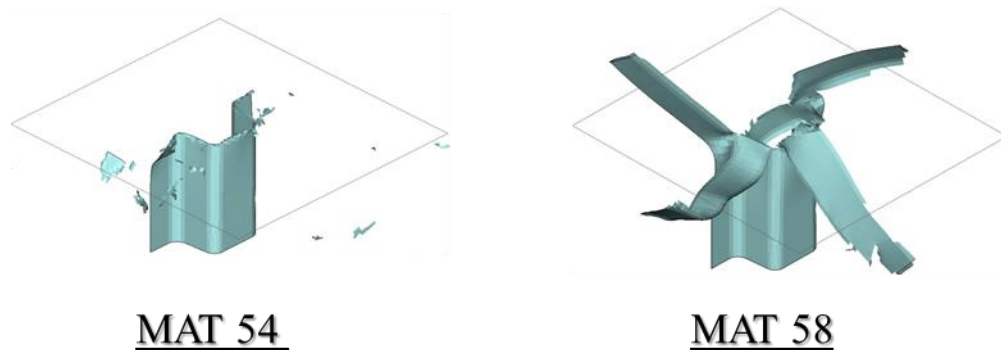
Figure 160. Axial crush response of hat channel specimens under quasi-static loading condition with layup 1 [0/±45/90]$_s$ for both MAT 54 and MAT 58 material models. Images correspond to the 200 mm crush distance during the simulation.

8.2 Comparison of CFRP and Baseline Steel Technology Demonstrators

One of the main objectives of this thesis was to design a reduced-scale side frame member technology demonstrator comprised of a CFRP laminated crush channel, using the validated numerical model. The crash performance of the designed technology demonstrator was compared to a similar hot-stamped steel structure developed by Tummers [16] (Figure 161).

<div align="center">a   b</div>
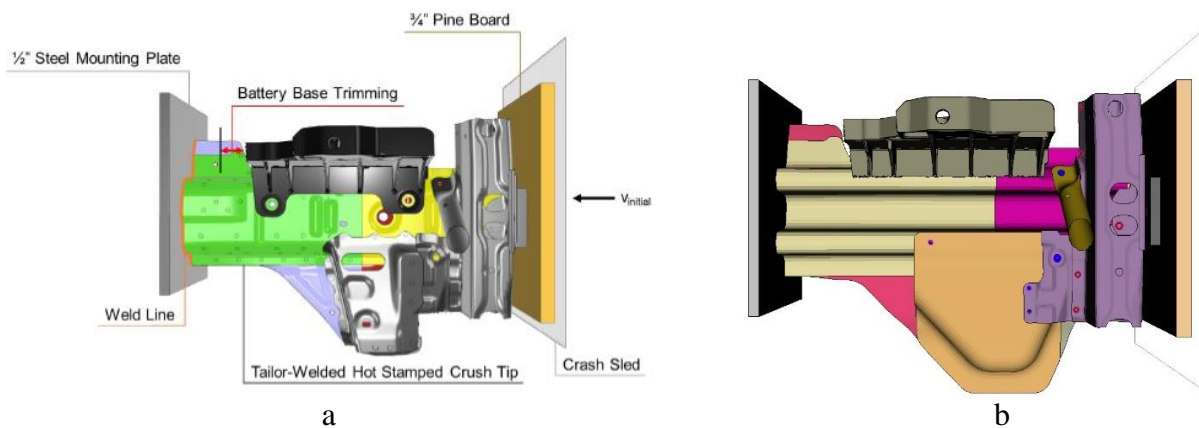
Figure 161. Numerical model comparison of reduced scale chassis side frame (a) baseline hot stamped steel [16] (b) UD-NCF composite assembly.

The side frame is the primary load carrying member usually designed as single part (metal as tailor welded part). The straight main channel designs without discontinuities were necessary to maximize the load transfer and energy absorption of crush rail (i.e., Design concept 4). The discontinuity triggered a weak zone with unusual buckling reducing the functionality of the crush rail. One of the main outcomes of the technology demonstrator design process was to gauge the relative performance of the structure for different stacking sequences, total laminate thicknesses and variations in the thickness along the CFRP main channel (Sections 7.3-7.5), which ultimately led to improved crash performance for the final design concept. The force-displacement response (Figure 162) and energy absorption data (Figure 163) of the technology demonstrator with $[0/\pm45/90]_s$ stacking sequence (8 plies) and ply-drop off (model #3) were compared to the hot stamped steel structure up to 250 mm of sled displacement.

The numerical results of the technology demonstrator with $[0/\pm45/90]_s$ stacking sequence (8 Plies) was similar to the hot stamped steel model with the increased second peak force and average crush force. This may be due to interaction of CFRP main parts with surrounding structures and position of plies in the

<div align="center">153</div>

stacking sequence. On placing plies less than 45° and 0° plies at the center improves the axial stiffness of the composite laminate which maximize the mean crush force and energy absorption of composite component. However, the results of ply drop off model predicted a similar trend, with the third peak formed at 200 mm of crush distance. This high third peak was caused from increased laminate stiffness and part rigidity. These high magnitude of third peak (440 kN) has a high possibility to cause injuries to the passengers during crash applications. However, the laminate stiffness should be optimized to avoid the potential injuries caused by the sudden high peaks in the force response. In addition to the weight savings, the amount of energy absorbed of the technology demonstrator with [0/±45/90]$_s$ stacking sequence (8 Plies) and Ply-drop off model (model #3) were higher than the hot stamped steel structure.
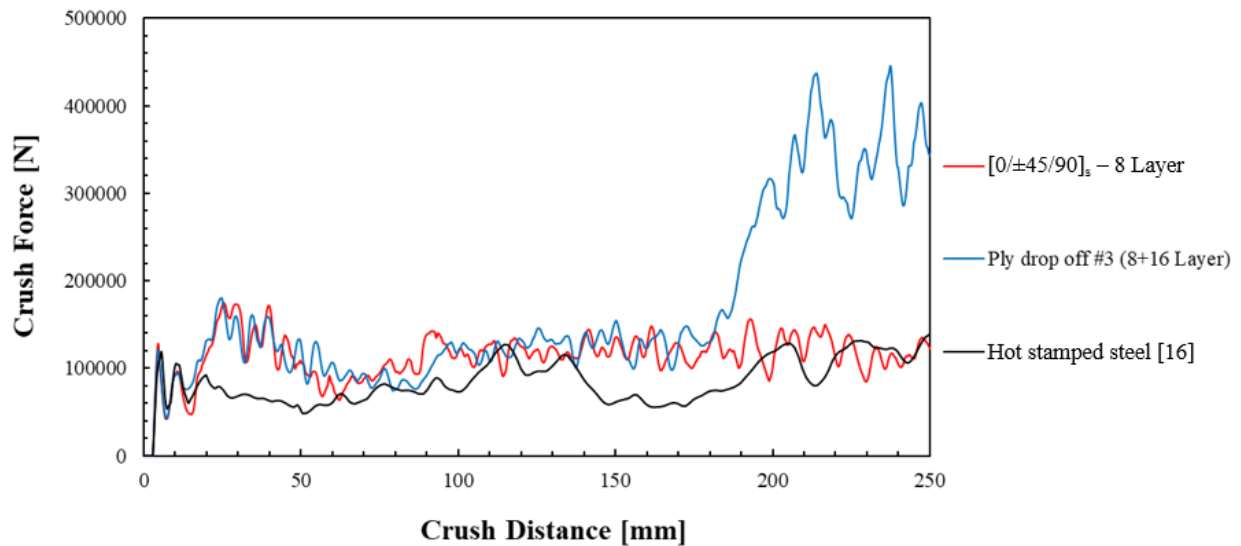
Figure 162. Comparison of crush force of constant thickness and ply drop off numerical models to hot stamped steel.

154
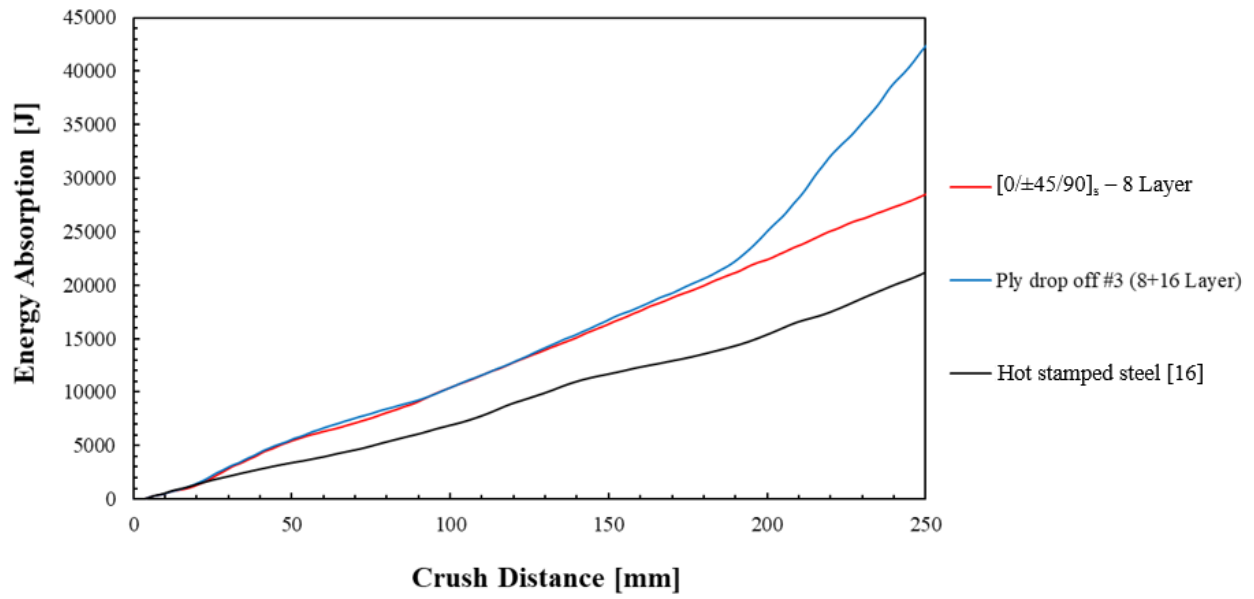
Figure 163. Comparison of energy absorption of constant thickness and Ply drop off numerical models to hot stamped steel.

Chapter 9
Conclusions

The overall aim of this thesis was to assess the feasibility of integrating CFRP non-crimp fabric (NCF) carbon fiber-reinforced plastic (CFRP) composite materials into the frontal energy absorbing structures of high-volume production light duty vehicles (LDV). A numerical modeling approach utilizing existing material models in the commercial finite element software LS-DYNA, namely MAT 54 and MAT 58, was developed to predict the axial crush response of an NCF CFRP composite straight hat channel component fabricated using a high pressure resin transfer molding (HP-RTM) process. The non-physical parameters of the material models were calibrated using available axial crush experimental data for the hat channels, and subsequently used to predict the axial crash response of similar hat channels under quasi-static and dynamic loading conditions. The validated numerical model was used to design a reduced-scale CFRP vehicle frontal crush structure technology demonstrator, and the crash simulation results were compared with that of a similar baseline steel structure that was available in the literature. The following conclusions were drawn from this research thesis.

- The single element numerical models were simulated with two distinct material models to represent the constitutive response of a lamina. The post-peak response of both material models was greatly influenced by non-zero values of the SLIM parameters.

- For hat channel simulations, the non-physical parameters in MAT 54 model, namely fiber compressive strain to failure (DFAILC), residual stress parameters (SLIMC1 and SLIMS) and softness reduction factor (SOFT), greatly influenced the crush response. MAT 58 model utilizes the same non-physical parameter values as MAT 54; however, erosion parameter (ERODS) and residual stress parameter (SLIMC1) primarily influences the predicted crush response.

- The results of the numerical predictions were correlated well with the existing hat channel experiments in two different loading rates (quasi-static and dynamic) and two different stacking sequences ($[0/\pm45/90]_s$ and $[\pm45/0_2]_s$). The numerical results of the MAT 54 model had improved accuracy, able to capture the crush response and crashworthiness metrics of the composite channel. However, the MAT 58 model overpredicted the initial peak force and underpredicted the average crush force and energy absorption. This limitation may have been caused by the modulus reduction laws utilized with the post-peak response of the lamina.

156

- The validated material model (MAT 54) was implemented to analyze the crash performance of the composite technology demonstrator. The W channel developed with an increased number of edges and radii produced the high stiffness and energy absorption characteristics, while being suitable for the main channel of the automotive side frame. The technology demonstrator model designed with separate parts (design concept 4: main channel and lower reinforcement part) exhibited a high amount of energy absorption at 28 kJ for 250 mm of crush distance.

- The stacking sequence and ply position greatly influenced the energy absorption characteristics of the composite technology demonstrator. Modeling the laminate sequence with plies less than 45° and 0° plies at center increased the axial stiffness and energy absorption of composite specimens. A minimum of 24 kJ ($[0/\pm60/90]_s$) and a maximum of 34 kJ ($[\pm45/0_2]_s$) energy absorption was achieved by modifying the ply orientation and position in the stacking sequence. Moreover, increasing the number of plies or thickness resulted in a stiffer response and increased the structural rigidity of the composite technology demonstrator.

- The technology demonstrator modelled with reduced thickness in the crush region and increased thickness in the middle region allowed a considerable weight savings of 29% (1.6 kg) corresponding to the hot stamped metallic structures with 81% increased energy absorption. Comparing with the baseline metallic, the composite demonstrator was 48% (3.7 kg) lighter.

- Ultimately, the composite technology demonstrator was concluded to be an excellent replacement for the conventional metallic structures. Additionally, the developed technology demonstrator reduces the 3 component conventional steel structures to 2 components.

9.1 Recommendations for future work

The following recommendations should be considered for future work:

- One of the observed failure modes for the hat channel axial crush experiments was splaying, which was not modelled in the numerical simulations. To possibly improve the predictive capabilities of the numerical model, a multi-layered shell approach with cohesive elements may be considered for the hat channel model.

- The material models considered for the numerical simulations were MAT 54 and MAT 58. However, other material models such as MAT 261, MAT 262, and MAT 213 (still in development) with reduced number of non-physical parameters should be further evaluated. The results of the numerical predictions are highly influenced by the lamina/laminate failure schemes in the material model; thus, this should be investigated further for all material models considered. Also, the strain rate sensitivity of the lamina material was not considered in this thesis and should be considered in future numerical studies.

- To potentially improve the predictive capabilities of the simulation models, the use of a non-local averaging scheme for modelling failure of plies and laminates can be investigated.

- Draping simulations for each component can be used to provide improved accuracy for the fiber orientation throughout the components. By mapping the fiber orientation angle for the crash components may increase the accuracy of numerical predictions.

- The numerical predictions of the composite technology demonstrator performed in this thesis revealed that the CFRP material was a suitable substitute for the conventional steel. However, experimental testing is required to validate the numerical predictions. Also, the full vehicle simulation with composite technology demonstrator is recommended to understand the performance of LDV in crash energy management applications.

- The numerical simulations of the composite technology demonstrator revealed that the supporting components surrounding the CFRP rail component became disconnected during progressive crushing. Thus, the current design may not be feasible in practice. It is recommended to investigate the front bumper beam assembly design to ensure that proper engagement with the CFRP rail is maintained during crushing.

- The establishment of composites for automotive structures require topological optimization, where the addition of ribs, thickness variations, and ply stacking combinations can be used to further improve the crush performance and light-weighting of composites structures. It is suggested that the usage of adhesive in addition to the bolt fixing improves the failure caused by surrounding structures.

- A full-frontal crash with the New Car Assessment Program (NCAP) testing condition was considered in this thesis. It is recommended to also evaluate the offset frontal crash configuration, which is a more challenging load condition for the CFRP technology demonstrator and may require further design optimization. Also, the performance of composite primary chassis frames in different crash configurations based on regulations such as Federal Motor Vehicle Safety Standards (FMVSS), Insurance Institute of Highway Safety (IIHS), European New Car Assessment Program (ENCAP) should be considered to further ensure the suitability of composites for crash energy management.

References

[1]. "Obama Administration Finalizes Historic 54.5 MPG Fuel Efficiency Standards | whitehouse.gov." [Online]. Available: https://obamawhitehouse.archives.gov/the-press-office/2012/08/28/obama-administration-finalizes-historic-545-MPG-fuel-efficiency-standard. [Accessed: 16-Jul-2020].

[2]. U. D. M.Ghosh, "The road ahead, National Highway Traffic Safety Administration, Report," 2016.

[3]. "Canada to copy Obama's fuel efficiency rules - The Globe and Mail." [Online]. Available: https://www.theglobeandmail.com/report-on-business/industry-news/energy-and-resources/canada-to-copy-obamas-fuel-efficiency-rules/article4508608/. [Accessed: 16-Jul-2020].

[4]. "BMW 7 Series Plant: Dingolfing, Germany | CompositesWorld." [Online]. Available: https://www.compositesworld.com/articles/bmw-7-series-plant-dingolfing-germany. [Accessed: 16-Jul-2020].

[5]. O. US EPA, "Final Rule for Model Year 2017 and Later Light-Duty Vehicle Greenhouse Gas Emissions and Corporate Average Fuel Economy Standards."

[6]. Roland Berger GmbH, "Automotive metal components for car bodies and chassis," *Glob. Mark. study*, no. February, p. 39, 2017.

[7]. S. Das, D. Graziano, V. K. K. Upadhyayula, E. Masanet, M. Riddle, and J. Cresko, "Vehicle lightweighting energy use impacts in U.S. light-duty vehicle fleet," *Sustain. Mater. Technol.*, vol. 8, pp. 5–13, Jul. 2016.

[8]. W. Joost, "Reducing Vehicle Weight and Improving U.S Energy Efficiency Using Integrated Computational Material Engineering," the Journal of the Minerals, vol. 64, no. 9, pp. 1032-1038, Mar. 2012

[9]. J. C. Kelly, J. L. Sullivan, A. Burnham, and A. Elgowainy, "Impacts of Vehicle Weight Reduction via Material Substitution on Life-Cycle Greenhouse Gas Emissions," *Environ. Sci. Technol.*, vol. 49, no. 20, pp. 12535–12542, Oct. 2015.

[10]. G. Zhu, G. Sun, H. Yu, S. Li, and Q. Li, "Energy absorption of metal, composite and metal/composite hybrid structures under oblique crushing loading," *Int. J. Mech. Sci.*, vol. 135, no. November, pp. 458–483, 2018.

[11]. A. Cherniaev and J. Montesano, "Thin-Walled Structures Predicting the axial crush response of CFRP tubes using three damage-based constitutive models," vol. 129, no. February, pp. 349–364, 2018.

[12]. J. Starke, "Carbon Composites in Automotive Structural Applications .," *BMW Gr.*, no. March, p. 22, 2016.

[13]. "Audi A8: steel makes a comeback." [Online]. Available: https://automotive.arcelormittal.com/news_and_stories/cases/2017AudiA8comebacktosteel. [Accessed: 16-Jul-2020].

[14]. N. Highway Traffic Safety Administration and U. Department of Transportation, "Mass Reduction for Light-Duty Vehicles for Model Years 2017-2025: Peer Review Comments Log," 2018.

[15]. P. Rosenberg, B. Thoma, P. F. Henning, F. C. Technologie, I. Fahrzeugsystemtechnik, and K. Institut, "Characterization of Epoxy and Polyurethane Resin Systems for Manufacturing of High - Performance Composites in High - Pressure Rtm Process," *SPE Automot.*, no. September, pp. 1–18, 2015.

[16]. M. Tummers, "Development of a Tailor-Welded Hot Stamped Side Frame Member," MASc thesis, University of Waterloo, Canada, 2019.

[17]. M. Nishi, K. Saito, and B. Ren, "Discrete FE modeling to simulate micro-fracture

modes in progressive crushing of fiber reinforced composite tubes," *ECCM 2018 - 18th Eur. Conf. Compos. Mater.*, no. July, 2019.

[18]. G. L. Farley and U. S. Army, "Crushing Characteristics of Continuous Fiber-Reinforced Composite Tubes," no. 1, pp. 37–50, 1992.

[19]. H. Hamada *et al.*, "Comparison of energy absorption of carbon/epoxy and carbon/PEEK composite tubes," *Compo*, vol. 23, no. 4, pp. 245–252, 1992.

[20]. V. M. Karbhari and J. E. Haller, "Rate and architecture effects on progressive crush of braided tubes," *Compos. Struct.*, vol. 43, no. 2, pp. 93–108, Oct. 1998.

[21]. C. Liebold, A. Haufe, T. Klöppel, S. Hartmann, and D. Gmbh, "Recent developments and trends for composite modeling in LS-DYNA Fachkongress Composite Simulation," no. February 2015, 2015.

[22]. R. Rolfes, M. Vogler, S. Czichon, B. Kriegesmann, H. Krüger, and E. Jansen, "State of the Art in Simulation of Composite Structures," *LS-Dyna Forum*, 2011.

[23]. A. Kaw, *Mechanics of composite materials*. 2005.

[24]. C. T. Herakovich, *Mechanics of fibrous composites*. New York: Wiley, 1998.

[25]. B. Agarwal, L. Broutman, and K. Chandrashekhara, *Analysis and performance of fiber composites*. 2017.

[26]. "Composite Reinforcements for Optimum Performance - 2nd Edition." [Online]. Available: https://www.elsevier.com/books/composite-reinforcements-for-optimum-performance/boisse/978-0-12-819005-0. [Accessed: 16-Jul-2020].

[27]. K. Vanclooster, S. V. Lomov, and I. Verpoest, "Experimental validation of forming simulations of fabric reinforced polymers using an unsymmetrical mould configuration," Composites Part A: Applied Science and Manufacturing, vol. 40, no. 4, pp. 530–539, Apr. 2009. [26] Horrocks AR, Anand SC. Handbook of technical textiles. 2000.

doi:10.1533/9781855738966.

[28].   A. Cherniaev, Y. Zeng, D. Cronin, and J. Montesano, "Quasi-static and dynamic characterization of unidirectional non-crimp carbon fiber fabric composites processed by HP-RTM," *Polym. Test.*, 2019.

[29].   E.A. Trejo Sandoval, "Characterizing the deformation response of a unidirectional non-crimp fabric for the development of computational draping simulation models," MASc thesis, University of Waterloo, Canada, 2020.

[30].   K. Chawla, *Composite materials: science and engineering*. 2012.

[31].   D. Magagnato and F. Henning, "RTM formfüllsimulation für unidirektional ver-stärkte faserverbundbauteile unter berück-sichtigung der lokalen faserorientierung und des faservolumengehalts," *Zeitschrift Kunststofftechnik/Journal Plast. Technol.*, vol. 2016, no. 3, pp. 135–156, 2016.

[32].   C. Liebold, A. Haufe, and S. Hartmann, "Integrative simulation for short and continuous fiber reinforced composites DYNAmore – The Company," pp. 1–26, 2016.

[33].   P. Maimí, P. P. Camanho, J. A. Mayugo, and C. G. Dávila, "A continuum damage model for composite laminates: Part II - Computational implementation and validation," *Mech. Mater.*, vol. 39, no. 10, pp. 909–919, Oct. 2007.

[34].   B. D. Agarwal, L. J. Broutman, and K. Chandrashekhara, *ANALYSIS AND PERFORMANCE OF FIBER COMPOSITES THIRD EDITION*. 2006.

[35].   S. T. Pinho, C. G. Dávila, P. P. Camanho, L. Iannucci, and P. Robinson, "Failure Models and Criteria for FRP Under In-Plane or Three-Dimensional Stress States Including Shear Non-Linearity," 2005.

[36].   L. Grauers, R. Olsson, and R. Gutkin, "Energy absorption and damage mechanisms in progressive crushing of corrugated NCF laminates: Fractographic analysis," *Compos. Struct.*,

2014.

[37].   E. M. Á.-F. TN and undefined 1998, "Characterization of impact damage in composite laminates."

[38].   "DEPARTMENT OF DEFENSE HANDBOOK COMPOSITE MATERIALS HANDBOOK VOLUME 3. POLYMER MATRIX COMPOSITES MATERIALS USAGE, DESIGN, AND ANALYSIS AMSC N/A AREA CMPS DISTRIBUTION STATEMENT A. Approved for public release; distribution unlimited," 2002.

[39].   L. Khoun and S. Bournival, "Impact Behaviour of Thin Carbon Fibre Reinforced Composites Components for Automotive Applications," *SPE Automot. Compos. Conf. Exhib. 2015, Novi, MI*, pp. 1–24, 2015.

[40].   S. W. Tsai and E. M. Wu, "A General Theory of Strength for Anisotropic Materials," *J. Compos. Mater.*, vol. 5, no. 1, pp. 58–80, Jan. 1971.

[41].   H. M. Deuschle and A. Puck, "Application of the Puck failure theory for fibre-reinforced composites under three-dimensional stress: Comparison with experimental results," *J. Compos. Mater.*, vol. 47, no. 6–7, pp. 827–846, Mar. 2013.

[42].   A. Puck and H. Schürmann, "Failure analysis of FRP laminates by means of physically based phenomenological models," *Compos. Sci. Technol.*, vol. 58, no. 7, pp. 1045–1067, Jul. 1998.

[43].   A. Puck and M. Mannigel, "Physically based non-linear stress-strain relations for the inter-fibre fracture analysis of FRP laminates," *Compos. Sci. Technol.*, vol. 67, no. 9, pp. 1955–1964, Jul. 2007.

[44].   G. A. O. Davies and X. Zhang, "Impact damage prediction in carbon composite structures," *Int. J. Impact Eng.*, vol. 16, no. 1, pp. 149–170, Feb. 1995.

[45].   L. Ma and D. Liu, "Delamination and fiber-bridging damage analysis of angle-ply

laminates subjected to transverse loading," *J. Compos. Mater.*, vol. 50, no. 22, pp. 3063–3075, Sep. 2016.

[46].   S. A. Muflahi, G. Mohamed, and S. R. Hallett, "Investigation of Delamination Modeling Capabilities for Thin Composite Structures in LS-DYNA®."

[47].   O. Shor and R. Vaziri, "Through-Thickness Element Splitting for Simulation of Delamination in Laminated Composite Materials," *13th Int. LS-DYNA Users Conf.*, pp. 1–10, 2014.

[48].   R. Borg, L. Nilsson, and K. Simonsson, "Simulation of low velocity impact on fiber laminates using a cohesive zone based delamination model," *Compos. Sci. Technol.*, vol. 64, no. 2, pp. 279–288, 2004.

[49].   C. Mcgregor, S. Mcclennan, R. 1, F. Ellyin, A. Poursartip, and A. Bouamoul, "ALIREZA FORGHANI."

[50].   M. Ilyas, F. Lachaud, C. Espinosa, and M. Salaün, "Dynamic delamination of aeronautic structural composites by using cohesive finite elements," 2009.

[51].   G. Kay, "Simulations of carbon fiber composite delamination tests," 2007.

[52].   "Standard Test Method for Mode I Interlaminar Fracture Toughness of Unidirectional Fiber-Reinforcced Polymer Matrix Composite," ASTM International, Tech. Rep., 2013.

[53].   "Standard Test Method for Mode II Interlaminar Fracture Toughness of Unidirectional Fiber-Reinforcced Polymer Matrix Composite," ASTM International, Tech. Rep., 2014.

[54].   M. Loikkanen, G. Praveen, and D. Powell, "10 th International LS-DYNA ® Users Conference Simulation of Ballistic Impact on Composite Panels 10 th International LS-DYNA ® Users Conference."

[55].   S. T. W. Lau, M. R. Said, and M. Y. Yaakob, "On the effect of geometrical designs and failure modes in composite axial crushing: A literature review," *Compos. Struct.*, vol. 94,

no. 3, pp. 803–812, 2012.

[56].   D. Liu, "Impact-Induced Delamination—A View of Bending Stiffness Mismatching," *J. Compos. Mater.*, vol. 22, no. 7, pp. 674–692, Jul. 1988.

[57].   S. A. Hitchen and R. M. J. Kemp, "The effect of stacking sequence on impact damage in a carbon fibre/epoxy composite," *Composites*, vol. 26, no. 3, pp. 207–214, Mar. 1995.

[58].   K. F. Nilsson, L. E. Asp, and A. Sjögren, "On transition of delamination growth behaviour for compression loaded composite panels," *Int. J. Solids Struct.*, vol. 38, no. 46–47, pp. 8407–8440, Nov. 2001.

[59].   R. Olsson, L. Asp, S. Nilsson, and A. Sjögren, "A Review of Some Key Developments in the Analysis of the Effects of Impact Upon Composite Structures," in *Composite Structures: Theory and Practice*, ASTM International, 2008, pp. 12-12–17.

[60].   P. Du Bois *et al.*, "VEHICLE CRASHWORTHINESS AND OCCUPANT PROTECTION."

[61].   B. P. Bussadori, K. Schuffenhauer, and A. Scattina, "Modelling of CFRP crushing structures in explicit crash analysis," *Compos. Part B Eng.*, vol. 60, pp. 725–735, 2014.

[62].   H. Kamel Ibrahim, *Design Optimization of Vehicle Structures for Crashworthiness Improvement*. 2009.

[63].   J. J. Carruthers, A. P. Kettle, and A. M. Robinson, "Energy absorption capability and crashworthiness of composite material structures: A review," *Appl. Mech. Rev.*, vol. 51, no. 10, pp. 635–649, Oct. 1998.

[64].   D. Hull, "A unified approach to progressive crushing of fibre-reinforced composite tubes," *Compos. Sci. Technol.*, vol. 40, no. 4, pp. 377–421, Jan. 1991.

[65].   G. C. Jacob, J. F. Fellers, J. M. Starbuck, and S. Simunovic, "Crashworthiness of Automotive Composite Material Systems," 2004.

[66]. A. Hallal, A. Elmarakbi, A. Shaito, and H. El-Hage, *Overview of Composite Materials and Their Automotive Applications*. 2013.

[67]. M. Okano, A. Nakai, and H. Hamada, "Axial crushing performance of braided composite tubes," *Int. J. Crashworthiness*, vol. 10, no. 3, pp. 287–294, 2005.

[68]. J. Obradovic, S. Boria, and G. Belingardi, "Lightweight design and crash analysis of composite frontal impact energy absorbing structures," *Compos. Struct.*, 2012.

[69]. G. Bames, I. Coles, R. Roberts, D. O. Adams, D. M. . J. Gamer, and J. A. V. N. T. S. C. (U.S.), "CRASH SAFETY ASSURANCE STRATEGIES FOR FUTURE PLASTIC AND COMPOSITE INTENSIVE VEHICLES (PCIVs) Final Report," United States. National Highway Traffic Safety Administration, Jun. 2010.

[70]. M. David and A. F. Johnson, "Effect of strain rate on the failure mechanisms and energy absorption in polymer composite elements under axial loading," *Compos. Struct.*, vol. 122, pp. 430–439, Apr. 2015.

[71]. L. Lampani, "Finite element analysis of delamination of a composite component with the cohesive zone model technique," *Eng. Comput. (Swansea, Wales)*, vol. 28, no. 1, pp. 30–46, 2011.

[72]. S. Boria, J. Obradovic, and G. Belingardi, "Experimental and numerical investigations of the impact behaviour of composite frontal crash structures," *Compos. Part B Eng.*, vol. 79, pp. 20–27, 2015.

[73]. Z. Liu, J. Lu, and P. Zhu, "Lightweight design of automotive composite bumper system using modified particle swarm optimizer," *Compos. Struct.*, 2016.

[74]. K. Saito, S. Hayashi, M. Kan, and M. Nishi, "A new modelling for Damage Initiation and Propagation of Randomly-Oriented Thermoplastic Composites," vol. 2, 2019.

[75]. G. Zhu, Z. Wang, A. Cheng, and G. Li, "Design optimisation of composite bumper

167

beam with variable cross-sections for automotive vehicle," *Int. J. Crashworthiness*, vol. 22, no. 4, pp. 365–376, 2017.

[76].   P. B. Ataabadi, D. Karagiozova, and M. Alves, "Crushing and energy absorption mechanisms of carbon fiber-epoxy tubes under axial impact," *Int. J. Impact Eng.*, 2019.

[77].   B. Harvey, "Private correspondence," MASc, University of Waterloo, Canada, 2019.

[78].   A. Suratkar, "Private correspondence," PhD, Western University, Canada, 2019.

[79].   J. Huang and X. Wang, "Numerical and experimental investigations on the axial crushing response of composite tubes," *Compos. Struct.*, vol. 91, no. 2, pp. 222–228, Nov. 2009.

[80].   E. Mahdi, A. M. S. Hamouda, and T. A. Sebaey, "The effect of fiber orientation on the energy absorption capability of axially crushed composite tubes," *Mater. Des.*, vol. 56, pp. 923–928, 2014.

[81].   A. G. Mamalis, D. E. Manolakos, M. B. Ioannidis, and D. P. Papapostolou, "Crashworthy characteristics of axially statically compressed thin-walled square CFRP composite tubes: Experimental," *Compos. Struct.*, vol. 63, no. 3–4, pp. 347–360, 2004.

[82].   R. Kalhor and S. W. Case, "The effect of FRP thickness on energy absorption of metal-FRP square tubes subjected to axial compressive loading," *Compos. Struct.*, vol. 130, no. 130, pp. 44–50, Oct. 2015.

[83].   X. X. Ã, M. E. Botkin, and N. L. Johnson, "Thin-Walled Structures Axial crush simulation of braided carbon tubes using MAT58 in LS-DYNA," vol. 47, pp. 740–749, 2009.

[84].   Y. Ren, H. Jiang, and W. Ji, "Improvement of Progressive Damage Model to Predicting Crashworthy Composite Corrugated Plate," pp. 45–66, 2018.

[85].   X. Zhao, G. Zhu, C. Zhou, and Q. Yu, "Crashworthiness analysis and design of composite tapered tubes under multiple load cases," *Compos. Struct.*, vol. 222, no. December

2018, p. 110920, 2019.

[86]. J. M. Starbuck, D. O. Adams, and M. Courteau, "Energy absorbing damage mechanisms in progressive crushing of composite tubes," *32nd Tech. Conf. Am. Soc. Compos. 2017*, vol. 2, pp. 1419–1432, 2017.

[87]. L. Pickett and V. Dayal, "Effect of tube geometry and ply-angle on energy absorption of a circular glass/epoxy crush tube - A numerical study," *Compos. Part B Eng.*, vol. 43, no. 8, pp. 2960–2967, 2012.

[88]. B. Rezaei, A. Niknejad, H. Assaee, and G. H. Liaghat, "Axial splitting of empty and foam-filled circular composite tubes - An experimental study," *Arch. Civ. Mech. Eng.*, vol. 15, no. 3, pp. 650–662, May 2015.

[89]. C. Peister, "Axial Crush Performance of Hot Stamped Tailor Welded Blanks," MASc thesis, University of Waterloo, Canada, 2019.

[90]. H. Luo, Y. Yan, X. Meng, and C. Jin, "Progressive failure analysis and energy-absorbing experiment of composite tubes under axial dynamic impact," *Compos. Part B*, vol. 87, pp. 1–11, 2016.

[91]. M. V. Kumar, "Design and Crash Analysis of Automotive Crush Box," vol. 2, no. July, 2017.

[92]. S. Boria, A. Scattina, and G. Belingardi, "Axial energy absorption of CFRP truncated cones," *Compos. Struct.*, vol. 130, no. 130, pp. 18–28, Oct. 2015.

[93]. C. Reuter, K. Sauerland, and T. Tröster, "Experimental and numerical crushing analysis of circular CFRP tubes under axial impact loading," *Compos. Struct.*, vol. 174, pp. 33–44, 2017.

[94]. A. G. Mamalis, D. E. Manolakos, G. A. Demosthenous, and M. B. Ioannidis, "Analytical modelling of the static and dynamic axial collapse of thin-walled fibreglass

composite conical shells," *Int. J. Impact Eng.*, 1997.

[95].   S. Patel, V. R. Vusa, and C. Guedes Soares, "Crashworthiness analysis of polymer composites under axial and oblique impact loading," *Int. J. Mech. Sci.*, 2019.

[96].   C. McGregor, R. Vaziri, and X. Xiao, "Finite element modelling of the progressive crushing of braided composite tubes under axial impact," *Int. J. Impact Eng.*, 2010.

[97].   C. McGregor, R. Vaziri, A. Poursartip, and X. Xiao, "Axial crushing of triaxially braided composite tubes at quasi-static and dynamic rates," *Compos. Struct.*, 2016.

[98].   H. Jiang, Y. Ren, and B. Gao, "Research on the progressive damage model and trigger geometry of composite waved beam to improve crashworthiness," *Thin-Walled Struct.*, vol. 119, no. September, pp. 531–543, 2017.

[99].   X. Han, S. Hou, L. Ying, W. Hou, and H. Aliyev, "On the fracture behaviour of adhesively bonded CFRP hat-shaped thin-walled beam under axial crushing load: An experimental and modelling study," *Compos. Struct.*, vol. 215, no. November 2018, pp. 258–265, 2019.

[100].   M. W. Joosten, S. Dutton, D. Kelly, and R. Thomson, "Experimental and numerical investigation of the crushing response of an open section composite energy absorbing element," *Compos. Struct.*, 2011.

[101].   P. Feraboli, B. Wade, F. Deleo, M. Rassaian, M. Higgins, and A. Byar, "Composites : Part A LS-DYNA MAT54 modeling of the axial crushing of a composite tape sinusoidal specimen," *Compos. Part A*, vol. 42, no. 11, pp. 1809–1825, 2011.

[102].   F. Deleo, B. Wade, P. Feraboli, P. Paolo, F. Uw, and M. R. B. R, "Crashworthiness of composite structures: experiment and simulation," *Am. Inst. Aeronaut. Astronaut.*, pp. 1–22, 2009.

[103].   Z. Zhang, W. Sun, Y. Zhao, and S. Hou, "Crashworthiness of different composite tubes

by experiments and simulations," *Compos. Part B Eng.*, 2018.

[104].   S. K. Krishnamoorthy, J. Höptner, G. Kopp, and H. E. Friedrich, "Prediction of structural response of FRP composites for conceptual design of vehicles under impact loading," *8th Eur. LS-DYNA User Conf.*, no. May, 2011.

[105].   S. Boria, "Sensitivity Analysis of Material Model Parameters to Reproduce Crushing of Composite Tubes," *J. Mater. Eng. Perform.*, vol. 28, no. 6, pp. 3267–3280, 2019.

[106].   M. Andersson and P. Liedberg, "Crash behavior of composite structures," MS thesis, Chalmers University, Sweden, pp. 23–54, 2014.

[107].   Dirk Lukaszewicz, "Automotive Composite structure for crashworthiness," *Adv. Compos. Mater. Automot. Appl.*, pp. 99–125, 2014.

[108].   S. Boria, J. Obradovic, and G. Belingardi, "Experimental and numerical investigations of the impact behaviour of composite frontal crash structures," *Compos. Part B*, vol. 79, pp. 20–27, 2015.

[109].   J. Wang *et al.*, "Design and experimental verification of composite impact attenuator for racing vehicles," *Compos. Struct.*, vol. 141, pp. 39–49, 2016.

[110].   D. O. E. Vto, S. Felix, D. S. A. Yocum, D. Board, and M. Jones, "Validation Of Material Models For Automotive Carbon Fiber Composite Structures Via Physical And Crash Testing (VMM Composites Project) U . S . Department of Energy (DoE) Final Closeout Technical Report," 2017.

[111].   S. H. Hesse, D. H. J. A. Lukaszewicz, and F. Duddeck, "A method to reduce design complexity of automotive composite structures with respect to crashworthiness," *Compos. Struct.*, vol. 129, pp. 236–249, 2015.

[112].   Y. Dixit *et al.*, "Full Frontal Crashworthiness of Carbon Fiber Composite Front Bumper Crush Can (FBCC) Structures," *Vol. 9 Mech. Solids, Struct. Fluids; NDE, Struct. Heal.*

Monit. Progn., p. V009T12A003, 2017.

[113].   C. Park, C. S. Kan, W. T. Hollowell, C. S. Kan, and W. T. Hollowell, "Evaluation of crashworthiness of a carbon-fibre- reinforced polymer (CFRP) ladder frame in a body- on-frame vehicle," vol. 8265, 2014.

[114].   F.-K. Chang and K.-Y. Chang, "A Progressive Damage Model for Laminated Composites Containing Stress Concentrations," *J. Compos. Mater.*, vol. 21, no. 9, pp. 834–855, Sep. 1987.

[115].   A. Matzenmiller, J. Lubliner, and R. L. Taylor, "A constitutive model for anisotropic damage in fiber-composites," *Mech. Mater.*, vol. 20, no. 2, pp. 125–152, Apr. 1995.

[116].   L. Software Technology Corporation, "LS-DYNA ® KEYWORD USER'S MANUAL VOLUME II Material Models LIVERMORE SOFTWARE TECHNOLOGY CORPORATION (LSTC)," 2014.

[117].   Z. Hashin, "Failure criteria for unidirectional fiber composites," *J. Appl. Mech. Trans. ASME*, vol. 47, no. 2, pp. 329–334, Jun. 1980.

[118].   S. T. Pinho, L. Iannucci, and P. Robinson, "Physically based failure models and criteria for laminated fibre-reinforced composites with emphasis on fibre kinking. Part II: FE implementation," *Compos. Part A Appl. Sci. Manuf.*, vol. 37, no. 5, pp. 766–777, May 2006.

[119].   S. T. Pinho, L. Iannucci, and P. Robinson, "Physically-based failure models and criteria for laminated fibre-reinforced composites with emphasis on fibre kinking: Part I: Development," *Compos. Part A Appl. Sci. Manuf.*, vol. 37, no. 1, pp. 63–73, Jan. 2006.

[120].   P. Maimí, P. P. Camanho, J. A. Mayugo, and C. G. Dávila, "A continuum damage model for composite laminates: Part I - Constitutive model," *Mech. Mater.*, vol. 39, no. 10, pp. 897–908, Oct. 2007.

[121].   C. Mcgregor, R. Vaziri, and X. Xiao, "International Journal of Impact Engineering

Finite element modelling of the progressive crushing of braided composite tubes under axial impact," *Int. J. Impact Eng.*, vol. 37, no. 6, pp. 662–672, 2010.

[122].   X. Han, S. Hou, L. Ying, W. Hou, and H. Aliyev, "On the fracture behaviour of adhesively bonded CFRP hat-shaped thin-walled beam under axial crushing load: An experimental and modelling study," *Compos. Struct.*, 2019.

[123].   R. Kalhor, H. Akbarshahi, and S. W. Case, "Numerical modeling of the effects of FRP thickness and stacking sequence on energy absorption of metal-FRP square tubes," *Compos. Struct.*, 2016.

[124].   M. Osborne, "Single-Element Characterization of the LS-DYNA MAT54 Material Model," 2012.

[125].   W. Bonnie and P. Faraboli, "Crushing Behavior of Laminated Composite Structural Elements : Experiment and LS-DYNA Simulation," 2016.

[126].   B. Watson, C.-H. Liao, M. J. Worswick, and D. S. Cronin, "Mode I traction-separation measured using rigid double cantilever beam applied to structural adhesive," *J. Adhes.*, vol. 96, no. 8, pp. 717–737, Jun. 2020.

[127].   Y. B. Liu, "Application of a Rate Dependent Cohesive Zone Model to Predict Impact Response in Adhesively Bonded Ultra-High Strength Steel Tubes," PhD thesis, University of Waterloo, Aug. 2019.

[128].   V. Tvergaard and J. W. Hutchinson, "THE RELATION BETWEEN CRACK GROWTH RESISTANCE AND FRACTURE PROCESS PARAMETERS IN ELASTIC-PLASTIC SOLIDS," 1992.

[129].   B. M. Khaled, L. Shyamsunder, N. Holt, C. G. Hoover, S. D. Rajan, and G. Blankenhorn, "Enhancing the predictive capabilities of a composite plasticity model using cohesive zone modeling," *Compos. Part A Appl. Sci. Manuf.*, vol. 121, pp. 1–17, Jun. 2019.

[130]. S. Marzi, O. Hesebeck, M. Brede, and F. Kleiner, "A Rate-Dependent, Elasto-Plastic Cohesive Zone Mixed-Mode Model for Crash Analysis of Adhesively Bonded Joints," 2009.

[131]. T. Achstetter, "Development of a Composite Material Shell-Element Model for Impact Applications." PhD thesis, George Mason University, United States of America, 2020.

[132]. S. J. DeTeresa *et al.*, "Experimental Results in Support of Simulating Progressive Crush in Carbon-Fiber Textile Composites," Livermore, CA (United States), Apr. 2001.

[133]. A. Sheldon, S. Dong, L. Graening, and K. Carney, "Parametric Optimization of CAE Material Models for Carbon-Fiber-Reinforced Polymer (CFRP) Composites Parametric Optimization of CAE Material Models for," *Present. NAFEMS World Congr. 2017*, no. July, 2017.

[134]. C. Gui, J. Bai, and W. Zuo, "Simplified crashworthiness method of automotive frame for conceptual design," *Thin-Walled Struct.*, 2018.

[135]. W. Xu and G. Li, "Finite difference three-dimensional solution of stresses in adhesively bonded composite tubular joint subjected to torsion," *Int. J. Adhes. Adhes.*, vol. 30, no. 4, pp. 191–199, Jun. 2010.

[136]. S. Malcolm, H. R&d, E. Nutwell, and A. Engineering, "6th European LS-DYNA Users' Conference 2.2.2 2.47 Spotweld Failure Prediction using Solid Element Assemblies."

[137]. R. R. Ambriz and D. Jaramillo, "Mechanical Behavior of Precipitation Hardened Aluminum Alloys Welds," in *Light Metal Alloys Applications*, InTech, 2014.

[138]. "Damage and Failure of Composite Materials - Ramesh Talreja, Chandra Veer Singh" ,2012.

[139]. S. Pilla, C. Lu, R. Cox, and J. D. Rehkopf, "Other SAE books of interest: Design of Automotive Composites Engineered Tribological Composites Automotive Carbon Fiber Composites," 2015.

Appendix A

The MAT 54 material card consists of nine rows and eight columns of data blocks.

Cards 1 and 2 (blue variables) represent the orthotropic elastic material parameters for the fiber and transverse directions. The material model assumes plane stress condition using shell elements in LS-DYNA. The out of plane stress definition σ_{cc} is zero which implies that delamination mode of failure dependent on Z-stress were not predicted using MAT 54 material model.

Cards 3 and 4 (red variables) controls the principal material direction for each element in numerical model. To control the anisotropic behavior of composites, it is essential to define the material directions (AOPT) based on either global, local material (lamina), or elemental (laminate) coordinate systems.

Card 5 (green variables) represents the strain-to-failure (DFAIL) parameters and additional non-physical parameters. The strain parameters control the lamina failure were the elements eroded upon reaching the failure strains. Card 6 represents the strength parameters for each directions and material selection parameter (CRIT) to define the material model. Cards 7 and 8 consists of some additional parameter for the composite material model.

Table A1. LS-DYNA MAT 54 material card.

	1	2	3	4	5	6	7	8
Card 1	MID	RO	EA	EB	(EC)	PRBA	(PRCA)	(PRCB)
Card 2	GAB	GBC	GCA	(KF)	AOPT			
Card 3				A1	A2	A3	MANGLE	
Card 4	V1	V2	V3	D1	D2	D3	DFAILM	DFAILS
Card 5	TFAIL	ALPH	SOFT	FBRT	YCFAC	DFAILT	DFAILC	EFS
Card 6	XC	XT	YC	YT	SC	CRIT	BETA	
Card 7	PFL	EPSF	EPSR	TSMD	SOFT2			
Card 8	SLIMT1	SLIMC1	SLIMT2	SLIMC2	SLIMS	NCYREF	SOFTG	
Card 9	LCXC	LCXT	LCYX	LCYC	LCSC	DT		

In Table A2 each parameter in the MAT 54 is explained with a short description.

Table A2. Description of MAT 54 material card parameters.

Parameter	Description
MID	LS-DYNA - Material Identification Number
RO	Mass density
EA	Youngs Modulus in longitudinal direction, E_1
EB	Youngs Modulus in transverse direction, E_2
(EC)	Youngs Modulus in normal direction, E_3
PRBA	Minor Poisson's ratio, v_{21}
(PRCA)	Minor Poisson's ratio, v_{23}
(PRCB)	Minor Poisson's ratio, v_{31}
GAB	Shear Modulus, G_{12}
GBC	Shear Modulus, G_{23}
GCA	Shear Modulus, G_{32}
(KF)	Bulk Modulus
AOPT	Principle Material Direction option
A1, A2, A3	For AOPT-2 A vector components
MANGLE	For AOPT-0 Material Angle
V1, V2, V3	For AOPT-3 V vector components
D1, D2, D3	For AOPT-2 D vector components
DFAILM	Maximum strain of matrix in tensile and compression modes
DFAILS	Maximum tensorial shear strain
TFAIL	Time step size for elemental degradation
ALPH	Nonlinear shear strain parameter
SOFT	Softening factor for crash front elements
FBRT	Softening parameter for fiber tensile strength
YCFAC	Softening parameter for fiber compressive strength
DFAILT	Maximum strain in fiber tension
DFAILC	Maximum strain in fiber compression
EFS	Effective failure strain

XC	Compressive Strength in fiber direction
XT	Tensile Strength in fiber direction
YC	Compressive Strength in matrix direction
YT	Tensile Strength in matrix direction
SC	Shear Strength
CRIT	Failure Criteria to select
BETA	Shear Stress weighing factor in fiber tensile mode
PFL	Percentage of layer failure
EPSF	Transverse shear strain damage initiation
EPSR	Transverse shear strain for final rupture
TSMD	Transverse shear maximum damage
SOFT2	Orthogonal softening reduction factor
SLIMT1	Minimum stress limit factor after maximum stress in fiber tension.
SLIMC1	Minimum stress limit factor after maximum stress in fiber compression.
SLIMT2	Minimum stress limit factor after maximum stress in matrix tension.
SLIMC2	Minimum stress limit factor after maximum stress in matrix compression.
SLIMS	Minimum stress limit factor after maximum shear.
NCYRED	Number of cycles for stress reduction
SOFTG	Softening factor for transverse shear
LCXC	Load curve ID for XC vs Strain rate
LCXT	Load curve ID for XT vs Strain rate
LCYC	Load curve ID for YC vs Strain rate
LCYT	Load curve ID for YT vs Strain rate
LCSC	Load curve ID for SC vs Strain rate
DT	Strain rate average

Appendix B

MAT 58 material model consists of nine rows and eight columns of data blocks.

Table B1. LS-DYNA MAT 58 material card.

	1	2	3	4	5	6	7	8
Card 1	MID	RO	EA	EB	(EC)	PRBA	TAU1	GAMMA1
Card 2	GAB	GBC	GCA	SLIMT1	SLIMC1	SLIMT2	SLIMC2	SLIMS
Card 3	AOPT	TSIZE	ERODS	SOFT	FS	EPSF	EPSR	TSMD
Card 4	XP	YP	ZP	A1	A2	A3	PRCA	PRCB
Card 5	V1	V2	V3	D1	D2	D3	BETA	
Card 6	E11C	E11T	E22C	E22T	GMS			
Card 7	XC	XT	YC	YT	SC			
Card 8	LCXC	LCXT	LCYT	LCSC	LCTAU	LCGAM	DT	
Card 9	LCE11C	LCE11T	LCE22C	LCE22T	LCGMS			

Card 1 and card 2 (blue variables) represent the orthotropic elastic material parameters for the fiber transverse directions. The material model assumes plane stress condition using shell elements in LS-DYNA.

Card 2 and card 3 (green variables) defines the non-physical parameters of the material model. The SLIM - residual stress parameter for each direction. ERODS parameter controls the elemental deletion after lamina failure. Some additional parameters like SOFT- controls crash front algorithms and FS parameter to select the choice of material likewise UD lamina or woven fabrics.

Card 4 & 5 (red variables) controls the principal material direction for each element in numerical model. To control the anisotropic behavior of composites it is essential to define AOPT which provides the material directions based on global, local material (lamina), or elemental (laminate) coordinate systems.

Card 6 (green variables) defines the strain-to-failure parameter and Card 7 has the strength parameters for each direction. Card 8 and Card 9 consists of strain rate dependent strength and strains for the composite material model.

In Table B2 each parameter in the MAT 58 is explained with a short description.

Table B2. Description of MAT 58 material card parameters.

Parameter	Description
MID	LS-DYNA - Material Identification Number
RO	Mass density
EA	Youngs Modulus in longitudinal direction, E_1
EB	Youngs Modulus in transverse direction, E_2
(EC)	Youngs Modulus in normal direction, E_3
PRBA	Minor Poisson's ratio, v_{21}
TAU1	Stress limit of Shear stress vs shear strain curve
GAMMA1	Strain limit of Shear stress vs shear strain curve
GAB	Shear Modulus, G_{12}
GBC	Shear Modulus, G_{23}
GCA	Shear Modulus, G_{32}
SLIMT1	Minimum stress limit factor after maximum stress in fiber tension.
SLIMC1	Minimum stress limit factor after maximum stress in fiber compression.
SLIMT2	Minimum stress limit factor after maximum stress in matrix tension.
SLIMC2	Minimum stress limit factor after maximum stress in matrix compression.
SLIMS	Minimum stress limit factor after maximum shear.
AOPT	Principle Material Direction option
TFAIL	Time step size for elemental degradation
ERODS	Effective failure strain
SOFT	Softening factor for crash front elements
FS	Failure surface types
EPSF	Transverse shear strain damage initiation
EPSR	Transverse shear strain for final rupture
TSMD	Transverse shear maximum damage
XP, YP, ZP	For AOPT-1 P vector components

A1, A2, A3	For AOPT-2 A vector components
EFS	Effective failure strain
(PRCA)	Minor Poisson's ratio, v_{23}
(PRCB)	Minor Poisson's ratio, v_{32}
V1, V2, V3	For AOPT-3 V vector components
D1, D2, D3	For AOPT-2 D vector components
BETA	Shear Stress weighing factor in fiber tensile mode
E11C	Maximum strain in fiber compression
E11T	Maximum strain in fiber tension
E22C	Maximum strain in matrix compression
E22D	Maximum strain in matrix tension
GMS	Maximum strain in shear
XC	Compressive Strength in fiber direction
XT	Tensile Strength in fiber direction
YC	Compressive Strength in matrix direction
YT	Tensile Strength in matrix direction
SC	Shear Strength
LCXT	Load curve ID for XT vs Strain rate
LCYC	Load curve ID for YC vs Strain rate
LCYT	Load curve ID for YT vs Strain rate
LCSC	Load curve ID for SC vs Strain rate
LCTAU	Load curve ID for TAU1 vs Strain rate
LCGAM	Load curve ID for GAMMA1 vs Strain rate
DT	Strain rate average
LCE11C	Load curve ID for E11C vs Strain rate
LCE11T	Load curve ID for E11T vs Strain rate
LCE22C	Load curve ID for E22C vs Strain rate
LCE22T	Load curve ID for E22T vs Strain rate